TECHNISCHE UNIVERSITÄT MÜNCHEN

Physik-Department
Lehrstuhl für Funktionelle Materialien

Tailoring titania nanostructures for application in solar cells

Nian Li

Vollständiger Abdruck der von der Fakultät für Physik der Technischen Universität München zur Erlangung des akademischen Grades eines

Doktors der Naturwissenschaften (Dr. rer. nat.)

genehmigten Dissertation.

Vorsitzender:	Prof. Dr. Martin Zacharias
Prüfer der Dissertation:	1. Prof. Dr. Peter Müller-Buschbaum
	2. Prof. Dr. Aliaksandr Bandarenka

Die Dissertation wurde am 09.08.2021 bei der Technischen Universität München eingereicht und durch die Fakultät für Physik am 13.10.2021 angenommen.

Abstract

In the present work, the upscale fabrication of titania films and optimization of their optoelectronic properties are studied for application in hybrid solar cells, quantum dot-sensitized solar cells, and perovskite solar cells. Within this scope, slot-die printing is used with the combination of a so-called block-copolymer-assisted sol-gel synthesis, with which the titania nanostructures are precisely tailored. The correlation between the crystalline properties of the polymers P3HT and PffBT4T-2OD and titania pore sizes is revealed. This is an essential knowledge required to optimize the crystallization behavior of P3HT and PffBT4T-2OD for hybrid solar cell applications. Moreover, by using in situ grazing-incidence small-angle X-ray scattering, the kinetic development of titania/PS-b-PEO hybrid structures during slot-die printing is investigated, which allows to understand the slot-die printing process and to fully exploit the potential of mesoporous titania films for scaling up solar cell fabrication. Furthermore, due to the advantages of Ge and its oxides, it is hypothesized that their introduction could improve the electronic (and optical) characteristic of TiO_2 for solar cell applications. Therefore, germanium nanocrystals (GeNCs) are introduced into a diblock-copolymer-templating sol-gel synthesis to fabricate ordered mesoporous TiO_2/GeO_x nanocomposite films for use as efficient photoanodes. The GeNC addition enhances the electron transfer, yielding an increase in short-circuit current density of exemplary perovskite solar cells and thus an enhanced device efficiency as well as a significantly reduced hysteresis.

Zusammenfassung

In der vorliegenden Arbeit werden die hochskalierbare Herstellung von Titandioxidfilmen und die Optimierung ihrer optoelektronischen Eigenschaften für die Anwendung in Hybridsolarzellen, Quantenpunkt-sensibilisierten Solarzellen und Perowskit-Solarzellen untersucht. In diesem Rahmen wird Slot-Die-Druck in der Kombination mit einer sogenannten Blockkopolymer-unterstützten Sol-Gel-Synthese verwendet, mit der die Titandioxid-Nanostrukturen präzise maßgeschneidert werden. Es wird die Korrelation zwischen den kristallinen Eigenschaften der Polymere P3HT und PffBT4T-2OD und den Porengrößen von Titandioxid ermittelt. Das ist erforderliches Wissen, um das Kristallisationsverhalten von P3HT und PffBT4T-2OD für Hybridsolarzellenanwendungen zu optimieren. Darüber hinaus wird durch die Verwendung von in situ Röntgen-Kleinwinkel-streuung unter streifendem Einfall die kinetische Entwicklung von Titanoxid/PS-b-PEO-Hybridstr-

ukturen während des Slot-Die-Drucks untersucht, worauf das erlangte Verständnis des Slot-die Druchkprozesses es ermöglicht, das Potenzial mesoporöser Titandioxidfilme für die Skalier- ung der Solarzellenherstellung voll auszuschöpfen. Darüber hinaus wird aufgrund der Vorteile von Ge und seinen Oxiden angenommen, dass deren Hinzunahme die elektronischen (und optischen) Eigenschaften von TiO_2 für Solarzellenanwendungen verbessern könnte. Dazu werden Germanium-Nanokristalle (GeNCs) in eine Diblock-Copolymer-Templat-Sol-Gel-Synthese eingeführt, um geordnete mesoporöse TiO_2/GeO_x-Nanokompositfilme zur Verwendung als effiziente Photoanoden herzustellen. Die Zugabe von GeNC verbessert den Elektronentransfer, was zu einer Erhöhung der Kurzschlussstromdichte repräsentativer Perowskit-Solarzellen und damit zu einer verbesserten Solarzelleffizienz sowie einer deutlich reduzierten Hysterese führt.

Contents

List of abbreviations

BCC ..... body-centered cubic

BHJ ..... bulk-heterojunction

CB ..... conduction band

DSSC ..... dye-sensitized solar cell

DWBA ..... distorted wave Born approximation

ETL ..... electron-transporting layer

FCC ..... fce-centered cubic

FF ..... fill factor

FTO ..... fluorine doped tin oxide, SnO_2:F

FWHM ..... full width at half maximum

GIS ..... grazing incidence scattering

GISAXS ..... grazing incidence small angle x-ray scattering

GIWAXS ..... grazing incidence wide angle x-ray scattering

HCl ..... hydrochloric acid

HOMO ..... highest occupied molecular orbital

HSC ..... hybrid solar cell

J/V ..... current density-voltage characteristics

J_{sc} ..... short-circuit current density

LUMO ..... lowest unoccupied molecular orbital

MPP ..... maximum power point

PL	photoluminescence
PS-b-PEO	polystyrene-block-polyethylene oxide
PSC	perovskite solar cell
QDSSC	quantum dot-sensitized solar cell
SDD	sample-detector distance
SEM	scanning electron microscopy
SLD	scattering length density
spiro-OMeTAD	2,2',7,7'-tetrakis(N,N di- *p*-methoxyphenyl-amine)9,9'-spiro-bifluorene
ssDSSC	solid-state dye-sensitized solar cell
TRPL	time-resolved photoluminescence
TTIP	titanium(IV)isopropoxide
UV/Vis	UV/Vis spectroscopy
V_{oc}	open-circuit voltage
VB	valence band
XPS	X-ray photoelectron spectroscopy
XRD	X-ray diffraction

1 Introduction

With the continuous development of industry, the demand for large energy consumption has attracted much attention. Most required energy is produced from the combustion of fossil fuels, such as oil, coal or natural gas [1]. However, these fuel resources become less and less, and simultaneously the environmental pollution caused by overuse of fossil fuels becomes more and more serious. To solve these problems, it is necessary to put forward an aim of developing sustainable and environmental-friendly energy technologies. Among the different renewable energy technologies, solar photovoltaics, which can convert solar energy into electricity, is a promising strategy, thereby gaining a large quantity of interest from researchers. With the last decades, various photovoltaic technologies emerged.

First generation solar cells are based on the crystalline and polycrystalline silicon, which still dominates the current photovoltaic market. Second generation solar cells are based on amorphous silicon and cadmium telluride (CdTe) and copper indium (gallium) diselenide (CIS or CIGS), which can be fabricated as thin-film solar cells. However, the rare elements applied in these materials and larger energy consumption limit their market expansion [2].

With the target of high efficiency and low cost, third generation solar cells have been extensively developed. Among these photovoltaics, polymer-inorganic hybrid solar cells (HSCs) [1], dye-sensitized solar cells (DSSCs) [3], quantum dot-sensitized solar cells (QDSSCs) [4] and perovskite solar cells (PSCs) [5] have established their prominence in this solar energy field. In particular, perovskite solar cells have reached an excellent efficiency of 25.5% [6], which holds high potential for the commercial application in the future. In these devices, inorganic semiconductors mainly act as the electron-transport layer, while in some cases they may also play as the scaffold for light harvesters [7]. Of many semiconductor metal oxides, titania (TiO_2) appears to be a favorable candidate, due to its high electron mobility [8], chemical and optical stability [9], low cost and non-toxicity [10].

In the present thesis, the main focus is chosen on titania-based hybrid active layers for HSCs, QDSSCs and PSCs, which use different light-absorbing materials, i.e. the donor polymer, quantum dots and perovskite compounds. In special, the titania morphology defines the interface area and provides pathways for charge carrier transport, thus influencing the final device performance [11, 12]. A promising route for producing nanostructured

TiO_2 films with interconnected network structures (and a high surface-to-volume ratio) is sol-gel chemistry with the combination of a diblock-copolymer template. This technique has proven to be a successful route to control the nanoparticle sizes and pore sizes of titania films [13–15].

Today, most research of such kind of wet chemical TiO_2 film fabrication focus on laboratory-scale deposition methods. As compared to these, the up-scale manufacturing technique such as slot-die printing, which opens the possibility for producing inorganic semiconductors on an industrial scale, deserves more attention. In addition to the large-scale fabrication of titania films, one also needs to focus on tailoring titania films to achieve better photovoltaic device performance by introducing metals, metal oxides, or semiconductors into the mesoporous titania. Since titania is used as an electron transport layer which is a necessary part of the functional stack forming the final device, also the optimization of its properties, such as electronic and optical characteristics, will be needed for further improvements in the device performance.

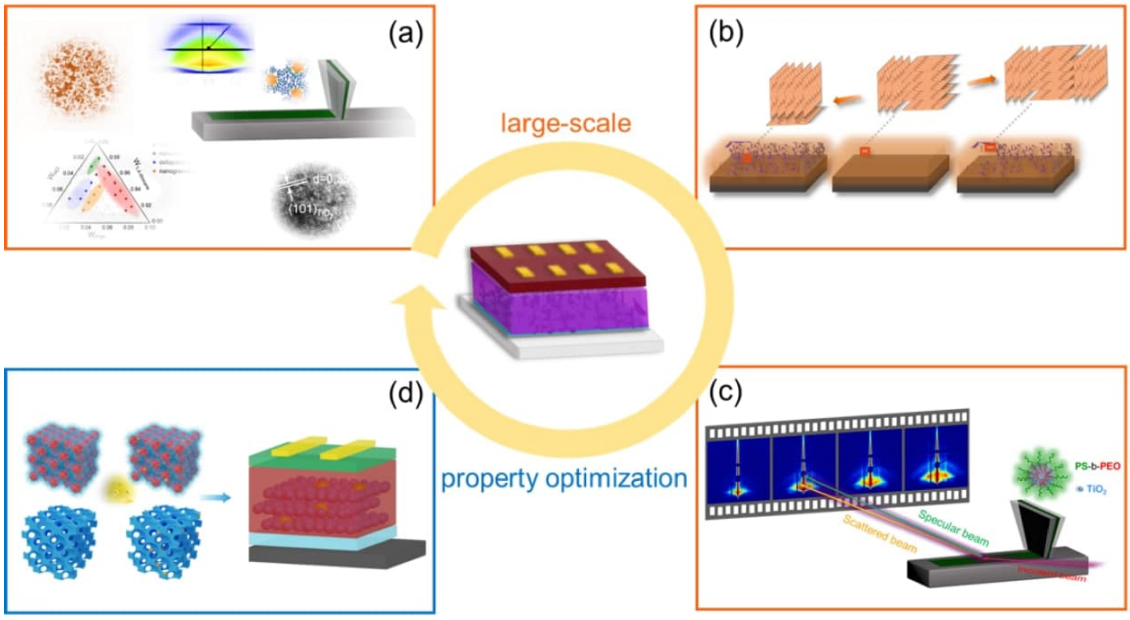

Figure 1.1: Schematic illustration of a titania-based thin-film solar cell with different research topics in the present thesis: (a) Morphology tailoring of slot-die printed titania films, (b) crystallization of a low band gap polymer in the printed titania mesopores, (c) structure evolution during slot-die printing, and (d) tailoring titania films via introducing germanium nanocrystals for efficient photoanodes.

The main target of the present thesis is to address the up-scale manufacturing of mesoporous TiO_2 films, the correlation between morphology and active layer (and solar cell

performance), and the optimization of optoelectronic properties of titania films. First, the theoretical background is introduced in chapter 2, including the synthesis of nanostructured titania films, titania based solar cells and the basic principle of X-ray scattering methods for investigating the film structures. Chapter 3 describes the characterization methods used in this thesis, followed by the sample preparation in chapter 4. Next, the research results are discussed from chapter 5 to chapter 8. Figure 1.1 shows an overview of four different research topics.

Slot-die printing is a simple and cost-effective thin-film deposition technique that is readily compatible with different kinds of solutions [16]. Based on this technique, which is favorable in industry, TiO_2 films can be easily prepared on a large scale. In chapter 5, by adjusting the weight fraction of reactants, the ternary morphology phase diagram of the printed titania films is probed after template removal. Various titania morphlogies, including foam-like nanostructures, nanowire aggregates, collapsed vesicles and nanogranules, are discussed. Moreover, the foam-like titania nanostructures are studied in detail since this type of morphology is highly desirable for solar cell applications.

In addition to the titania film with a bicontinuous network and a suitable pore size, a high degree of crystallinity of the conjugated polymer and its backbone orientation in face-on direction with respect to the substrate also play a significant role on the efficiency of bulk heterojunction (BHJ) HSCs [17, 18]. Therefore, in chapter 6, the correlation between the crystallization behavior of the low band gap polymer PffBT4T-2OD and the pore size of slot-die printed mesoporous titania films is studied. For a comparison, P3HT is also backfilled into the same different types of printed mesoporous scaffolds. The key properties, namely lattice constant, crystal sizes and orientations of both polymers, are extracted and correlated to the titania pore sizes.

As mentioned in the above two chapters, slot-die printing is used to fabricate mesoporous titania films. A fundamental understanding of the structure evolution during printing is of high significance in tailoring titania films. In chapter 7, important insights into the self-assembly of the slot-die printed titania/polystyrene-block-polyethylene oxide (PS-b-PEO) micelles into ordered hybrid structures are provided. After calcination, the surface and inner morphologies of the obtained nanostructured titania films are compared with the spin-coated analogs. Finally, the mesoporous TiO_2 film via slot-die printing is applied in QDSSCs.

In addition to the morphology tailoring of titania films, the optimization in its optoelectronic property is also of especial importance for device performance. In chapter 8, the hypothesis that the introduction of germanium nanocrystals (GeNCs) could improve the electronic and optical characteristics of TiO_2 for solar cell applications, is investigated. Based on a diblock-copolymer templated sol-gel synthesis, GeNCs are introduced

to fabricate mesoporous TiO_2/GeO_x nanocomposite films. The morphology, crystal phase, chemical composition and optical properties of the nanocomposite films are examined after thermal annealing in air and compared with films undergoing an argon annealing. Specifically, the charge-carrier dynamics of the air-annealed TiO_2/GeO_x nanocomposite films are studied, and this kind of nanocomposite films is used in PSCs. Accordingly, the correlation between the charge-carrier dynamics of the functional stacking layers, the mesoporous TiO_2-GeNC/perovskite system, and the photovoltaic performance of the exemplary perovskite solar cells is discussed. Moreover, the device performance is also correlated to the pore sizes of the nanocomposite films.

The final chapter 9 summarizes the major finding of the present thesis, and simultaneously gives a brief outlook for further studies.

2 Theoretical aspects

The present chapter introduces basic theoretical aspects releted to titania-based solar cells. In section 2.1, mesoporous titania, as an electron-transporting layer (ETL) is discussed, mainly regarding its properties and its fabrication. Afterwards, a brief overview about titania-based solar cells is present in section 2.2. As a significant method to probe thin films, accordingly, basic concepts and principles of X-ray scattering are emphasized in the final section 2.3.

2.1 Synthesis of nanostructured titania films

Nanostructured titania, especically in anatase phase, has been widely applied as an ETL due to its wide bandgap, long charge-carrier lifetime and high electron mobility [19, 20]. Nanostructured TiO_2 films with a high surface-to-volume ratio and an interconnected network morphology, e.g., in the type of mesoporous TiO_2 structures, are desirable in solar cell applications [21]. Fabrication and structural control of mesoporous titania films, and fundamental understanding of its structure evolution are the key objectives. In this thesis, a so-called diblock-copolymer template-assisted sol-gel synthesis route is liked for the fabrication of mesoporous titania films with nanostructures. Therefore, the basic propertis of titania are introduced in section 2.1.1, followed by an overview of backgrounds of the diblock copolymer template and its phase separation in section 2.1.2. Related reactions for Ti-O cross-linking and 3D network formation are explained in section 2.1.3. In the last section 2.1.4, the sol-gel synthesis and a diblock copolymer template are combined to tailor titania strutcures.

2.1.1 Basic properties of titania

TiO_2 has three polymorphs, anatase, rutile and brookite [22]. All these three phases exhibit high density, high refractive index and large band gap. The detailed parameters are included in Table 2.1. Both, anatase and brookite are metastable, while rutile is the stable phase. Due to the difficulties in syntehsis of a pure phase, brookite has been rarely

Crystal phase	Density (g cm^{-3})	Refractive index	Band gap
Anatase	3.83	2.57	3.2
Rutile	4.24	2.95	3.0
Brookite	4.17	2.81	3.1-3.4

Table 2.1: Basic properties of titania: crystal phases and their corresponding refractive index, density and energy bandgap [23, 25–27].

studied [23, 24]. Therefore, two important polymorphs, anatase and rutile, are mainly discussed in this section.

The crystal structures and crystal parameters, the Ti-Ti interatomic distances, and the O-Ti-O bond angles for these two phases [28, 29], are shown in Figure 2.1. Both anatase and rutile are tetragonal, in which each Ti atom is coordinated to six O atoms and each O atom coordianted to three Ti atoms. Moreover, in both cases, the TiO_6 octahedron is slightly distorted with two different Ti-Ti bond distances and some of the O-Ti-O bond angles deviating from 90° [30]. The distortion in anatase is larger than in rutile. In rutile, the octahedrons bond to each other at opposite edges, which leads to a linear packing of the octahedrons. While in anatase, the highly distorted octahedrons bond to each other at adjacent edges, resulting in a zigzag packing of the octahedrons. In contrast, this linear packing of TiO_6 octahedron in rutile leads to shorter Ti-Ti distances (3.57 Å and 2.96 Å) than that in anatase (3.79 Å and 3.04 Å) [20]. Therefore, the value of volume per molecule is higher for anatase. Moreover, this closer packing is also the reason why the rutile phase exhibits higher density and thermodynamical stability.

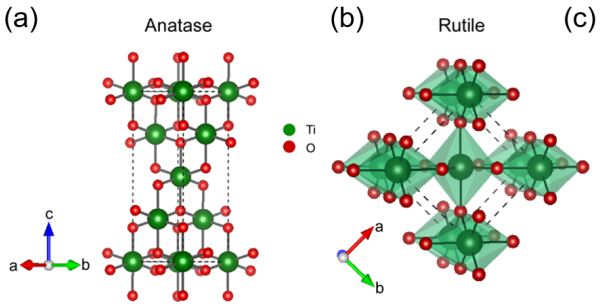

	Anatase	Rutile
Lattice constants (Å)	a = 3.784 c = 9.515	a = 4.5936 c = 2.9587
Space group	$I4_1/amd$	$P4_2/mnm$
Molecule/cell	4	2
Volume/molecule (Å^3)	34.061	31.2160
Ti-Ti bond length (Å)	3.79 3.04	3.57 2.96
O-Ti-O bond angle	77.7° 92.6°	81.2° 90.0°

Figure 2.1: Crystal structures of titania with their corresponding crystal parameters. The parameters are based on [28, 29].

Anatase and rutile are both indirect semiconductors, with band gaps of 3.0 eV and 3.2 eV [26, 31], respectively. These large band gaps allow for a good UV absorbing ability.

The absorption edge of anatase titania appears at the wavelength of 388 nm [32] and the absorption edge of rutile titania at 410 nm [33]. Therefore, titania can be used in sun protection cream to prevent UV irradiation. Also, for solar cells including organic materials, the compact titania film is an alternative choice as a rather electron conducting (or hole blocking) layer, which hinders UV light from irradiating photoactive polymers or molecules.

In addition to crystallinity, the grain size of titania nanoparticles is also an important aspect. As well known, nanostructured titania with a high surface-to-volume ratio has many applications, such as photocatalysis, lithium-ion batteries and photovoltaics. When the titania grain size decreases to nanoscale lengths, smaller than its exciton Bohr radius, quantum size effects occur as excitions are squeezed [34]. With these effects influencing electronic and optical properties of titania, a smaller titania size normally leads to a larger band gap [35]. For example, the indirect band gap of mesoporous titania (around 3.4 eV) is slightly larger than that of bulk anatase TiO_2 (3.2 eV) [36]. Increased optical band gap have also been reported in other nanostructured titania films such as nanotube arrays [37]. In addition, these nanoscale-size structures with a high surface-to-volume ratio induce a high density of trap states [38], since most defects might appear on the surface.

2.1.2 Diblock copolymers

Diblock copolymers consist of two blocks of different homopolymers A and B, which covalently bond together. This kind of polymer is named as polyA-block-polyB, or in short PA-b-PB. The degree of polymerization N_A and N_B of each block represents the number of monomeric repeating units. The volume fractions f_A and f_B can be calculated as

$$f_A = \frac{V_A}{V_A + V_B} \tag{2.1}$$

$$f_B = \frac{V_B}{V_A + V_B} = 1 - f_A \tag{2.2}$$

Segment-segment interactions in block copolymers are commonly described by the Flory-Huggins interaction parameter χ [39, 40], which is determined by Equation 2.3. It specifies the degree of incompatibility between block A and B.

$$\chi = \chi_S + \frac{\chi_H}{T} \tag{2.3}$$

where χ_S and χ_H are often considered as entropic and enthalpic contributions, respectively and T the temperature. With a smaller value of χ, the interaction between block A and B is more favorable and a mixing phase is promoted. Generally, diblock copolymers with immiscible blocks will undergo microphase separation and self-assemble into a variety of morphologies, e.g. body-centered cubic (BCC) spheres, hexagonally-packed cylinders, bicontinuous gyroids, and lamellae (Figure 2.2). This process is driven by a small mixing entropy and an unfavorable enthalpy. Besides, the covalent bond linking two blocks, which prevent phase separation also needs to be considered. The microphase separation of diblock copolymers is related to three parameters: the total degree of polymerization (N = N_A +N_B), the volume fractions of block A and B (f_A, f_B), and the χ parameter.

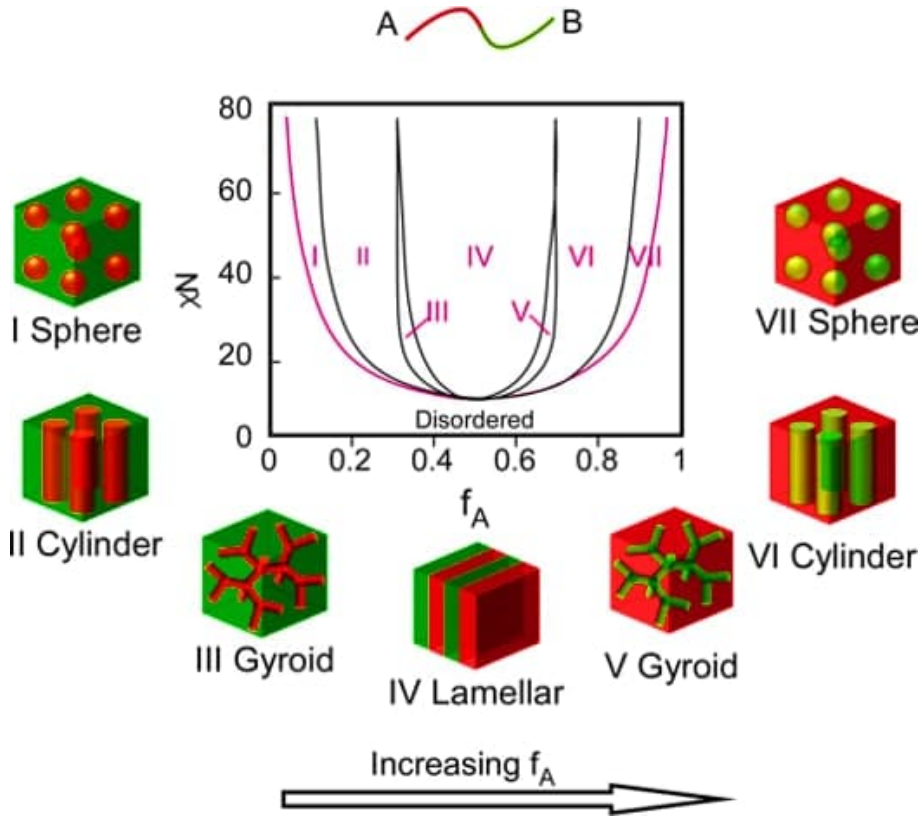

Figure 2.2: Theoretical phase diagram of AB diblock copolymer. The order-to-order structures are indicated as: body-centered cubic spheres, hexagonally packed cylinders, bicontinuous gyroids, and lamellae.The red line indicates the order-to-disorder transition. The figure is based on [41].

The degree of microphase separation depends on the segregation product, χN. With decreasing χN, or increasing temperature, the incompatibility between two blocks decreases, while combinatorial entropy increases. Copolymers exhibit order-to-disorder transition

(ODT) and form disordered structures. In the case of a symmetric diblock copolymer (f_A = 0.5), the critical point of χN is around 10.5 [42]. For $\chi N < 10.5$, a disordered phase is obtained. Close to 10.5, the segregation strength is weak and thus the so-called weak segregation limit (WSL) is introduced. For $\chi N \gg 10.5$, the segregation strength is strong and two blocks can fully separate with well-defined interfaces. As a result, the strong segregation limit (SSL) is observed [43].

Via the self-consistent mean-field (SCMF) theory, the phase diagram of diblock copolymers is predicted [42, 43], as shown in Figure 2.2. With a fixed χN above the ODT and increasing f_A, the morphologies start from body-centered cubic spheres, passing through hexagonally packed cylinders and bicontinuous gyroids, to lamellae. When the composition is inverted, morphological inversion takes place. These morphologies and their transition are verified in experimental studies.

Compared with self-assembly of diblock copolymers in bulk (Figure 2.2), the introduction of solvent increases the complexity for the case in solution. According to solubility of blocks in water, diblock copolymers can be divided into amphiphilic, double hydrophilic and double hydrophobic systems. Among them, amphiphilic copolymers are widely studied. Self-assembly of the amphiphilic diblock copolymer in solution can form diverse morphologies: spherical micelles, rods, bicontinuous structures, lamellae, vesicles, etc. It has been reported that the major factors influencing the morphology of the aggregates in the solution are the copolymer composition and concentration, water content, nature of the common solvent, presence of additives (acid, salt, or base), etc [44–47]. For example, working with the polystyrene-b-poly(acrylic acid) (PS-b-PAA) copolymer in the dioxane–water system [48], one can observe that with increasing water content, the morphologies change from spheres, to rods and then to vesicles, as shown in Figure 2.3. The formation of various morphologies is mainly governed by the stretching degree of the core-forming blocks, the interfacial tension between the micellar core and surrounding solvents, and the repulsive interactions among the corona-forming chains [49]. Thus, micellar morphology transition is driven by minimizing total free energy of the specified system.

2.1.3 Basic principles of sol-gel synthesis

There are several preparation routes to fabricate nanostructured titania films, such as the hydrothermal method, chemical vapor deposition, electrodeposition, etc [50, 51]. In addition to these, a favorable route for controllable titania structures is the so-called sol-gel process, which is a wet chemical technique [52]. It has been well established for fabrication of metal-oxides, ceramics, and/or ceramic-organic materials. Typically,

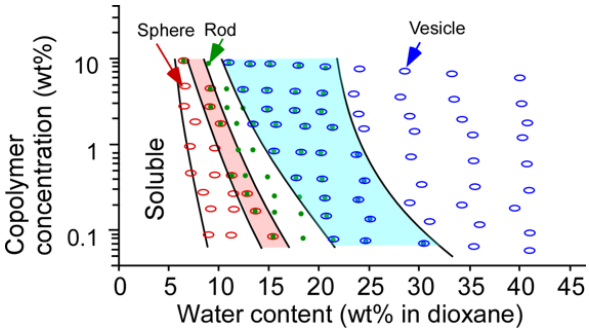

Figure 2.3: Phase diagram of PS-b-PAA in dioxane-water as functions of the copolymer concentration and water content. The colored circles indicate different phases: sphere (red), rod (green) and vesicle (purple). The colored regions correspond to phase-coexistence regions: sphere and rod coexisting phases (red), and rod and vesicle coexisting phases (blue). The figure is based on [48].

metal alkoxides are used as precursors, and undergo hydrolysis reaction to form small inorganic nanoparticles, the so-called sol. Subsequently, these nanoparticles cross-link with each other, to form the so-called gel, which is a three dimensional (3D) network with interconnected structures. For precursors, metal alkoxides normally contain a core of a metal atom and several organic groups R outside the core. In the case of titania, the precursors can be written as $Ti(OR)_4$. Different types of R significantly influence chemical activity.

The sol-gel process can be exemplarily illustrated via $Ti(OR)_4$. With presence of water, $Ti(OR)_4$ will react with H_2O (referred to as hydrolysis) according to Equation 2.4.

$$(RO)_3Ti{-}OR + H_2O \leftrightharpoons (OR)_3Ti{-}(HO) + R{-}OH \tag{2.4}$$

in which a alkoxide group (OR) is replaced by a hydroxyl group (OH). $Ti(OR)_4$ can simultaneously react with more than one water molecule until all alkoxide groups are replaced. That is complete hydrolysis when m = 4 in the following Equation.

$$Ti(RO)_4 + mH_2O \leftrightharpoons (HO)_m{-}Ti{-}(OR)_{4-m} + mR{-}OH \tag{2.5}$$

Then, condensation reactions yield cross-linking of two partially hydrolyzed monomers via a Ti-O-Ti bond. Two monomers form oxygen bridges and release a H_2O or ROH molecule as following.

$$(RO)_3Ti{-}OH + HO{-}Ti(OR)_3 \leftrightharpoons (RO)_3{-}Ti{-}(OR)_3 + H_2O \tag{2.6}$$

$$(RO)_3Ti{-}OR + HO{-}Ti(OR)_3 \leftrightharpoons (RO)_3{-}Ti{-}(OR)_3 + R - OH \tag{2.7}$$

Finally, a 3D network, consisting of a large quantity of Ti-O bonds, is established. The hydrolysis and polycondensation reactions can be influenced by many parameters, such as the type of titania precursors, water content, with or without catalyst and its type, ratio of reactants, pH-value, temperature, and aging time [53]. In the present thesis, hydrochloric acid (HCl) is used as the catalyst, which provides a acidic environment for hydrolysis and condensation reactions. Thus, the active sites for linkage dominate at the end of chains instead of the center. This acidic environment promotes hydrolysis reactions over condensation reactions, resulting in a delayed gelation process [54]. Note that it is especially beneficial for the formation of elongated structures, in comparison of bulky, compact aggregates of titania obtained with the absence of HCl.

2.1.4 Structure tailoring with the polymer template

The sol-gel technique only provides limited control for the fabrication of TiO_2 nanostructures. Therefore, to obtain an ordered TiO_2 morphology with interconnected nanostructures and a large surface-to-volume ratio, which is beneficial for charge carrier generation and transport, an amphiphilic diblock copolymer is used as the structure-directing template, in combination with the above discussed sol-gel synthesis. As mentioned in section 2.1.3, diblock copolymers go through microphase separation and self-assembly, and then form diverse morphologies. In the present thesis, with the aid of a so-called "good-bad" solvent pair, the diblock copolymer in solution can form micellar structures, such as spherical micelles. A "good" solvent, also termed as a non-selective solvent, can dissolve both hydrophobic and hydrophilic blocks of the amphiphilic polymer. While a selective solvent is used to dissolve only one block, which is also called a "bad" solvent. With adding small amounts of the bad solvent like water, the interfacial energy between the hydrophobic domain and the surrounding solvents increases and thus hydrophobic blocks tend to aggregate in order to decrease the surface free energy [55]. Finally, the as-obtained micellar system is a dynamic equilibrium due to the reversible process of fusion and separation of the micelles.

Schematic illustration of a diblock-copolymer template-assisted sol-gel route is present in (Figure 2.4). To fabricate titania nanostructures, the titania precursor, is added into the polymer solution. It is notable that the precursor needs to selectively incoporate into one of the blocks. In the present thesis, an amphiphilic diblock copolymer poly(styrene-block-ethylene oxide) (PS-b-PEO) is selected as the structure template and titanium(IV)isopropoxide (TTIP) as the titania precursor. TTIP will incoporate in the hydrophilic PEO domains via hydrogen bonds (Figure 2.4a). Simultaneously, it will undergo hydrolysis and condensation reactions, which results in the formation of Ti-O co-

valent bonds. Random motion of massive small micelles might significantly increase the possibility of mutual collision of two micelles, which causes the cross-linking of Ti-O between adjacent PEO domains (e.g. Figure 2.4b). Therefore, the 3D network formation of Ti-O bonds is established. This incoporation between the titania precursor and the hydrophilic block and the cross-linking effect may influence the dynamic equilibrium of micelles, and thus results in unique nanostructures in the deposited TiO_2/polymer hybrid film.

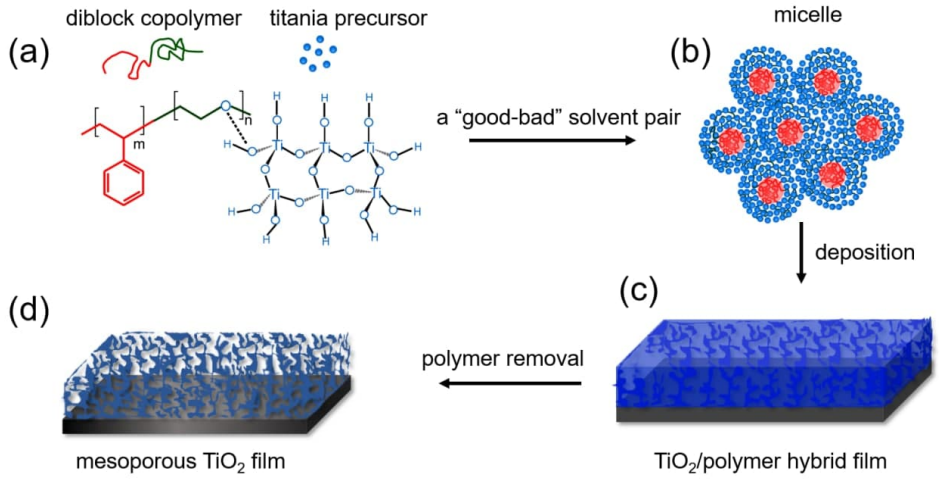

Figure 2.4: Schematic illustration of fabrication of nanostructured titania films using a diblock-copolymer template-assisted sol-gel synthesis route.

Typically, different kinds of micellar morphologies can be achieved by adjustment of the ratio of solvents, catalysts, and titania precursors [56,57]. In the present thesis, this point is investigated in detail, and a special focus is set on the influence of the weight fraction of the titania precursor. Apart from shape tailoring, the ratio of shell thickness (L) over radius of micellar cores (C) can be regulated by the block lengths of the amphiphilic diblock copolymer, which enables to influence micellar ordering in solutions [58].

Except for the factors mentioned above, also the deposition process significantly influences the film morphology (Figure 2.4c). The central point of film deposition is the removal of solvents and solidification of samples [59]. During solvent evaporation, on one hand, the diblock copolymer will undergo structural rearrangements to decrease the system energy. On the other hand, cross-linking of TiO_2 species hinders the tendency of rearrangements. The final film morphology depends on the balance of these two major opposing processes. If the former process dominates, films prefer to form ordered structures. In the latter case, a less ordered structure is favored. That can also explain why different deposition methods yield various morphologies or influence the order degree of

film structures. For example, spin coating is a non-equilibrium process with a ultrafast angular speed, which can freeze-in structures within seconds. In contrast, solution-casting, blade-casting and printing are slow processes, which provide sufficient time for polymer chains to undergo structural rearrangements during solvent evaporation.

After deposition of the sol-gel solution, the TiO_2/polymer hybrid films can be further post-treated with the solvent or thermal annealing. Generally, these treatments are aimed to improve polymer chain mobility and thus to promote structural rearrangements. The last but necessary step is removal of the polymer template. Normally thermal annealing at 500 °C is applied to combust this structure-directing polymer template and enable titania crystallization (Figure 2.4d). Additionally, some low-temperature routes, such as UV irradiation, oxygen plasma and solvent extraction [60–62], can be applied to remove polymers and obtain mesoporous titania films.

2.2 Titania based solar cells

Among different kinds of third generation solar cell devices, various forms of TiO_2 mainly act as electron acceptor and provide path for electron transport. Additionally, in some cases, they may also act as the scaffold for light harvesters. The solar cell devices studied in the present thesis are adopting TiO_2 as the electron acceptor, thereby denoted as titania based solar cells. Accordingly, based on device architecture, titania based solar cells are divided into solid-state dye-sensitized solar cells (ssDSSCs), hybrid solar cells (HSCs), quantum dot-sensitized solar cells (QDSSCs) and perovskite solar cells (PSCs). In the present thesis, hybrid bulk heterojuction solar cells (HBSCs), QDSSCs and PSCs are primarily focused. Detailed introduction of the working principle for HBSCs is given in section 2.2.1. Also, the related backgrounds for QDSSCs and PSCs are briefly described in section 2.2.2 and section 2.2.3, respectively.

2.2.1 Hybrid bulk heterojunction solar cells

Different from organic solar cells, the active layer in HBSCs consists of inorganic TiO_2 and organic materials. Therefore, this kind of solar cells is supposed to have advantages of the inorganic materials such as low cost, chemical stability and controllable nanostructures, and simultaneously posses the merits of conjugated polymers such as light weight, ease of production and processing flexibility [63]. In the present thesis, we adopt the low band gap polymer PffBT4T-2OD as donor, and emphasize the TiO_2/PffBT4T-2OD hybrid active layer which paves a way for hybrid photovoltaic applications.

Figure 2.5 shows schematic illustration of an exemplary HBSC in inverted geometry, which stacks different layers with different functions. For the so-called bottom contact, typically rigid glass substrates are used, which are covered by transparent conductive oxides (TCO) like fluorine doped tin oxide (FTO). Next, a hole blocking layer is deposited on the transparent electrode to block transport of positive charge carriers. On top of the hole blocking layer the active layer is placed, where several important steps take place (detailed introduction as below). The metal electrode serves as a counter electrode, which is usually a metal (e.g. gold, silver).

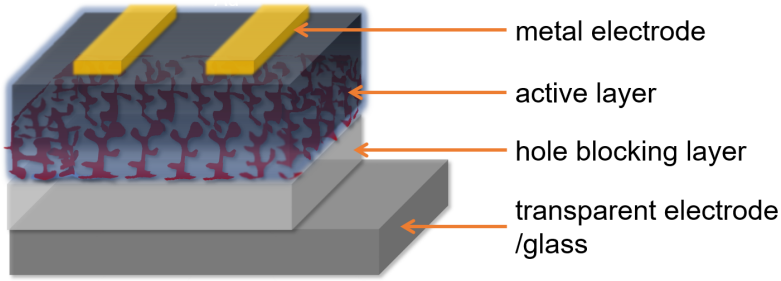

Figure 2.5: Schematic setup of a HBSC in inverted geometry. For HBSCs in the present thesis, the active layer consists of an inorganic electron conducting material (titania; red) and a solid organic hole conducting material (e.g. PffBT4T-2OD; dark blue).

The principle processes in HBSCs based on the literature [64] are illustrated in Figure 2.6 by an energy level diagram with an example of TiO_2 as an electron conducting material and the low band gap polymer PffBT4T-2OD as a hole conducting material.

Absorption

Typically, incoming light is absorbed by the organic polymer in the active layer, according to the Lambert-Beer law.

$$A(\lambda) = -log_{10}\left(\frac{I_t(\lambda)}{I_0(\lambda)}\right) = \alpha(\lambda) L log_{10} e \tag{2.8}$$

where $I_t(\lambda)$ is the transmitted intensity of the incident beam going through the sample, $I_0(\lambda)$ the reference beam intensity, $\alpha(\lambda)$ absorption coefficient of the specific material, and L the light path length through the sample.

With the condition of α above 0, and if the energy of the incoming photo, E_{photon}, is equal to, or higher than the band gap energy ΔE_{gap} of the absorbing polymer, the excitation of an electron from the highest occupied molecular orbital (HOMO) to the lowest unoccupied molecular orbital (LUMO) takes place, as shown in Figure 2.6a.

$$E_{photon} = \frac{hc}{\nu} \geq \Delta E_{gap} = E_{LUMO} - E_{HOMO} \tag{2.9}$$

Here, HOMO and LUMO refer to the energy shift of bonding π- and antibonding π^*-bands, respectively. For conducting polymers, a conjugated π-electron system, which consists of alternated single and double bonds, is required. In conjugated polymers, the electrons which result from the sp^2 hybridization are delocalized in alternated double bonds (or referred to π-orbitals) along the polymer chain. With conjugated bonds, π-orbitals overlap with each other, which leads to forming bonding π- and antibonding π^*-bands. Under the ground state, all π-electrons are occupied in the HOMO, leaving the LUMO empty. When absorbing the photon, the electron can jump from the HOMO to the LUMO, referred to the excited state.

The excited electron is coupled to the hole via Coulomb interaction. This coupled electron-hole pair in conductive polymers is called exciton. Usually, in contrast to most inorganic materials, the exciton generated in conductive polymers (also referred to the Frenkel-type exciton) exhibits stronger binding energy, and thus higher energy is required for its dissociation. However, thermal energy at room temperature only provides energy in the order of some meV, which is not sufficient to seperate the exciton into free charge carriers. Thus, the exciton needs to diffuse towards the interface between a donor polymer and titania.

Diffusion

Figure 2.6b shows the exciton diffuses to the interface. Within the polymer domain, there are two primarily processes for energy transfer [65, 66]. The first is called trivial transfer process (sometimes referred as photon reabsorption). Another process is called Förster transfer (dipole-dipole coupling). Förster transfer dominates in the short-ranged energy transfer (distances below 10 nm). For longer distances, trivial transfer is the main process. In this case, the exciton movement can be regarded as a random hopping process between neighboring polymer sites without a preferential direction. Therefore, we use the overall diffusion length L_e, which depends on the diffusion coefficient (D_e) and the lifetime of the exciton (τ_e), to describe the travel distance of the exciton before recombining. For common organic semiconductors, e.g. PffBT4T-2OD in the present thesis, the lifetime is typically in the order of nanoseconds, thus yielding diffusion lengths of smaller than 20 nm [67]. Accordingly, the polymer domain size in radius should be less than 20 nm so that excitons can reach the interface before they recombine. In HBSCs, this size is determined by the pore size of mesoporous titania films.

Dissociation

After reaching the interface, the exciton has to be dissociated (Figure 2.6c). The exciton can be separated when the energy offset between the LUMO of the donor polymer and the conduction band of the inorganic material is larger than the Coulomb binding energy of the exciton [68]. Two types of exciton dissociation may occur at the interface. One is that the electrons are injected to the conduction band of titania, because titania has a high electron affinity. Second, it is possible that energy is firstly transferred from the donor polymer to titania, followed by that the holes are transferred from the valence band (VB) of titania to the ground state of the donor polymer. However, the latter case is not favorable due to the increasing possibility for charge carrier recombination. Therefore, the choice of the donor polymer play a crucial role, the energy level of which needs to be matched with the band gap of titania.

Transport and extraction

After exciton dissociation, electrons are transported through nanostructured TiO_2 to the transparent electrode (Figure 2.6d). Electron mobility in nanostrutcured TiO_2 is much lower than that in a single anatase titania crystal. Various defects lead to the trap states in nanostructured TiO_2 films, which significantly influences transport rate and thus results in a low electron mobility. It was reported that the transport-limiting traps are primarily present at the titania surface [69]. This suggests the traps might be proportional to the roughness and porosity of mesoporous TiO_2 films. However, titania films with a high surface-to-volume ratio are beneficial for interfacial charge carrier tranfer rates [57]. For the final device performance, we have to balance these two contradictory processes, thereby the film morphology being of necessity to be investigated.

The positive charge carriers transport from the p-type semiconductor, e.g. conjugated polymers in HBSCs, to the metal electrode. For the fabrication of quantum dot-sensistized solar cells (QDSSCs) and perovskite solar cells (PSCs) which will be introduced below, 1,2-ethanedithiol (EDT) treated PbS QDs and spiro-OMeTAD are used as the solid-state hole-transporting material (ssHTM), respectively.

Finally, charge carriers are collected by the electrodes (Figure 2.6e), which is also significant to the overall efficiency. The charge collection yield is highly related to the energy levels of each component and the interfacial contacts between the active layer (donor polymers and inorganic materials) and the electrodes [68].

As seen in Figure 2.6, five consecutive steps are believed to take place within HBSCs, and each step has an efficiency. (1) η_a is the photo absorption efficiency, which depends on the absorption coefficient of the donor polymer and its film thickness. (2) η_{diff} indicates

the ratio of the number of excitons that reach the interface to the number of generated excitons. (3) η_{diss} indicates the ratio of the number of the separated excitons to the number of excitons at the interface between the donor polymer and the inorganic material. (4) η_{tr} indicates the ratio of the number of free charge carriers reaching the electrodes to the number of generated free charge carriers. (5) η_{co} indicates the ratio of the number of charge carriers collected externally to the number of charge carriers at the electrodes. The multiple of each efficiency determines the efficiency of converting the incident photons into the photogenerated electrons. This efficiency is also called external quantum efficiency (EQE):

$$EQE = \eta_a \eta_{diff} \eta_{diss} \eta_{tr} \eta_{co} \tag{2.10}$$

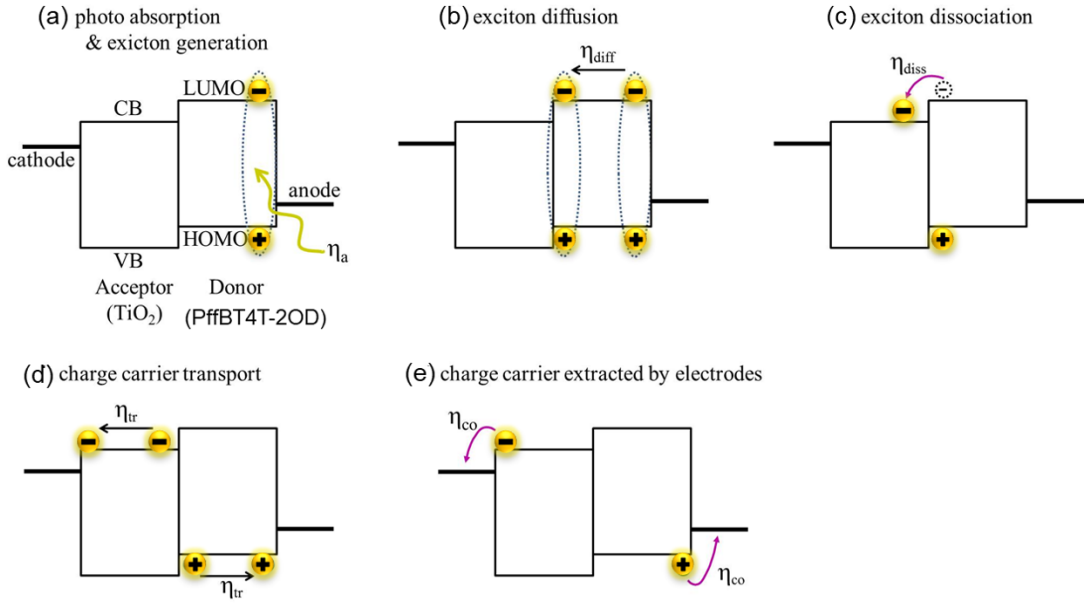

Figure 2.6: Principle processes occuring in a hybrid bulk heterojunction solar cell. CB and VB are referred to the conduction band and valence band of titania, respectively. LUMO and HOMO are referred to the lowest unoccupied molecular orbital and highest occupied molecular orbital of the donor polymer, e.g. PffBT4T-2OD, respectively. The figure is based on [64, 68].

2.2.2 Quantum dot-sensistized solar cells

Recently, sensitizers of quantum dots (QDs) such as CdS [70], CdSe [71], PbS [72], Bi_2S_3 [73] and InP [74], have attracted numerous attention for promising photovoltaic devices. As compared to sensitizers widely applied in DSSCs, the band gap of QDs can be tuned via control of the QD size. Moreover, the relatively high extinction coefficients

of QDs can enhance the light harvesting ability of the photoanode and thus improve the device efficiency. Besides, QDs have some unique properties, such as the multiple exciton generation possibility and solution processability, which can be compatible with various deposition methods, making them attractive for photovoltaic applications [75].

Figure 2.7 shows the schematic illustration of the QDSSC architecture present in this thesis. Different from HBSCs and ssDSSCs, the active layer in QDSSCs consists of titania nanoparticels and PbS QDs, which act as the light absorber to generate excitons. The 1,2-ethanedithiol (EDT) treated PbS QDs are used as the hole-transporting layer (HTL). The working principle of QDSSCs is similar to that of ssDSSCs, considering in some cases QDs are regarded as a simple alternative dye. Exciton generation and dissociation take place in the active layer. Electrons are transferred via tunneling into the ETL, titania. Holes get transferred into the HTL. Then free charge carriers will be transported to the electrodes and finally extracted by the respective electrodes.

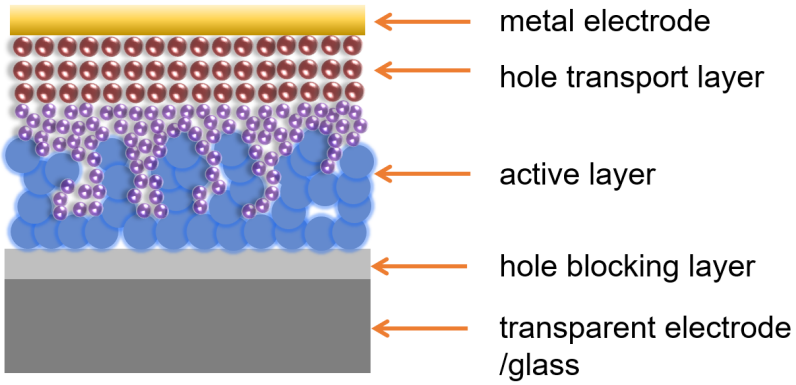

Figure 2.7: Schematic setup of a QDSSC device. For QDSSCs in the present thesis, the active layer consists of titania nanoparticles (blue) and PbS QDs (purple). The 1,2-ethanedithiol (EDT) treated PbS QDs are used as the hole-transporting layer (HTL).

2.2.3 Perovskite solar cells

Organic-inorganic hybrid perovskites have many advantages for photovoltaic applications, such as the high absorption coefficient, high carrier mobility, long carrier diffusion length and low density of trap states [76–78]. Thus, perovskite solar cells (PSCs) have attracted a large quantity of attention and made extraordinary progresses. These progresses in PSC development lead to an impressive efficiency of 25.5% [6]. The schematic illustration of the perovskite solar cell architecture in this thesis is present in Figure 2.8a, and the energy level diagram based on the literature [79] is shown in Figure 2.8b. Electrons are

efficiently injected from the perovskite layer into the mesoporous titania, and holes are transferred from perovskite into the HTL, namely spiro-OMeTAD.

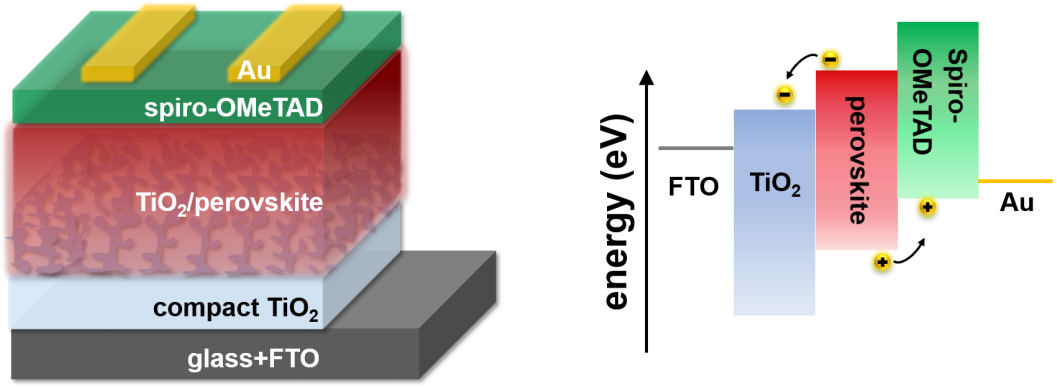

Figure 2.8: (a) Schematic setup of a PSC device. (b) Schematic energy level diagram of a PSC device.

Current-voltage hysteresis

The so-called current (J)-voltage (V) hysteresis behavior refers to the reverse scan (voltage biased from V_{oc} to 0 V) shows mismatching with the forward scan (voltage biased from 0 V to V_{oc}). Hysteresis phenomena have been observed not only in PSCs, but also in other types of solar cells like silicon and DSSCs. In 2014 Henry Snaith et al. first reported anomalous hysteresis, and observed that hysteresis predominantly arose from the hybrid perovskite materials itself and depended on the contact materials [80]. They also proposed three possible reasons, namely (1) bulk or surface defects of perovskite which act as traps for charges, (2) ferroelectricity, (3) excess ions due to interstitial defects being able to migrate.

Charge trapping/detrapping is related to defects in perovskite films, in which defects can be formed at shallow level near conduction/valence band and/or at deep level within the band gap. Defects at shallow level might play as dopants, thereby enhancing charge transport [81]. Deep defects, associated with non-radiative recombination [82, 83], could cause hysteresis behavior because charge trapping or detrapping at deep-defect sites leads to a delayed response [84]. Such deep trap sites most likely occur at the interface, surface or grain boundary. Ion migration, regraded as a potential origin of hysteresis, is related to defects in the perovskite [85, 86], where we need to take all constituents of the organic cation, inorganic lead cation and halide anion into consideration. Ferroelectricity is related

to property of certain non-conducting crystals or dielectrics, which show spontaneous electric polarization. Via an application of an appropriate electric field, the induced polarization is reversed in direction. Ferroelectric property was first found in the $MAPbI_3$ thin film [87], where ferroelectric domains were approximate to the grain size. This ferroelectric domain might influence charge carrier extraction.

2.3 X-ray scattering

Within the frame of the present thesis, X-ray scattering techniques are a powerful tool to probe the inner film morphology and crystal structures with high statistic relevance. The basic principles of scattering techniques are introduced in 2.3.1, followed by a short introduction about X-ray diffraction (XRD) in section 2.3.2. Then grazing-incidence small- and wide-angle X-ray scatteirng (GISAXS/GIWAXS) are explained in section 2.3.3 and section 2.3.4 in detail.

2.3.1 Basic principles

X-ray can be described as a plane electromagnetic wave with its electric field vector $\vec{E}(\vec{r})$. When it travels through a medium with a position-dependent refractive index n($\vec{r}$), the propagation follows the Helmholtz equation as below [88]. For structural investigation in the present thesis, elastic X-ray scattering is used, with the energy of the incoming X-ray beam being equal to the energy of the scattered X-ray beam.

$$\nabla^2\vec{E}(\vec{r}) + k^2n^2(\vec{r})E(\vec{r}) = 0 \tag{2.11}$$

in which $\vec{r}$ is the position of the electromagnetic wave, $\vec{k}$ is the wave vector, and k is the modulus of the wave vector, which can be described by the wavelength λ with $k = 2\pi/\lambda$. In general, the refractive index for X-ray in matter can be given by

$$n(\vec{r}) = 1 - \delta(\vec{r}) + i\beta(\vec{r}) \tag{2.12}$$

It depends on the dispersion δ and absorption β. In the case of a homogeneous medium far away from the absorption edges, both δ and β depend on the X-ray wavelength λ and can be written as Equation 2.13 and Equation 2.14, respectively.

$$\delta = \rho\frac{\lambda^2}{2\pi} \tag{2.13}$$

$$\beta = \mu \frac{\lambda}{4\pi} \tag{2.14}$$

where ρ is the scattering length density (SLD) of the homogeneous medium and μ the linear absorption coefficient. The SLD, $\rho = r_e \rho_e$, depends on the classic electron radius, $r_e = 2.814 \times 10^{-5}$ Å, and the electron density of the investigated material ρ_e. Generally, δ ranges from 10^{-5} to 10^{-6}. It is of order 10^{-5} in solids and only around 10^{-8} in air. The imaginary part β is usually smaller than δ. Therefore, the refractive index of X-ray is slightly less than 1. X-ray scattering experiments are closely related to the difference in SLD, e.g. the difference in electron density of the investigated material. This difference is regarded as scattering contrast and is mainly dependent on the element type.

Bulk samples are well studied in transmission geometry, whereas for thin-film samples the seriously reduced scattering volume gives rise to a weak scattering signal. To overcome this problem, a reflection geometry using grazing angles is used since it can provide the enlarged scattering volume, and inner film structures are accessible. The geometries for two different scattering cases under the mode of grazing-incidence angels, the specular and diffuse scattering, are schematically illustrated in Figure 2.9.

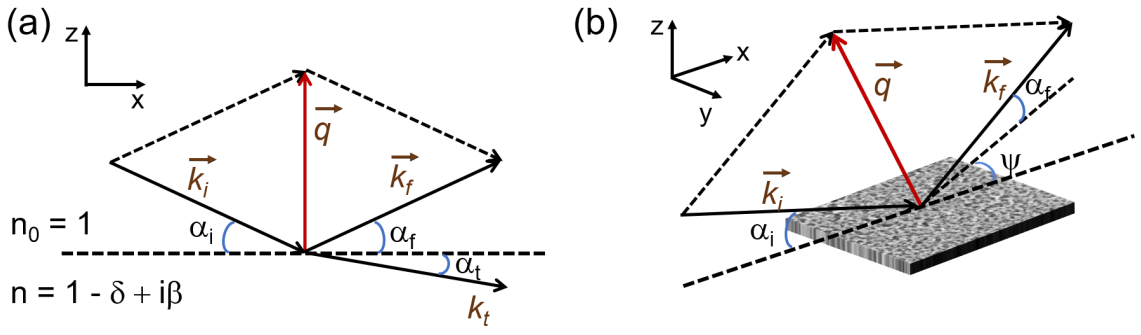

Figure 2.9: Schematic geometry of (a) specular scattering $\alpha_i = \alpha_f$ and (b) diffuse scattering.

Typically, a photon with $\vec{k_i}$ impinges onto the film sample under a shallow angle α_i ($\alpha_i \ll 1°$), with the x-axis in the xz-plane. The reflected beam $\vec{k_f}$, exiting the sample under an exit angle α_f ($\alpha_f = \alpha_i$), is called specular beam. Also, this beam stays in the same plane, xz-plane, as the incident beam (Figure 2.9a). $\vec{k_t}$ is the transmitted beam (below horizon). Commonly, in GISAXS the transmitted signal is not detectable due to the high absorption of the sample stage and sample. The momentum transfer from the incident beam to the reflected beam is described as the scattering vector $\vec{q}$. Since elastic scattering

is considered, as mentioned above, the scattering vector only changes its direction, but its modulus, $q = 2\pi/\lambda$, remains unchanged.

In the case of diffuse scattering, the scattered beam is not only present in the scattering plane, xz-plane, but also present in the xy-plane with an additional scattering angle ψ (see Figure 2.9b). Or it fullfills $\alpha_f \neq \alpha_i$.

Snell's law, also known as the law of refraction, is used to describe the refraction at the interface between air and the medium with a refractive index n.

$$n_0 \cos(\alpha_i) = n \cos(\alpha_t) \tag{2.15}$$

where α_t is the exit angle of $\vec{k_t}$, and n_0 is 1. In the case of total reflection (X-ray passes from air to the medium), α_t is equal to 0. With $\alpha_t = 0$, if $\alpha_i = \alpha_c$, we can obtain the following Equations [89, 90]. The critical angle α_c is dependent of the material.

$$\cos(\alpha_c) = n \tag{2.16}$$

$$n^2 = \cos^2(\alpha_c) \approx 1 - {\alpha_c}^2 \tag{2.17}$$

$$\alpha_c \approx \sqrt{2\delta} = \lambda\sqrt{\frac{\rho}{\pi}} \tag{2.18}$$

where ρ is the scattering length density of the scattering material as mentioned above. The reflectivity, transmittivity and the penetration depth depend on the incident angle α_i, the density and absorption of the medium, and the wavevector [89]. When $\alpha_i < \alpha_c$, totally external reflection occurs and the transmitted wave becomes very weak. X-ray propagates along the film surface with a minimal penetration depth. Due to the small penetration depth, it is called the evanescent wave. Accordingly, this region is called the evanescent regime. In this case, we can obtain the structure information about the near-surface region in the film. When $\alpha_i > \alpha_c$, we can obtain more information from the bulk film.

2.3.2 X-ray diffraction

The crystal structure of the sample can be investigated with X-ray diffraction. Crystals are regular arrays of atoms, as shown in Figure 2.10, acting as periodic gratings for X-rays. Atoms scatter X-rays, mainly by the atoms' electrons. When X-rays strike the electrons, it produces secondary spherical waves. Due to the regular array of scatter centers, a regular array of spherical waves will be produced. Each crystal structure has its own set of lattice parameters, resulting in the unique scattering pattern. This provides a way to identity the material and its respective crystal structure.

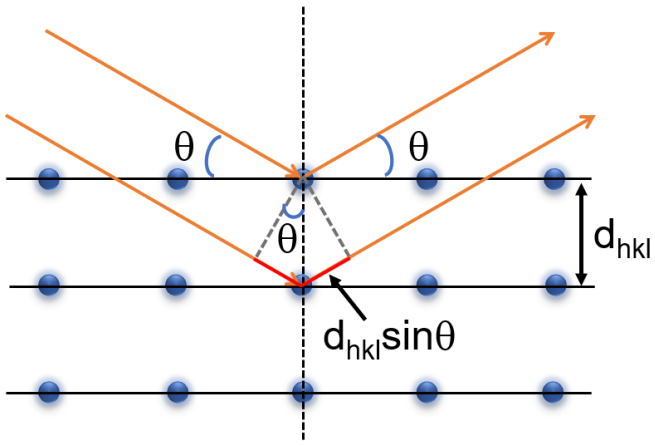

Figure 2.10: Schematic illustration of the Bragg equation. The incoming beam (indicated as the orange line) interacts with the scatter centers, namely the electron clouds of the atoms (indicated as the blue circle), which are located on the lattice planes of the crystal structure with a specific spacing of d_{hkl}.

When the X-ray beam is scattered from two neighboring lattice planes of a crystal, interference will occur, as shown in Figure 2.10, resulting in different intensities. The angle θ between the plane and the X-ray beam gives rise to a path-length difference. When the Bragg equation is fulfilled, the constructive interference will occur, namely the maximum intensity appearing. That is a path-length difference is an integer multiple n of the X-ray wavelength λ:

$$2d_{hkl}\sin(\theta) = n\lambda \tag{2.19}$$

where d_{hkl} is the lattice spacing of the crystal structure and (hkl) the Miller indices. Typically, the angle (2θ) between the incoming and scattered X-ray beam is used as the Bragg reflex. Considering the relative position of the resulting reflexes (normally plotted in dependence of 2θ), the crystal structure of the material can be identified. In addition to the peak position, we can obtain the crystallite size distribution from the peak shape. The crystallite size can be calculated by [91]:

$$\varepsilon_{obs} - \varepsilon_{instr} = \frac{K\lambda}{Dcos\theta} + 4\varepsilon_{str}tan\theta \tag{2.20}$$

where ε_{obs} is the line width, ε_{instr} the instrumental broadening, K the Scherrer constant which has a typical value of about 0.9 but varies with the crystallite shape, λ the X-ray wavelength, D the crystallite size and ε_{str} the strain. Considering the fact that the

instrumental broadening and strain are much lower than the actual line broadening, they can be neglected, thereby the crystallite size D_{hkl} along $< hkl >$ direction is estimated by

$$D_{hkl} = \frac{K\lambda}{\Delta(2\theta)\cos(\theta)} \tag{2.21}$$

where $\Delta(2\theta)$ is the full width half maximum (FWHM) of the Bragg peak at 2θ. The angle θ can be converted to q, therefore the Sherrer equation can be written by

$$D_{hkl} = \frac{2\pi K}{\Delta q_{hkl}} \tag{2.22}$$

$$q = \frac{4\pi sin\theta}{\lambda} \tag{2.23}$$

where Δq_{hkl} is the integral line width, and is calculated by the FWHM of the Bragg peak.

2.3.3 Grazing-incidence small-angle X-ray scattering

Grazing-incidence small-angle X-ray scattering (GISAXS) is powerful to investigate the surface and inner morphologies of a thin film in a large length scale ranging from nanometer to micrometer. Due to the very limited amount of material available for investigation on the thin film, we use a very shallow incident angle (typically $\alpha_i \ll 1°$). This very small angle allows a large footprint on the film. The length of the footprint in beam direction, l, is calculated by:

$$l = \frac{h}{tan(\alpha_i)} \tag{2.24}$$

where h is the size of the incident beam. For example, if $\alpha_i = 0.4°$, and a X-ray beam size $= 20 \times 30\ \mu m^2$, the illuminated area is increased by more than 2 orders of magnitudes.

The basic geometry for grazing-incidence X-ray scattering (GIXS) is illustrated above (Figure 2.9). Here, we schematically sketch the GISAXS scattering geometry using Figure 2.11. The film surface defines the xy plane with the x-axis oriented along the X-ray beam direction. The y-axis is perpendicular to the scattering plane, namely the xz plane. We assume a fixed wavelength λ. When doing the measurements, the incident angle α_i is selected as well as the sample-to-detector distance (SDD). Therefore, the quasi-monochromatic X-ray beam with the wavevector $\vec{k_i}$ (the wave number $k = (2\pi)/\lambda$) impinges onto the sample surface under α_i and is scattered along $\vec{k_f}$ under an exit angle α_f and an out-of-plane angle ψ. In the present thesis, elastic scattering phenomena are considered, therefore, the scattering wavevector $\vec{q}$ is given by [90, 92]

$$\vec{q} = \frac{2\pi}{\lambda}\begin{pmatrix} q_x \\ q_y \\ q_z \end{pmatrix} = \frac{2\pi}{\lambda}\begin{pmatrix} \cos(\alpha_f)\cos(\psi) - \cos(\alpha_i) \\ \cos(\alpha_f)\sin(\psi) \\ \sin(\alpha_f) + \sin(\alpha_i) \end{pmatrix}. \tag{2.25}$$

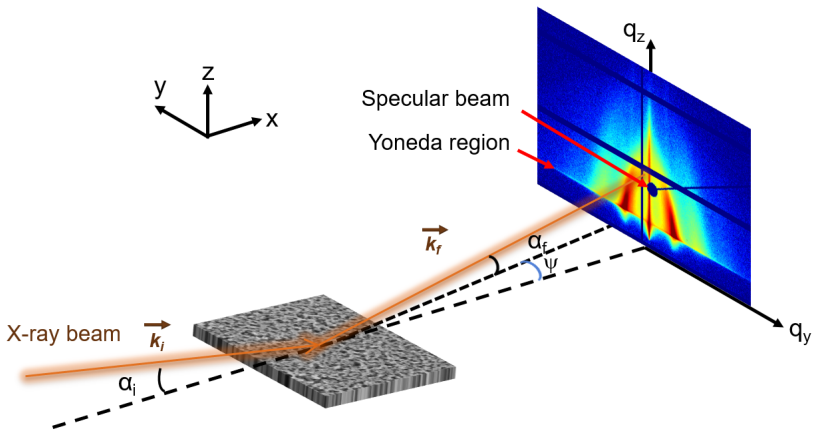

Figure 2.11: Schematic illustration of the GISAXS geometry. The incident angle is denoted as α_i, the exit angle denoted as α_f, and the out-of-plane angle denoted as ψ. The sample-to-detector distance ranges typically from 1 up to 10 m [93]. The main characteristic features are the specular beam and the Yoneda region.

The lateral component (q_x, q_y) is used to probe the lateral structure of the film. Due to the very small α_i and α_f, q_x is approximated to 0, and is therefore neglected. Under grazing incidence, reflection/refraction at the sample interface and the substrate interface occur. Thus, the Born approximation (BA) is not sufficiently valid, and the diffuse scattering is typically analyzed within the framework of the distorted-wave Born approximation (DWBA) [94]. In the simple BA, the form factor is the Fourier transform of the shape function of the scattering object. However, in the DWBA, for the case of a object on the substrate, four terms, affecting the scattering, have to be considered. That is, in addition to a normal scattering event, first a reflection followed by scattering, or a reflection after the scattering, or reflection, followed by scattering and then a second reflection, as shown in Figure 2.12.

In order to do some quantified analysis, in the present thesis a further simplification is used via the effective interface approximation (EIA) [92,95]. That is instead of the full 2D GISAXS pattern being analyzed, data is only analyzed as a function of q_y with a constant q_z. Therefore, we can obtain the information regarding the lateral structures. For $\alpha_i \gg$

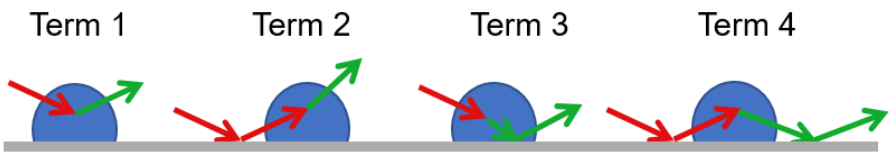

Figure 2.12: Schematic illustration of the four terms involved in the scattering of a object on the solid substrate in the DWBA model. The first term corresponds to the simple Born approximation. The color change of the arrows indicate the scattering event.

α_c, and with a constant q_z, the diffuse scattering intensity in the DWBA simplifies for an EIA, and the differential cross section $\frac{d\sigma}{d\Omega}$ is given by

$$\frac{d\sigma}{d\Omega} = \frac{A\pi^2}{\lambda^4}(1-n^2)^2 \mid T_i \mid^2 \mid T_f \mid^2 P_{diff}(\vec{q}) \propto P_{diff}(\vec{q}) \tag{2.26}$$

where A is the illuminated area, λ is the wavelength, n is the refractive index, $\mathrm{T}_{i,f}$ are the Fresnel transmission function of the incoming and outgoing beams, $P_{diff}(\vec{q})$ is the diffuse scattering factor.

If the exit angle is equal to the critical angle of the investigated material, the Fresnel transmission functions have a maximum, which contribute to a pronounced scattering intensity, called the Yoneda peak, or Yoneda region [96]. Since the critical angle depends on the scattering length density (SLD), the Yoneda peak is the material dependent scattering signal. Because time-of-flight grazing-incidence small-angle neutron scattering (TOF-GISANS) allows us to probe the same information with a fixed incident angle and a varied wavelength [97]. The scattering length density (SLD, ρ) can be obtained from the slope of the linear fit of critical angle (also referred to the Yoneda peak) versus wavelengths of the neutron. The porosity Φ of the probed material, e.g. mesoporous TiO_2, can be calculated as:

$$\Phi = 1 - \frac{\rho_m}{\rho_{th}} \tag{2.27}$$

where ρ_m and ρ_{th} are the measured and the theoretical SLD of the probed material, respectively.

Note that Equation 2.26 also strongly depends on another parameter, the refractive index n. The scattering amplitudes and material sensitivity can be enhanced by tuning the X-ray energy if n shows sufficient dependence on the photon wavelength.

In the case of identical objects in a geometrical arrangement, the diffuse scattering factor can be approximated by

$$P_{diff}(\vec{q}) \propto N|F(\vec{q})|^2 S(\vec{q}) \tag{2.28}$$

where N is the number of scattering objects, $F(\vec{q})$ the form factor and $S(\vec{q})$ the structure factor. A description of the form factor depends on the type of scattering objects, i.e. cylinder or sphere.

To be further convenient for the quantified analysis, the local monodisperse approximation (LMA) is introduced for the coupling between different scattering objects and their spatial positions [92, 94]. In the LMA, the scattering weight of each object is replaced by its mean value over the size distribution. The scattering intensities from monodisperse subsystems are incoherently summed up. Besides, cross coupling between different substructures is not included. Therefore, within the LMA, such a model is depicted as

$$P_{diff}(\vec{q}) \propto \sum_k N_k|F_k(\vec{q})|^2 S_k(\vec{q}) \tag{2.29}$$

For the data modeling, the form factors of spheres or standing cylinders are used in the present thesis. Typically for the mesoporous film, the scattering objects are assumed to have a cylindrical shape with a Gaussian distributed size. The interference function of a 1D paracrystalline lattice is introduced. This spatial distribution is related to the structure factor.

In a low concentration of scatters, the $S(\vec{q})$ tends to be approximately 1 since there is no interference between the scattered objects [94]. Oppositely, the form factor and structure factor are strongly correlated.

2.3.4 Grazing-incidence wide-angle X-ray scattering

Figure 2.13a shows the basic geometry for grazing-incidence wide-angle X-ray scattering (GIWAXS) experiment, which is similar to GISAXS with respect to the setup geometry. We can regard GIWAXS as an extension of GISAXS, only changing the sample-to-detector distance (SDD) to a much shorter value, normally around several centimeters [98]. This shifting allows to record the scattered signal under large exit angles, which provides structural information on the sub-nanometer scale (atomic length scale). That means we can use GIWAXS to investigate the atomic and molecular distances of the material. Also, due to a larger angular range accessible with the same detector (pixel size), accordingly, each pixel will collect intensity from a larger angular range. This contributes to more signal, but also more background in each pixel. In order to decrease the strong scattering signal

from the substrate, especially for the amorphous-material support such as glass or polymer foils, typically the incident angle is larger than the critical angle of the investigated material, but lower than the critical angle of the substrate.

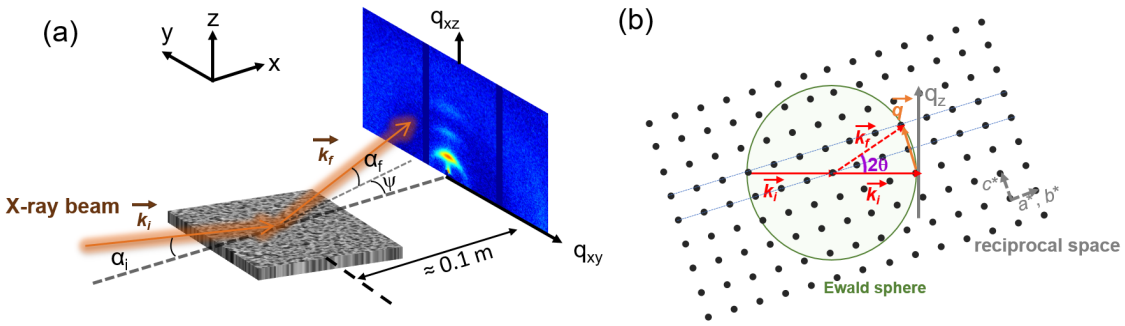

Figure 2.13: Schematic illustration of (a) the GIWAXS geometry and (b) the principle of a GIWAXS experiment.

In the analysis of GIWAXS data, the crystalline information of semiconduting polymers such as P3HT or PffBT4T-2OD in the present thesis can be revealed. Extracted key properties are lattice constants, crystal sizes and orientations. Figure 2.14a-d show four scenarios of GIWAXS patterns in organic polymers for solar cell application. In the case of a highly crystalline film with an orientation of all crystal planes parallel to the substrate and a lattice spacing of d, well pronounced Bragg peaks with a distance of $2\pi/d$ are observed, only in the vertical direction (Figure 2.14a). If all crystal planes in the film show parallel and perpendicular orientations, Bragg peaks appear in the out-of-plane (vertical) and in-plane (horizontal) directions, as shown in Figure 2.14b. Here the definition/nomenclature for out-of-plane and in-plane is slightly different from that in GISAXS. If a more textured film has the crystal planes which are not perfectly horizontal alignment, but with a small angular distribution like in Figure 2.14c, Bragg peaks along the vertical direction become broaden. In the case of powder-like films with random orientations, Bragg peaks will smear out into Debye-Scherrer rings (Figure 2.14d). Due to the limited crystallinity and non-ideally ordered orientation in polymer materials, their GIWAXS patterns are primarily similar to the last two cases.

Figure 2.14e schematically shows an edge-on oriented P3HT crystal with the lamellar stacking in [100] direction and the π-π stacking in [010] direction. Accordingly, the P3HT out-of-plane (100) Bragg peak is observed together with its in-plane (010) Bragg peak. In

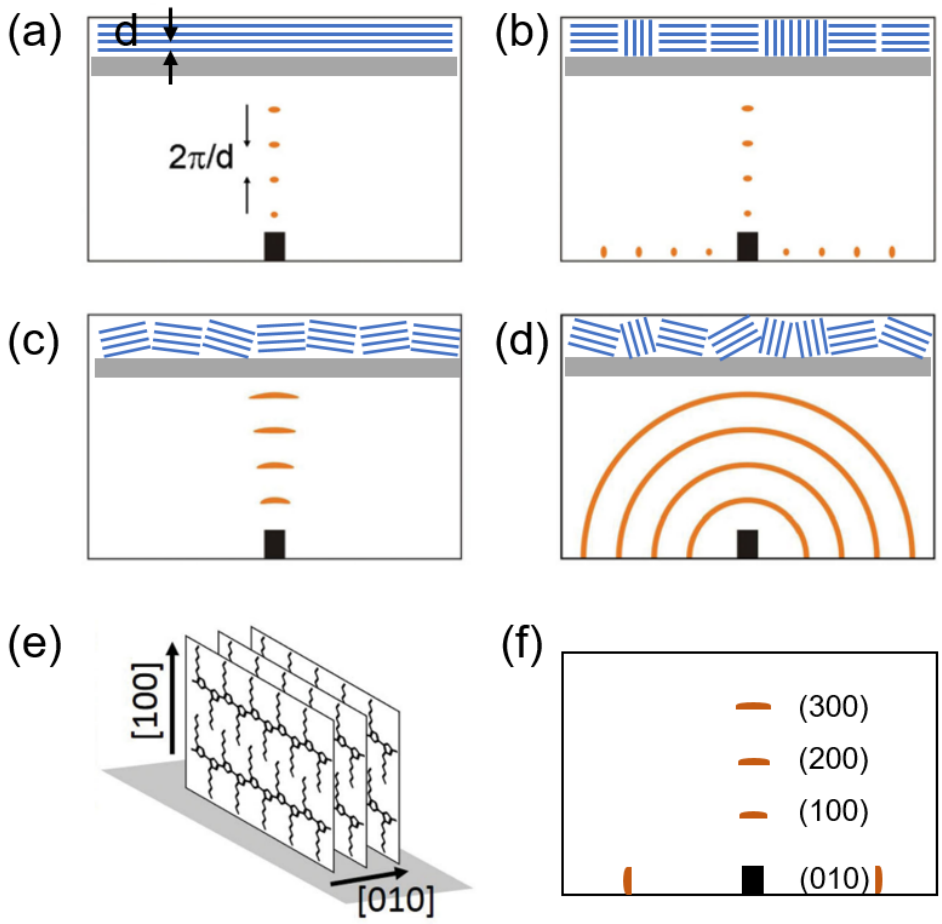

Figure 2.14: Schematic illustration of different lamellar stackings in films with the corresponding 2D GIWAXS data in the case of (a) ideal lamellar stacking parallel to the substrate, (b) ideal lamellar stacking parallel and perpendicular to the substrate, (c) textured lamellar stacking parallel to the substrate and (d) disordered lamellar stacking. (e) schematic illustration of an edge-on oriented P3HT crystal with the lamellar stacking in 100 direction and the π-π stacking in 010 direction and (f) its corresponding 2D GIWAXS pattern. The figure is based on [98].

addition, the (200) and (300) Bragg peaks of P3HT might also appear in the GIWAXS pattern.

For crystallized inorganic materials, single atoms are the scatter centers for X-ray in GIWAXS. In this way, the basic principle of this measurement technique is similar to XRD and Equation 2.19 can be also applied here. However, compared to XRD, the incident angle α_i is fixed with the incident beam $\vec{k_i}$. All possible scattered directions of $\vec{k_f}$ are on a sphere in reciprocal space, called Ewald sphere, and only the reciprocal lattice coinciding with the surface of Ewald sphere can fulfill the Laue condition.

Figure 2.13b shows the basic principle of a GIWAXS experiment. The reciprocal space

is the Fourier transform of the real space structure, where the lattice structure can be denoted using the reciprocal lattice vector a^*, b^* and c^*. The surface of the Ewald sphere intersects with certain reciprocal lattice points, thereby fulfilling the Laue condition. In this case, the momentum vector is transferred to the final wavevector $\vec{k_f}$, and the momentum transfer is described as $\vec{q}$. The angle between the incoming wavevector $\vec{k_i}$ and the outgoing wavevector $\vec{k_f}$ is 2θ, in both real and reciprocal space. As a result, q_x has a non-negligible contribution to the $\vec{k_f}$ direction. In GIWAXS measurements, the momentum transfer q is projected to a 2D detector, and thus the q_x contribution cannot be neglected in the 2D GIWAXS pattern. The contribution of q_x increases with α_f.

In order to extract structural information, the raw 2D GIWAXS pattern will be reconstructed into the reciprocal-space coordinate system [99,100]. The x-axis in the GIWAXS pattern is now q_r instead of q_x, and q_r is given by

$$q_r = \sqrt{{q_x}^2 + {q_y}^2} \tag{2.30}$$

This transformation results in a missing wedge because $q_r = 0$ is not accessible. In general, we can present GIWAXS data: (1) plotting q_z versus q_r (as shown in Figure 2.15b) or (2) plotting $q = |\vec{q}|$ versus the azimuthal angle χ (as shown in Figure 2.15c). For the crystal orientation analysis, we can perform azimuthal cuts, also called tube cuts, along the q position of the specific (hkl) plane. Or, like in the organic crystalline polymer, typically sector integrals (radial/cake cuts) in the vertical direction (e.g. χ values from -15° to 15°) and/or the horizontal direction (e.g. χ values from 75° to 85°) are performed in the representation of q_z versus q_r.

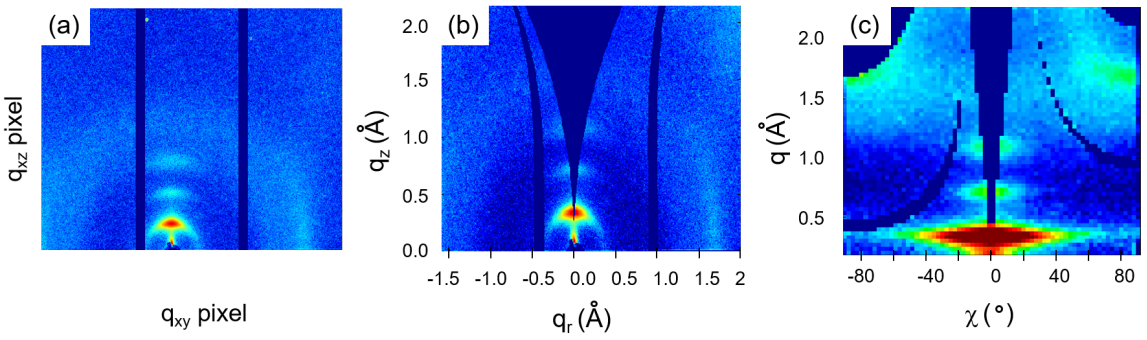

Figure 2.15: Different representations of 2D GIWAXS data: (a) A raw 2D GIWAXS image recorded by the detector, (b) q_z versus q_r, and (c) q versus χ.

3 Characterization methods

In this chapter, various techniques are described to characterize the mesoporous TiO_2 films, the TiO_2 based active layers and the respective solar cells. In section 3.1, the real- and reciprocal-space imaging methods are introduced to investigate the structure of the mesoporous TiO_2 film and the related active layer. The spectroscopic and electronic characterizations are given in section 3.2. For each characterization method used in the present thesis, the measurement parameter, basic working principle and data analysis software are provided.

3.1 Structural characterizations

To optimize the photovoltaic performance, the surface and inner film morphology, crystallinity and the film thickness of the active layer, in particular that of the inorganic TiO_2 material, need to be investigated. This has been done with real-space techniques, including height profilometry (section 3.1.1), optical microscopy (section 3.1.2) and scanning electron microscopy (section 3.1.3), and with reciprocal space techniques, such as X-ray diffraction (section 3.1.4), transmission electron microscopy (section 3.1.5) and grazing incidence scattering (section 3.1.6 and section 3.1.7).

3.1.1 Height profilometry

In the present thesis, a height profilometer (DektakXT Stylus Profiler, Bruker) is used to measure the film thickness. The working principle is schematically illustrated in Figure 3.1. First, a scratch is made in the film to fully remove a small piece of the film and expose the substrate. Then, the sample is placed at the center of the movable stage, and the diamond-tipped stylus (radius of 2 μm) is lowered down until contact is made with the sample surface via a constant force. The sample stage is moved, and the stylus scans perpendicularly over the scratch. The height distance between the substrate and film (valley and hill shown in the profile) gives the film thickness. For each sample, at least 5 measurements are taken to obtain an average film thickness with sufficient statistics. All the measurements are performed with a contact force of 1 mg, a scan speed of 35 μm s^{-1},

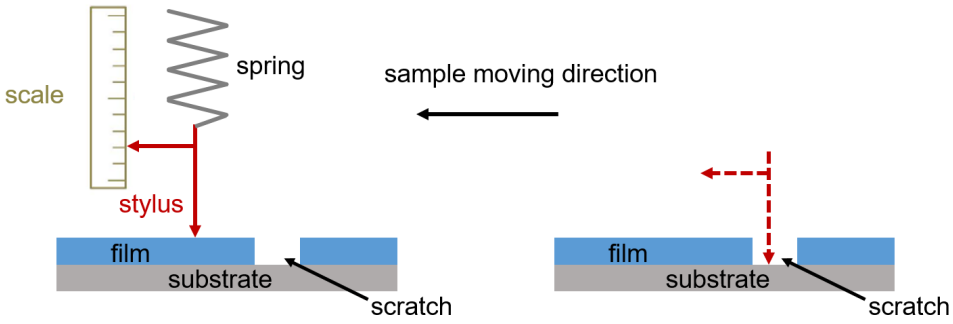

Figure 3.1: Schematic illustration of the height profilometry for measuring film thicknesses. As the sample stage is moved, the stylus scans over the scratch made on the sample. The height distance between the substrate and the film represents the film thickness.

and a scan length of around 700 μm. Data acquisition and analysis are carried out with the software Vision64 (Bruker).

3.1.2 Optical microscopy

Optical microscopy (OM) is used to investigate the surface structure and homogeneity of the films on the micrometer length scale. An Axiolab A microscope (Carl Zeiss) with a series of lenses (from 1.25x to 100x) can be used to magnify the object. Simultaneously, a PixeLink USB Capture BE 2.6 charge coupled device (CCD) camera provides digital images with a resolution of 1280x1024 pixel. The various magnifications and resolutions are summarized below. A halogen Hal 100 lamp is used to illuminate the sample surface. Data analysis such as contrast can be carried out with the software ImageJ.

Magnification	Resolution (μm/pixel)
1.25x	6.26
2.5x	3.11
10x	0.82
50x	0.17
100x	0.082

Table 3.1: Available magnifications and corresponding resolutions of the optical microscope (Axiolab A, Carl Zeiss).

3.1.3 Scanning electron microscopy

Scanning electron microscopy (SEM) is used to probe the surface morphology of the mesoporous TiO_2 film. In contrast to OM, electrons instead of light are used in SEM as the illumination source. As electrons have a shorter wavelength than visible light, a higher resolution is accessible with a SEM, thereby enabling the structure to be probed on the nanometer scale.

All SEM measurements in the present thesis are performed via a FESEM Gemini NVision 40 instrument (Carl Zeiss) together with the software SmartSEM. The instrument is located at Walter-Schottky-Institut/ZNN of TU Munich. Electrons are generated by a field emission gun with a tungsten filament. The electrons are then accelerated by a voltage of several kV and focused on the sample surface through magnetic and electrostatic lenses. The resulting electron beam scans the sample surface in a manner, so-called line by line. Secondary electrons, which are emitted by the sample, are collected by the detector at a small distance away from the sample surface. In addition to secondary electrons, backscattering electrons can also be collected by the corresponding detector, which, however, are not used in the present thesis. For each scanned position, the intensity of the secondary electrons is recorded. This intensity primarily depends on the material, surface morphology, beam size and the incident angle between beam and sample surface. Since the beam size and incident angle are fixed via beam alignment, the obtained grey scaled image with varying brightness is dependent on the material and surface morphology.

The parameters used in the present thesis are as follow. The acceleration voltage is set at 3-5 kV, the working distance (distance between the sample to the gun) at around 3.5 mm, and an aperture size of the primary electron gun at around 10 μm.

3.1.4 X-ray diffraction

X-ray diffraction (XRD) is used to examine the crystallinity of a sample, e.g. TiO_2 or GeO_x. Crystal structures, crystal sizes or degrees of crystallinity of the material can be obtained. XRD measurements are carried out on a Bruker D8 ADVANCE X-ray diffractometer. X-rays are generated through a copper (Cu) anode, which is operated at the voltage of 40 kV and the current of 40 mA. The characteristic Cu K_α radiation is emitted with a wavelength of 1.54 Å. The X-ray beam impinges on the sample at an angle θ, and the specularly reflected beam is detected at the same angle θ. To obtain high quality XRD spectra, slits of 0.6 mm are used to collimate the X-ray before impingement on the sample and again before the detector. The coupled 2θ mode is applied. Typically, a scan range from 20° to 60° is used with a step size of 0.04° for the mesoporous TiO_2

thin film. Due to the very thin thickness, each step is scanned for 25 s. In this case, approximately 8 h are needed for each sample.

The XRD data is analyzed with the software Jade using the Powder Diffraction File (PDF) from the International Centre for Diffraction Data (ICDD). Thus, the TiO_2 crystal structure can be identified by comparing the peaks in the obtained XRD spectra with the standard peaks for anatase or rutile phase from ICDD. In addition, as mentioned in section 2.3.2, with the extracted full width at half maximum (FWHM), the crystal size can be estimated via the Scherrer equation. For example, in chapter 5, the crystallite sizes of the anatase TiO_2 (101) peaks are estimated by the Scherrer equation using the XRD line broadening.

3.1.5 Transmission electron microscopy

Transmission electron microscopy (TEM) is a powerful technique to investigate various material characteristic information, including morphology, size distribution, crystal structure, strain, etc [101]. This technique can provide very high spatial resolution up to the level of atomic dimensions. In the present thesis, TEM is mainly used to further investigate the crystal structure of TiO_2 and GeO_x. TEM samples must be very thin as the electron beam must pass through the sample. The sample thickness depends on the sample density and the electron acceleration voltage. After interaction with the sample, electrons are either unscattered or scattered, and different information about the sample is obtained.

Compared to SEM, which also uses electrons as an excitation source, TEM provides better image resolution due to the instrument consisting of a series of parallel lens in a vertical column (as seen in the schematic in Figure 3.2). In addition, TEM shows more various kinds of analytical measurements. There are many techniques in TEM, which are mainly classified into image, spectroscopy, and diffraction techniques. Some of these techniques are described below.

Bright field (BF) TEM and dark field (DF) TEM

In the imaging mode, the objective aperture is inserted in the back focal plane of the objective lens, where the diffraction pattern is formed in the reciprocal space. If we use the objective aperture to choose only the central beam, the transmitted electrons pass through the aperture as well as very few scattered electrons. This contributes to a bright field image. In the dark field mode, the unscattered electrons are excluded from the aperture and the scattered electrons are selected instead. In comparison of these two

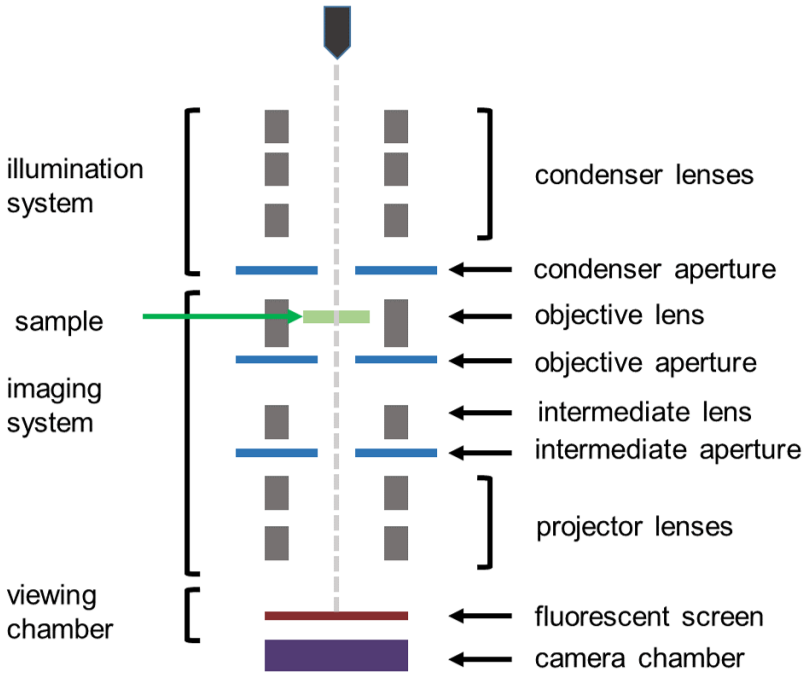

Figure 3.2: Schematic illustration of the working principle of TEM.

types, bright field images are the most commonly image used in TEM. Only when the bright field image is not clear, the dark field mode is used to enhance contrast.

Selected-area electron diffraction (SAED)

In the diffraction mode, a selected area aperture is used to virtually choose an area from the sample, from which the signal forming the diffraction pattern will be displayed. SAED can be used to analyze the crystal structure and crystal orientation.

High-resolution TEM (HRTEM)

The imaging mechanism of high-resolution TEM (HRTEM) is based on the phase contrast, which arises from the interference between the transmitted beam and the diffracted beam. Thus, a projection of atom arrangements will be imaged. For this measurement, a very thin sample is required, typically in the thickness of less than 50 nm (as thin as possible).

In the present thesis, all the TEM measurements are conducted with a Philips CM-200 FEG instrument, operated at 200 kV with a camera length of 340 mm. The instrument is located at the Chair of Materials Physics, Institute of Materials Science, University of Stuttgart. The SAED and HRTEM data are analyzed with the software Gatan.

3.1.6 Grazing-incidence small-angle X-ray scattering

Grazing-incidence small-angle X-ray scattering (GISAXS) is used to investigate the surface and bulk structure of the mesoporous films in the present thesis. The basic working principle of this technique is described in section 2.3.3. The GISAXS measurements presented in this thesis are carried out at the MiNaXS beamline P03 of the PETRA III storage ring at DESY (Hamburg, Germany) [102], or with the in-house Ganesha SAXSLAB instrument at TU Munich.

For the in-house Ganesha SAXSLAB instrument, the X-ray energy is fixed at near 8 keV, which corresponds to a X-ray wavelength of 1.54 Å. The sample-detector distance (SDD) is set at 1045 ± 3 mm. The scattering signal is collected with a Pilatus 300 K detector (Dectris Ltd) with dimensions 487 × 619 pixels (pixel size 172 μm × 172 μm) in vacuum. Due to the limited flux, the specular X-ray reflection, where the exit angle is equal to the incident angle, is not shielded by a beamstop. According to the scattering length density, the theoretical critical angle of titania is 0.27°, while those of the substrate Si and SiO_x are 0.15°and around 0.22°, respectively. For the structure-directing template PS-b-PEO, the theoretical critical angles of the PS and PEO blocks are 0.15°and 0.16°, respectively.

In the case of the synchrotron based GISAXS measurement, the X-ray energy is normally chosen at around 11-13 keV, and the SDD is set between 3000-5000 mm at beamline P03 at DESY. A Pilatus detector (1M, Dectris Ltd.) with dimensions 981 × 1043 pixels (pixel size 172 μm × 172 μm) is used to record scattering signal. Due to the long SDD, a vacuum flight tube is installed in the X-ray pathway, in order to minimize air scattering. The direct beam and specular beam are shielded by beamstops, thereby protecting the detector from oversaturation.

The horizontal line cuts, which include the information about the lateral structure of the investigated film, are performed at the material-dependent Yoneda peak region using the software DPDAK [103]. To quantify characteristic length scales of the structure, the horizontal line cuts are modeled within the framework of the distorted wave Born approximation (DWBA) using the effective interface approximation (EIA), the local monodisperse approximation (LMA) and a 1D paracrystalline lattice. More details are given in section 2.3.3. Within this model, the scattering objects are assumed to have a cylindrical or spherical shape with a Gaussian size distribution, also referred to as the form factors. The center-to-center distances between the neighboring objects are referred to as the structure factors. Figure 3.3 shows an example of a horizontal line cut of the 2D GISAXS data with the applied modeling. From the model, the radius and the corresponding center-to-center distance can be extracted. Vertical line cuts or the off-centered

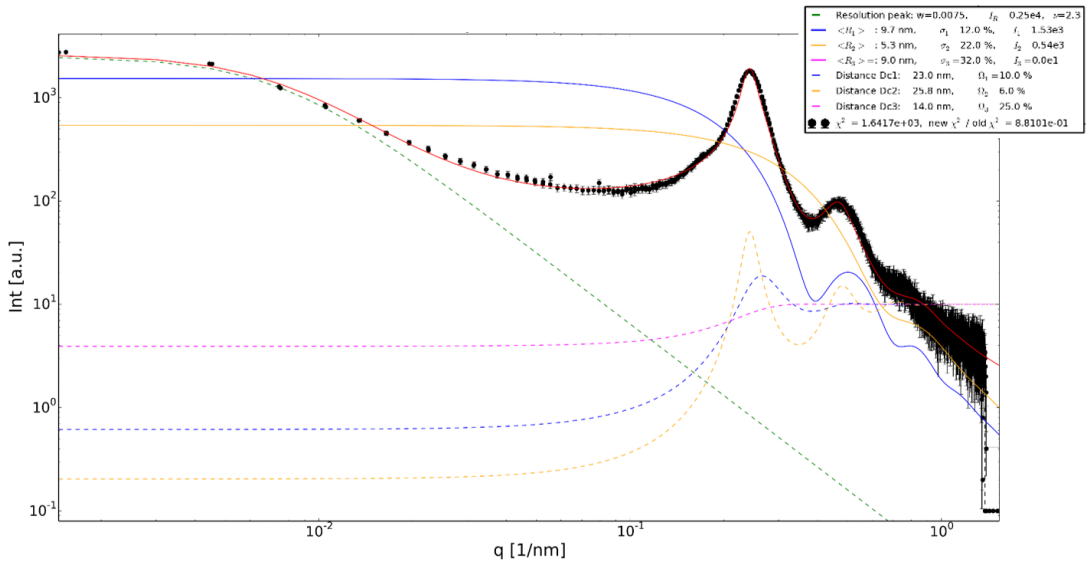

Figure 3.3: Example of the applied GISAXS modeling of a horizontal line cut of the 2D GISAXS data. In the inset, w, ν, I_R refer to the width, exponention and intenisty for the resolution peak. $< R >$, σ and I refer to the average domain radius and its width (standard deviation) of a Gaussian distribution around the central value. D_c and Ω refer to the mean interdomain distance and its width (standard deviation) of a Gaussian distribution around the central value.

vertical line cuts can be analyzed, to obatin the information about the film perpendicular to the substrate.

3.1.7 Grazing-incidence wide-angle X-ray scattering

Grazing-incidence wide-angle X-ray scattering (GIWAXS) measurements are performed in this thesis to reveal the crystalline properties of PffBT4T-2OD and P3HT. More details are given in chapter 6. Key properties that can be extracted are lattice constants, crystal sizes and crystal orientations. The basic working principle of this technique is described in section 2.3.4. All of the GIWAXS measurements in the present thesis are performed with the in-house Ganesha SAXSLAB instrument at TU Munich.

Here, the X-ray wavelength is 1.54 Å, and the sample-detector distance and an incident angle are 106 mm and 0.4°, respectively. The scattering signals for all X-ray measurements are recorded with a Pilatus 300 K detector (Dectris Ltd) with a pixel size of 172 μm $\times$ 172 μm. In the GIWAXS measurements, a resolution of $\Delta q \approx 0.013$ Å^{-1} is achieved. The direct beam is blocked with the beamstop to protect the detector from oversaturation.

Because of the measurement geometry in GIWAXS (as shown in Figure 2.13), the 2D detector image is a distorted version of the reciprocal crystal lattice [99]. To reconstruct the raw 2D GIWAXS data into the reciprocal-space coordinate system, some corrections need to be applied including solid-angle correction, efficiency correction, and polarization correction [104].

The solid angle correction accounts for the measurement geometry, as the recorded scattering intensity is related to the solid angle with respect to the scattering center and the pixel area. The efficiency correction mainly considers that scattered X-rays under different exit angles travel different path lengths, though the surrounding medium (like air). This contributes to different medium attenuation and thus variations in absorption. Thus, for the GIWAXS experiments performed with the in-house Ganesha SAXSLAB instrument, where scattered X-rays travel in the vacuum system, the path length for the efficiency correction should be set to 0. But, for the GIWAXS measurement performed at the beamline, usually, the sample-detector distance should be taken. For the polarization correction, "unpolarized" is chosen for the lab measurement, and "horizontal" polarization for the synchrotron based measurement.

The above mentioned corrections are done with the Matlab-based software GIXSGUI (developed by the Advanced Photon Source, Argonne National Laboratory, USA). The 2D GIWAXS data before and after these corrections is shown in Figure 2.15a and b, respectively. For analyzing the crystallinity of the organic polymer, the vertical and/or horizontal-sector integrals are taken from the corrected reciprocal space patterns, as shown in Figure 2.15c. The integration curve like in Figure 3.4a is obtained. After subtracting the background (indicated by the red curve) from the substrate in a normalized way by taking the beam intensity into account Figure 3.4b, the resulting curve (Figure 3.4c) is finally fitted with Gaussian functions. According to the peak center and FWHM from the Gaussian function, the lattice constant and crystallite size can be determined.

3.2 Spectroscopic and electronic characterizations

To reveal the material composition of the mesoporous nanocomposite films, X-ray photoelectron spectroscopy (XPS) is introduced in section 3.2.1. Additionally, an important insight into the optoelectrical properties of the mesoporous films and the related active layers needs to be provided. Within this frame, ultraviolet-visible (UV-Vis) spectroscopy and photoluminescence (PL) spectroscopy are explained in section 3.2.2 and section 3.2.3, respectively. Finally, the current-voltage characteristic measurements, performed under simulated AM 1.5 sunlight at 100 mW cm^{-2} irradiance, are used to evaluate the solar cell performance.

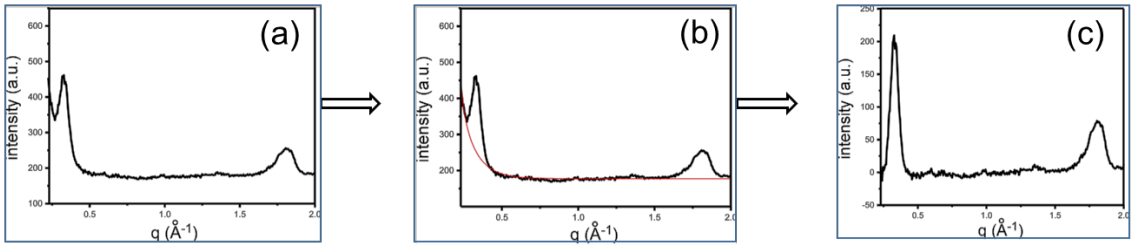

Figure 3.4: An exemplary background subtraction for the integration curve of a P3HT-backfilling active layer. The background (indicated by the red curve) is subtracted in a normalized way, which takes the beam intensity into account: (a) measured data, (b) data and background (red), and (c) after background subtraction.

3.2.1 X-ray photoelectron spectroscopy

X-ray photoelectron spectroscopy (XPS) is used in the present thesis to reveal the elemental composition of the TiO_2/GeO_x nanocomposite films (chapter 8). This technique is intrinsically surface-sensitive and thus delivers information on the outermost layer of the films (typically < 10 nm below surface). XPS measurements are conducted using a custom-built UHV system (located at Surface and Interface Physics (E20) at TU Munich) operated at a base pressure of approximately $2{\times}10^{-10}$ mbar. A conventional twin-anode X-ray source delivering Al K_α ($h\upsilon = 1486.6$ eV) and Mg K_α ($h\upsilon = 1253.6$ eV) radiation is used as the excitation source. Photoelectron spectra are recorded employing a hemispherical electron energy analyzer (ES200 spectrometer, AEI Scientific Apparatus Ltd). The binding energy scale is calibrated using the Au 4f7/2 line (binding energy: 84.0 eV) from a small Au stripe attached to the sample holder.

For the XPS measurements, films are spin-coated on Si substrates. The electron detection angle is fixed at around 40°. Survey scans are recorded with a pass energy of 20 eV and the zoomed-in regions of the Ge 2p3/2, Au 4f and C 1s core levels with a pass energy of 10 eV. Spectra are acquired with both available K_α emission lines and calibrated in binding energy via the Au 4f7/2 core-level line and alignment of the C 1s photoemission.

3.2.2 UV/Vis spectroscopy

In the present thesis, the optical absorption of the active layer and/or the transmittance of the mesoporous TiO_2 film from the ultraviolet to near infrared region are probed with a Lambda 35 UV-Vis spectrophotometer (PerkinElmer). The instrument is equipped with two lamps, a halogen lamp and a deuterium lamp. The deuterium lamp provides UV light

in the range of 190-326 nm. The halogen lamp provides light in the near infrared and the visible range from 326-1100 nm. Typically, the scan speed is set to 120 nm min^{-1}, the spectra slit width set to 1 nm, and a glass substrate is used as a reference sample.

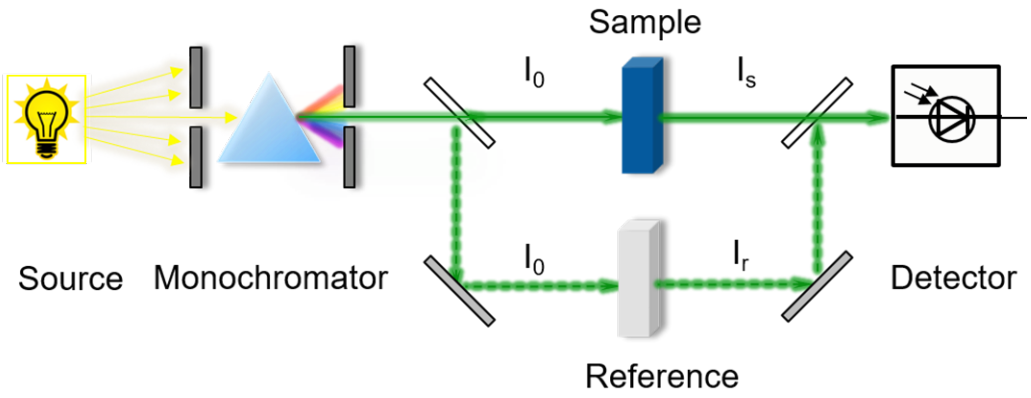

Figure 3.5: Schematic setup of a UV/Vis spectrophotometer.

Figure 3.5 shows the schematic setup of a UV/Vis spectrophotometer. Grating monochromators ensure the generation of a monochromatic beam. During the measurement, the incoming beam is split into two beams. One beam probes the sample, while the other beam passes through the reference sample. Both outgoing beams are detected by photodiodes, seperately. The ratio of the transmitted intensity through the sample and the transmitted intensity through the reference is recorded. From this measured intensity ratio, the absorbance (A) is calculated via the Lambert-Beer law

$$A(\lambda) = -log_{10}\left(\frac{I_t(\lambda)}{I_0(\lambda)}\right) = \alpha(\lambda) L log_{10} e \tag{3.1}$$

where $I_t(\lambda)$ is the transmitted intensity of the incident beam going through the sample, $I_0(\lambda)$ the reference beam intensity, $\alpha(\lambda)$ the absorption coefficient of the specific material, and L the light path length through the sample (also called the layer thickness).

The optical band gaps of the film are then estimated from the absorbance or transmittance UV-Vis spectra using the Tauc equation

$$\alpha h\upsilon = A(h\upsilon - E_g)^n \tag{3.2}$$

in which A is a constant, α is the absorption coefficient of the material, hυ is the photon energy, and E_g is the optical band gap. In the case of an indirect band gap n equals 2, and in the case of a direct band gap n equals 1/2. Anatase TiO_2 exhibits an indirect band gap, therefore n = 2 is applied to estimate the optical band gap.

3.2.3 Photoluminescence spectroscopy

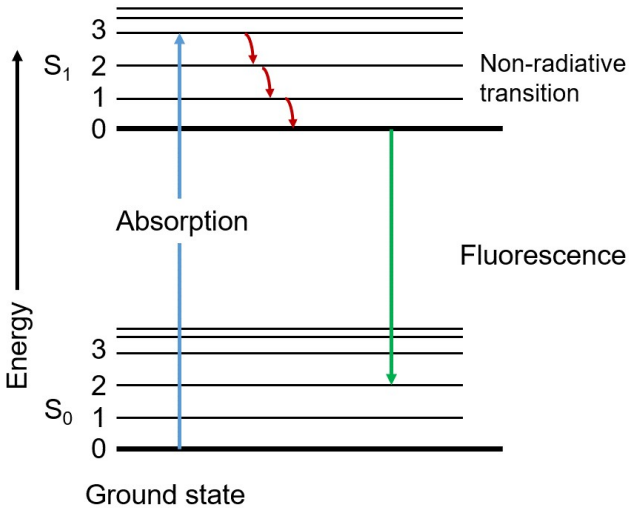

Figure 3.6: Schematic illustration of Jablonski diagram including vibrational levels for absorbance, non-radiative decay, and fluorescence.

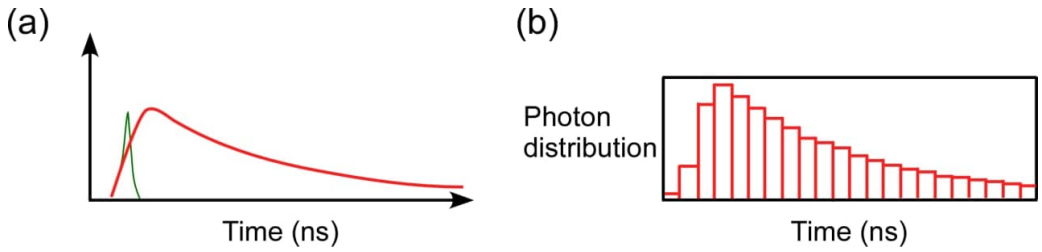

Figure 3.7: Schematic illustration of working principle of TCSPC: (a) A measured waveform, (b) a histogram of the number of photons detected for the time difference.

Photoluminescence (PL) spectroscopy is a non-destructive, contactless method to probe the electronic structure of materials [105]. PL is the light emission process from a sample after absorption of photons. After photo excitation, electrons within a material in the ground state will be excited and occupy the permissible higher energy states. When electrons return to their equilibrium states, the excess energy is released. This process may include the emission of light (a radiative process) and/or a non-radiative process, as shown in Figure 3.6. The quantity of the emitted light, PL intensity, is related to the relative contribution of the radiative process.

The return to equilibrium is also known as recombination and, as mentioned above, can involve both radiative and non-radiative processes. The information of charge carrier recombination is of significance in the solar cell performance. In chapter 8, compared with the pristine TiO_2 film, marked photoluminescence (PL) quenching is observed in the FTO/compact TiO_2/mesoporous TiO_2-GeNC/perovskite systems, indicating a reduced recombination of generated charge carriers at the ETL/perovskite interface. This enhanced charge extraction process can be attributed to the intrinsic property of a high electron mobility of the ETLs established by introducing GeNCs.

Time-resolved photoluminescence (TRPL) is a tool to study the charge carrier dynamics of the functional stacking layers as in the perovskite solar cells. Time-correlated single photon counting (TCSPC) is a common method to perform TRPL measurements. The basic working principle of TCSPC is shown in Figure 3.7. The sample is illuminated by a laser pulse, finally resulting in the waveform as shown in Figure 3.7a. The time between the sample excitation by a laser pulse and the arrival of the emitted photon at the detector is measured, and is the x-axis in Figure 3.7b. The number of photons is detected for this time difference, is the y-axis in Figure 3.7b. When much less than 1 photon per excitation pulse is detected, the histogram as shown in Figure 3.7b represents the decay curve. Typically, the multi-exponential decay functions are used to fit the decay curve. Then the decay times τ, amplitudes of the components A and number of decay times are extracted. The amplitude-weighted average lifetime τ_{v1} is calculated by the equation:

$$\tau_{v1} = \sum_i \alpha_i \tau_i \tag{3.3}$$

The intensity-weighted average lifetime τ_{v2} is calculated by the equation:

$$\tau_{v2} = \frac{\sum_i \alpha_i \tau_i^2}{\sum_i \alpha_i \tau_i} \tag{3.4}$$

where τ_i is the decay lifetime for different components and α_i is the amplitude fraction of each lifetime component.

In the present thesis, the steady-state PL and TRPL measurements are carried out on a Picoquant Fluotime 300 spectrofluorometer with an excitation wavelength of 370 nm. The instrument is located at the Chair of Physical Chemistry, LMU. For the PL/TRPL measurements, the compact TiO_2 is spin-coated at the clean FTO substrate (3500 rpm, 30s), and followed by the mesoporous layer (see section 4.2.1). Finally, the perovskite layer is fabricated, as described in section 4.3.2.

3.2.4 IV characterization

To evaluate the photovoltaic performance of solar cells, e.g. perovskite solar cells in chapter 8, I-V measurements are conducted using the Keithley 2611B Source Meter under simulated AM 1.5 sunlight at 100 mW cm^{-2} irradiance generated by a solar simulator (LOT-Quantum Design GmbH). The intensity is calibrated with a KG-5 filtered Si reference cell. The aperture-defined active area of the solar cells is 0.12 cm^2. For each sample, eight solar cells are fabricated to obtain device data statistics.

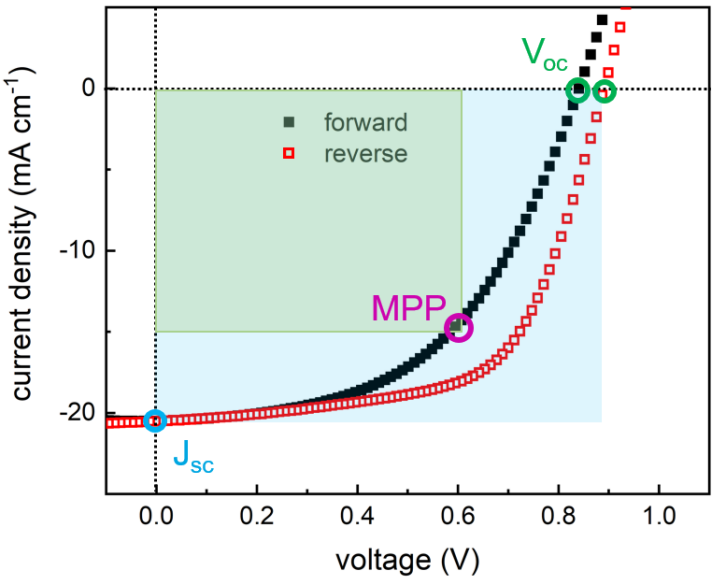

Figure 3.8: An illustration of exemplary J-V curves of a perovskite solar cell. V_{oc}, J_{sc} and maximal power point (MPP) are indicated. The reverse scan is indicated as the red rectangle, and the forward scan is indicated as the black rectangle.

Exemplary J-V curves of a perovskite solar cell are shown in Figure 3.8. The voltage V is swept from -0.2 V to 1.2 V and the current I is recorded for each pixel. The current density $J = 1/\mathrm{A}$ is then calculated using the pixel area. From the J-V curve measured under illumination, the related photovoltaic parameters such as open-circuit voltage V_{oc}, short-circuit current density J_{sc}, maximum power point (MPP), power conversion efficiency (PCE) and fill factor (FF), are extracted. As shown in Figure 3.8, V_{oc} is obtained when $J = 0$ and J_{sc} is obtained when $V = 0$. Generally, V_{oc} is related to the band states of the n- and p-type semiconductors in the active layer, while J_{sc} relies on many factors, such as charge carrier generation, separation, transportation and extraction.

In Figure 3.8, the point where the power density of $P = JV$ is maximum is referred to as the maximum power point (MPP) (indicated by the purple circle). The fill factor (FF) is the ratio of the maximum achievable power density (determined from the MPP

indicated by the green area) and the theoretical maximum possible power density, P_{max} = $V_{oc}J_{sc}$ (indicated by the blue area) and is given as

$$FF = \frac{P_{MPP}}{P_{max}} = \frac{V_{MPP}J_{MPP}}{V_{oc}J_{sc}} \tag{3.5}$$

The power conversion efficiency (PCE) is defined as the ratio of the output power (P_{out}) and the input power (P_{in}):

$$PCE = \frac{P_{out}}{P_{in}} = \frac{V_{oc}J_{sc}FF}{P_{AM1.5}} \tag{3.6}$$

The well-known hysteresis behavior is shown in the JV-characteristics (Figure 3.8), in which the reverse scan (indicated as the red rectangle) shows higher performance than that of the forward scan (indicated as the black rectangle). The theoretical part about the hysteresis behavior is introduced in section 2.2.3.

4 Sample preparation

The materials, preparation processes of mesoporous titania films and the related solar cell fabrication (quantum dot-sensitized solar cells (QDSSCs) and perovskite solar cells (PSCs)) are introduced in this chapter. The key materials used in this thesis are described in section 4.1, the preparation of mesoporous titania films in section 4.2, the photovoltaic device fabrication in section 4.3 and sample preparation for cross-section SEM in section 4.4.

4.1 Materials

In the following section, the titania precursor, the structure-directing polymer template and the p-type semiconductors will be primarily introduced. Some materials used in the QDSSCs and PSCs will be mentioned in section 4.3.

Titania precursor

The titania precursor used in the present thesis is titanium(IV)isopropoxide (TTIP, 97%), which is purchased from Sigma-Aldrich, Germany. It is a transparent liquid with a relative density of 0.96 g mL^{-1}. Its stoichiometric formula is $Ti[OCH(CH_3)_2]_4$, and the corresponding chemical structure is shown in Figure 4.1a.

Structure-directing polymer template

The amphiphilic diblock copolymer polystyrene-block-poly(ethylene oxide) (PS-b-PEO) is used as a structure-directing template. It is purchased from Polymer Source Inc., Canada. The number average molecular weight (M_n) of the PS block and the PEO block is 20.5 kg mol^{-1} and 8 kg mol^{-1}, respectively. The polydispersity index is 1.02. The PS block is hydrophobic, while the PEO block is hydrophilic. The chemical structure of PS-b-PEO is shown in Figure 4.1b.

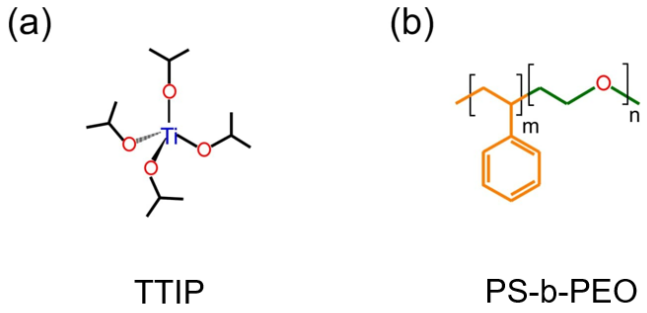

Figure 4.1: Chemical structures of TTIP and PS-b-PEO.

Poly(3-hexylthiophene) (P3HT)

As one of the most well-studied p-type polymers, P3HT has HOMO and LUMO levels of -5.2 eV and -3.2 eV respectively and its band gap is around 1.9 eV [106]. With the alkyl chains, P3HT has good solubility, which is typically dissolved in chlorobenzene, toluene, etc at room temperature [97,107]. In addition, the high hole mobility of up to 0.1 cm^2 V^{-1} s^{-1} enables P3HT to be used as a hole transport material in solar cell applications. The polymer is purchased from Ossila Ltd., United Kingdom. The weight average molecular weight (M_w) is 65.2 kg mol^{-1} and a regioregularity of 95.7%. The chemical structure of P3HT is shown in Figure 4.2a.

Poly[(5,6-difluoro-2,1,3-benzothiadiazol-4,7-diyl)-alt-(3,3‴-di(2-octyldodecyl)-2,2′;5′,2″;5″,2‴-quaterthiophen-5,5‴-diyl)](PffBT4T-2OD)

PffBT4T-2OD is a novel semiconducting p-type polymer with a low band gap of 1.65 eV. Its HOMO and LUMO levels are located at -5.34 eV and -3.69 eV [18], respectively. PffBT4T-2OD has an excellent hole mobility (1.5-3.0 $\times$ 10^{-2} cm^2 V^{-1} s^{-1}) and high crystallinity [17]. Also, a relatively long exciton diffusion length enables PffBT4T-2OD to have large domain sizes up to 30-40 nm in diameter [108]. These properties make PffBT4T-2OD showing high performance in organic solar cells, yielding device efficiencies of about 11% in single junction organic solar cells [18, 109]. Note that PffBT4T-2OD can only be dissolved in dichorobenzene or the mixture solvent of chlorobenzene and dichlorobenzene (1:1 v/v) at elevated temperature of around 110 °C [18]. The polymer used in this thesis is purchased from Cal-OS Inc., USA. The weight average molecular weight (M_w) is 131 kg mol^{-1} and the polydispersity index is 1.76. The chemical structure of PffBT4T-2OD is shown in Figure 4.2b.

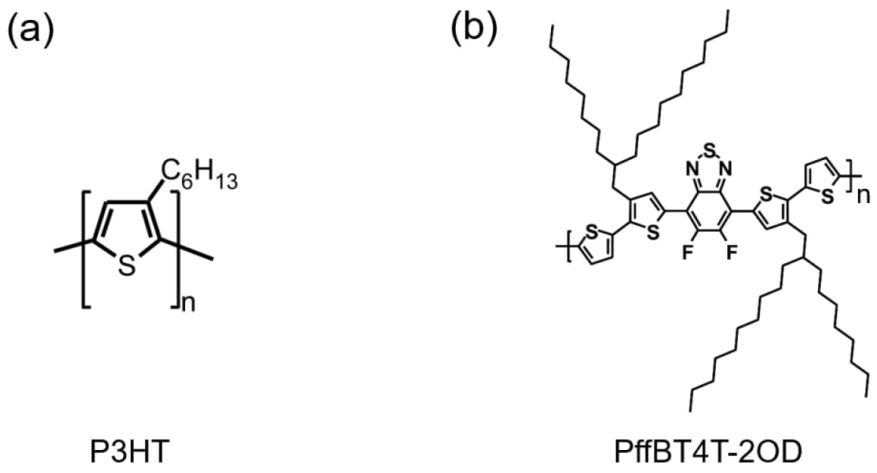

Figure 4.2: Chemical structures of P3HT and PffBT4T-2OD.

4.2 Preparation of mesoporous titania films

With the combination of a diblock-copolymer templating sol-gel synthesis with the different deposition methods, the mesoporous titania films are fabricated, as shown in Figure 4.3.

4.2.1 Preparation of titania sol-gel solution

In the present thesis, two different sol-gel protocols are used. The main difference between them is the adopted solvent: one is using 1,4-dioxane (chapter 5 and chapter 6), another is using toluene and 1-butanol (chapter 7 and chapter 8).

Sol-gel solution with 1,4-dioxane

PS-b-PEO is a structure-directing template, TTIP a titania precursor, and 1,4-dioxane in combination with hydrochloric acid (HCl) a good-bad solvent pair. First, PS-b-PEO is dissolved in the good solvent 1,4-dioxane with stirring for 30 min. After complete dissolution, the solution is filtered with polytetrafluoroethylene filters (PTFE) with a pore diameter of 0.2 μm to obtain a homogeneous solution, in which both PS and PEO chains can stretch well (as illustrated in Figure 4.3a). Additionally, TTIP and HCl are diluted with 1,4-dioxane, respectively and mixed on the shaker for 10 min. Each solution mixture with almost equal volume is infused into the polymer solution using a microfluidic

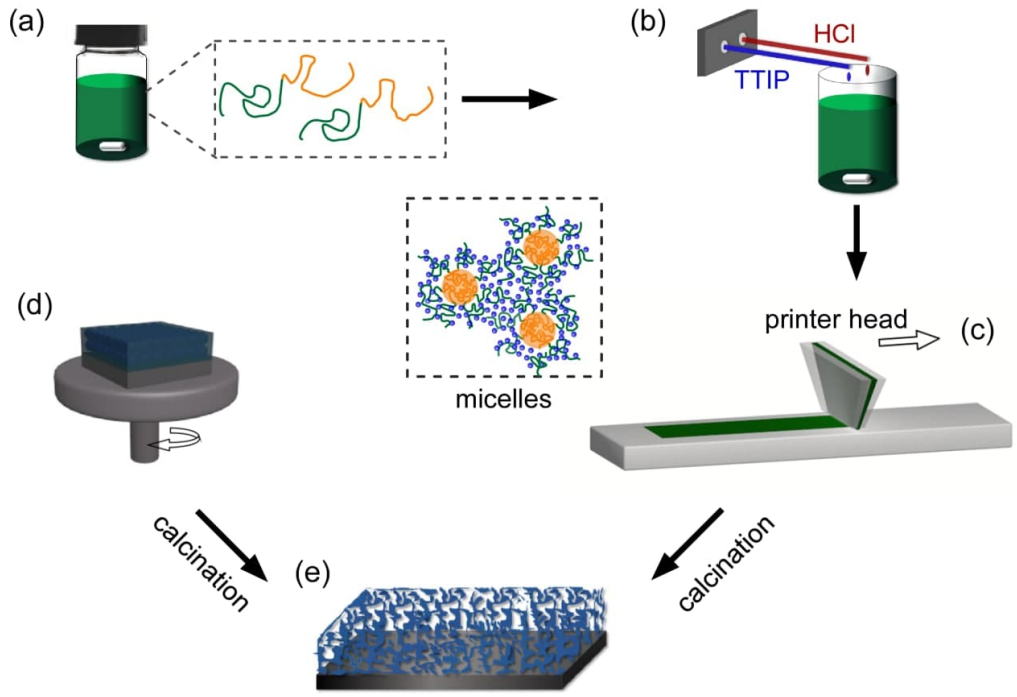

Figure 4.3: Schematic illustration of the fabrication of mesoporous titania thin films. (a) Dissolution of the diblock copolymer template (PS-b-PEO) in a good solvent, (b) addition of the titania precursor (TTIP) and bad solvent (HCl), depositing the sol-gel solution with (c) slot-die printing and (d) spin coating, (e) final mesoporous titania films obtained after calcination. Reproduced with permission from JOHN WILEY AND SONS, Copyright 2019 [110].

device (PHD 2000 infuse/withdraw, Harvard Apparatus) with a flow rate of 0.25 mL min^{-1} under vigorous stirring (as illustrated in Figure 4.3b). More details about the microfluidic device used in sol-gel synthesis are described by Rawolle et al. [11]. The obtained micelles in solution have hydrophobic PS cores and hydrophilic PEO shells, with TTIP being incorporated inside the PEO domains. The concentration of the polymer in the final solution is kept constant at 16.50 mg mL^{-1}.

In chapter 5, the weight ratios of $w_{1,4-dioxane}$, w_{TTIP} and w_{HCl} are varied to tailor the morphology of titania. While only four different compositions: $w_{1,4-dioxane}/w_{HCl}/w_{TTIP}$ = 97.5%:1%:1.5%, 97%:1%:2%, 96%:1.5%:2.5%, 96%:1%:3%, are investigated in chapter 6.

Sol-gel solution with toluene and 1-butanol (TB)

PS-b-PEO acts as a structure-directing template and TTIP as a titania precursor. The toluene (T) and 1-butanol (B) mixed solvent and HCl serve as a so-called "good-bad" solvent pair.

For the slot-die printing (chapter 7), the sol-gel solution with toluene and 1-butanol (TB) is prepared as follows. Initially, ∼50 mg PS-b-PEO is dissolved in a solvent mixture (1 mL) of toluene and 1-butanol (72.8 wt% toluene and 27.2 wt% 1-butanol forming a binary azeotrope). After complete dissolution, the polymer solution is filtered via a polytetrafluoroethylene (PTFE) filter with a pore diameter of 0.2 μm. Next, 185 μL TTIP is diluted by 856 μL of the mixed solvent and then added into the polymer solution. Later, 44.4 μL HCl is diluted with 500 μL of the mixed solvent, and then carefully added dropwise under vigorous stirring into the polymer solution. The weight fractions of the toluene and 1-butanol mixture, TTIP and HCl is set at 90%:8%:2%.

For the sol-gel solution with pre-synthesized germanium nanocrystals (GeNCs) [111] used in chapter 8, the solution preparation process is as below. First, 100 mg PS-b-PEO is dissolved in a TB mixed solvent (3607 μL). After 30 min, a polytetrafluoroethylene (PTFE) filter with a pore diameter of 0.2 μm is used to filter the completely dissolved polymer solution. Subsequently, 382.4 μL TTIP is added into the polymer solution after diluting by 500 μL TB solvent. Similarly, 101.4 μL HCl is diluted with 500 μL TB solvent and then cautiously added dropwise under vigorous stirring. Finally, the titania sol-gel solution is stirred for about 30 min at room temperature.

The functionzed GeNCs with dodecyl chains and average sizes of 7-9 nm are pre-synthesized [111]. The dodecyl functionalization enables GeNCs to be stored as a suspension in toluene for further utilization. Five different types of solutions with the weight ratios of GeNCs to TiO_2 of 0, 0.5, 1.0, 2.5, and 5.0 wt% are prepared as follows. The sol-gel solution is divided into 5 portions, each of 700 μL. After ultrasonic dispersion for approximately 10 min, GeNCs (5 mg mL^{-1}) are added into these 5 specified portions with the volumes of 0 μL, 14.2 μL, 28.4 μL, 71.0 μL and 142.0 μL, separately. Finally, titania films with five pre-defined concentrations of GeNCs are fabricated.

4.2.2 Deposition methods

In the following sections the deposition methods used in the present thesis will be described. The main deposition method used for the sol-gel solution is slot-die printing (as illustrated in Figure 4.3c). However, for the sol-gel solution with pre-synthesized germanium nanocrystals in chapter 8, spin coating is used to fabricate the mesoporous films (as illustrated in Figure 4.3d).

Slot-die printing

A general procedure to print films with the slot-die technique will be explained. The final sol-gel solution can be deposited on a pre-cleaned silicon (Si), or glass or fluorine-doped

tin oxide (FTO)-coated glass substrate by printing. The dry film thickness in case of slot-die coating can be controlled by [112]:

$$d = \frac{f}{Sb}\frac{c}{\rho} \tag{4.1}$$

where d is the film thickness (cm), f is the solution flow rate (cm^3 min^{-1}), S is the printing speed (cm min^{-1}), b is the printing width (cm), c is the concentration of the printing solution (g cm^{-3}) and ρ is the density of the dry film (g cm^{-3}). The target TiO_2 film thickness is obtained by optimizing the distance between the substrate and printer head, the solution flow rate and printing speed. Afterwards, the sample remains in the printer chamber for drying in a closed environment.

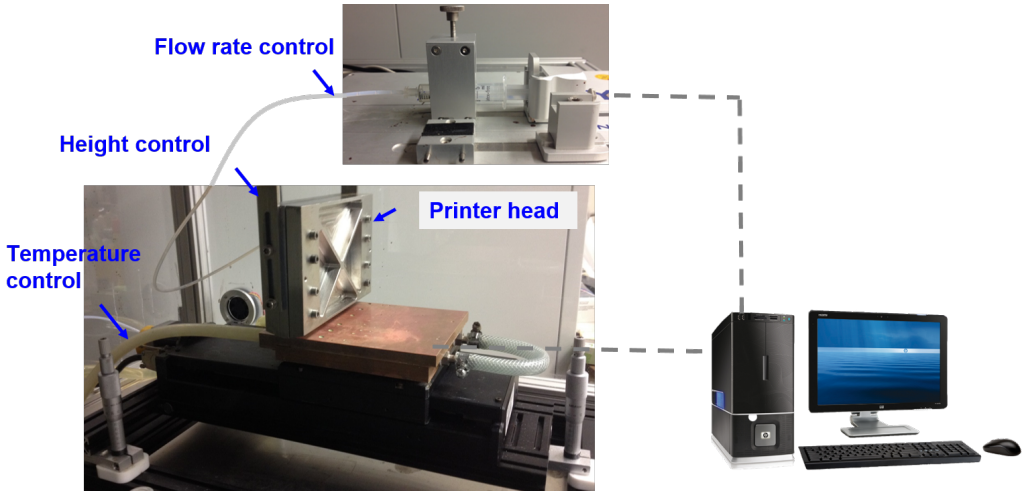

Figure 4.4: An overview of Slot-die printing set up. This home-made set up is designed and built by Sebastian Max Günther.

For the printer used in chapter 5 and chapter 6, as shown in Figure 4.4, it is designed and built by Sebastian Max Günther from the group. While the printer used in chapter 7, as shown in Figure 4.5, is designed and built by Sebastian Grott and Rodrigo Delgado Andrés from the group. Both printing devices consist of three main parts: printer head, syringe pumping system and linear stage.

For the printing parameters for preparing mesoporous TiO_2 in chapter 5 and chapter 6, the printing parameters are the same. That is the printing velocity of 5 mm s^{-1} and solution flow rate of 10 μL s^{-1}. The final titania thickness after calcification is set to around 200 nm. For the corresponding parameters used in chapter 7, the solution flow rate is set at 100 μL/min, the printing velocity at 7 mm/s with an acceleration of 5 mm/s^2 and the distance between substrate and printer head as around 0.4 mm.

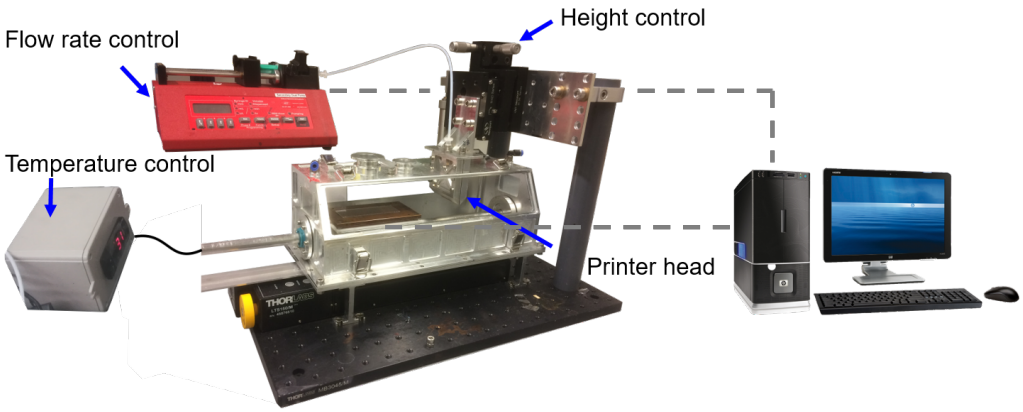

Figure 4.5: An overview of Slot-die printing set up. This home-made set up is designed and built by Sebastian Grott and Rodrigo Delgado Andrés from the group.

Spin coating

In laboratory-scale deposition processes, spin coating is a widely used technique to obtain homogeneous films. Spin coating is performed with a Delta 6 RC TT (Süss MicroTec Lithography GmbH) spin coater. Generally, the spin coating process can be divided into four steps. (1) The cleaned substrate is placed on the rotation table in the center of the spin coater, and fixed with a vacuum pump. (2) The solution is dropped onto the substrate, and spread over the substrate. (3) The substrate is rotated at a high angular speed, and thus most of the solution is flung off the substrate. (4) The majority of the solvent evaporates rapidly, caused by airflow during rotation. Thus, spin coating is a nonequilibrium process with a ultrafast speed. Finally, a thin film is obtained. In addition to the angular speed and acceleration, the film thickness also depends on the solvent, the viscosity and concentration of the solution. In the case of films derived from pure polymer solution, the film thickness can be roughly estimated by the Schubert equation [113]

$$d = C\omega^{-\frac{1}{2}} c_0 M_W^{\frac{1}{4}} \tag{4.2}$$

in which C is an empirical constant, ω is the angular speed, c_0 is the solution concentration and M_W is the molecular weight of the polymer. In most cases, the film thickness can be increased by adjusting the angular speed and acceleration, or by repeating the spin coating process.

For preparing mesoporous TiO_2 in chapter 8, spin coating is performed on silicon (Si) and glass substrates (2000 rpm for 60 s). Oxygen plasma cleaning (10 min, 200 W) of the substrates is used to improve the film homogeneity.

4.3 Photovoltaic device fabrication

In the present thesis, two different photovoltaic devices: QDSSCs and PSCs are fabricated. Differences between these two device architectures (see Figure 2.7 and Figure 2.8) are the absorbing material and the hole-transporting layer (HTL). For etching and cleaning fluorine-doped tin oxide (FTO)-coated glass substrates, as well as for preparing the compact titania layer, a standard protocol/methodology is followed [114], as shown in Figure 4.6a,b. As for the mesoporous film (Figure 4.6c), the sol-gel solution and deposition methods are described above.

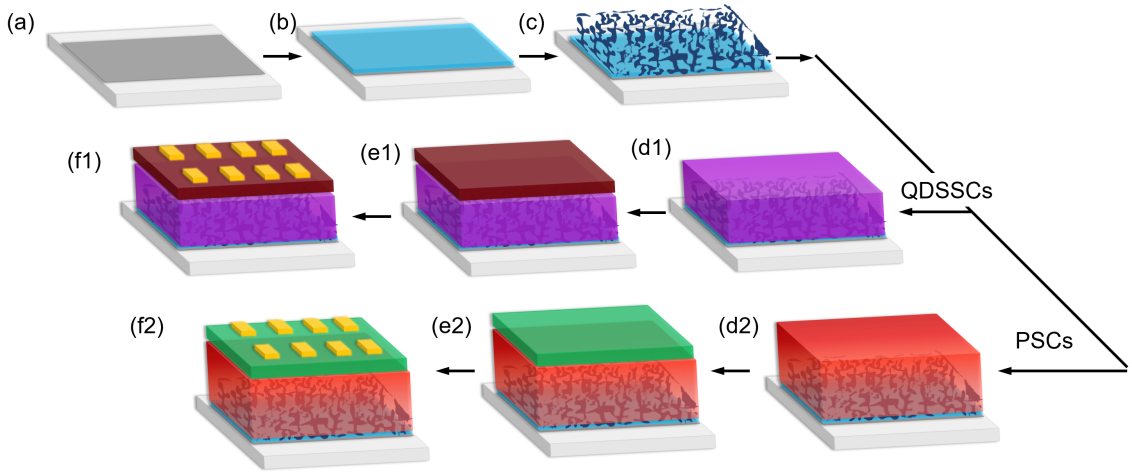

Figure 4.6: Schematic illustration of the fabrication of QDSSCs and PSCs. On (a) etched FTO sheets, (b) the compact TiO_2 is deposited as an electron blocking layer, then (c) the mesoporous TiO_2 film is fabricated. Next, (d1)-(e1) the QD ink layer, and the EDT-treated QD layer as the HTL are fabricated. Alternatively, (d2)-(e2) the perovskite layer and the spiro-OMeTAD layer as the HTL are fabricated. (f1) and (f2) gold top contacts are deposited via thermal evaporation.

FTO glass slides are etched with zinc powder and HCl (8 M). Then FTO glass slides are cleaned with Hellmanex cleaning solution in an ultrasonic bath (15 min), followed by deionized (DI) water (15 min), acetone (15 min), ethanol (15 min) and isopropanol (15 min). After treatment with oxygen plasma for 10 min, the compact titania solution is used [114], and then a thin compact titania layer is spin coated on the cleaned FTO substrates (3500 rpm, 30 s). The samples are immediately annealed at 150 °C for 5 min and subsequently are calcined at 500 °C for 45 min (heating rate of 300 °C h^{-1}) and then treated with oxygen plasma for 30 min. Afterwards, the mesoporous films are prepared (see section 4.2). Then the resulting films are calcined at 500 °C for 2 h (heating rate of 60 °C h^{-1}).

4.3.1 Quantum dot-sensitized solar cells (QDSSCs)

Figure 4.6d1-f1 shows the basic steps, including the deposition of the light absorbing material and the hole-transporting layer (HTL), for QDSSC fabrication. The lead sulfide (PbS) quantum dot (QD) ink (around 200 mg mL^{-1} in butylamine) is deposited onto the mesoporous TiO_2 substrate by single-step spin-coating at 2500 rpm for 30 s (Figure 4.6d1). For the HTL (Figure 4.6e1), the oleic acid capped PbS QDs (50 mg mL^{-1} in octane) are spin-coated at 3000 rpm for 30 s onto the QD ink layer. Next, the film is spin-coated with 1,2-ethanedithiol (EDT) in acetonitrile (0.02 % v:v) for the ligand exchange treatment and then is rinsed with acetonitrile twice. To achieve the suitable thickness of the HTL, the spin-coating procedure is repeated with the same parameters. The information related to the QDs can be found in the literature [115]. Finally, gold top contacts are deposited via thermal evaporation (Figure 4.6f1).

4.3.2 Perovskite solar cells (PSCs)

Figure 4.6d2-f2 shows the counterpart for PSC fabrication. The perovskite precursor solution is prepared by dissolving formamidinium iodide (FAI, 1.0 M), lead iodide (PbI_2, 1.05 M), methylammonium bromide (MABr, 0.2 M), and lead bromide ($PbBr_2$, 0.2 M) in a mixed solvent of anhydrous N,N-dimethylformamide (DMF) and dimethylsulfoxide (DMSO) (4:1, volume ratio) of 800 mL. The precursor is dropped on the mesoporous TiO_2 samples. Then, the samples are spin-coated with 5000 rpm for 30 s in the nitrogen glove box with O_2 and $H_2O < 10$ ppm, and 90 μL chlorobenzene is added at the end of the fabrication progress (5 s before ending). 72.3 mg Spiro-OMeTAD is dissolved in 1 mL chlorobenzene with additives of 17.5 μL bis(trifluoromethylsulfonyl)-imide lithium salt (Li-TFSI) solution (520 mg mL^{-1} in acetonitrile), and 28.8 μL 4-tert-butylpyridine (TBP). After the substrates are cooled down to room temperature, 60 μL spiro-OMeTAD is dropped on the perovskite layers at 3000 rpm for 20 s. After spin-coating, the substrates are kept in a desiccator with silica gel (RH < 10 %) for 24 hours. A 80 nm-thick gold electrode is thermally evaporated under vacuum. Finally, the PSC devices are kept in a desiccator with silica gel (RH < 10 %) before measuring the power conversion efficiency (PCE).

4.4 Sample preparation for cross-section SEM

For doing cross-section measurements, firstly a line is scratched by a diamond cutter and made on the backside of the sample. Then, the sample is treated by liquid nitrogen for

around 1 min. After taking out the sample from the liquid nitrogen, it is immediately put on the edge of a metal, and slightly hit. Accordingly, the sample is broken along the scratching line. In order to obtain a sharp edge, the treatment via liquid nitrogen is necessary. But for some polymers and QDs, liquid nitrogen will be not suitable due to the damage of the materials.

This sample preparation process is the same as for side-view SEM measurements. But for cross-section SEM, a specified stage is used (as shown in Figure 4.7a), in the case of which the cross section of the sample is measured in the same way as the sample surface. Or the stage is the same as that for measuring sample surfaces (as shown in Figure 4.7b), but the methods of sample mounting for the surface and cross-section measurements are different.

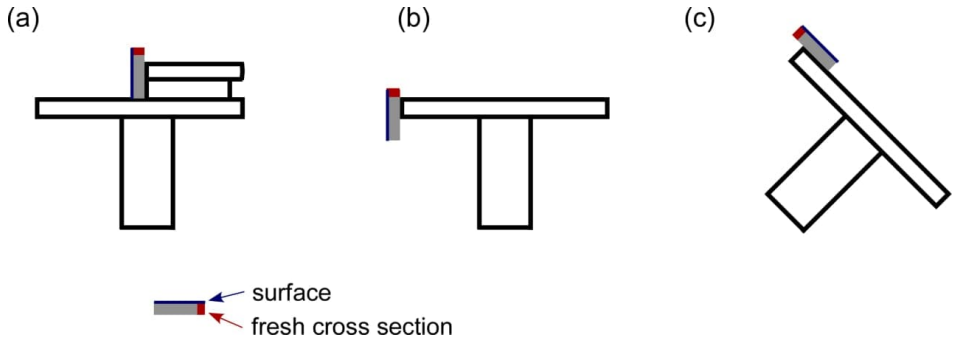

Figure 4.7: Schematic illustration of sample mounting at the stage for (a), (b) cross-section and (c) side-view measurements: (a) a specified stage, (b) the same stage as for surface measurements, but a different mounting method, and (c) the same stage and same mounting method, but the stage titled.

Side-view SEM measurements are performed to check the backfilling situation of the donor polymers in the active layer (chapter 6). For side-view measurements, the stage and mounting method are the same as used for surface measurements. Typically, samples are titled in respective to the electron beam (around 40–45 degree) for a better view, as shown in Figure 4.7c. Due to this large titled degree, it rather present a side view rather than a cross section. Also, in this way, the capping polymer layer residing on the surface can be observed.

5 Morphology phase diagram of slot-die printed titania films

This chapter is based on the published article: Morphology phase diagram of slot-die printed TiO_2 films based on sol-gel synthesis (N. Li et al., Adv. Mater. Interfaces, 2019, 1900558, 1–9, DIO: 10.1002/admi.201900558). Reproduced from Ref [110] with permission from JOHN WILEY AND SONS, Copyright 2019.

Nanostructured titania (TiO_2) films are chemically stable, non-toxic, low cost and have a controllable nano-morphology [9, 10, 26, 116]. Due to these advantages, they contribute to a wide range of applications, such as in the field of photocatalysis [117], gas sensing [15], lithium-ion batteries [118], supercapacitors [119], and biomaterials [120]. In addition, nanostructured TiO_2, especially in its anatase polymorph, has attracted great attention in the field of photovoltaics due to its wide bandgap, high electron mobility and long charge-carrier lifetime [20, 121–123]. As electron transport layer in solid-state dye-sensitized solar cells and hybrid solar cells, nanostructured TiO_2 films with a high surface-to-volume area and interconnected network are desirable because they hold the potential to improve the generation of charge carriers and inhibit electron-hole recombination [11,12]. The combination of sol-gel chemistry with an amphiphilic block copolymer acting as a structure-directing template was proven to be a promising route for producing nanostructured TiO_2 films [52,61]. The obtained sol-gel solution can be directly deposited by various film fabrication techniques, such as spin coating [124], solution casting [125], doctor blading [126], spray coating [127] or inkjet printing [128].

To date, most attention of such kind of wet chemical TiO_2 film fabrication has only been paid to laboratory-scale deposition processes, such as the spin coating technique, which are less well suited for e.g. fabrication of solar cells. In contrast, large-scale coating processes, such as spray coating, are highly attractive since they enable a simple, low-cost production of films on almost any surfaces [107,124]. However, spray coating needs a carrier gas as deposition aid. Moreover, similar to inject printing, in spray coating it is also challenging to control the film thickness due to the lack of facile models describing the wet film thickness [129]. Other large scale deposition methods such as screen printing require the adjustment of viscosity with the help of a large amount of additives, which turned out

to be challenging for precise control of the film morphology on the nanoscale [130, 131]. To address this issue, we focus on the printing technique with a slot die coater, which is an alternative industry-scale technique, to prepare TiO_2 films based on wet-chemical processes with similar solution viscosities as used in spin coating. In addition, this printing technique enables to fabricate multilayer films with high efficiency and high cost-saving since all the ink can be applied to fabricate films without waste of material [16].

So far, slot-die printing has been mainly used in fabricating organic semiconducting devices out of tailored inks [132,133]. For example, Garnier et al. reported that all-polymer field-effect transistors were fabricated by only using a printing technique, and the devices showed excellent performance [134–137]. Recently, the structure evolution of active layers of organic solar cells was investigated with in-situ measurements during printing because the morphology plays a significant role in the photovoltaic performance of these devices [135–137]. In addition, an external field (magnetic field and electric field) can be employed in the printing process to direct structures, since slot-die printing is a uniaxial deposition method unlike spray coating. Also, it allows for structural rearrangement within sufficient solvent-evaporation time [16, 138]. For example, Xia et al. successfully printed magnetic thin films with oriented structures applying an external magnetic field [16]. Therefore, unlike the screen-printing TiO_2 powder pastes as for example reported by Ito et al. [130], the slot-die printing combined with sol-gel solution provides not only the accessibility but also various external methods to control the film morphology for different applications. However, this printing applied in inorganic semiconductors or hybrid solar cells is rarely reported today.

In this chapter, we provide a new route to fabricate nanostructured TiO_2 films on large scale. The synthesis is performed by the combination of sol-gel chemistry with the diblock copolymer template polystyrene-block-polyethylene oxide (PS-b-PEO), in which TTIP is used as the precursor and 1,4-dioxane together with hydrochloric acid (HCl) as a good-bad solvent pair. In section 5.2, the morphology phase diagram of printed titania films after template removal is achieved by adjusting the weight fraction (w) of 1,4-dioxane, HCl and TTIP. Surface and inner morphologies of printed titania films are probed with scanning electron microscopy (SEM) and grazing incidence small-angle X-ray scattering (GISAXS), respectively, since the mesoscopic behavior of TiO_2 structures greatly affects their final performance. In addition, we further study the region of foam-like morphology in more detail (section 5.3) since this type of morphology is highly desirable for photovoltaic applications. The foam-like titania network is excellently suited to have a high interface with the p-type counterpart and offers a percolating network for charge carrier transport. Besides the morphology, the crystallinity of TiO_2 is another critical parameter affecting the photovoltaic usefulness, as higher crystallinity is more beneficial for the transport

of photogenerated charge carriers [139]. Therefore, in section 5.4 the crystal phase and crystallinity of titania at different calcination temperatures in air are detected by X-ray diffraction (XRD) and high crystalline anatase titania is proven with transmission electron microscopy (TEM) upon the calcination temperature of 450 °C.

5.1 Printer and printing parameters

The sol-gel solution preparation is described in section 4.2.1. The diblock copolymer PS-b-PEO (the number molecule weight of PS and PEO is 20.5 and 8 kg mol^{-1}, respectively) is used. The concentration of the polymer in the final solution is kept constant at 16.50 mg mL^{-1}, while the weight ratios of $w_{1,4-dioxane}$, w_{HCl} and w_{TTIP} are varied to tailor the morphology of titania. A total of 21 composition points are studied for data as shown in Figure 5.1. For each composition point, around 10 slot-die printed TiO_2 samples are fabricated in average to achieve sufficient experimental statistics.

After stirring the mixed sol-gel solutions for 45-60 min, the final solution is deposited on precleaned silicon (Si) or fluorine-doped tin oxide (FTO)-coated glass substrates with the size of 25 x 75 mm^2 by printing. In the present chapter, the printer (as shown in Figure 4.4), designed and built by Sebastian Max Günther, is used. The printing velocity is 5 mm s^{-1} and solution flow rate is 10 μL s^{-1}. In our case, the TiO_2 film thickness is set to about 200 nm by optimizing the distance between the substrate and printer head, the solution flow rate, and printing speed. Afterwards, the sample remains in the printer chamber (10 min) for drying in a closed environment.

5.2 Morphology phase diagram influenced by weight ratio

In photovoltaic applications, different film morphologies can provide tailored surface-to-volume ratios in combination with optimized charge carrier transport routes, thereby influencing the solar cell efficiency. For example, Wang et al. investigated the photovoltaic performances induced by three different ZnO film morphologies including foam-like, worm-like and sphere-like, and found the devices with worm-like ZnO structures exhibit highest power conversion efficiencies as compared with other morphologies [140]. Therefore, the ternary phase diagram of printed TiO_2 nanostructures within the probed composition area is investigated and shown in Figure 5.1. The phase diagram is measured by adjusting $w_{1,4-dioxane}$, w_{HCl} and w_{TTIP}. It can be divided into four regions of different titania nanostructures, namely foam-like nanostructures (red area in Figure 5.1),

nanowire aggregates (green area in Figure 5.1), collapsed vesicles (blue area in Figure 5.1) and nanogranules (yellow area in Figure 5.1).

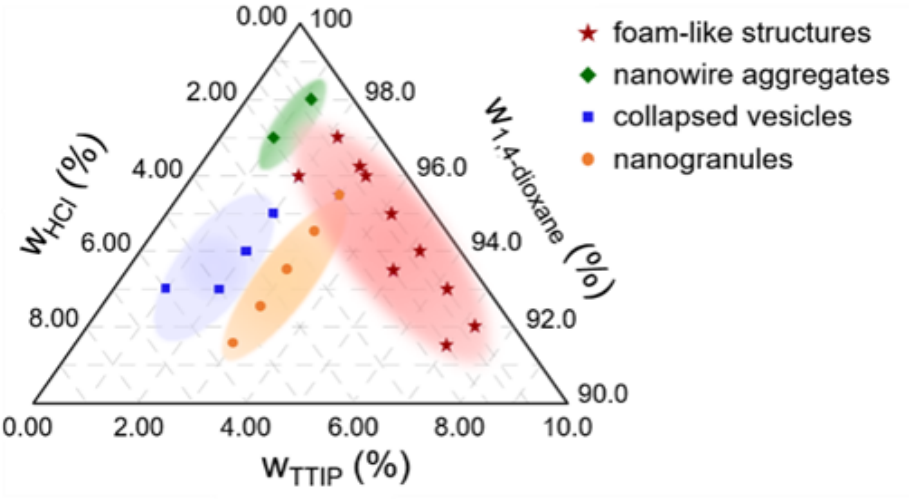

Figure 5.1: Phase diagram of printed TiO_2 films after calcination with varied weight fractions of 1,4-dioxane, HCl and TTIP. Four types of titania nanostructures are observed as indicated with the different colored symbols and areas: Foam-like nanostructures (red stars), nanowire aggregates (green diamonds), collapsed vesicles (blue squares) and nanogranules (orange spheres). Reproduced from Ref [110] with permission from JOHN WILEY AND SONS, Copyright 2019.

The four different morphologies selected from each region of the phase diagram are exemplarily shown in Figure 5.2. These morphologies are referred to their corresponding compositions, namely composition 1, 2, 3 and 4 (denoted as C1, C2, C3 and C4, respectively). The composition region of each nanostructure morphology is primarily consistent with the morphology phase diagram of TiO_2 nanostructures prepared via spin-coating as reported by Cheng et al. [57]. However, when using printing the variety of achievable titania nanostructures is smaller than that fabricated by spin-coating. One possible reason is that spin-coating is a non-equilibrium process with ultra-fast speed, which can freeze-in structures within fractions of seconds [141]. In contrast, printing provides sufficient time with polymer chain mobility during solvent evaporation, and finally an equilibrium structure can be formed according to a study about the effect of evaporation time on the phase separation behavior of the block copolymer, in which the final TiO_2 morphology becomes stable after 80 s evaporation time [122]. Furthermore, the resulting morphology greatly depends on the different parameters of the spin-coating process such as acceleration and spinning speed, in addition to the nature of the sol-gel solution. Comparing to a study

of various zinc oxide (ZnO) nanostructures by spin-coating, Sarkar et al. obtained similar morphologies within a broader compositional region than that of printed TiO_2 [142]. However, this might be related to the different physical and chemical properties of the individual materials used.

5.2.1 Surface morphology

Micro-phase separation of the amphiphilic diblock copolymer PS-b-PEO induced by the good-poor solvent pair, tends to form core (PS domain)-shell (PEO domain) structures [143]. It has been reported that the major factors influencing the morphology of the aggregates in the solution are the copolymer composition and concentration, water content, nature of the common solvent, presence of additives (acid, salt or base), etc [44–47]. The formation of various morphologies is mainly governed by the stretching degree of the PS blocks, the interfacial tension between the PS cores and the surrounding solvents, and repulsive interactions among the PEO chains [49].

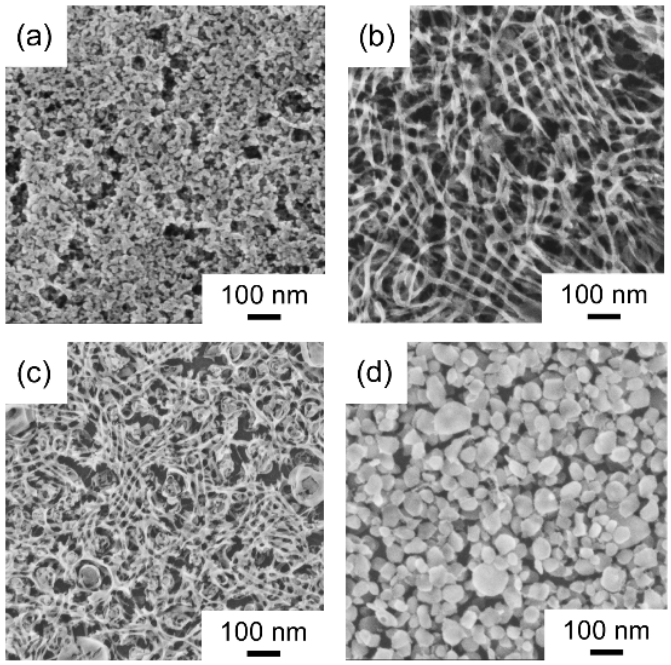

Figure 5.2: SEM images of printed titania films with varied weight fraction of 1,4-dioxane, HCl and TTIP after calcination: (a) $w_{1,4-dioxane}/w_{HCl}/w_{TTIP}$ = 96%:0.75%:3.25% (C1), (b) $w_{1,4-dioxane}/w_{HCl}/w_{TTIP}$ = 97%:2%:1% (C2), (c) $w_{1,4-dioxane}/w_{HCl}/w_{TTIP}$ = 95%:3%:2% (C3), and (d) $w_{1,4-dioxane}/w_{HCl}/w_{TTIP}$ = 95.5%:1.5%:3% (C4). Reproduced from Ref [110] with permission from JOHN WILEY AND SONS, Copyright 2019.

As shown in the phase diagram (Figure 5.1), a foam-like nanostructure area is found at a

lower weight fraction of HCl (w_{HCl} less than or equal to 2%). The process of forming such nanostructures can be assumed as following. Firstly, the polymer chains stretch well in the good solvent 1,4-dioxane. With gradually adding small amount of HCl, which serves as a bad solvent for the PS block, the interfacial energy between PS domains and the surrounding solvents increases and thus PS blocks tend to aggregate in order to decrease the surface free energy [55]. As a result, spherical micellar structures are formed in the solution with PS cores and PEO shells. Meanwhile, TTIP incorporated into PEO domains by hydrogen bonds, undergoes the hydrolysis and condensation reaction, which results in the formation of Ti-O covalent bonds [57]. Random motion of massive small spherical micelles in the solution significantly increases the possibility of mutual collision of two micelles, which causes the cross-linking of Ti-O beyond adjacent PEO domains. Therefore, the three-dimensional network formation of Ti-O bonds is greatly enhanced [142]. During calcination the templating block copolymer is combusted and TiO_2 crystallizes. Thus, a foam-like nanostructure with a large surface area is obtained as shown in Figure 5.2a. For w_{TTIP} less than or equal to 1%, only nanowire aggregates (Figure 5.2b) are observed. With further addition of HCl, a mixed morphology of nanowire aggregated and collapsed vesicles (Figure 5.2c) appears as shown in Figure 5.1, agreeing well with the morphology transition reported by Eisenberg [48]. In their case, PS-b-PAA was applied as the amphiphilic block copolymer, 1,4-dioxane as a good solvent for both blocks, and water as a bad solvent for the PS block. With increasing water content, the micellar morphology gradually changed from spherical aggregates, over sphere and cylinder mixtures, to cylinders, to cylinder and vesicle mixtures, and finally to vesicles [48]. An increase of bad solvent leads to an increasing surface energy between PS blocks and the surrounding solvents in the solution, while the repulsive interactions among PEO domains might not change much, because both, 1,4-dioxane and HCl, are good solvents for PEO chains [48]. Thus, larger spherical micelles tend to form to decrease the interfacial energy. During the PS-core enlarging, the stretching of the PS blocks increases, which leads to an increase of the free energy of the related component [48]. However, when the stretching degree is too high, a spherical micellar aggregate has to change into cylindrical shape to minimize the surface area to reach a new balance of the interfacial tension, PEO-shell repulsion and stretching of the PS chains [48, 57]. Analogically, the transition from cylinder to vesicle is also driven by decreasing the surface energy [48]. When w_{HCl} is roughly more than 2% and w_{TTIP} is increased, the thickness of the titania wall of the vesicles will rise since more TTIP material is present to undergo hydrolysis and condensation. Thus, the granular morphology is obtained as presented in Figure 5.2d. Overall, there is no obvious boundary among the neighboring morphology phases. For example, at $w_{1,4-dioxane}/w_{HCl}/w_{TTIP}$ = 95.5%:1.5%:3%, both nanogranules and foam-like nanostructures can be observed.

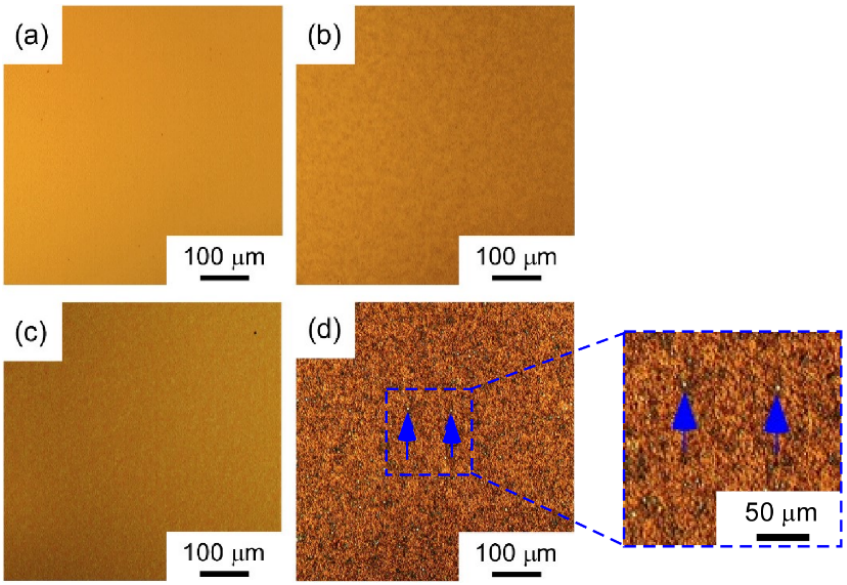

Figure 5.3: OM images of printed titania films with varied weight fraction of 1,4-dioxane, HCl and TTIP after calcination: (a) $w_{1,4-dioxane}/w_{HCl}/w_{TTIP}$ = 96%:0.75%:3.25% (C1), (b) $w_{1,4-dioxane}/w_{HCl}/w_{TTIP}$ = 97%:2%:1% (C2), (c) $w_{1,4-dioxane}/w_{HCl}/w_{TTIP}$ = 95%:3%:2% (C3), and (d) $w_{1,4-dioxane}/w_{HCl}/w_{TTIP}$ = 95.5%:1.5%:3% (C4). Blue arrows in (d) indicate some white light spots, implying the large aggregates. Reproduced from Ref [110] with permission from JOHN WILEY AND SONS, Copyright 2019.

OM measurements are performed to investigate the homogeneity of the printed titania films on a large scale (Figure 5.3). The films revealing a foam-like structure show the most uniform surface (Figure 5.3a), whereas the films classified as nanogranule structures present a distinctive contrast (Figure 5.3d). Moreover, some white light spots can be observed in Figure 5.3d (exemplary marked with blue arrows), which might result from the formation of large-sized clusters during the deposition of the titania films. Additionally, Figure 5.2 also shows nanogranule structures with the biggest average size, which is consistent with the OM results.

5.2.2 Inner morphology

For photovoltaic applications, the inner morphology of mesoporous titania films is of a great importance, since the generation of charge carriers occurs at the donor-acceptor interface [67, 144]. In addition, the charge carriers need to be transported along the corresponding donor and acceptor materials to the respective electrodes. Thus, it is necessary to know the size of the nanostructures and pores of the titania films. GISAXS has shown to be a powerful tool to detect buried structures of thin films and allow for the

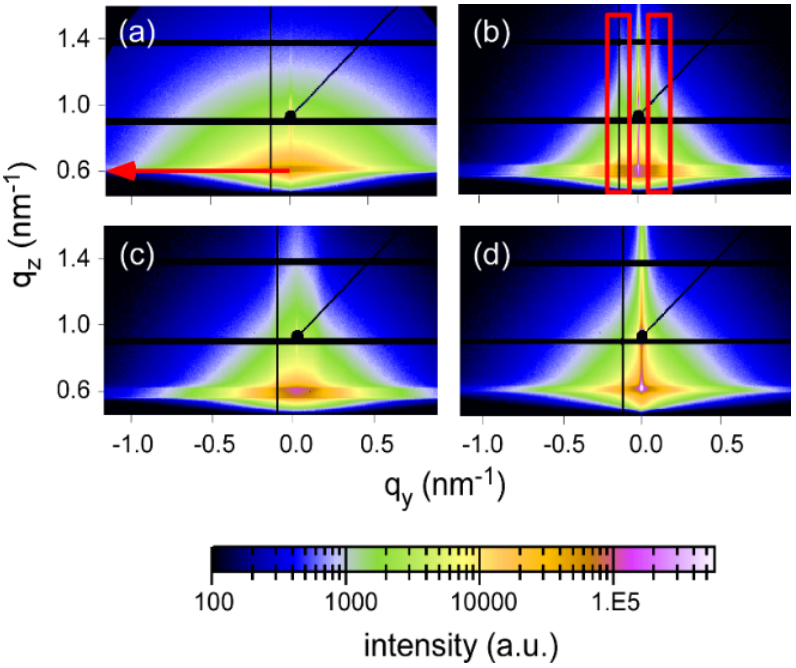

Figure 5.4: 2D GISAXS data of printed titania films with varied weight fraction of 1,4-dioxane, HCl and TTIP after calcination: (a) $w_{1,4-dioxane}/w_{HCl}/w_{TTIP}$ = 96%:0.75%:3.25% (C1), (b) $w_{1,4-dioxane}/w_{HCl}/w_{TTIP}$ = 97%:2%:1% (C2), (c) $w_{1,4-dioxane}/w_{HCl}/w_{TTIP}$ = 95%:3%:2% (C3), and (d) $w_{1,4-dioxane}/w_{HCl}/w_{TTIP}$ = 95.5%:1.5%:3% (C4). The specular reflection for all the samples is shielded by a circular beamstop. The red arrow in (a) displays the exemplary position where the horizontal line cuts are performed. Two red rectangles in (b) indicate the prominent Bragg scattering rods. All the images are in the same intensity scale. Reproduced from Ref [110] with permission from JOHN WILEY AND SONS, Copyright 2019.

determination of a large range of the length scales from nanometer to micrometer with a high statistical relevance [145]. In contrast, local real-space imaging techniques such as SEM, can probe only small areas of the surface morphology [95]. The two-dimensional (2D) GISAXS data of the calcined titania films for the different morphologies are displayed in Figure 5.4. The specular reflected X-ray beam, occurring at the exit angle equal to the incident angle, is blocked by a circular beamstop to avoid oversaturation of the detector. The observed intensity maximum is located at the so called Yoneda peak region [98], which is correlated to the material dependent critical angle and is in this case induced by TiO_2. To quantify the information about the lateral structures in the TiO_2 films, horizontal line cuts are done at the Yoneda peak position along the q_y direction by the software DPDAK, as indicated by the red arrow in Figure 5.4a. Moreover, two vertical Bragg rods are observed in Figure 5.4b (as indicated by the red rectangle), which implies

a certain structural order in lateral direction originated in the nanowire morphology of the film [146].

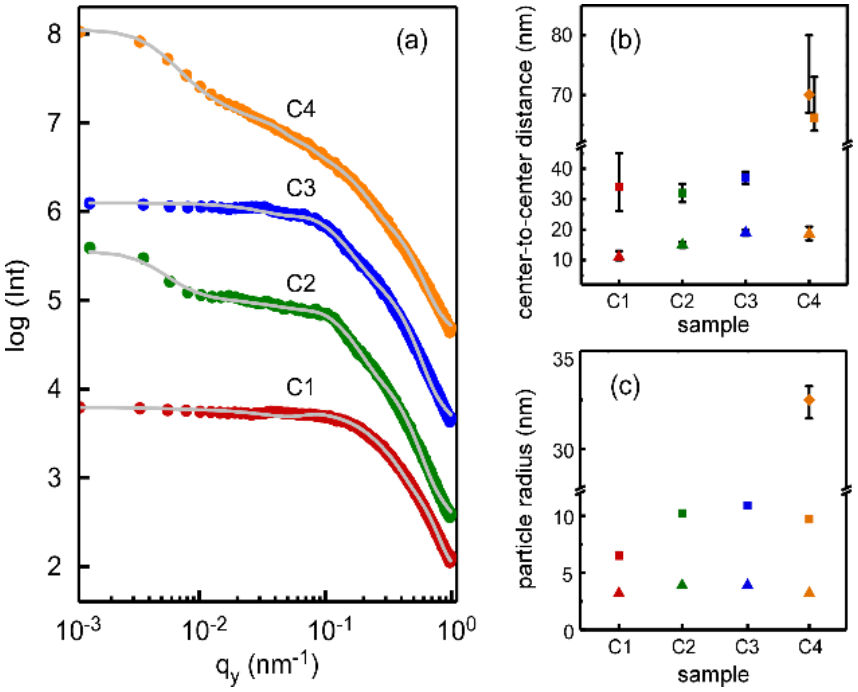

Figure 5.5: (a) Horizontal line cuts of 2D GISAXS data of printed titania films with varied weight fraction of 1,4-dioxane, HCl and TTIP after calcination: (a) $w_{1,4-dioxane}/w_{HCl}/w_{TTIP}$ = 96%:0.75%:3.25% (C1), (b) $w_{1,4-dioxane}/w_{HCl}/w_{TTIP}$ = 97%:2%:1% (C2), (c) $w_{1,4-dioxane}/w_{HCl}/w_{TTIP}$ = 95%:3%:2% (C3), and (d) $w_{1,4-dioxane}/w_{HCl}/w_{TTIP}$ = 95.5%:1.5%:3% (C4). The grey lines represent the fits to the data. All data points and fits are shifted along the y-axis for clarification. Extracted characteristic length scales: (b) Center-to-center distance and (c) particle size in different TiO_2 morphology films as a function of the weight fraction of 1,4-dioxane, HCl and TTIP. Rhombi represent the large cluster in the titania films of nanogranules and squares represent the large-sized structures in other films. Triangles represent the small-sized structures. Reproduced from Ref [110] with permission from JOHN WILEY AND SONS, Copyright 2019.

The horizontal line cuts for the TiO_2 films with different morphologies are plotted in Figure 5.5a. To gain more details about the structures inside the films, the cuts are modelled in the framework of the distorted-wave Born approximation (DWBA) using the effective interface approximation (EIA) and the local monodisperse approximation (LMA), assuming the scattering objects have a cylindrical shape distributed over one-dimensional paracrystal lattices [92, 147–149]. All the data are successfully fitted using two form factors except for the films with nanogranular morphology which require three different cylinder-shaped objects for the best fits. Based on this model, the best fits are

shown as grey solid lines in Figure 4a. The center-to-center distances, represented by the structure factor, and the corresponding particle radii, represented by the form factor, are extracted and plotted as a function of the composition of 1,4-dioxane, TTIP and HCl (Figure 5.5b,c). The small-sized structures in all films have similar particle radii of about 3.2-3.9 nm irrespective of the composition, while the corresponding center-to-center distances slightly increase as the morphologies change from foam-like, to nanowire aggregates, then to collapsed vesicles, finally to nanogranules. The average pore size is approximated by [61]:

Pore size = center-to-center distance – 2 × particle radius

Thus, the size of small pores in foam-like structure is calculated to be 4.6 ± 2 nm, and it gradually rises to 12.4 ± 2.5 nm for the nanogranules. However, the big-sized structures in the films within foam-like, nanowire aggregate and collapsed vesicle morphology show the opposite trend. The center-to-center distances remain constant within the error bars, whereas the related radii show a slight increase with the morphology transitions. Therefore, the pore size of foam-like structure shows the biggest value of 21 ± 11 nm, which is beneficial for the backfilling of hole-transporting materials in hybrid solar cells [150]. For the nanogranules, although the middle-sized structure (big-sized structures for other morphologies) has a particle radius similar to that of nanowire aggregates and collapsed vesicles, it has a larger center-to-center distance. Consequently, it has a bigger pore size of 46.8 ± 11 nm. Unlike two characteristic form and structure factors used in the other morphologies, another one is required to understand the microstructure of the nanogranules, which is due to the formation of large clusters with the averaged radius of 32.5 ± 1 nm. Overall, for the big-sized structures in all films, the radii are increasing when the morphologies transform from foam-like, to nanowire aggregates, then to collapsed vesicles, finally to nanogranules. This increase is probably related to the general decrease in surface area caused by the morphology transitions, which is contributed to the increase in the particle size.

On the one hand, pore sizes of titania films in the range around 40 nm could decrease the possibility of exciton recombination [151]. On the other hand, the larger pore sizes are favorable for the infiltration with hole-transporting materials [140]. Comparing with nanowire aggregates and collapsed vesicles, the foam-like titania films possess suitable and larger big-sized pores of 21 ± 11 nm. It is believed that the big-sized pores play a primary role in the application for hybrid solar cells [124]. While compared to nanogranules, the foam-like titania films have a high surface area and an interconnected network structure, which are promising for providing continuous paths for electron transport and thereby for producing high photovoltaic performance. Thus, the foam-like area in the

morphology phase diagram is investigated in detail by fine adjusting the weight fraction of the components.

5.3 Impact of titania precursor on foam-like mesoporous titania films

In order to investigate the influence of the ratio of $w_{1,4-dioxane}$, w_{TTIP} and w_{HCl} on the evolution of the foam-like nanostructures, we keep w_{HCl} fixed at 0.75% and about 1.5%, respectively, while w_{TTIP} and $w_{1,4-dioxane}$ are varied.

5.3.1 TiO_2 films at low weight fraction of HCl

Surface morphology

For the first ratio of $w_{HCl} = 0.75\%$, the w_{TTIP} increases from 3.25% to 7.25% with an increment of 2%. The resulting surface morphologies are measured with SEM and shown in Figure 5.6a-c. It is found that the sample with the lowest concentration of TTIP ($w_{TTIP} = 3.25\%$) shows the highest uniformity, whereas some large pores with a diameter of about 100 nm are present in the samples with higher TTIP amounts. The appearance of large pores on the surfaces of films with high TTIP content might be related to a denser foam-structure. This might hinder the effective removal of the template during calcination, which leads to less uniform film surfaces. However, this hierarchical TiO_2 structures (in Figure 5.6c) might enhance light scattering, and then result in an absorption improvement [150].

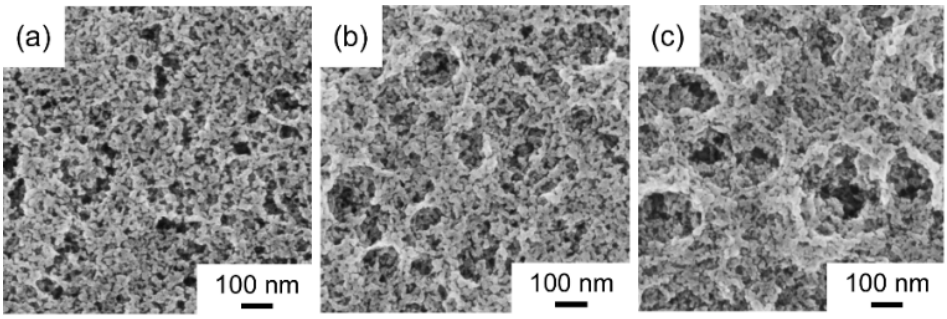

Figure 5.6: SEM images of foam-like TiO_2 films with keeping w_{HCl} at 0.75% and varying w_{TTIP} from: (a) 3.25%, (b) 5.25% to (c) 7.25%. Reproduced from Ref [110] with permission from JOHN WILEY AND SONS, Copyright 2019.

Inner morphology

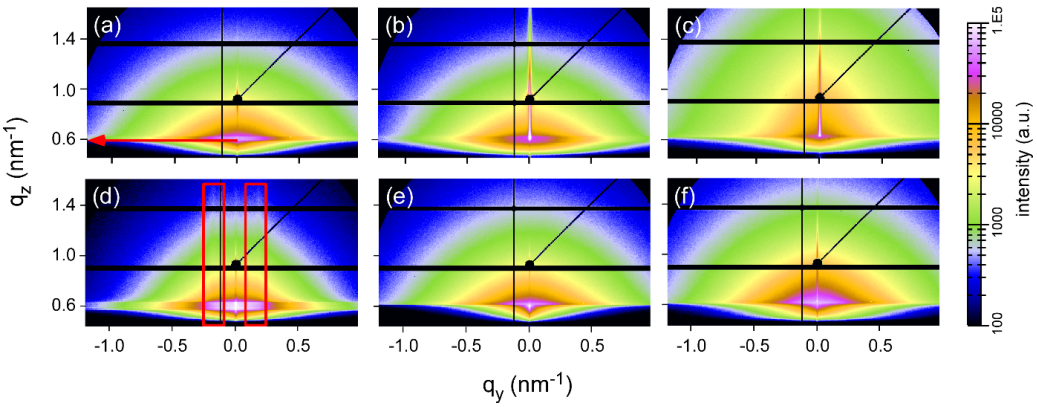

Figure 5.7: 2D GISAXS data of foam-like TiO_2 thin films at constant w_{HCl} of 0.75% and varying w_{TTIP} of (a) 3.25%, (b) 5.25% and (c) 7.25%, and constant w_{HCl} at about 1.5% and varying w_{TTIP} of (d) 2%, (e) 5% and (f) 7% after calcination. The red arrow in (a) displays the exemplary position where the horizontal line cuts are performed. Two red rectangles in (d) indicate the prominent Bragg scattering rods. Reproduced from Ref [110] with permission from JOHN WILEY AND SONS, Copyright 2019.

The GISAXS data of the foam-like titania films with different w_{TTIP} are shown in Figure 5.7a-c. The horizontal line cuts of the 2D GISAXS data have been done along q_y at the Yoneda peak position (Figure 5.7a). The cuts are fitted using the same model as described above. All curves are fitted with two characteristic structure and form factors. Figure 5.8a depicts the horizontal line cuts with their corresponding fits. The extracted center-to-center distances and their relative structure sizes are depicted as a function of w_{TTIP} in Figure 5.8b,c. For the small-sized structures, all films have the same radii of about 3.1 $\pm$ 0.2 nm irrespective of the w_{TTIP}. Moreover, the center-to-center distances remain unchanged within the error bars as well. Therefore, the small-sized pores of these three films can be seen as constant for different w_{TTIP}. A different behavior is observed for the big-sized structures. The center-to-center distances still stay unchanged within the experimental errors with increasing the w_{TTIP}, but the corresponding radii increase together with the amount of TTIP. The radius increases might be due to the fact that more TTIP contributes to larger titania nanostructures. As a consequence, the size of the pores between big-sized structures decreases with increasing w_{TTIP}, showing the same tendency as the report in case of spray-coating by Su et al. [152], and have the highest value of 21 $\pm$ 11 nm at the low w_{TTIP} of 3.25% (namely $w_{1,4-dioxane}$ of 96%).

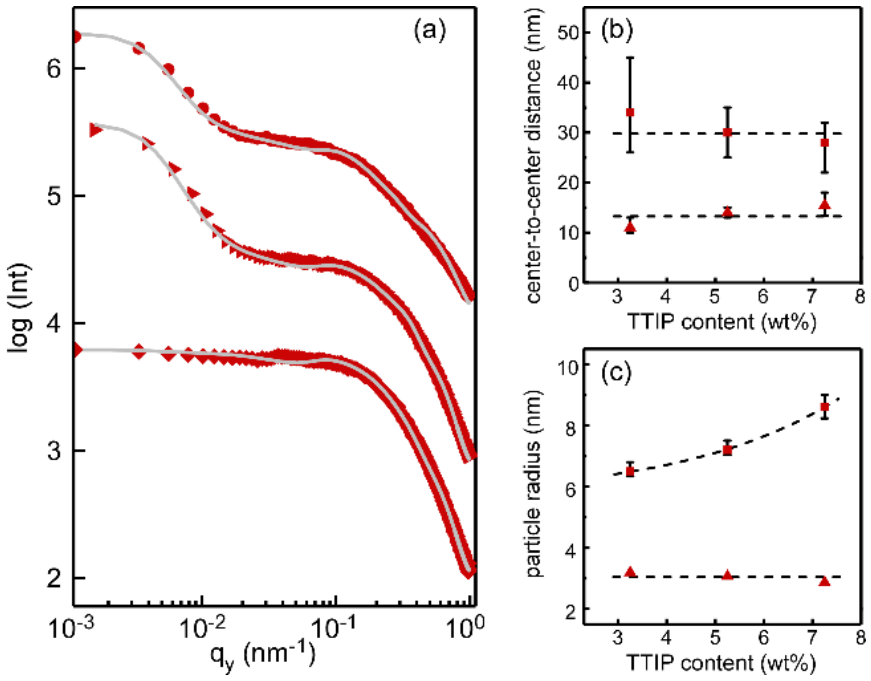

Figure 5.8: (a) Horizontal line cuts of 2D GISAXS data obtained from foam-like TiO_2 films with keeping w_{HCl} fixed at 0.75% and varying w_{TTIP} of 3.25%, 5.25% and 7.25% from bottom to top. The grey lines represent the fits to the data. All data and fits are shifted along the y-axis for clarification. Extracted characteristic length scales: (b) Center-to-center distance and (c) structure size in the foam-like TiO_2 thin films as a function of w_{TTIP}. Squares represent the large-sized structures. Triangles represent the small-sized structures. Reproduced from Ref [110] with permission from JOHN WILEY AND SONS, Copyright 2019.

5.3.2 TiO_2 films at high weight fraction of HCl

Surface morphology

For the second experimental scenario, the w_{HCl} is set to a higher amount of about 1.5%, while w_{TTIP} is increased from 2%, to 5%, and finally to 7%. The surface morphologies investigated by SEM are displayed in Figure 5.9a-c. It is noticeable that the film homogeneity deteriorates with increasing TiO_2 films at low weight fraction of HCl, showing the same tendency as the counterpart with low w_{HCl}. In particular, Figure 5.9a shows a well-mixed phase of nanostructures and mesoporous without titania aggregates and cracks, indicating a mesoporous nature of a foam-like morphology can be fabricated in a large area by printing.

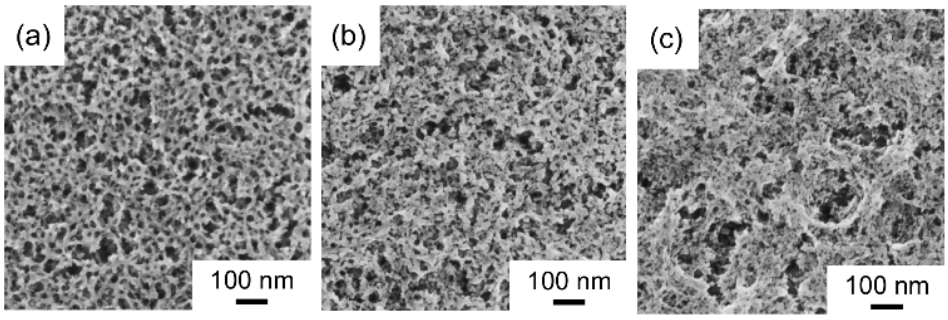

Figure 5.9: SEM images of foam-like TiO_2 films with keeping w_{HCl} at about 1.5% and varying w_{TTIP} from (a) 2%, (b) 5% to (c) 7%. Reproduced from Ref [110] with permission from JOHN WILEY AND SONS, Copyright 2019.

Inner morphology

The GISAXS data of the foam-like films for different w_{TTIP} is shown in Figure 5.7d-f. Two Bragg rods (marked with the red rectangles) can be seen in Figure 5.7d, indicating certain ordered nanostructuring existing inside the films for $w_{TTIP} = 0.02$. This observation is consistent with the SEM result shown in Figure 5.9a. The horizontal line cuts of the corresponding 2D GISAXS data are depicted in Figure 5.10a. To fit the extracted line cuts the same model is applied, as mentioned earlier. The model results are shown as solid grey lines in Figure 5.10a. Two center-to-center distances and structure sizes are extracted and plotted as a function of w_{TTIP} as seen in Figure 5.10b,c. For the big-sized structures, the center-to-center distances stay constant and the radii increase with increasing the concentration of TTIP, showing the same tendency as the aforementioned samples with the w_{HCl} of 0.75%. The big-sized pores possess a largest value of 11.8 ± 6 nm at a low w_{TTIP} of 2% (corresponding $w_{1,4-dioxane}$ of 96%). The small-sized structures reveal a center-to-center distance and radii, which are independent of w_{TTIP}. Therefore, the small-sized and big-sized structures for the foam-like titania films behave similar for the low and high w_{HCl} content.

5.4 Crystallinity of the printed titania films

In addition to the morphology, the crystal phase and crystallinity of TiO_2 also play a critical role in the photovoltaic performance. Generally, the anatase phase of TiO_2 is preferable for photovoltaic and photocatalytic applications because it has a higher charge carrier mobility [139]. Furthermore, high crystallinity can facilitate the transport of photo-generated charge carriers [153]. Both, the crystal phase and crystallinity strongly depend

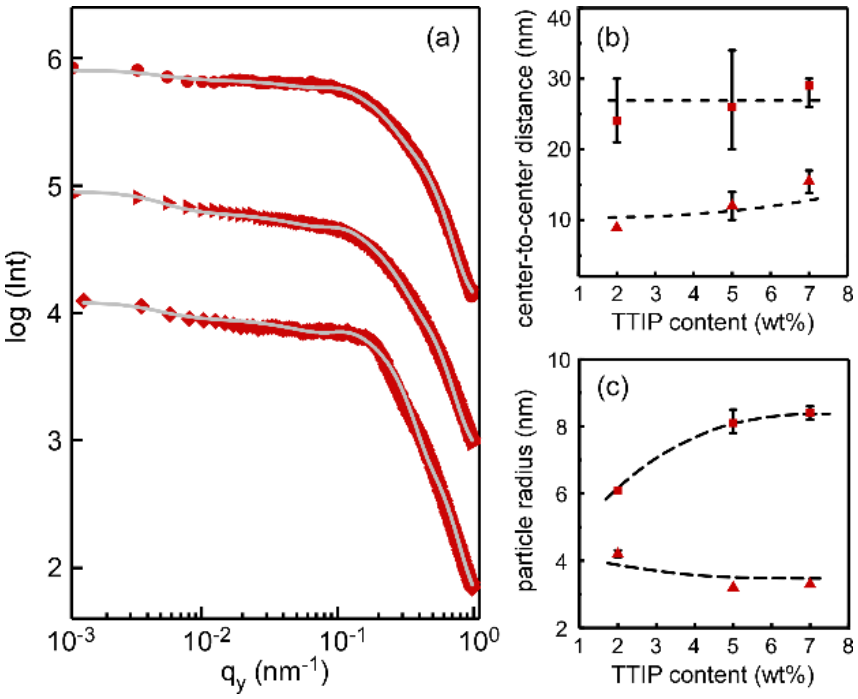

Figure 5.10: Horizontal line cuts of 2D GISAXS data obtained from foam-like TiO_2 films with keeping w_{HCl} at about 1.5% and varying w_{TTIP} of 2%, 5% to 7% from bottom to top. The grey lines represent the fits to the data. All data and fits are shifted along the y-axis for clarification. Extracted characteristic length scales: (b) Center-to-center distance and (c) structure size in the foam-like TiO_2 films as a function of w_{TTIP}. Squares represent the large-sized structures. Triangles represent the small-sized structures. Reproduced from Ref [110] with permission from JOHN WILEY AND SONS, Copyright 2019.

on the calcination temperature [154–156]. It has been reported that an increase in calcination temperature increases the crystallite size of anatase TiO_2 as well as the crystallinity, but may lead to a phase transition from anatase to rutile [57]. The hybrid films from a spherical micellar solution are printed on FTO substrates. Subsequent calcination at different temperatures were performed to obtain highly crystalline anatase phase and to remove the template. Figure 5.11a shows the XRD patterns of foam-like titania films after calcination at 450 °C, 500 °C and 550 °C, respectively. According to the reference data (anatase, JCPDS 21-1272, in the bottom of Figure 5.11a) from the International Center for Diffraction Data (ICDD), the anatase phase is identified for all films. No other crystal phase of TiO_2 is observed, which is consistent with the observation that the anatase phase TiO_2 is obtained at 400-700 °C, whereas the rutile phase appears at 800 °C [152]. Besides the anatase TiO_2, all the other peaks derive from the SnO_2 phase and thus, can be correlated to the FTO substrate. The crystallite sizes of the anatase TiO_2 (101) peaks are estimated by the Scherrer equation using the XRD line broadening. When the calcination

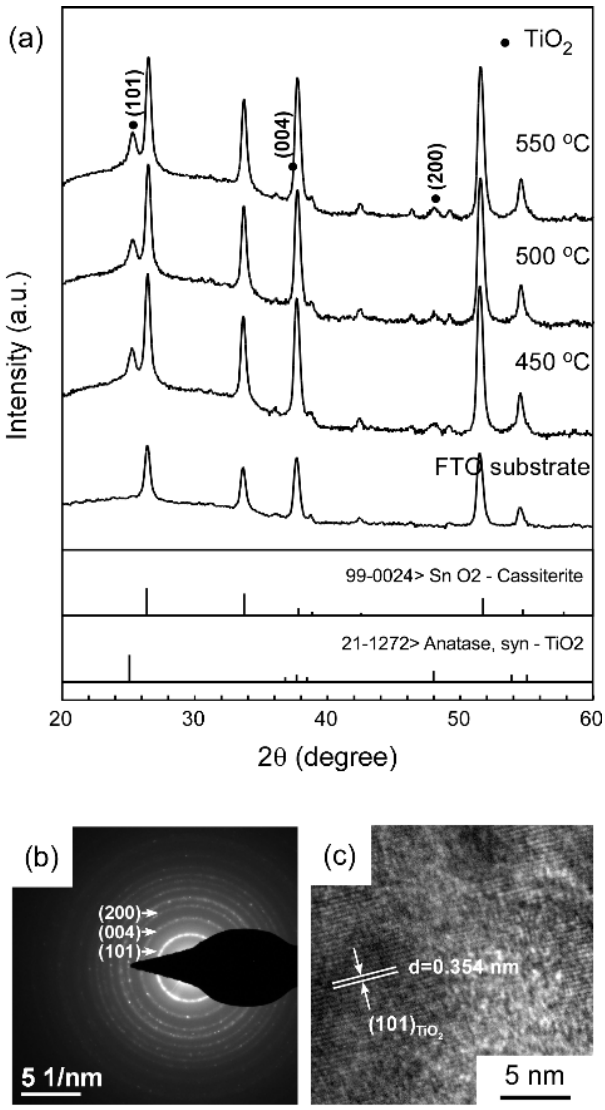

Figure 5.11: (a) XRD patterns of foam-like titania films after calcination at 450 °C, 500 °C and 550 °C. (b) SAED pattern and HRTEM images of foam-like TiO2 calcined at 450 °C. Reproduced from Ref [110] with permission from JOHN WILEY AND SONS, Copyright 2019.

temperatures increase from 450 °C, to 500 °C and finally to 550 °C, the crystallites remain unchanged in size with the error bars (16.1 ± 0.4 nm, 16.3 ± 0.5 nm and 16.4 ± 0.4 nm, respectively).

In addition to the XRD characterization, the foam-like titania films calcined at 450 °C are investigated by TEM. The selected-area electron diffraction (SAED) in Figure 5.11b displays a series of spotty diffraction pattern rings, which corresponds to the multi-crystalline anatase TiO_2 phase. The first three rings from the center to the exterior region represent (101), (004), and (200) lattice planesin anatase TiO_2, which agrees well

with the XRD results in Figure 5.11a. The related high resolution TEM image (Figure 5.11c) shows a well-resolved lattice spacing of 0.354 nm, which is consistent with the lattice spacing of the anatase (101) plane. Therefore, additional evidence is provided by TEM, proving that even at a low calcination temperature of 450 °C, well crystallized anatase titania is obtained.

5.5 Summary

We demonstrate that nanostructured titania films are successfully fabricated via combining the diblock-copolymer assisted sol-gel synthesis with a printing technique, which opens the possibility for producing inorganic semiconductors on an industrial scale. The surface and inner structures of different morphologies, containing foam-like structure, nanowire aggregates, collapsed vesicles and nanogranules, are detected by SEM and GISAXS measurements, respectively. SEM reveals morphology phase diagram of titania films by adjusting the weight fraction of 1,4-dioxane, HCl and TTIP. Moreover, the inner morphology investigated by GISAXS shows the radii of the big-sized structures increase in all films when the morphologies change from foam-like, to nanowire aggregates, then to collapsed vesicles, finally to nanogranules. In addition, the surface and inner morphology of foam-like films area are probed in more detail. Both, the small-sized and big-sized structures show in general the same behavior for the low and high w_{HCl} content with increasing w_{TTIP}. At low w_{TTIP} of 3.25% and low w_{HCl} of 0.75%, the big-sized pores of the foam-like films reveal the highest value of 21 ± 11 nm. The highly crystalline anatase titania is verified by XRD and TEM. Therefore, the provided printing route for structuring foam-like TiO_2 nanocomposite films holds high potential for application in solar cell devices, since foam-like mesoporous TiO_2 structures were applied in solid-state dye-sensitized solar cells with high efficiency already [157].

6 Nanoscale crystallization of polymers P3HT and PffBT4T-2OD in titania mesopores

This chapter is based on the published article: Nanoscale crystallization of a low band gap polymer in printed titania mesopores (N. Li et al., Nanoscale, 2020, 12, 4085–4093, DIO: org/10.1039/c9nr08055d). Reproduced from Ref. [158] with permission from the Royal Society of Chemistry.

In the previous chapter, slot-die printed TiO_2 films are investigated in detail. In this chapter, the primary focus is on the crystallization behavior of the model polymer P3HT and the low band polymer PffBT4T-2OD in printed TiO_2 mesopores, which paves the way for hybrid solar cell (HSC) applications.

HSCs and solid-state dye-sensitized solar cells (ssDSSCs) have attracted considerable attention for solar energy conversion since they promise to combine the advantages of both organic and inorganic materials [107]. Among those are benefits such as low-cost synthesis [159], ease of production [136], and controllable nano-scale morphology [136,160], while maintaining a high structural robustness through the inorganic scaffold [161]. Extensive studies investigated the usability of titania, or titania as an electron transport material in such HSCs and ssDSSCs [162–164]. Especially, bulk heterojunction (BHJ) ssDSSCs based on interpenetrating titania networks showed high efficiencies above 10% [165,166]. Similar to the paradigm of BHJ organic photovoltaics (OPVs), the following key properties were also found to have a positive effect on the efficiency of HSCs and ssDSSCs: A bicontinuous network with small domain sizes of 10-20 nm in radius, a high degree of crystallinity of the conjugated polymer and its backbone orientation in face-on direction with respect to the substrate [17, 18]. By ensuring the above-mentioned conditions, charge dissociation and transport were especially improved, which directly translated into an overall enhanced photovoltaic performance [153, 167].

To date, the combination of sol-gel chemistry and an amphiphilic block copolymer template has been proven to be a procurable method to tailor the nanostructures of mesoporous titania films [11, 124]. Compared to the numerous studies reporting the fab-

rication of titania mesostructures, much less attention was paid to the backfilling of these mesostructures. Even for the widely studied hole-transport material (HTM), poly(3-hexylthiophene) (P3HT), only a few studies exist targeting the crystallization behavior under spatial confinement. For example, Aryal et al. used nanoimprint lithography to fabricate ordered P3HT nanostructures and simultaneously to control polymer chain alignment [168]. Martín et al. produced P3HT nanowires with diameters ranging between 15 nm and 350 nm using nanopore anodic aluminum oxide (AAO) templates via two processing routes (drying a solution and cooling from the melt) [169]. They observed that solution-processed P3HT nanowires were amorphous and porous. Thus, no relationship between crystal orientation and pore diameter was accessible. Song et al. investigated the degradation of P3HT-titania-based solid-state dye-sensitized solar cells using two kinds of mesoporous titania films, one with large pores and the other with small pores [124]. In the active layer with large pores the P3HT crystallites remained stable, while for the case of an active layer with small pores the volume fraction of crystalline P3HT decreases under continuous solar illumination, demonstrating the importance of the pore size for applications [124].

Recently, the low bandgap conjugated polymer, PffBT4T-2OD, was used to achieve device efficiencies of about 11% in single junction organic solar cells [18, 109]. So far, this donor polymer is only used in OPVs, but appears also promising for HSCs, because it has several beneficial characteristics: (1) PffBT4T-2OD has an excellent hole mobility (1.5 - 3.0 $\times$ 10^{-2} cm^2 V^{-1} s^{-1}) and high crystallinity [17], (2) a relatively long exciton diffusion length enables PffBT4T-2OD to have large domain sizes up to 30-40 nm in diameter [108], (3) even in thick active layers around 300 nm, PffBT4T-2OD shows high performance in OPV devices [18]. Thus, the application of PffBT4T-2OD as a HTM in HSCs might also pave the way to achieve high efficiencies. In HSCs, conjugated polymers are typically backfilled into mesoporous inorganic films to form a heterojunction configuration of the active layers. It was reported that the pore sizes, the infiltration methods and the used temperatures greatly affect the crystalline properties and the device efficiency [170, 171]. To fully exploit the potential of PffBT4T-2OD for HSC applications, it is necessary to probe its crystallization inside mesoporous titania films. To the best of our knowledge, no studies exist which investigate the PffBT4T-2OD crystallization behavior in dependence on the scale of the surrounding mesoscale structure.

Herein, the application of an industry-scale technique is demonstrated, namely slot-die printing, to fabricate mesoporous titania films via a wet-chemical approach. Mesoporous titania films with different pore sizes are prepared via a so-called block copolymer template assisted sol-gel synthesis. Subsequently, PffBT4T-2OD is infiltrated into the tailored titania pores. For a comparison, P3HT-backfilled active layers are also prepared. Dif-

ferent infiltration processes have to be applied for P3HT and PffBT4T-2OD to ensure an efficient pore filling. The surface and inner morphologies of the printed titania films are probed with scanning electron microscopy (SEM) and grazing incidence small-angle X-ray scattering (GISAXS), respectively. The optical response of the active layers is measured by ultraviolent-visible (UV-Vis) measurements. Grazing incidence wide-angle X-ray scattering (GIWAXS) measurements are performed to reveal the influence of titania pore sizes on the crystalline properties of PffBT4T-2OD and P3HT. Extracted key properties are lattice constants, crystal sizes and orientations. Interestingly, an increased ratio of face-on orientation is found in large-pore titania-PffBT4T-2OD active layers. This knowledge is seen as an essential piece required to optimize the crystallization behavior of PffBT4T-2OD for HSC applications.

6.1 Printing of porous nanostructured titania films

The details about the synthesis procedure of the titania sol–gel is described in section 4.2.1. The diblock copolymer PS-b-PEO (the number molecule weight of PS and PEO is 20.5 and 8 kg mol^{-1}, respectively) is used. The concentration of the polymer in the final solution is kept constant at 16.50 mg mL^{-1}, whereas the weight fraction (w) of 1,4-dioxane, HCl and TTIP is varied to tailor nanostructures of titania films. Four different compositions: $w_{1,4-dioxane}/w_{HCl}/w_{TTIP}$ = 97.5%:1%:1.5%, 97%:1%:2%, 96%:1.5%:2.5%, 96%:1%:3%, are investigated and denoted as 1.5 wt% TTIP, 2.0 wt% TTIP, 2.5 wt% TTIP and 3.0 wt% TTIP, respectively.

Next, the resulting solution is printed on silicon and glass substrates, and further remained in the printer chamber for solvent evaporation at constant 20 °C ensured through a water-cooling system. In the present chapter, the printer (as shown in Figure 4.4), designed and built by Sebastian Max Günther, is used. The printing parameters, such as the distance between the substrate and printer head, the solution flow rate and printing speed are optimized to obtain a film thickness around 200 nm. Here, the printing velocity is 5 mm s^{-1} and solution flow rate is 10 μL s^{-1}.

6.2 Infiltration of donor polymers into the printed mesoporous titania films

Infiltration methods used for P3HT and PffBT4T-2OD are schematically represented in Figure 6.1 and differ in their details due to the difference in molecular weight and solubility of these two conjugated polymers as described in section 4.1. The infiltration selected for

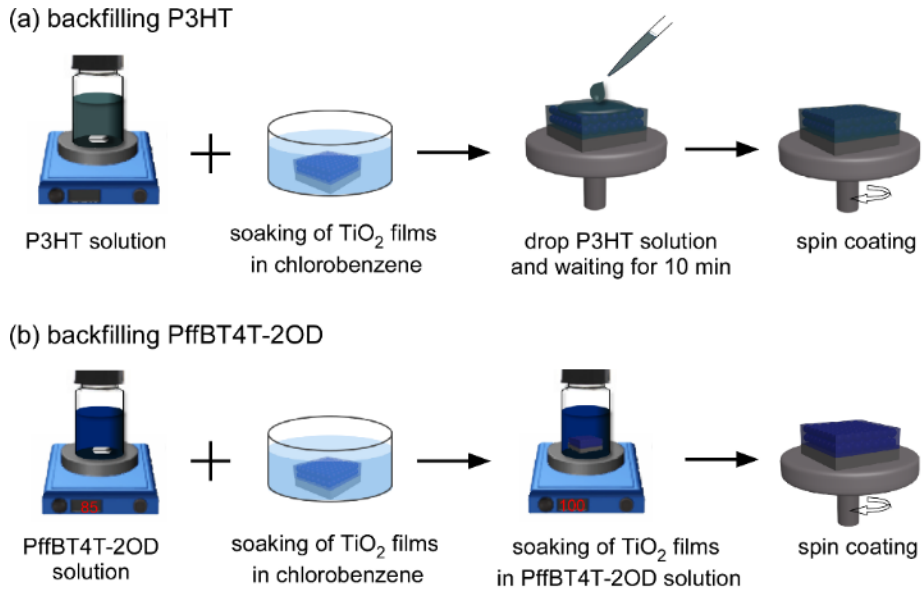

Figure 6.1: Schematic illustration of infiltration of donor polymers into the printed mesoporous titania films: (a) P3HT and (b) PffBT4T-2OD. Reproduced from Ref. [158] with permission from the Royal Society of Chemistry.

P3HT (Figure 6.1a) is similar to a routine developed by Rawolle et al. [97], which enables a degree of backfilling efficiency of 84%. For this purpose, P3HT is dissolved in CB with a concentration of 10 mg mL^{-1} and then stirred overnight at room temperature. Additionally, the titania films are immersed in the pure solvent CB for 45 min to remove the trapped air inside the nanopores [97]. Then the P3HT solution is drop-casted on the mesoporous titania film. After waiting for 10 min, spin coating is performed (600 rpm for 10 s, 1500 rpm for 100 s). A pure P3HT film is prepared on a silicon/glass substrate under the same conditions as a reference sample. In case of PffBT4T-2OD the infiltration process is adopted as seen in Figure 6.1b. At first, PffBT4T-2OD is dissolved in a CB/DCB solvent mixture (volume ratio = 1:1). The polymer solution (concentration = 7 mg mL^{-1}) is stirred overnight at 85 °C. After soaking in the pure CB solvent for 45 min, titania films are transferred into a PffBT4T-2OD solution and immersed for 10 min at 100 °C. Then the samples are taken out and immediately spun at the speed of 800 rpm for 120 s. Finally, the titania/PffBT4T-2OD active layers are annealed at 100 °C for 1 h under nitrogen atmosphere. Similarly, a pure PffBT4T-2OD reference sample is fabricated on a silicon/glass substrate.

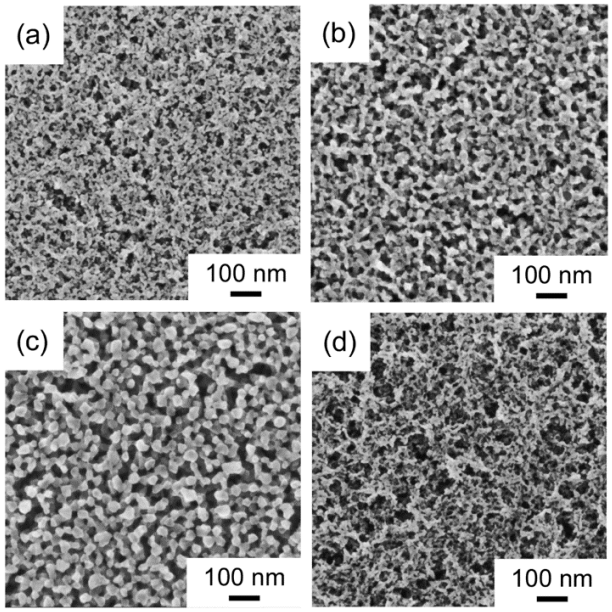

Figure 6.2: SEM images of the mesoporous titania films deposited by printing from solutions containing different weight fractions of TTIP: w_{TTIP} of (a) 1.5%, (b) 2.0%, (c) 2.5% and (d) 3.0%. Reproduced from Ref. [158] with permission from the Royal Society of Chemistry.

6.3 Slot-die printed mesoporous titania films

In addition to the deposition methods like spin coating and slot-die printing, deviations in the weight fraction of the reactants might also change the titania film morphologies as commonly described in a ternary phase diagram [110]. Four titania films with different pore sizes are fabricated from solutions with varying TTIP weight fractions (w_{TTIP}) of 1.5%, 2.0%, 2.5% and 3.0%.

6.3.1 Surface morphology

The corresponding surface morphologies after removal of the structure-directing block copolymer are measured by SEM and shown in Figure 6.2. All films exhibit a foam-like mesoscale structure. Particularly at 2.0 wt% TTIP and 2.5 wt% TTIP, an improved homogeneity and order is seen. The presented SEM images prove that homogeneous printing of mesoporous titania films with a certain order is possible.

6.3.2 Inner morphology

To gain more insights about the inner morphologies, GISAXS measurements are performed to quantify the size of the nanostructures and pores inside the titania films. The

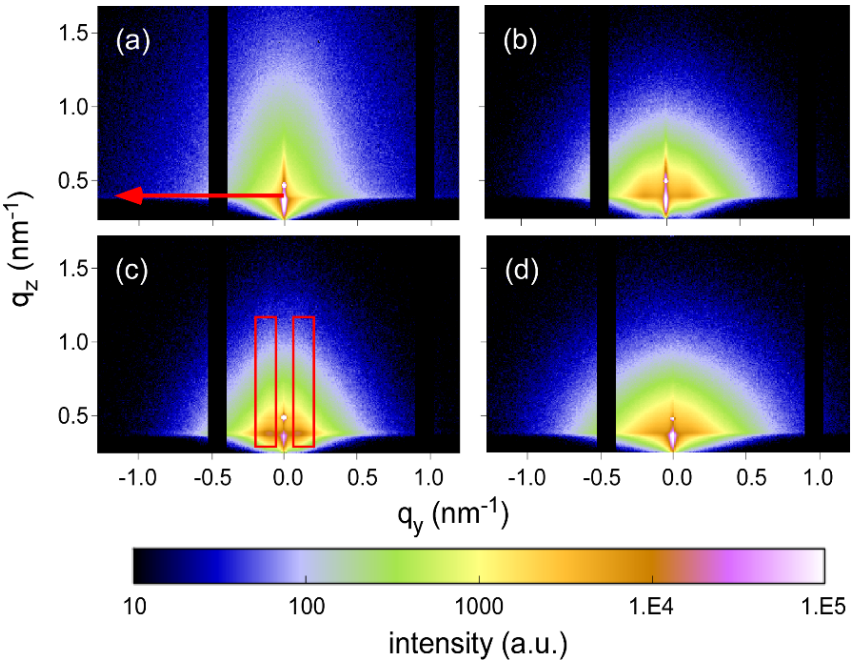

Figure 6.3: 2D GISAXS data of the mesoporous titania films deposited by printing after calcination, cast from solution with different w_{TTIP} values of (a) 1.5%, (b) 2.0%, (c) 2.5% and (d) 3.0%. The red arrow in (a) indicates the exemplary position where the horizontal line cuts are performed. The red rectangles in (c) indicate two vertical Bragg scattering rods. All the images are in the same intensity scale. Reproduced from Ref. [158] with permission from the Royal Society of Chemistry.

GISAXS data of the printed titania films after calcination with different w_{TTIP} is displayed in Figure 6.3. Two vertical Bragg rods (as indicated with the red rectangles) in Figure 6.3b and Figure 6.3c imply a relatively highly ordered lateral structural of the films with w_{TTIP} of 2.0% and 2.5%. This result is in good agreement with the corresponding SEM images shown in Figure 6.2b and Figure 6.2c. The horizontal line cuts of the 2-dimensional (2D) GISAXS data and corresponding modeling results are plotted in Figure 6.4a. More precise information about extraction of line cuts and modeling is provided in the theoretical part. From data modeling, three characteristic center-to-center distances (structure factor) and structure sizes (cylinder form factor) are extracted and depicted as a function of w_{TTIP} in Figure 6.4b and Figure 6.4c. For the small-sized and middle-sized structures, the nanoparticle radii primarily stay unchanged irrespective of the TTIP content, whereas their related center-to-center distances depend slightly on w_{TTIP}. A different behavior is seen for the radii of big-sized structures, showing an increasing trend with increasing the TTIP concentration. This observation is consistent with our previous work, which might be ascribed to the formation of large titania aggregation

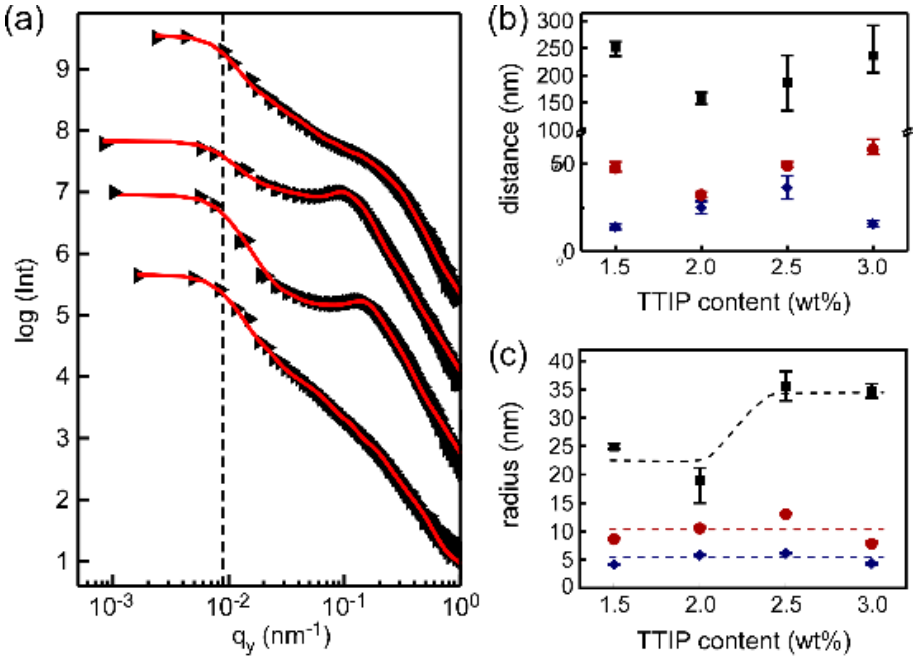

Figure 6.4: (a) Horizontal line cuts of 2D GISAXS data of the mesoporous titania films deposited by printing from solutions containing different weight fractions of TTIP: w_{TTIP} of 1.5%, 2.0%, 2.5% and 3.0% from bottom to the top. The red curves represent the fits to the data. All data and corresponding fits are shifted along the intensity axis for clarity of the presentation. Extracted characteristic length scales: (b) Center-to-center distance and (c) particle radius in the printed mesoporous titania films as a function of w_{TTIP}. Black squares represent the large-sized structures. Red circles represent the middle-sized structures. Blue rhombi represent the small-sized structures. The resolution limit is marked by a vertical dashed line, indicating that the maximum lateral structure which can be resolved is 690 nm. Reproduced from Ref. [158] with permission from the Royal Society of Chemistry.

clusters induced by excessive TTIP [110]. Anyhow, the big-sized structures are rare with volume fractions of only 2.2%, 8.5%, 0.7% and 1.2% for the titania films with increasing the w_{TTIP} [172]. Pore sizes related to the small-sized structures are approximated to be (5.6 ± 1.5) nm for titania films with 1.5 wt% TTIP, using a model reported by Sarkar et al [146]: Pore size = (center-to-center distance between nanoparticles – 2 × nanoparticle radius). The small-sized pores with sizes as low as about 6 nm are typically too small for infiltration with conjugated polymers and therefore play no significant role in the infiltration. Simultaneously, the big-sized structures are scarce in number, so that we can infer that the middle-sized pores play the prominent role in the infiltration process with conjugated polymers. Moreover, for the middle-sized structures, the pore sizes exhibit a tendency similar as the corresponding center-to-center distances, reading (30.6 ± 2.8) nm,

(11.4 ± 2.0) nm, (23.1 ± 1.5) nm and (43.0 ± 5.0) nm for the samples with increasing w_{TTIP} (Figure 6.5). The middle-sized pores are favorable for photovoltaic devices, since the domain sizes with diameters in the range of around 40 nm appear highly promising for reducing the possibilities of exciton recombinations [173, 174].

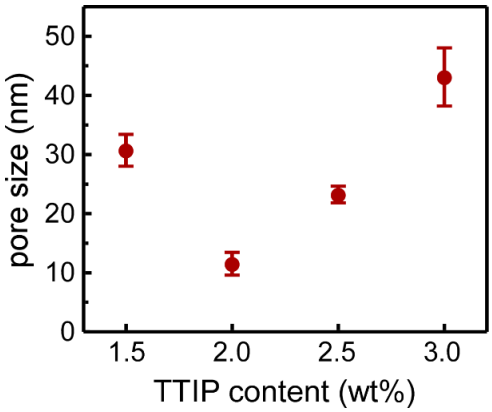

Figure 6.5: Extracted characteristic length scales: pore size in the printed titania thin films as a function of w_{TTIP}. Red circles represent middle-sized structures. Reproduced from Ref. [158] with permission from the Royal Society of Chemistry.

6.4 Optical properties of hybrid active layers

Figure 6.6 shows the side view SEM measurements before and after backfilling, revealing a good infiltration for two exemplary mesoporous titania types (w_{TTIP} of 1.5% and 2.0%). All samples are tilted in respective to the electron beam (around 40-45 degree) for a better view. The characteristic structure sizes of around 20 nm in the inset of Figure 6.6d, which are similar to two times of the extracted structure radii in Figure 6.5c. Both P3HT (Figure 6.6b and Figure 6.6e) and PffBT4T-2OD (Figure 6.6c and Figure 6.6f) are successfully infiltrated into the mesoporous titania matrix with different pore sizes. Moreover, all fabricated active layers display only a thin polymer overlayer on top of the backfilled titania films, which will be needed to avoid short-cuts in real device applications in HSCs.

To further investigate the absorption behavior in dependence of pore sizes, the four hybrid films discussed above (P3HT and PffBT4T-2OD, each infiltrated into mesoporous titania films printed from w_{TTIP} of 1.5% and 2.0%) are deposited on glass substrates. No aggregation is observed, which might lead to variations in the absorption features [56, 175, 176]. Irrespective of the mesoporous titania type, all main absorption peaks within the

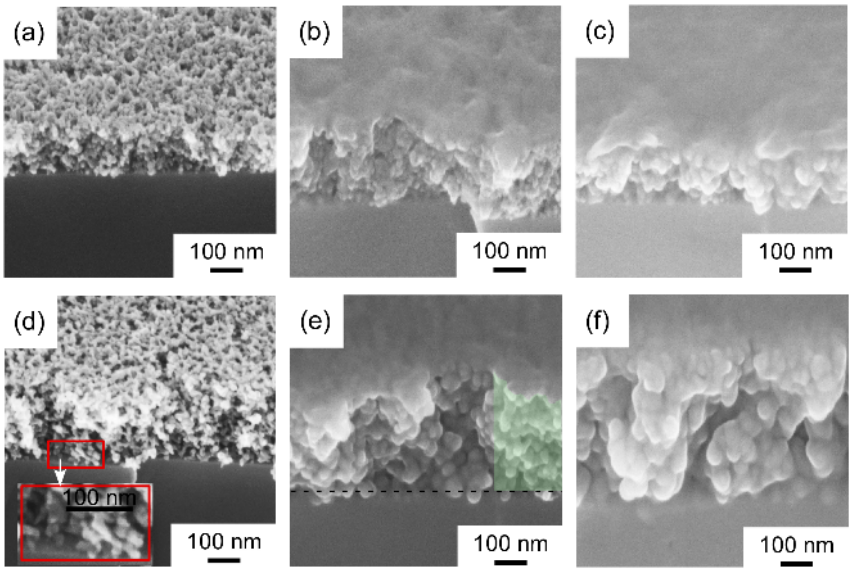

Figure 6.6: Side view SEM images of the mesoporous titania films deposited by printing from solutions with w_{TTIP} of (a) 1.5% and (d) 2.0%. The printed mesoporous titania films are backfilled with P3HT for (b) w_{TTIP} of 1.5% and (e) w_{TTIP} of 2.0%. Similarly, printed mesoporous titania films are backfilled with PffBT4T-2OD for (c) w_{TTIP} of 1.5% and (f) w_{TTIP} of 2.0%. In the inset of (d), zoom into the area marked with a red rectangle as an example to show characteristic structure sizes. In (e) the right hand side of the image is false-colored to indicate the titania layer (light green). Reproduced from Ref. [158] with permission from the Royal Society of Chemistry.

range of 400-800 nm in Figure 6.7 originate from the absorbance of P3HT and PffBT4T-2OD, respectively. Furthermore, the backfilled films with the $w_{TTIP} = 1.5\%$ display higher absorption coefficients than those based on $w_{TTIP} = 2.0\%$, since only very thin capping layers are trapped on the surface. One reason for increased absorption might be correlated to a larger pore size of the $w_{TTIP} = 1.5\%$ - titania scaffold facilitating the infiltration process with donor polymers as reported by Wang et al. in case of ZnO films [140]. This result indirectly indicates an efficient backfilling of the titania films.

6.5 Crystallization of polymers inside titania pores

For the performance of titania-based HSCs, not only the morphology of the active layers is of great importance, but also the crystallization of the donor polymers inside the pores matters strongly, since the crystalline region mainly contributes to the current. Thus, GIWAXS measurements are performed to probe the lattice constants and crystal sizes of PffBT4T-2OD and P3HT for comparison as well as the molecular orientation inside meso-

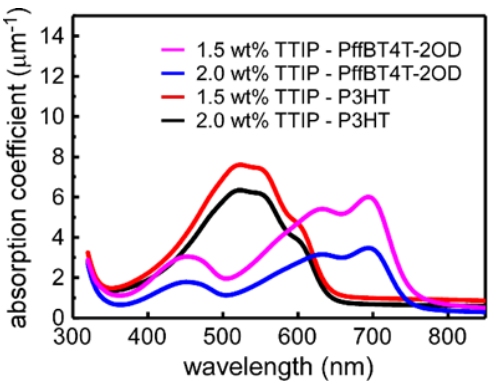

Figure 6.7: Absorption coefficients of active layers based on the mesoporous titania films deposited by printing from solutions with w_{TTIP} of 1.5% and 2.0%. The red and black curves indicate the printed mesoporous titania films are backfilled with P3HT for w_{TTIP} of 1.5% and w_{TTIP} of 2.0%, respectively. The magenta and blue curves indicate the printed mesoporous titania films are backfilled with PffBT4T-2OD for w_{TTIP} of 1.5% and w_{TTIP} of 2.0%, respectively. Reproduced from Ref. [158] with permission from the Royal Society of Chemistry.

pores of nanostructured titania films. All four different types of the printed mesoporous titania films are backfilled with the donor materials and then examined with GIWAXS. As only a very thin polymer capping layer with several nanometers thickness resides on the surface (Figure 6.6b, Figure 6.6c, Figure 6.6e, Figure 6.6f) and the incident angle in the GIWAXS experiment is chosen well above the critical angles, the dominant GIWAXS scattering signals originate from the P3HT/PffBT4T-2OD inside the titania pores of the backfilled films.

6.5.1 Crystallization of P3HT inside the titania pores

Figure 6.8 illustrates the corrected 2D GIWAXS data of the corresponding P3HT-backfilled active layers and a P3HT reference sample. Q-reshaping, solid angle, conversion and polarization corrections are performed on the raw 2D GIWAXS data using the software GIXSGUI [99]. In Figure 6.8, the isotropic diffraction ring at q = 17-18 nm^{-1} in the active layers primarily represents the (101) crystal plane of anatase titania with random orientations [177]. Additionally, the P3HT out-of-plane (100) peak is most pronounced for all films, indicating an edge-on predominated orientation of the P3HT crystals [178].

For a quantitative analysis, the vertical-sector integrals, taken from the corrected reciprocal space patterns, are background-subtracted from the substrate in a normalized way taking the beam intensity into account and then fitted with Gaussian functions as shown in Figure 6.9a. It is found that the high intensities of P3HT (100) Bragg peaks

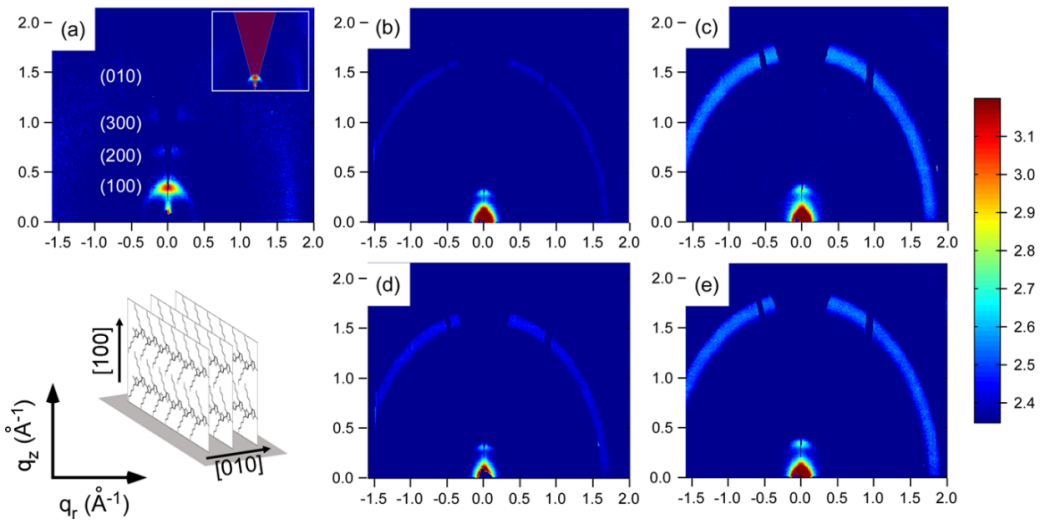

Figure 6.8: 2D GIWAXS data of (a) a pure P3HT reference sample the P3HT-backfilled titania films deposited by printing from solutions with different TTIP weight fractions: (b) 1.5%, (c) 2.0%, (d) 2.5% and (e) 3.0%. For all samples, the azimuthally integrals are performed from -15°to 15°(vertical direction) to extract quantitative information about edge-on oriented P3HT crystals. The performed cake cuts are as shown in the inset of panel (a). The schematic (left corner) shows an edge-on oriented P3HT crystal with the lamellar stacking. Reproduced from Ref. [158] with permission from the Royal Society of Chemistry.

appear in all films. The weak shoulders visible at q ≈ 7.2 and 11.5 nm^{-1} are consistent with the reported (200) and (300) peaks of P3HT, respectively [179, 180]. Additionally, a broad peak originates from both P3HT and titania at 17-18 nm^{-1} in all active layers. Particularly, P3HT is known to have a peak at 17.4 nm^{-1} (010) and anatase titania is known to cause a peak at 17.8 nm^{-1} (101) [124]. These broad peaks show slight deviations in position, which might be associated with stresses developed along with the mesoporous titania films during calcination. Thus, the P3HT (100) peak is chosen as an indication for the polymer crystallization. The q-positions of the (100) peaks are determined via Gaussian fitting and thereby lamellar stacking distances (d) are calculated by $d = 2\pi q^{-1}$. In addition, the full width at half-maximum (FWHM) is related to the crystal size as described by the Scherrer equation (see section 2.3.2) with the assumption of a constant paracrystallinity. Overall, extracted stacking distances and crystal sizes, such as 1.83 and 8.5 nm for the P3HT reference sample, are in good agreement with the reported values in P3HT:[6,6]-phenyl-C61-butyric acid methyl ester (P3HT:PCBM) systems [160, 179, 181].

Figure 6.9b and Figure 6.9c show the lamellar stacking distances and crystal sizes of P3HT (100) in the active layers as a function of the printed titania pore sizes. The lamellar stacking distances of the P3HT (100) peak decrease with increasing pore sizes,

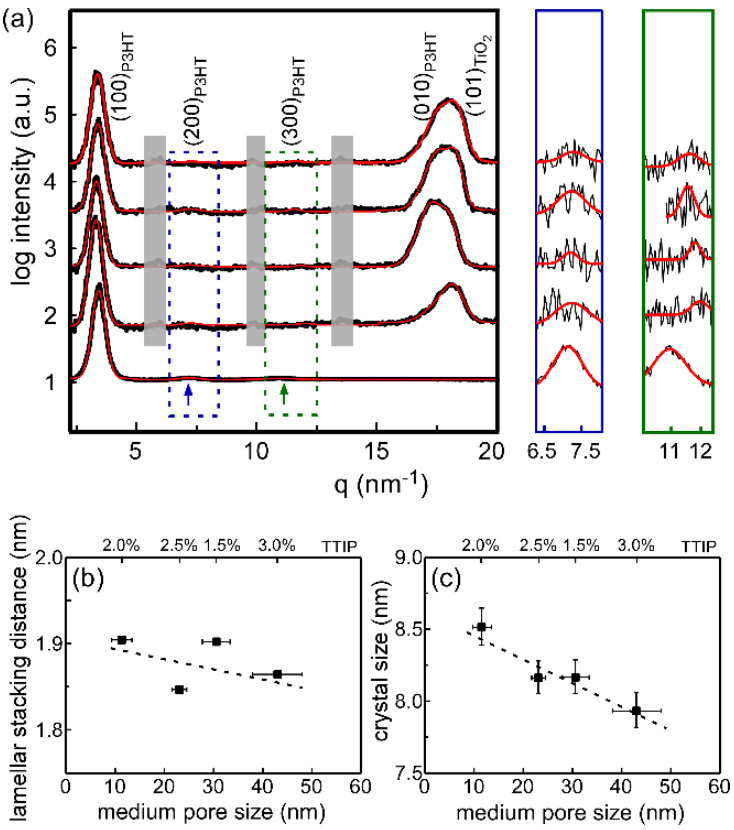

Figure 6.9: (a) Sector integrals of 2D GIWAXS data in edge-on direction (χ from -15° to 15°, vertical direction) for a pure P3HT reference sample and the P3HT-backfilled titania films deposited by printing from solutions with different TTIP weight fraction: w_{TTIP} of 1.5%, 2.0%, 2.5% and 3.0% from the bottom to the top. The red lines represent the Gaussian fits to the data. The purple and green arrows indicate characteristic features corresponding to P3HT lamellar stacking peaks: (200) and (300) Bragg peaks. The zoom-in regions at q = 6.3-8.3 nm^{-1} and 10.0-12.5 nm^{-1} focus on the P3HT (200) and (300) Bragg peaks with low intensity, respectively. All observed peaks are indexed. (b) Lamellar stacking distances and (c) crystal sizes of P3HT (100) Bragg peak as a function of the printed titania pore sizes. Reproduced from Ref. [158] with permission from the Royal Society of Chemistry.

agreeing well with the observation reported earlier [124]. This decrease manifests that a denser packing of the P3HT chains forms in the larger-pore active layer, which probably results from a reduction of stacking defects of the polymer backbones [160]. A similar tendency is found for the crystal sizes, where P3HT crystallite sizes decrease from 8.5 nm to 7.9 nm with an increase in the titania pore sizes.

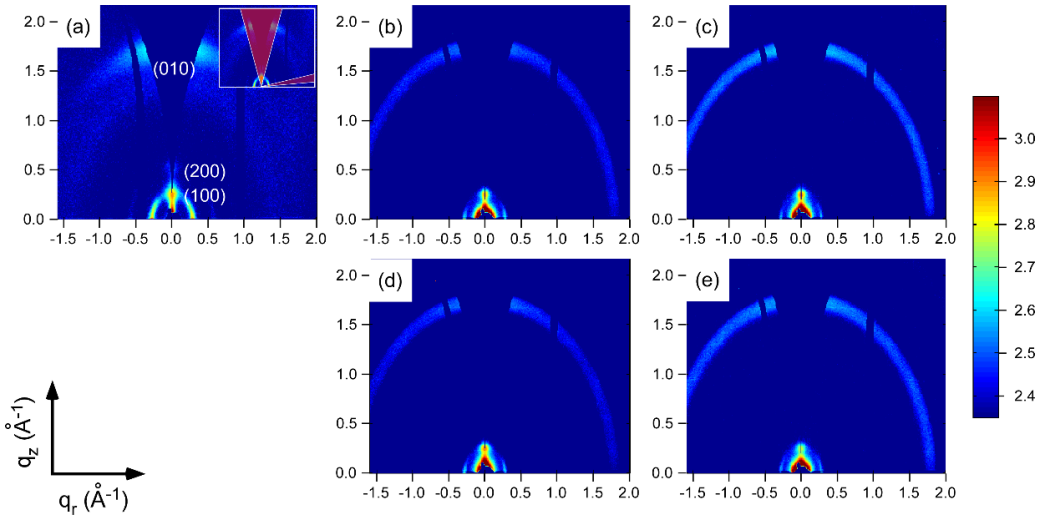

Figure 6.10: 2D GIWAXS data of (a) a pure PffBT4T-2OD reference sample and the PffBT4T-2OD-backfilled titania films deposited by printing from solutions with different TTIP weight fractions: (b) 1.5%, (c) 2.0%, (d) 2.5% and (e) 3.0%. For all samples, the azimuthal integrals are done from -15°to 15°(vertical direction) and 75°to 85°(horizontal direction) to extract quantitative information about the edge-on and face-on oriented PffBT4T-2OD crystals. Reproduced from Ref. [158] with permission from the Royal Society of Chemistry.

6.5.2 Crystallization of PffBT4T-2OD inside the titania pores

For the PffBT4T-2OD-backfilled active layers, the same analysis procedure is applied as for the P3HT-backfilled sample discussed above. The 2D GIWAXS data with corrections are shown in Figure 6.10. Similarly, the active layers show one isotropic diffraction ring at q = 17-18 nm^{-1}, mainly originating from the highly crystalline titania. However, unlike P3HT, all films with PffBT4T-2OD exhibit prominent (100) Bragg peaks from the polymer in both, edge-on and face-on orientation. Particularly, for the PffBT4T-2OD reference sample, the intensity of the (010) Bragg peak along the vertical direction exceeds that in the horizontal direction, implying that face-on oriented PffBT4T-2OD crystals dominate in the film. Note that the difference in preferential orientation between P3HT and PffBT4T-2OD crystallization of reference samples might also be related to differences in the deposition routines [17]. They correspond to two different infiltration routines for the active layers, which are a necessity to ensure an efficient backfilling. Additionally, the individual thermodynamic and kinetic properties of each polymer type during crystallization have to be considered [182].

The vertical- and horizontal- sector integrals after subtracting the background and their corresponding Gaussian fits are displayed in Figure 6.11a and Figure 6.11b. For both, edge-on direction (Figure 6.11a) and face-on direction (Figure 6.11b), all samples exhibit a

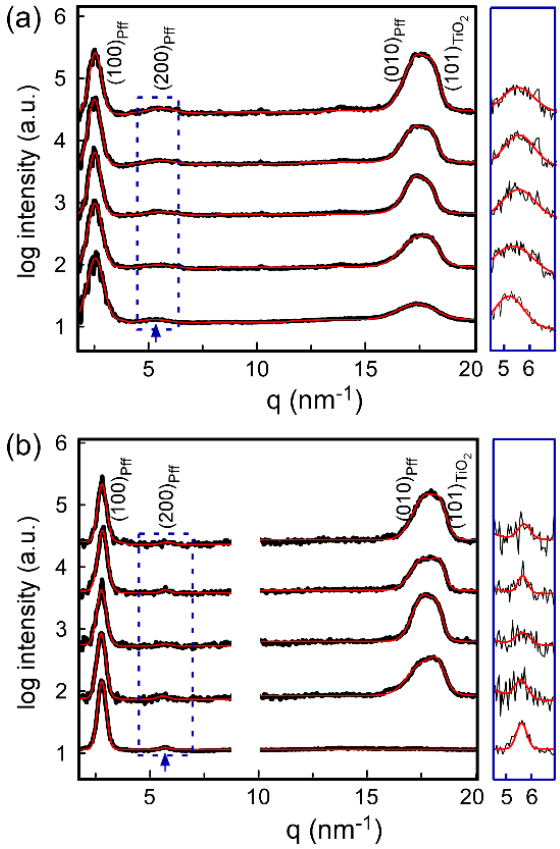

Figure 6.11: Sector integrals of 2D GIWAXS data in (a) edge-on direction (χ from -15°to 15°, vertical direction) and (b) face-on direction (χ from 75°to 85°, horizontal direction) for a pure PffBT4T-2OD reference sample and the PffBT4T-2OD-backfilled titania films deposited by printing from solutions with different TTIP weight fraction: w_{TTIP} of 1.5%, 2.0%, 2.5% and 3.0% from the bottom to the top. The red lines represent the Gaussian fits to the data. The data and the responding fits are shifted along the y-axis for clarity of the presentation. Reproduced from Ref. [158] with permission from the Royal Society of Chemistry.

strong (100) Bragg peak as well as a weak (200) peak at q ≈ 5.6 nm^{-1}. The PffBT4T-2OD (010) peak of the reference sample appears at 17.4 nm^{-1}, consistent with values reported in literature [17]. Like the P3HT-backfilled active layers, this broad peak is an overlap of PffBT4T-2OD (010) and titania (101) peaks. Furthermore, the PffBT4T-2OD (100) peak is selected as an indicator for crystallization and is analyzed in dependence of the titania pores. The lamellar spacing distances and crystal sizes of all films in face-on direction are close to the observations reported by Ma et al., namely d = 2.24 nm and crystallite size of 12.6 nm [17]. However, these values in face-on direction differ from those in edge-one direction, probably due to the anisotropic crystallization of PffBT4T-2OD [183, 184].

The lamellar stacking distances and crystal sizes of PffBT4T-2OD (100) as a function

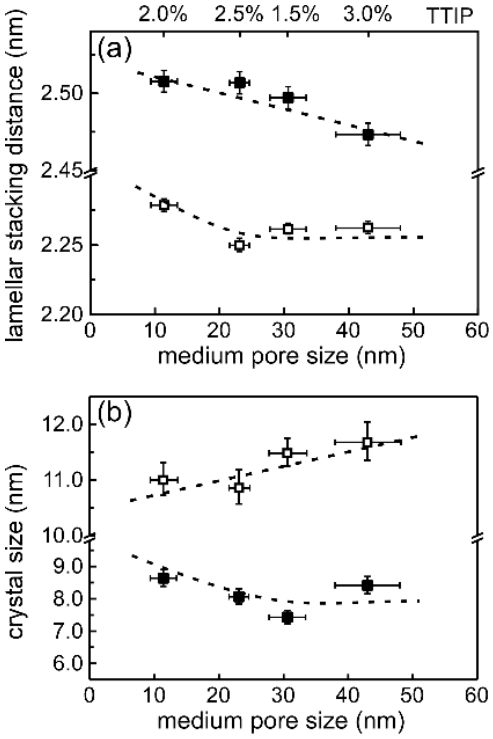

Figure 6.12: (a) Lamellar stacking distances and (b) crystal sizes of PffBT4T-2OD (100) Bragg peak as a function of printed titania pore sizes. The information about PffBT4T-2OD, derived from the (100) Bragg peaks in edge-on and face-on directions is indicated by solid and empty squares, respectively. Reproduced from Ref. [158] with permission from the Royal Society of Chemistry.

of the printed titania pore sizes are depicted in Figure 6.12a and Figure 6.12b. The same trend as observed for the case of confined P3HT crystallization above is observed for an edge-on direction of composite PffBT4T-2OD/titania samples. Lamellar stacking distances and crystal sizes of PffBT4T-2OD (100) decrease with an increase of titania pore sizes. However, a different behavior is found for the face-on direction. The lamellar stacking distances still decrease with increasing the pore sizes, but the corresponding crystal sizes increase together with the sizes of titania pores. Thus, irrespective of the crystal orientation, denser stacking of PffBT4T-2OD chains is preferentially found in larger titania pores. In contrast to the observations in case of P3HT and for the face-on direction, bigger PffBT4T-2OD crystallite sizes are preferentially formed in a titania confinement with larger pores. In the case of syndiotactic polystyrene (sPS) infiltratedin anodic alumina oxide (AAO) templates, Wu et al. found that the polymer chains favorably crystallize parallel to the pore axis (in the vertical direction) at smaller nanopore diameters, whereas the preferential orientation is perpendicular to the long nanopores (in the horizontal direc-

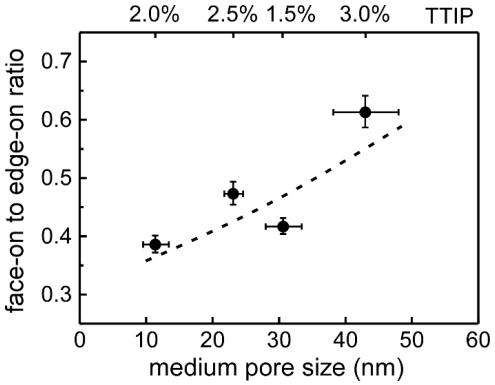

Figure 6.13: Face-on to edge-on ratio of PffBT4T-2OD (100) Bragg peak as function of the printed titania pore size. The area ratio of the PffBT4T-2OD (100) Bragg peaks is compared in in-plane and out-of-plane directions. Reproduced from Ref. [158] with permission from the Royal Society of Chemistry.

tion) at larger pore diameters [185, 186]. A similar result was reported for poly(ethylene oxide) (PEO) in AAO templates [182, 187]. Although the investigated mesoporous titania templates show interconnected network structures, unlike AAO templates with a well-defined pore axis, our observations based on GISAXS cylindrical modeling are in agreement with these earlier findings. With an increase in the titania pore sizes, a horizontal (face-on) orientation of the polymer chains is preferred, as this facilitates crystal growth [187]. As a result, a faster growth speed in face-on direction contributes to bigger polymer crystals. In contrast, bigger crystals form in smaller pores as the crystal orientation is inverted. Besides the crystal sizes also the ratio between face-on to edge-on orientation of the PffBT4T-2OD crystallites is of interest as a function of the printed titania pore sizes (Figure 6.13). Scattering intensities of the PffBT4T-2OD (100) Bragg peaks are compared in face-on and edge-on direction. It can be seen that the face-on to edge-on ratio increases with the titania pore sizes, further indicating face-on crystallites preferably form in larger pores.

6.6 Summary

In this part, the crystallization behavior of P3HT and PffBT4T-2OD in the printed mesoporous titania films with different pore sizes is studied via GIWAXS. A successful printing of mesoporous titania films is highly promising for large-scale deposition in an industrial environment. Characterization of fabricated titania frameworks is carried out with GISAXS. P3HT and PffBT4T-2OD are successfully infiltrated into the printed mesoporous titania films as proven by SEM. Moreover, UV-Vis conveys that larger titania

mesopores are highly advantageous for efficient backfilling of a donor material. With respect to the crystallization behavior of the donor polymers, lattice constants, crystal sizes and orientations are determined in dependence on the size of titania mesopores. Irrespective of the crystal orientation, PffBT4T-2OD chains with a denser stacking are preferentially observed for larger titania pores, which is consistent with the results for P3HT-backfilled samples. For the edge-on direction, both PffBT4T-2OD-backfilled and P3HT-backfilled active layers show in general the same trend of increasing crystallite sizes with decreasing titania pore sizes. In contrast, and for the face-on direction, the opposite tendency of increasing PffBT4T-2OD crystallite sizes with increasing titania pore sizes was observed. Thus, a high face-on to edge-on ratio is favored in a titania nanoconfinement with larger pores. These findings are of crucial importance for crystalline properties and future efficiency optimization/enhancement in one of the most promising material combinations for hybrid photovoltaic applications.

7 In situ Study of mesoporous titania films during slot-die printing

This chapter is based on the published article: In situ study of order formation in mesoporous titania thin films templated by a diblock copolymer during slot-die printing (N. Li et al., ACS Appl. Mater. Interfaces, 2020, 12 (51), 57627–57637, DIO: org/10.1021/acsami.0c18851). Adapted with permission from Ref. [188] Copyright (2020) American Chemical Society.

Our previous works introduce the slot-die printed mesoporous titania films with tailored nanostructures, and crystallization of P3HT and PffBE4T-2OD in the printed titania mesopores. Printing is interesting e.g. for upscaling solar cells where titania films with an interconnected mesoporous network and a large surface-to-volume ratio are desired as photoanodes. A fundamental understanding of the structure evolution during printing is of high significance in tailoring these films. In this work, we provide important insights into the self-assembly of the slot-die printed titania/polystyrene-block-polyethylene oxide (PS-b-PEO) micelles into ordered hybrid structures in real-time via in situ grazing-incidence small-angle X-ray scattering (GISAXS).

The synthesis of nanostructured titania (TiO_2) films has attracted considerable attention for decades, since these films have intriguing physical and chemical properties, like high electron mobility [8], chemical stability [189] and non-toxicity [10]. These advantages enable them to be widely used in different fields, such as photocatalysis [190], lithium-ion batteries [191], supercapacitors [119], and photovoltaics [162, 163]. Nanostructured TiO_2 films with a large effective surface area and an interconnected network morphology, e.g. in the type of mesoporous TiO_2 structures [159], were used as an electron transport layer in photovoltaic devices like hybrid solar cells [1], dye-sensitized solar cells (DSSCs) [164], solid-state dye-sensitized solar cells (ssDSSCs) [165, 166], perovskite solar cells [192], and quantum dot (QD) solar cells [4]. To achieve high device efficiencies, controlling the nanoscale morphologies is necessary. To achieve such control, an amphiphilic diblock copolymer (DBC) like polystyrene-block-polyethylene oxide (PS-b-PEO) as a structure-directing template was commonly used in sol-gel synthesis approaches [193]. Due to a so-called good-bad solvent pair, the amphiphilic DBC undergoes microphase separation

and therewith self-assembles into a core/shell-like micellar structure [143]. By adjusting the weight fraction of solvents, catalysts and titania precursors, the template DBC can form different kinds of micellar morphologies, such as spherical micelles, cylindrical micelles, lamellae or vesicles [56, 57]. Apart from shape tailoring, the ratio of shell thickness (L) over radius of micellar cores (C) can be regulated by the block lengths of the DBC, which enables to influence micellar ordering in solutions. For example, McConnell et al. studied a series of polystyrene-block-polyisoprene (PS-b-PI) block copolymers with different L/C ratios and observed face-centered cubic (FCC) and body-centered cubic (BCC) phases of the spherical diblock copolymer micelles in their gel-like regions [58]. The authors found that FCC packing was more stable for spherical micelles with a large core and a thin shell, while BCC favorably occurred at an inverted chain architecture [58].

To date, on a base of the sol-gel technique, various solution-processing deposition methods were applied for fabricating titania films, such as spin coating [194], spray coating [195], inkjet printing [129], doctor-blade coating [196] and slot-die printing [110]. Among these preparation techniques, slot-die printing has attracted special interest recently, since it is an industrial scale technique and allows for simple production of films on most substrates at low cost. In particular, it provides the feasibility to control the film thicknesses and to perform multilayer-film fabrication with high efficiency [112]. Moreover, solutions with low viscosities can be used directly in slot-die printing and close to equilibrium can be achieved for solutions with slow solvent evaporation rate [110]. In such cases, the organic chains/ligands have sufficient time to arrange themselves via minimizing energy during printing. Moreover, the film formation process during slot-die printing can be well investigated in situ with advanced scattering methods such as grazing-incidence small-angle X-ray scattering (GISAXS) [197]. For example, Liu et al. [136] and Pröller et al. [160] performed in situ GISAXS and revealed the structure evolution of slot-die printed polymer:fullerene active layers of organic solar cells. Chen et al. followed the kinetics of colloidal PbS QDs via in situ GISAXS during printing, and observed that an FCC superlattice stacking transformed into a BCC nested FCC stacking due to the large ratio of the ligand-shell thickness over the QD-core radius [198].

In situ GISAXS has proven to be a powerful tool for the study of thin-film structure formation processes and was also successfully employed in monitoring the structure evolution of titania/polymer-template hybrid films during thin film deposition processes. For example, Song et al. observed the morphology formation of titania/PS-b-PEO hybrid thin films during dry spray coating in real-time [124]. In contrast, Su et al. used a wet spray deposition, and reported a different structure development process of the hybrid nanostructures [127]. These findings manifest that, even for the same deposition method, the structure formation closely depends on the deposition parameters such as temperature.

However, all these in situ GISAXS studies were related to spray coating of titania hybrid films, while in situ GISAXS studies of slot-die printed titania films are, to the best of our knowledge, still not yet found in the literature. Since commonly the film morphology differs when using different deposition methods, knowledge from other deposition methods cannot be easily transferred [160]. Therefore, to deeply understand industry-scale coating processes such as printing and to fully exploit the potential of mesoporous titania films for scaling up solar cell fabrication, it is necessary to provide insights into the kinetic development of titania-DBC hybrid structures, which after calcination can be transferred into mesoporous titania films.

In this chapter, the titania-DBC micellar solution containing the templating DBC PS-b-PEO, is synthesized with a sol-gel approach. We use the slot-die printing technique to deposit the tailored titania/PS-b-PEO micelles with a spherical shape consisting of a hard Ti-O-PEO core and a soft PS shell [199]. By using in situ GISAXS, the nanostructure evolution of the titania/PS-b-PEO hybrid film, particularly the formation process of the ordered structures, is tracked in a real-time scale during the slot-die printing. Based on this in situ study, we propose that the spherical core-shell micelles assemble in two different ways. At the interfaces between the micelles and both, air and solid substrate, an FCC structure is establishing, whereas a defect-rich mixed FCC and BCC structure forms in the bulk. The final printed hybrid titania/PS-b-PEO film is studied with ex situ GISAXS measurements at different incident angles and with scanning electron microscopy (SEM). The combination of in situ and ex situ information provides a possibility for understanding the mechanisms, which govern the self-assembly of the spherical titania/PS-b-PEO micelles, and for demonstrating the significant role of interface effects in printing. After calcination, the resulting titania films are studied as well. As a reference, spin-coated titania films are fabricated via using the same solution and calcination conditions. In comparison to the spin-coating method, a more ordered structure is achieved in the mesoporous titania film via slot-die printing. Therefore, printing of titania/PS-b-PEO hybrid films is promising for using the resulting titania films after calcination in energy conversion devices. This knowledge is of vital importance to tailor titania morphologies and is expected to pave the way for the up-scaled fabrication of solar cells, like QDSSCs or DSSCs based on titania photoanodes.

7.1 Set-up and protocol for in situ experiments

Figure 7.1 schematically shows the experiment set-up for in situ GISAXS measurements. In this chapter, the set-up, as shown in Figure 4.5, is designed and built by Sebastian Grott and Rodrigo Delgado Andrés from the group. The printing of the titania/PS-

b-PEO micelle solution is carried out with a home-made slot-die coater. In our case, the film thickness is controlled by the solution flow rate, the printing velocity and the distance between substrate and printer head. Here, the solution flow rate is set at 100 μL/min, the printing velocity at 7 mm/s with an acceleration of 5 mm/s^2 and the distance between substrate and printer head as around 0.4 mm. The temperature is chosen at room temperature and precleaned silicon (Si) is used as the substrate for the printing deposition. The in situ measurement is performed at beamline P03/MiNaXS of the PETRA III storage ring at DESY (Hamburg, Germany) [102]. The printing protocol for the in situ GISAXS measurement is composed of 0.1 s exposure + 11.9 s waiting in alternating sequence. With an X-ray exposure of only 0.1 s per frame and sample movement, beam damage is avoided. The lateral moving direction starts from the freshly deposited solution spot to the other side along the long strip sample, in order to fully track the entire film formation process during printing. After 40 cycles, a GISAXS scan measurement is immediately carried out along the printing direction covering the in situ measurement region to perform the beam damage test.

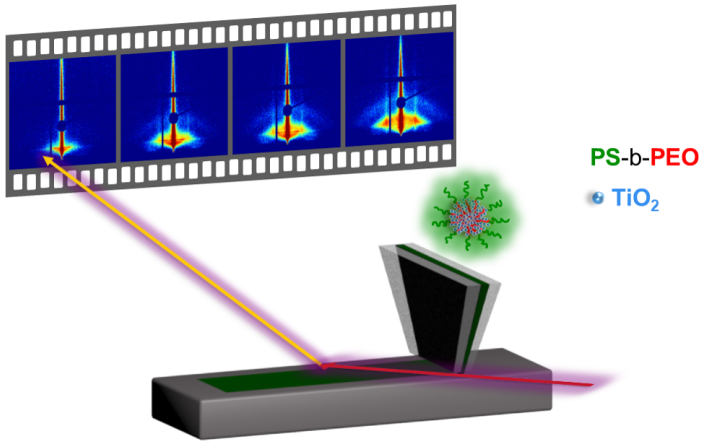

Figure 7.1: Schematically illustration of the experimental set-up for in situ GISAXS measurement during slot-die printing. Adapted with permission from Ref. [188] Copyright (2020) American Chemical Society.

7.2 Morphology evolution during slot-die printing

To establish the hybrid titania/PS-b-PEO films via slot-die printing, a sol-gel synthesis approach is selected. During the sol-gel process, the PS and PEO blocks form spherical micelles with a core-shell structure. Titanium(IV)isopropoxide (TTIP) undergoes hy-

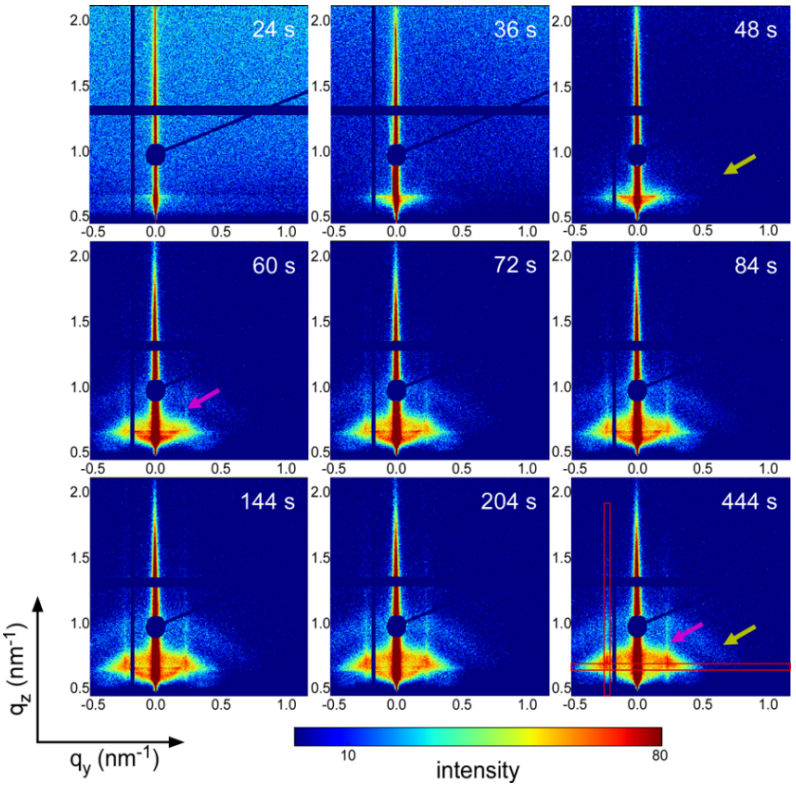

Figure 7.2: Selected in situ 2D GISAXS data during the printing of the titania/PS-b-PEO micellar solution at different times as indicated. The position of the prominent rod-like Bragg peak is indicated as the purple arrows and the strong higher-order ring-like scattering feature is marked with the dark yellow arrows. The red vertical and horizontal boxes display the positions of the off-centered vertical and horizontal line cuts, respectively. A circular beamstop is placed at the position of the specular reflection. All the patterns are present with the same intensity scale. For each image, the acquisition time is 0.1 s. Adapted with permission from Ref. [188] Copyright (2020) American Chemical Society.

drolysis and condensation reactions to build Ti-O networks, which allows titania species being anchored in the PEO domains via hydrogen bonds. The prepared solution consists of spherical micelles with a Ti-O-PEO core and PS shell.

Figure 7.2 shows selected 2D GISAXS data of the titania/PS-b-PEO hybrid film during in situ printing. The scattering intensity increases over time mainly because a large amount of solvent evaporates. A higher-order ring-like structure (as indicated by the dark yellow arrows in Figure 7.2) can be seen with a weak intensity at t $\geq$ 48 s, and the intensity gradually increases over time. A rod-like peak (as indicated by the purple arrows in Figure 7.2) is observed at t $\geq$ 60 s. To quantify the vertical nanostructure evolution during printing, off-centered vertical line cuts of the 2D GISAXS data are performed at the rod-like peak position (integrated over q_y = (-0.22) - (-0.25) nm^{-1}, shown as the

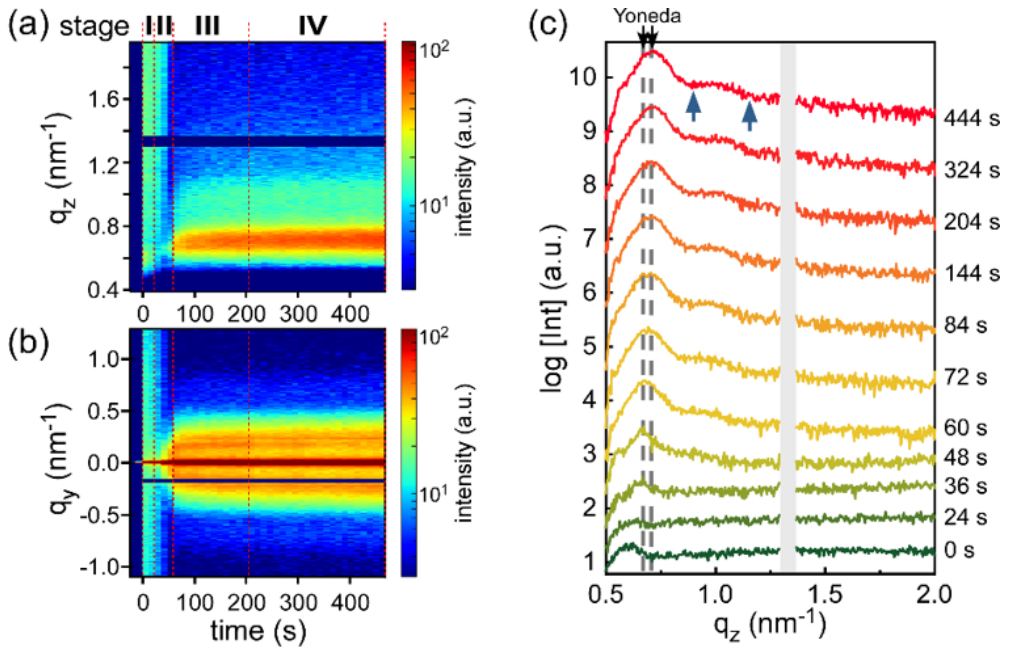

Figure 7.3: 2D intensity mappings of (a) q_z and (b) q_y as a function of time. Corresponding curves of (c) off-centered vertical plotted from bottom to top with increasing time. All the curves are shifted along the intensity axis for clarification of the presentation. The dashed gray lines show the Yoneda peak positions of the titania/PEO mixture. The blue arrows indicate the intensity modulations in the vertical direction. The inter-module detector gap is shown with a grey shaded area. Adapted with permission from Ref. [188] Copyright (2020) American Chemical Society.

red vertical box in Figure 7.2). Similarly, to obtain the horizontal morphology changes, horizontal line cuts are made at the Yoneda peak region of the titania/PEO mixture (integrated over q_z = 0.65 - 0.69 nm^{-1}, shown as the red horizontal box in Figure 7.2) due to its scattering signal prevailing over the PS block [124].

7.2.1 Vertical and lateral nanostructure evolution

Figure 7.3a and Figure 7.3b display the temporal signal intensity evolution in vertical and horizontal direction via 2D mappings of q_z and q_y as a function of time extracted from the off-centered vertical and horizontal line cuts, respectively. By combining the Figure 7.3a,b, the entire printing process of the hybrid film can be divided into four stages: The solution state (stage I, $0 \leq t \leq 24$ s), the wet state (stage II, $24 < t \leq 60$ s), the gel state (stage III, $60 < t \leq 204$ s) and the dry state (stage IV, $204 < t \leq 444$ s). In stage I, the titania/PS-b-PEO micelles have random motions in the solution, which contributes to a liquid-like broad diffuse scattering. Then all the main structural

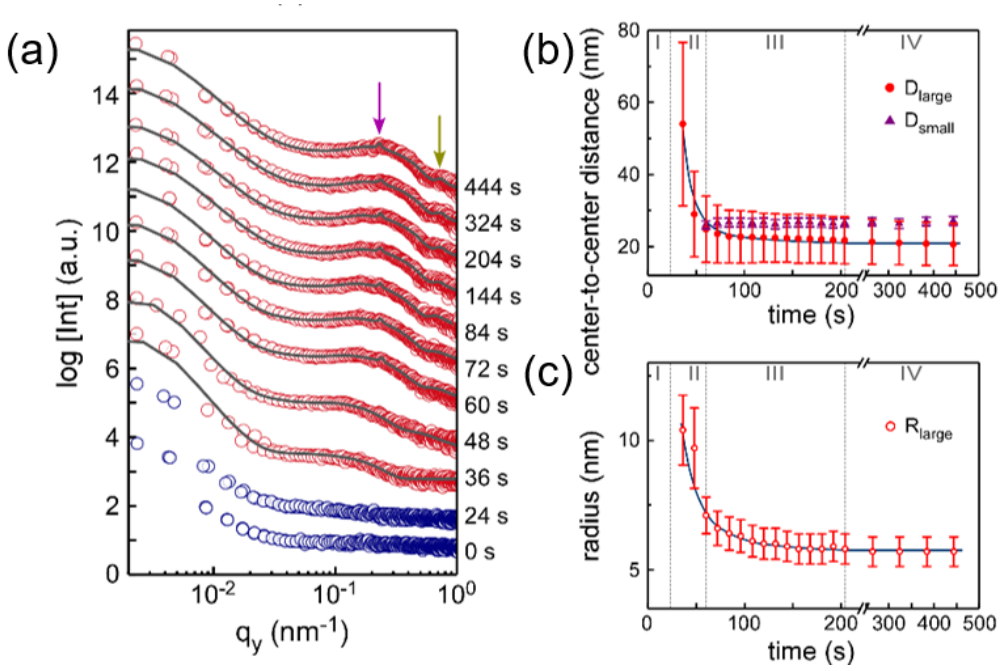

Figure 7.4: (a) Horizontal line cuts plotted from bottom to top with increasing time. The solid gray curves are the fits to the data. All the curves are shifted along the intensity axis for clarification of the presentation. Extracted characteristic length scales: (b) Center-to-center distance and (c) domain radius of the titania/PEO mixture as a function of time. The large structure is marked as red circles. The small structure from the surface is marked as purple triangles, but only its center-to-center distance is extracted due to the low intensity. The dark yellow arrow represents the higher-order peak of the large structure. The purple arrow suggests the rod-like Bragg peak from the film surface. Adapted with permission from Ref. [188] Copyright (2020) American Chemical Society.

scattering features form in stage II, such as the characteristic side peaks or the ring-like signature (Figure 7.2). After that, no additional scattering signals appear along the q_z and q_y directions over time, which implies that the basic film structures, after having been established gradually, tend to pack without adding new characteristic structures (stage III). Finally, stable film structures are formed in stage IV.

In order to gain further insights into the vertical structure formation process of the titania/PS-b-PEO hybrid film, selected off-centered vertical line cuts are analyzed (Figure 7.3c). At the initial stage I, the random micelle density distributions dominate within the solution-like film. In stage II, during solvent evaporation the intensity increases at around $q_z = 0.66$ nm^{-1}, which is related to the characteristic Yoneda peak of the titania/PEO mixture being well established at t = 36 s. Its occurrence indicates that only with an adequate solvent evaporation the sufficient X-ray contrast between the micelles

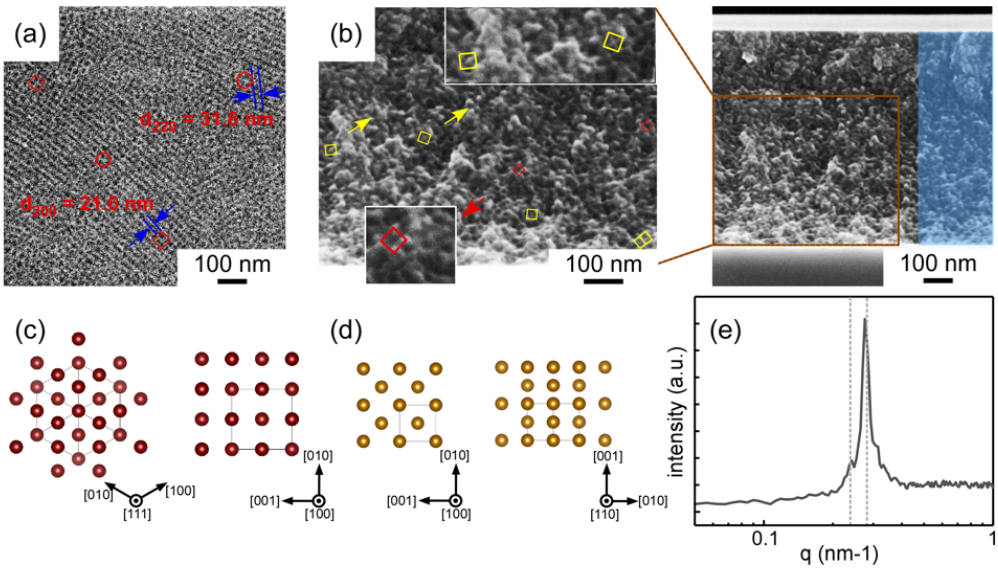

Figure 7.5: Selected in situ 2D GISAXS data during the printing of the titania/PS-b-PEO micellar solution at different times as indicated. The position of the prominent rod-like Bragg peak is indicated as the purple arrows and the strong higher-order ring-like scattering feature is marked with the dark yellow arrows. The red vertical and horizontal boxes display the positions of the off-centered vertical and horizontal line cuts, respectively. A circular beamstop is placed at the position of the specular reflection. All the patterns are present with the same intensity scale. For each image, the acquisition time is 0.1 s. Adapted with permission from Ref. [188] Copyright (2020) American Chemical Society.

and the solvent environment is reached in the wet film. With further solvent evaporation, a more prominent Yoneda peak is observed at t = 60 s. At t > 60 s (stage III), a second prominent Yoneda peak in the curves occurs at slightly higher position $q_z \approx 0.69$ nm^{-1}, implying that the titania/PS-b-PEO micelles form two differently dense packings in the gel film. Moreover, intensity modulations along q_z (marked as blue arrows in Figure 7.3c) result from resonant diffuse scattering due to a long-range interface correlation in the titania/PS-b-PEO hybrid film in the vertical direction appearing at t = 48 s [200]. With less residual solvent, these intensity oscillations become stronger, suggesting an improved correlation for the drier film. Based on the local minima positions ($q_z \approx 0.89$ nm^{-1} and 1.15 nm^{-1}, as shown with the blue arrows at t = 444 s in Figure 7.3c), the correlated thickness d_c, a long-range correlated length in the vertical direction [201], as calculated, is around 24 nm.

To follow the characteristic structural changes in the horizontal direction during printing, horizontal line cuts are analyzed. Representative line cuts are plotted in Figure 7.4a together with model fits. All line cuts are modeled within the framework of the distorted

wave Born approximation (DWBA) employing the effective interface approximation (EIA) and the local monodisperse approximation (LMA) [92,147–149]. Spherical models are used to describe the micelles according to the SEM images (bright spots in Figure 7.5a,b). For stage I ($t \leq 24$ s), no obvious scattering features are observed in the curves, because the titania/PS-b-PEO micelles are in a solution state with free motion. In stage II, an additional intensity peak appears as a signature of established in-plane structures (see e.g. $t = 36$ s line cut), which becomes more pronounced with time in the wet film. During drying (see e.g. $t = 48$ s), in the high q_y region, a next feature, namely a weak broad peak, appears between 0.55 nm^{-1} and 0.85 nm^{-1} (as indicated with a dark yellow arrow in Figure 7.4a). It corresponds to the weak ring-like scattering intensity in the 2D GISAXS data in Figure 7.2, and is considered as a higher-order peak. Since $t = 60$ s, a small sharp peak arises at $q_y = 0.22$ - 0.25 nm^{-1}, which originates from the periodic structure arrangement of the micelles in the gel film. In agreement with the surface SEM data (Figure 7.5a) this well-ordered structure is attributed to a surface structure.

From data modeling, center-to-center distances and domain radii of the titania/PEO domains are extracted (Figure 7.4b and Figure 7.4c). The center-to-center distance of the large structure has, for example, a value of (54 ± 23) nm at $t = 36$ s, and decreases rapidly until $t = 60$ s. Afterwards, it decreases slightly (stage III) and finally remains constant at (21 ± 6) nm within the error bars. The evolution of the corresponding radius of the large structure has a similar trend as the center-to-center distance. An initial value of (10.4 ± 1.4) nm for the radii of the large structure decreases to (5.7 ± 0.6) nm. The decrease of center-to-center distances and radii is mainly a result of the solvent evaporation. Thereafter, the morphology is arrested and undergoes only minor changes due to lacking mobility. The tendency of this structure development is in good agreement with the structural evolution of the sprayed deposited titania films reported earlier [124, 127]. In contrast, for the structure from the film surface (denoted as small structure), a stable center-to-center distance with a narrow Gaussian distribution is extracted with a value of (27.1 ± 1.2) nm existing from $t = 60$ s to the end. This indicates a well-ordered structure being present at the hybrid film surface. Different from the general intensity increase of the scattering features of the large structure, this Bragg peak intensity remains constant over time, indicating a dry surface during the film formation process. The center-to-center distances of the surface structure are equivalent to those from the inner morphology at the final stage. This suggests that a center-to-center distance with a Gaussian distribution is overall dominating the titania/PS-b-PEO hybrid film.

7.2.2 Micellar packing evolution

To understand the micellar packing inside the titania/PS-b-PEO hybrid film during film formation, the 2D GISAXS data is further analyzed from sector integrals. We use χ values from 25°to 40°(as shown in Figure 7.6a) to avoid the strong scattering from the periodic structure on the film surface. Their corresponding prominent reflections appear on both sides of the specular beam (q_y = 0.22 - 0.25 nm^{-1}) and are assigned to a hexagonal arrangement of the titania/PEO cores on the surface monolayer [202]. The presence of the FCC structure of the micelles is verified with SEM (in Figure 7.5a), in which hexagonal and square packings are dominant on the film surface [203]. In addition, the ring-like scattering signal from the bulk indicates a certain center-to-center distance for the titania/PEO cores without a preferential orientation, like expected for a polycrystalline micellar packing.

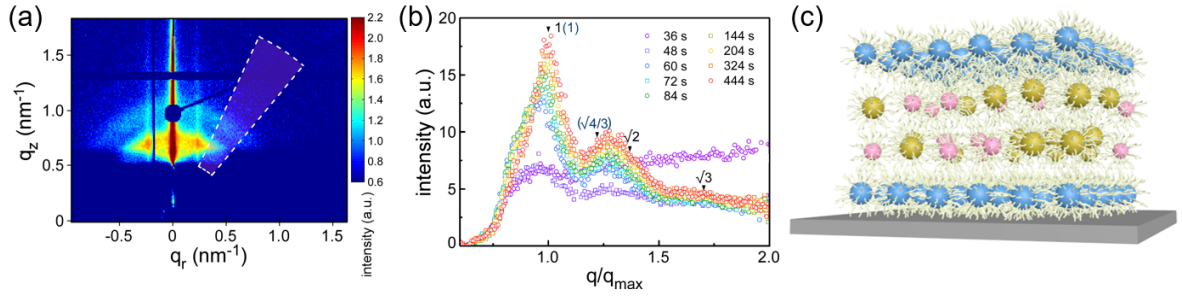

Figure 7.6: (a) 2D GISAXS data of the titania/PS-b-PEO film prepared via slot-die printing at t = 444 s showing the area of radial integration (χ from 25° to 40°) as indicated with a dashed box. (b) Respective sector integrals of the selected 2D GISAXS data plotted as a function of normalized q/qmax with an acquisition time of 0.1 s. Peak position ratios of FCC (blue) and BCC (black) phases are indicated. (c) Schematic 3D view of the micellar arrangement in the printed titania/PS-b-PEO film. FCC structures at the film surface and the film/substrate interface are indicated in blue with a well-ordered arrangement. The mixed FCC and BCC structures of the bulk are indicated in dark yellow and pink, respectively. Adapted with permission from Ref. [188] Copyright (2020) American Chemical Society.

The sector integrations are plotted in Figure 7.6b as a function of normalized wave vector q/q_{max} to clarify the micellar packing inside the titania/PS-b-PEO film. The position of the first Bragg peak with the maximum intensity of the final dry film (t = 444 s) is taken for the normalization of q. The inner film structure forms in stage II. For example, at t = 48 s, the second Bragg peak appears with a broad width in good agreement with the development of the lateral structures. Moreover, when t = 60 s, both the first and second Bragg peaks show a prominent increase in their intensity. Afterwards, both peaks

are slightly getting more pronounced and narrower over time, indicating that the hybrid film is nearly dried at t = 60 s, which marks the transition from the wet to the gel state. This observation agrees well with the results of the vertical structure evolution. All peaks can be indexed with a BCC ($q/q/q_{max} = 1, \sqrt{2}, \sqrt{3}$) structure combined with an FCC ($q/q/q_{max} = 1, \sqrt{4}/\sqrt{3}$) structure [204], as indicated with arrows on the top of the profile at t = 444 s (Figure 7.6b). Some peaks indexed with both FCC and BCC structures show small deviations from the theoretically expected positions, which originates from lattice distortions (defects) in the real stacking situation [205]. The found peak position ratios suggest a defect-rich mixed FCC and BCC phase in the bulk for the titania/PS-b-PEO film. The similar results obtained from the measurement of the hybrid film immediately after the in situ printing process are provided in the Figure 7.7.

Thus, whereas an FCC structure is existing at the film surface, a mixed FCC and BCC structure without special orientations is present in the bulk. At the film/substrate interface one might expect also the presence of an ordered micellar structure [206]. Figure 7.6c sketches schematically the packing of the hybrid titania/PS-b-PEO film.

7.3 Morphology of the final printed hybrid film

To investigate the final printed hybrid film, three different incident angles are carefully chosen for ex situ GISAXS measurements. Since the penetration depth of the X-ray beam in GISAXS closely depends on the incident angle, it is possible to probe both, near-surface and bulk morphology of films [89]. Figure 7.8a-c show the 2D GISAXS data of the final printed hybrid film at incident angles of 0.15°, 0.25°and 0.39°, respectively. Compared to the in situ data taken during printing, the main scattering features are seen as well, however, in the ex situ data they are more pronounced. This enhancement of scattering features indicates that the final printed hybrid film exhibits a further improved-order structure as compared to the hybrid film after 444 s. At the end of the in situ measurements, still a small quantity of residual solvent inside the film might enable a gradual rearrangement of the micellar packing into a more ordered and denser structure [207,208], similar to studies about the assembly of nanocrystal superlattices and their structural stability [209,210]. The vertical line cuts of the 2D GISAXS data (at around $q_y = 0$ nm^{-1}) are plotted as a function of the exit angle α_f in Figure 7.8d. The specular X-ray reflection, where the exit angle is equal to the incident angle [211], is not shielded by a beamstop due to using an in-house SAXS instrument (Figure 7.8d). The Yoneda peak region [96], which is determined by the critical angle of the titania/PEO mixture, is marked as a dashed rectangle in Figure 7.8d. Thus, the measurement at the incident angle of 0.15°, which is below the critical angles of the investigated materials, is sensitive to near-surface

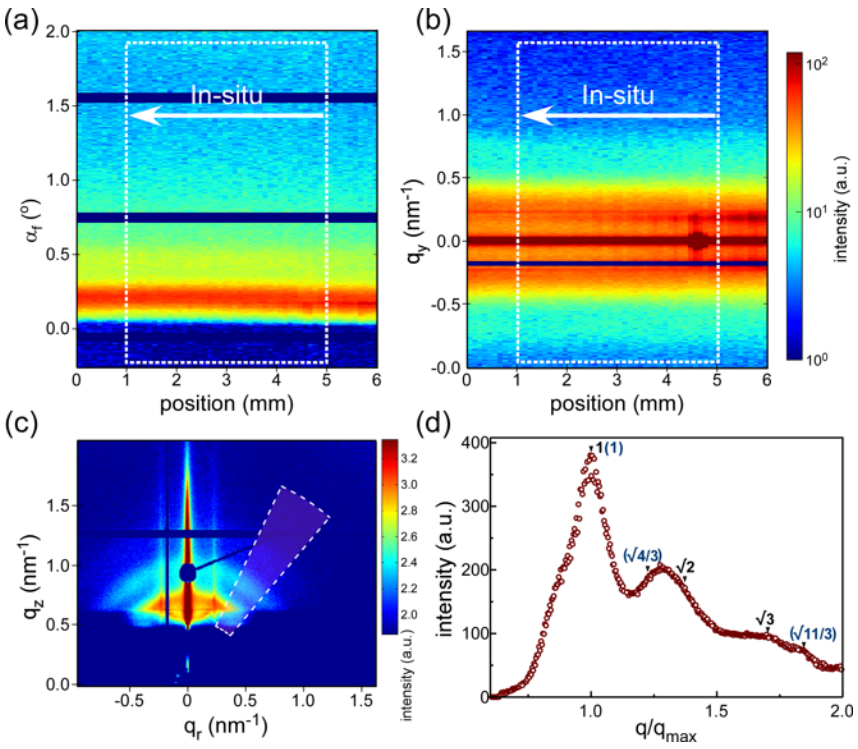

Figure 7.7: 2D mappings of (a) the off-centered vertical and (b) the horizontal line cuts from the respective 2D GISAXS data taken with an acquisition time of 0.1 s. All off-centered vertical line cuts are integrated over q_y = (-0.22) - (-0.25) nm^{-1} and plotted versus position. All horizontal line cuts are integrated over q_z = 0.65 - 0.69 nm^{-1} and plotted versus position. The region and relative direction for the in-situ experiment are marked in (a) and (b) with the dashed box and white arrow. (c) Integrated 2D GISAXS data of the ex-situ experiment. (d) The azimuthal integral is done for χ values from 25°to 40°as a function of q/q_{max}. Adapted with permission from Ref. [188] Copyright (2020) American Chemical Society.

structures [212]. In the scattering from the near-surface structure, on the 2D detector a prominent rod-like Bragg peak at q ≈ 0.23 nm^{-1} is seen together with a weak second-order peak at q ≈ 0.48 nm^{-1} (as indicated as two purple arrows in Figure 7.8a). At both larger incident angles, which result in probing bulk structures, these two surface-related peaks are significantly weaker. Moreover, the intensity of three characteristic peaks from the bulk morphology attributed to the first-, second- and third-order Bragg peaks of the micellar structure inside the film (marked with white, orange and green arrows in Figure 7.8c) is strongly pronounced.

Horizontal line cuts of 2D GISAXS data are made at the material-dependent Yoneda peak region (Figure 7.9a). From the strong Bragg peaks, center-to-center distances of the titania/PEO domains are extracted via a Lorentzian fit to the q_y profiles (see Figure 7.10).

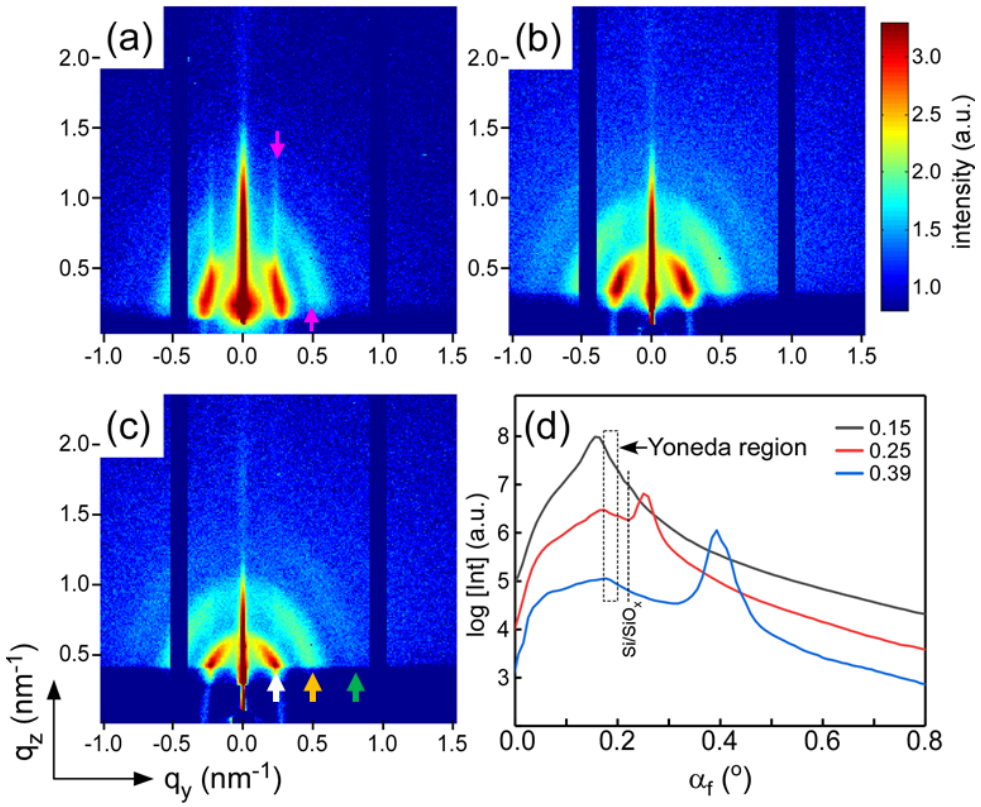

Figure 7.8: 2D GISAXS data of the final printed hybrid titania/PS-b-PEO film measured at different incident angles: (a) 0.15°, (b) 0.25°and (c) 0.39°. The purple arrows indicate a prominent rod-like Bragg peak and its second-order peak, which originate from the film surface. Arrows with different colors mark the peaks caused by the bulk structure: first-order (white), second-order (orange), and third-order peak (green). All the patterns are present with the same intensity scale. (d) Vertical line cuts of the corresponding 2D GISAXS data at around q = 0 nm^{-1}. The cuts are present versus α_f and shifted along the y-axis for clarification with decreasing the incident angles (from bottom to top). The dashed rectangle and line indicate the Yoneda peak regions of the titania/PEO mixture and Si/SiO_x, respectively. Adapted with permission from Ref. [188] Copyright (2020) American Chemical Society.

Due to the different incident angles, the peak positions, corresponding to the center-to-center distances, show a slight shift that might be due to diffraction effects [213] (as seen in Figure 7.9a). Besides, it needs to consider that the length scales of surface structures show a small difference from the bulk. The obtained value (26.9 ± 1.8) nm at the incident angle of 0.39°(similar to the in situ experiment) is consistent with the aforementioned center-to-center distances from the in situ studies.

Figure 7.9b displays the zoom-in region of the q_y range of 0.09-1.2 nm^{-1} with indexing of the FCC and BCC Bragg peak positions. The peak positions of each scattering profile

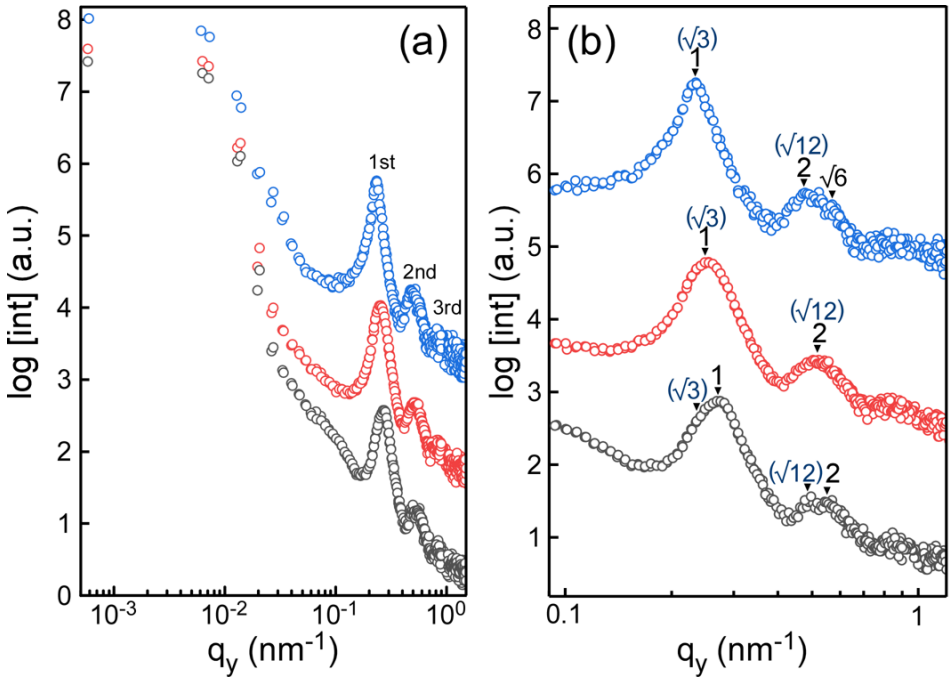

Figure 7.9: (a) Horizontal line cuts of 2D GISAXS patterns of the final printed hybrid titania/PS-b-PEO film at different incident angles: 0.15°, 0.25°and 0.39°from bottom to top. For clarity, all curves are shifted along the intensity axis. The first-order, second-order and third-order peaks are marked on the top of the curves. (b) Zoom-in region of q_y profiles in the range of 0.09 - 1.2 nm^{-1} with FCC (blue indexes) and BCC (black indexes) Bragg peak positions. Adapted with permission from Ref. [188] Copyright (2020) American Chemical Society.

are fitted via Lorentzian functions (like in Figure 7.10). A sequence of peaks, which corresponds to either the FCC structure (indicated with blue ratios in Figure 7.9b) or the BCC structure (indicated with black ratios in Figure 7.9b) appears in the data irrespective of the incident angle. In the near-surface part, at the incident angle of 0.15°, the Bragg peaks from the FCC phase match the positions of the rod-like features (marked as the purple arrows in Figure 7.8a). In general, all observations from the GISAXS data are in good agreement with those from the corresponding surface and cross-section SEM images, as seen in Figure 7.5a and Figure 7.5b, respectively.

Therefore, the ex situ analysis of the final printed hybrid films provides further insights adding to the information gained in the kinetic study. The micellar morphology at the interfacial layers varies from the bulk structures, which is attributed to interactions with the interfaces [206]. Due to the formation of Ti-O bonds as discussed above, the micelles have a hard Ti-O-PEO core and a soft shell. An FCC structure of the micelles with hard cores prefer to enable a dense packing, whereas the soft shells favor structures that can minimize the interfacial area between the adjacent micelles [214, 215]. The less dense

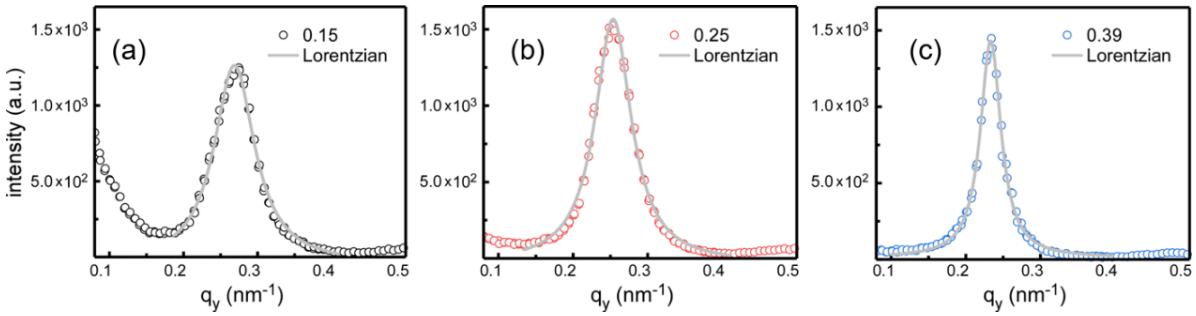

Figure 7.10: Horizontal line cuts in the interesting q_y range of 0.1 - 0.5 nm^{-1} showing the first order Bragg peak of the printed hybrid titania/PS-b-PEO film measured at different incident angles: (a) 0.15°, (b) 0.25°and (c) 0.39°. The gray lines represent Lorentzian fits to the data. Adapted with permission from Ref. [188] Copyright (2020) American Chemical Society.

packing in a BCC structure was e.g. reported in case of nanocrystals with a large L/C ratio, in which the flexible ligands or organic chains occupy interstitial space [209, 216]. Balancing both competing effects, namely maximum packing fraction and minimum interfacial area, to minimize the total free energy of the self-assembly system, gives rise to the observed film morphology, in which the defects arise from the limited mobility during film formation via printing.

7.4 Morphology of calcined samples

Finally, the printed hybrid titania/PS-b-PEO film is calcined and examined via SEM and ex situ GISAXS. Such calcined film would be of use e.g. as a mesoporous titania photoanode for solar cells. For comparison, the spin-coated titania film is fabricated using the same solution and calcination process.

7.4.1 Surface morphology of the calcined samples

Figure 7.11a and Figure 7.11b show the surface SEM images of the printed and spin-coated titania films, respectively. In contrast to the surface morphology of the spin-coated titania film, for the printed titania film a more ordered surface structure is visible. To quantify the degree of structural order, 2D fast Fourier-transformation (2D-FFT) patterns are extracted from the respective SEM images and shown as the insets on top right corners of each image. Compared with the spin-coated film which shows a ring-like pattern, the 2D-FFT of the printed film exhibits a set of hexagonal spots together with its higher orders (a magnification image shown in Figure 7.11c). Thus, a significantly enhanced

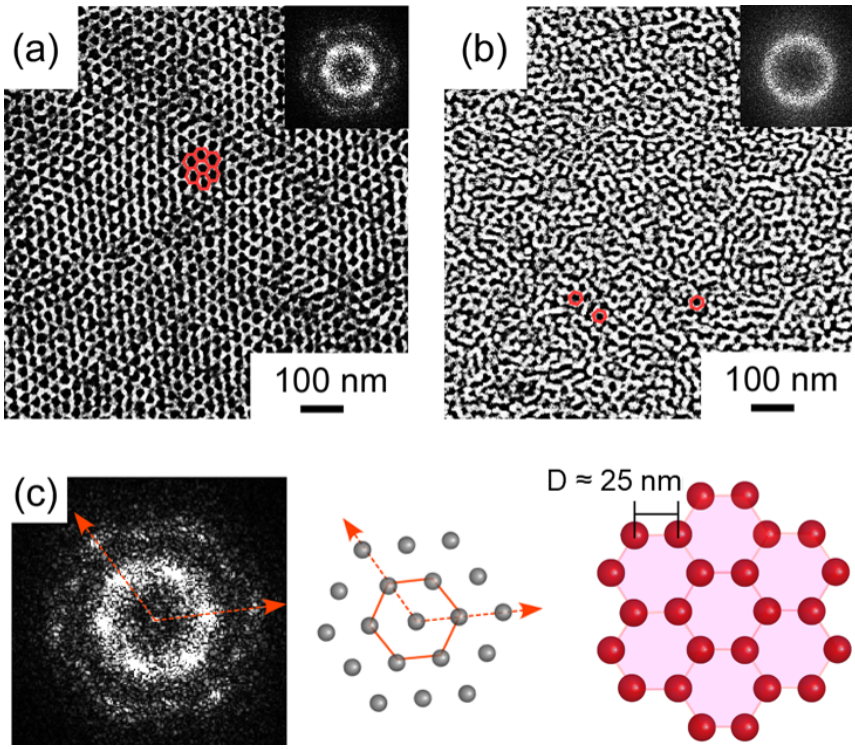

Figure 7.11: Surface SEM images of (a) the slot-die printed and (b) spin-coated titania film after calcination. The corresponding 2D-FFT patterns are displayed in the insets on top right corners. (c) A magnification 2D-FFT pattern of the printed film and its relevant illustration: one set of the hexagonal lattice as indicated with black spots. Schematic of the titania nanoparticles forming a honeycomb-like structure is exemplarily indicated with red circles. Adapted with permission from Ref. [188] Copyright (2020) American Chemical Society.

order is present in the printed titania film. This set of hexagonal lattice corresponds to the honeycomb-like arrangement of titania nanoparticles (as indicated with red circles). Moreover, from the power spectral density (PSD) analysis (Figure 7.12a), the center-to-center distances of the titania nanoparticles for the printed and the spin-coated samples are calculated to be 25.3 nm with a standard deviation of 2.0 nm and 23.6 nm with a standard deviation of 3.6 nm, respectively.

7.4.2 Inner morphology of the calcined samples

After calcination the titania films are also studied with GISAXS (Figure 7.13a,b). In the 2D GISAXS data, the characteristic side maxima (symmetrically in the range of q_y = 0.15 - 0.3 nm^{-1}) are more prominent for the printed titania film, even with a higher film thickness (compared with Figure 7.12b and Figure 7.12c). This reflects the higher degree of order being preserved in the printed film, since disorder leads to a loss

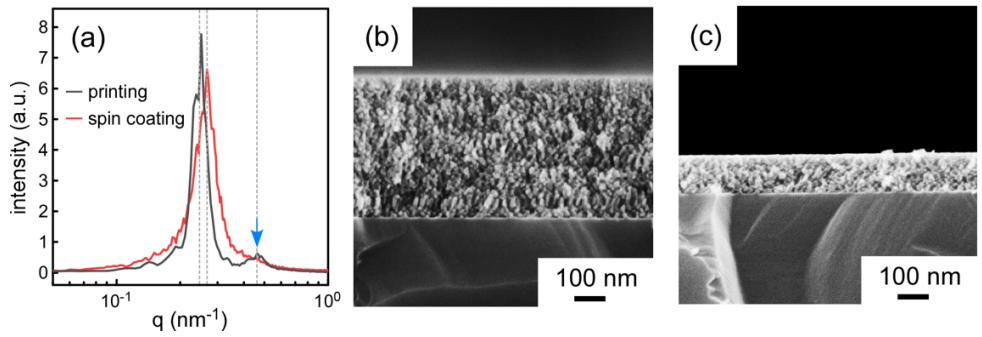

Figure 7.12: (a) PSD functions of the printed and spin-coated titania/PS-b-PEO film after calcination. Cross-section SEM images of the (b) printed and (c) spin-coated titania/PS-b-PEO films after calcination. Adapted with permission from Ref. [188] Copyright (2020) American Chemical Society.

of interference for the spin-coated titania film [95, 217]. The rod-like Bragg peaks (purple arrows in Figure 7.13a and Figure 7.13b) originate from the strong scattering of the surface structure. In case of the printed film, the peak positions of both scattering rods are at q $\approx$ 0.16 and 0.26 nm^{-1} (characteristic ratio 1.63 close to $\sqrt{2}/1$). This suggests a hexagonal packing of the mesoporous structure on the surface of the printed titania film, which agrees well with the SEM results. In case of the spin-coated titania film, only one rod-like peak is observed at $q_y \approx 0.18$ nm^{-1}. Accordingly, the hexagonal packing is not well developed and defect-rich. Moreover, the first peak position is found at a smaller q_y value in case of the printed titania film, which is in good agreement with the trend extracted from the PSD profiles (Figure 7.12a). The horizontal line cuts at the titania Yoneda peak position (white arrow in Figure 7.13b) are analyzed with a model assuming cylindrically shaped objects in agreement with the cross-section SEM images (Figure 7.12b). A cylinder-shape was used already earlier in other studies successfully for modeling mesoporous titania films [110, 124]. It is indicative of aggregations caused by calcination, during which the spherical micelles aggregate and then form into cylinder-like titania nanoparticles as shown in Figure 7.12b. Figure 7.13c depicts the horizontal line cuts and the corresponding fits. Based on a sharp peak as well as a weak higher-order peak (indicated by the arrows in Figure 7.13c) in both profiles, one can deduce that ordered inner structures with some long-range lateral correlations may exist in both films.

Two characteristic structures for both films are extracted from the GISAXS modeling as displayed in Figure 7.14a,b. For the printed film, the titania nanoparticle radii of (8.5 $\pm$ 0.8) nm with the related center-to-center distances of (26 $\pm$ 11) nm are acquired and denoted as the big-sized structure (indicated with blue triangles), which is attributed to disordered titania clusters with a wide distribution. Another small-sized structure

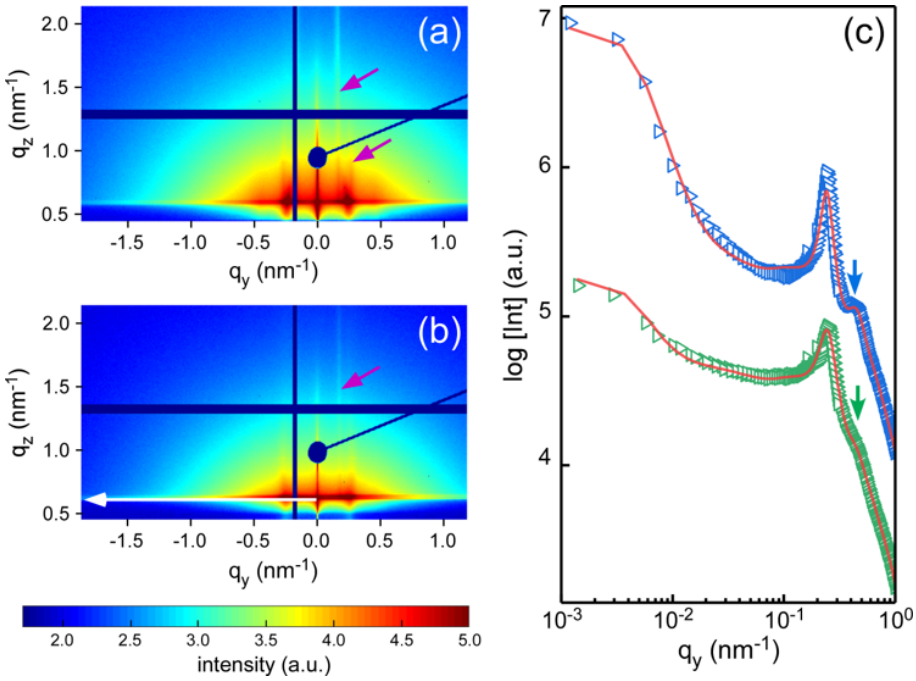

Figure 7.13: 2D GISAXS data of (a) slot-die printed and (b) spin-coated titania films after calcination. A circular beamstop is placed at the position of the specular reflection, inter detector module gaps seen as horizontal and vertical non-counting areas, and the horizontal line cut position illustrated with a white arrow. Data present integration of 100 frames of 0.1 s. (c) Horizontal line cuts of 2D GISAXS data of the slot-die printed (top) and spin-coated (bottom) titania film after calcination. The red lines are the fits to the data. The curves are shifted along the intensity axis for clarification of the presentation. The blue and green arrows indicate a higher-order structure in both films. Adapted with permission from Ref. [188] Copyright (2020) American Chemical Society.

(indicated with red circles) has the titania nanoparticle radii of (5.7 ± 2.1) nm and center-to-center distances of (25.1 ± 2.1) nm, corresponding to ordered titania nanoparticles insides the film, which agrees well with the findings in Figure 7.13c. It yields titania mesopore sizes of (13.7 ± 4.7) nm following the model reported by Sarkar et al. [146]. As for the spin-coated film, the similar results are quantified. That means apart from the big-sized structure with (9.0 ± 0.9) nm in radii and (25 ± 10) nm in interparticle distances, the small-sized structure with the titania nanoparticle radii of (5.5 ± 2.2) nm and its corresponding center-to-center distances of (23.8 ± 2.5) nm is obtained, which results in a slight decrease of the mesopore sizes of (13 ± 5) nm for the ordered inner structure. In addition, the center-to-center distances of both films extracted from the GISAXS data are close to the values from the PSD analysis calculated from SEM (as indicated with dark yellow crosses in Figure 7.14a). Comparing with the spin-coated film,

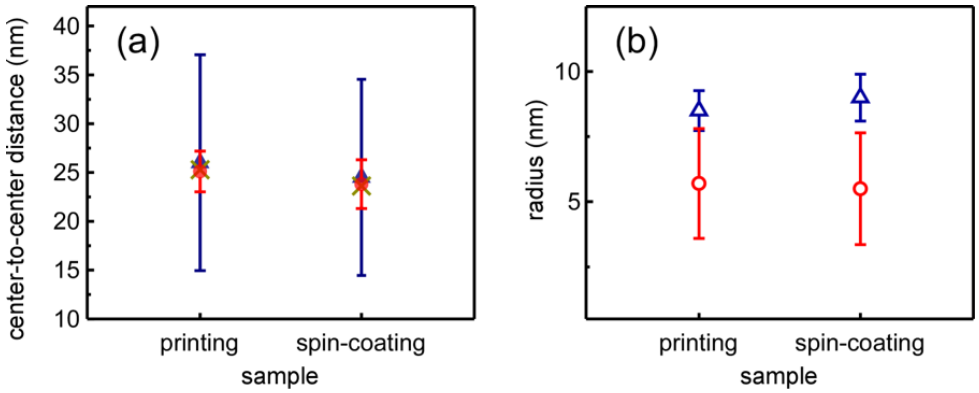

Figure 7.14: Extracted characteristic length scales: (a) Center-to-center distance and (b) particle radius of the titania films after calcination with different deposition methods: slot-die printing and spin coating. Blue triangles and red circles represent the big-sized and small-sized structures, respectively. Dark yellow crosses are the center-to-center distances from the PSD analysis extracted from the corresponding surface SEM images. Adapted with permission from Ref. [158] Copyright (2020) American Chemical Society.

the center-to-center distances of the printed one are larger for the big-sized and small-sized structures as extracted from GISAXS, and for the SEM analysis.

Thus, the morphology introduced during printing of the hybrid titania/PS-b-PEO film is preserved via the applied calcination. Pattern collapse is avoided and the nanoscale structure is preserved [218].

7.5 Quantum dot-sensitized solar cells

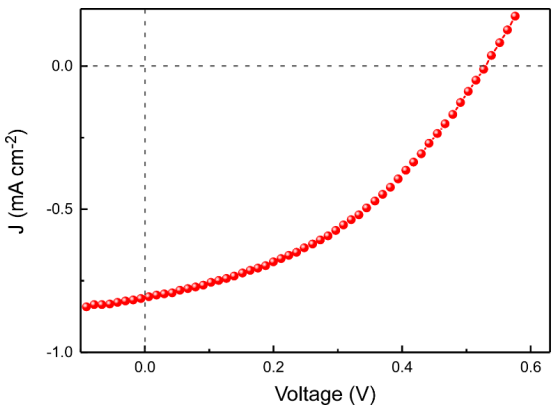

Figure 7.15: Current-voltage characteristic of the QD-sensitized solar cell based on the titania film via slot-die printing.

In Figure 7.15, the working quantum dot-sensitized solar cell (QDSSC) demonstrates the deposition of slot-die printing is a promising large-scale fabrication for photoanodes. The QDSSC devices show the power conversion efficiency (PCE) of 0.13 ± 0.02 %, open-circuit voltage (V_{oc}) of 0.52 ± 0.01 V, short-circuit current density (J_{sc}) of 0.74 ± 0.05 mA cm^{-2}, and fill factor (FF) of 37 ± 4 %. The V_{oc} is comparable to the reported value in the literature [115], since it is related to the energy levels between the electron-transporting layer TiO_2 and the PbS QD ink layer. It demonstrates that compared to the commonly used ZnO and SnO_2, TiO_2 is also a good photoanode candidate for PbS QDs. However, the J_{sc} is much lower than the literature with J_{sc} of above 20 mA cm^{-2}. One possibility is that the PbS QD ink is not fully backfilled into the mesoporous TiO_2 film. This low J_{sc} limits the improvement of the QDSSC efficiency.

The investigation of the exemplary QDSSC is far from optimization of device efficiency, but it shows the combination of the slot-die printed titania film with large-scale fabrication of solar cells can be promising in the future.

7.6 Summary

We investigate the self-assembly of slot-die printed titania/PS-b-PEO micelles into ordered structures in real-time using in situ GISAXS. This synchrotron-based approach provides a vital insight into the structural evolution of titania/PS-b-PEO hybrid films. A well-ordered surface structure is established and remains stable during the entire film formation. In contrast, inside the film, center-to-center distances and radii of the titania/PEO domains decrease rapidly in the initial stage, then decay slowly, and stay constant at the end of the printing. Thereby a defect-rich mixed FCC and BCC structure establishes in the film bulk, whereas at the film surface an FCC structure is formed. The printed films are compared with the spin-coated analogues, since today spin coating is typically more used to fabricate mesoporous titania films based on a sol-gel synthesis approach. We observe for the hybrid films as well as for the final calcined titania films a higher degree of order when using printing. During printing, the micelles have more possibility to self-assemble into better ordered structures as compared to the very rapid and highly non-equilibrium spin coating process. Thus, the large-scale deposition technique slot-die printing is beneficial for achieving better ordered mesoporous titania films, which will be of interest for the up-scale fabrication of photoanodes and provides an essential guide for morphology optimization for photovoltaic applications, like hybrid solar cells or DSSCs. Usability of the printed film is demonstrated with QDSSC devices.

8 Tailoring titania films via introducing germanium nanocrystals

This chapter is based on the published article: Tailoring ordered mesoporous titania films via introducing germanium nanocrystals for enhanced electron transfer photoanodes for photovoltaic applications (N. Li et al., Adv. Funct. Mater., 2021, 2102105, DIO: org/10.1002/adfm.202102105). Reproduced from Ref [219] with permission from JOHN WILEY AND SONS, Copyright 2021.

In chapter 5, chapter 6 and chapter 7, we pay attention to the up-scale deposition method, slot-die printing, for fabrication of mesoporous TiO_2. In this chapter, germanium nanocrystals (GeNCs) are introduced to tailor mesoporous titania (TiO_2) films for obtaining more efficient anodes for photovoltaic applications.

Nanostructured titania (TiO_2) has established its prominence in many fields, such as photocatalysis [220], lithium-ion batteries [221] and photovoltaics [130, 222]. This considerable research interest is closely related to its favorable chemical stability, wide bandgap, and large surface-to-volume ratio [10, 159]. In particular, mesoporous titania films with interconnected network structures have been successfully implemented in photovoltaic devices such as hybrid solar cells (HSCs) [1], dye-sensitized solar cells (DSSCs) [3], quantum dot-sensitized solar cells (QDSSCs) [4], and perovskite solar cells (PSCs) [5]. To date, the certified efficiency of DSSCs reached 12.3% [164], while progress in PSC development has led to an impressive efficiency of $> 20\%$ [223]. These advances strongly depended upon the development of superior sensitizers (dye molecules, quantum dots, perovskite compounds) and/or hole-transport materials. In stark contrast, far fewer studies have focused on designing and tailoring the electron-transport layer (ETL) such as titania films, to achieve better photovoltaic device performance. Since the ETL is an inherent part of the functional stack forming the final device, also its optimization will be needed for further improvements in the device performance.

Tailoring the titania ETL has the potential to impact on a variety of photovoltaic technologies because it offers important advantages that include optimized energy levels, increased charge carrier concentration, and reduced interfacial recombination [4, 224, 225]. Among the available tailoring approaches, one that is particularly promising relies on the

incorporation of (doping) metals, metal oxides, or semiconductors into the mesoporous titania. Germanium and its oxides have attracted enormous attention in this regard, partly because they have several beneficial properties: (1) Ge shows a very high electron mobility, which is higher than that of silicon [226]. (2) The optical transparency in visible and near-ultraviolet regions and the wide bandgap enable GeO_2 to be utilized like other transparent conducting oxides such as tin oxide (SnO_2) and TiO_2 [227]. (3) In the absence of water, Ge/GeO_x materials exhibit a small hysteresis behavior [226]. These advantages make Ge and its oxides interesting for the optoelectronic industry [228, 229], and thus, it is hypothesized that the introduction of them could improve the electronic (and optical) characteristics of TiO_2 for solar cell applications. Previous studies showed that adding germanium oxide to TiO_2 anodes provided an alternative approach to enhance DSSC efficiency [7, 230]. Duan et al. designed TiO_2/GeO_2 nanocrystallite anodes to enhance the interference light intensity, consequently increasing the electron density [7]. Simultaneously, attention was paid to TiO_2-Ge composites for their potential application in photovoltaics [231–233]. The photoconductivity of TiO_2-Ge films suggested that the nanocomposite can be an ideal photovoltaic semiconductor [231]. Ahmad et al. also reported that the nanocomposite TiO_2 with 2 wt% Ge nanoparticles showed improved electron transfer ability compared to pristine TiO_2 nanoparticles [232].

To date, so-called diblock-copolymer (DBC)-assisted sol-gel synthesis has proven to be a favorable route to establish titania nanostructures in a controlled fashion [110, 234]. The general sol-gel approach provides a facile solution deposition route that is readily compatible with a variety of film deposition processes ranging from laboratory-scale coating like spin coating [61] to industrial-scale coating like spray coating [195] and slot-die printing [110]. Sol-gel methods also facilitate the dopant incorporation and the resulting doped-films can possess uniform morphology with continuous and pinhole-free structures [20]. With the utilization of a DBC, which acts as a structure-directing template, a large variety of nanostructures can be achieved by self-assembly [235]. In our study, due to the surface functionalization, the GeNCs maintain their solubility in solvents and have a preferential selectivity to a specified block of a DBC [111, 236]. In addition, due to effects like steric hindrance, the possibility of forming big germanium nanocrystal (GeNC) agglomerates can be mitigated by the DBC matrix [236]. These factors contribute to the exquisite tailoring of the mesoporous TiO_2 nanostructures by introducing GeNCs in combination with the metal oxide precursor.

In this chapter, we report a new approach that combines dodecyl functionalized GeNCs of 7-9 nm average sizes with the sol-gel chemistry and affords ordered mesoporous TiO_2/GeO_x films. In doing so, we have succeeded in improving the electronic characteristics, such

as the electron transfer mobility and hysteresis behavior of PSCs, via introducing GeNCs in TiO_2 photoanodes [226].

GeNCs are added to the titania sol-gel reaction mixture in a series of pre-defined GeNCs:TiO_2 weight ratios. The sol-gel reaction mixture consists of an amphiphilic DBC template polystyrene-block-polyethylene oxide (PS-b-PEO) and a titania precursor titanium(IV)isopropoxide (TTIP). Thermal annealing in air removes the PS-b-PEO template and the aliphatic surface functionalities on the GeNC surfaces; this process yields mesoporous TiO_2/GeO_x nanostructures. For comparison and also to obtain a purer Ge phase, argon atmosphere-annealed nanocomposite films are also prepared. The resulting surface and inner morphologies are investigated via scanning electron microscopy (SEM) and grazing incidence small-angle X-ray scattering (GISAXS), respectively. The crystalline properties and elemental composition of the nanocomposite films are probed by transmission electron microscopy (TEM), and X-ray photoelectron spectroscopy (XPS), respectively. The optical properties are observed via ultraviolet-visible spectroscopy (UV-Vis). Irrespective of the GeNC addition, the air-annealed nanocomposite films possess ordered mesoporous morphologies, high crystallinity, and good transparency, which appear highly promising for solar cell applications. By comparison, the Ge richer phase obtained from films annealed in argon atmosphere are less promising because they show lower transmittance. In this context, we focus on the air-annealed nanocomposite films concerning use in photovoltaics and explore their application as photoanodes in PSCs. To better understand the photovoltaic characteristics of the air-annealed nanocomposite films, we choose to investigate their charge carrier dynamics and find that introducing GeNCs can boost the electron transfer from the perovskite layer to the ETL, which contributes to an increased short-circuit photocurrent density (J_{sc}), thus achieving an enhanced power conversion efficiency (PCE). Simultaneously, the addition of GeNCs can strongly suppress the hysteresis of the PSCs. This knowledge is of great significance for tailoring the mesoporous TiO_2 films for efficient photoanodes and is expected to be useful in other solar cell systems as well, such as for example DSSCs.

8.1 Tailoring titania morphology via introducing GeNCs

To investigate the influence of pre-synthesized GeNCs on the morphology of mesoporous TiO_2 films, we prepare five films containing pre-defined weight contents of GeNCs (wt% GeNCs in TiO_2 of 0, 0.5, 1.0, 2.5 and 5.0; samples are denoted as 0 wt% GeNCs, 0.5 wt% GeNCs, 1.0 wt% GeNCs, 2.5 wt% GeNCs and 5.0 wt% GeNCs, respectively) via a DBC-assisted sol-gel method. After spin coating (2000 rpm for 60 s), the hybrid

TiO_2/GeNC/PS-b-PEO films are thermally annealed at 500 °C in air or argon atmosphere for 2 hours.

8.1.1 Surface morphology

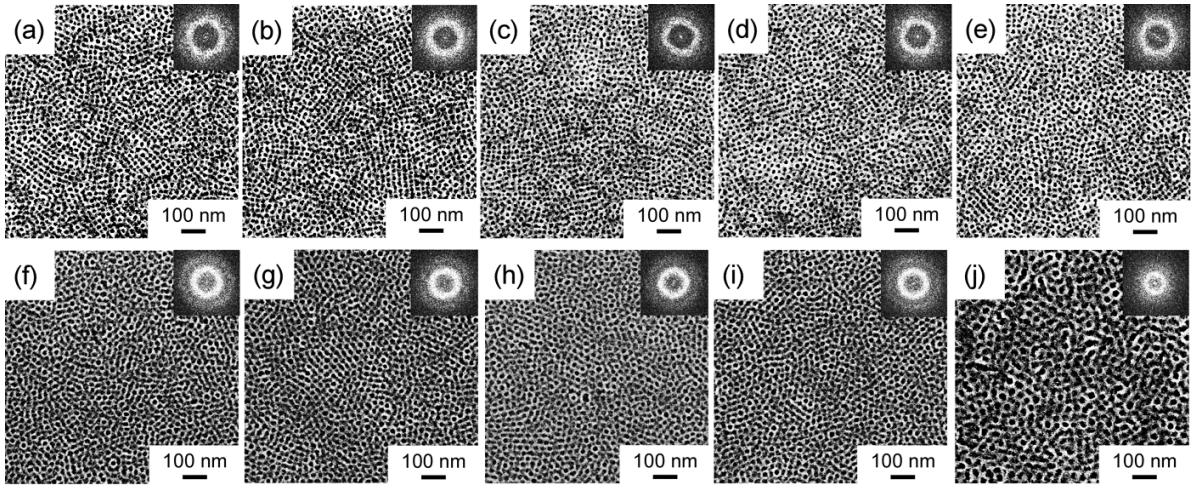

Figure 8.1: Top-view secondary electron SEM images of the TiO_2/GeNC films after thermal annealing at 500 °C in air: (a) 0 wt%, (b) 0.5 wt%, (c) 1.0 wt%, (d) 2.5 wt%, and (e) 5.0 wt% GeNCs, or in argon atmosphere: (f) 0 wt%, (g) 0.5 wt%, (h) 1.0 wt%, (i) 2.5 wt%, and (j) 5.0 wt% GeNCs. Insets show corresponding 2D-FFT patterns. Reproduced from Ref [219] with permission from JOHN WILEY AND SONS, Copyright 2021.

Figure 8.1 shows representative secondary electron SEM images of the TiO_2/GeNC film surfaces after thermal annealing in air or argon atmosphere. All air-annealed TiO_2/GeNC films display similar well-defined sponge-like nanostructures (i.e., a mesoporous structure with an interconnected network, Figure 8.1a-e), which indicates that the addition of GeNCs does not influence the overall film surface morphologies. Close inspection reveals hexagonal and square mesopore packings on the film surfaces that are similar to what has been previously reported for the surface structure of TiO_2/PS-b-PEO hybrid films [188]. To further evaluate the degree of structural order in the present films, two-dimensional fast Fourier transform (2D-FFT) patterns are calculated from the respective SEM images and shown as insets in Figure 8.1a-e. A first-order ring is seen in the 2D-FFT of the 0 wt% GeNCs film consistent with the presence of a well-defined nearest-neighbor ordering of the nanostructures. Importantly, the degree of order is not deteriorated by adding the GeNCs. The related power spectral density (PSD) functions (Figure 8.2a) display a similar q value for the position of the correlation peak for all TiO_2/GeNC films (gray dashed line). It suggests that irrespective of the amount of GeNCs, the average center-

to-center distances of the nanostructures have a value of 23.0 ± 0.5 nm in the case of the TiO_2/GeNC films annealed in air. In contrast to the air-annealed films, the morphologies and 2D-FFT patterns of the argon atmosphere-annealed films (see Figure 8.1f-i) change at 5.0 wt% GeNCs. Only at lower GeNC concentrations (0 to 2.5 wt%) the morphologies and characteristic center-to-center distances of the nanostructures remain unchanged. At 5.0 wt% GeNCs the surface morphology is changed (Figure 8.1j) and shows a reduced degree of order as seen from the 2D-FFT pattern and PSD functions (Figure 8.2b). Thus, the higher GeNC loading starts to perturb the DBC-templating and thereby deteriorates the structure regularity when films are processed using argon atmosphere annealing [201].

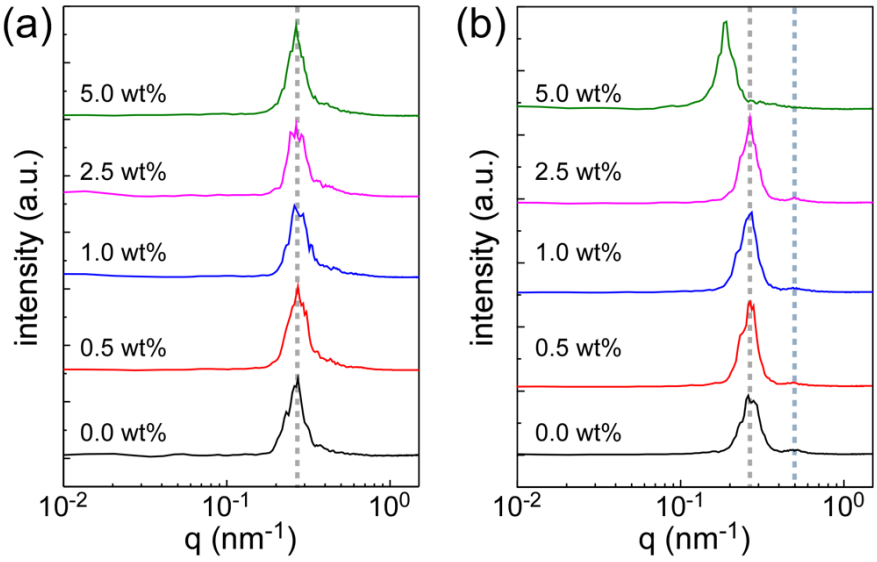

Figure 8.2: PSD functions extracted from the surface SEM images of the TiO_2/GeNC films after thermal annealing at 500 °C in (a) air and (b) argon atmosphere for films with 0 wt% GeNCs, 0.5 wt% GeNCs, 1.0 wt% GeNCs, 2.5 wt% GeNCs and 5.0 wt% GeNCs from bottom to top. The gray dashed lines indicate the position of the correlation peak. In the case of argon atmosphere annealing a second-order peak is also indicated. Reproduced from Ref [219] with permission from JOHN WILEY AND SONS, Copyright 2021.

All samples possess mesoporous structures with an interconnected network suggesting the annealing atmospheres play a minor role in the formation of a porous sponge-like morphology. In addition, the TiO_2/GeNC films annealed in air have a smaller average nanoparticle size than that in argon atmosphere, which agrees well with the observation reported elsewhere [237].

8.1.2 Inner morphology

In addition to the surface morphologies, the buried structures of the present films are of importance because they directly influence charge carrier transport and the final device performance [140]. To gain additional insight into the nature of the internal morphologies of the films in terms of characteristic structures like center-to-center distances and radii of the TiO_2/GeO_x domains, GISAXS measurements are performed.

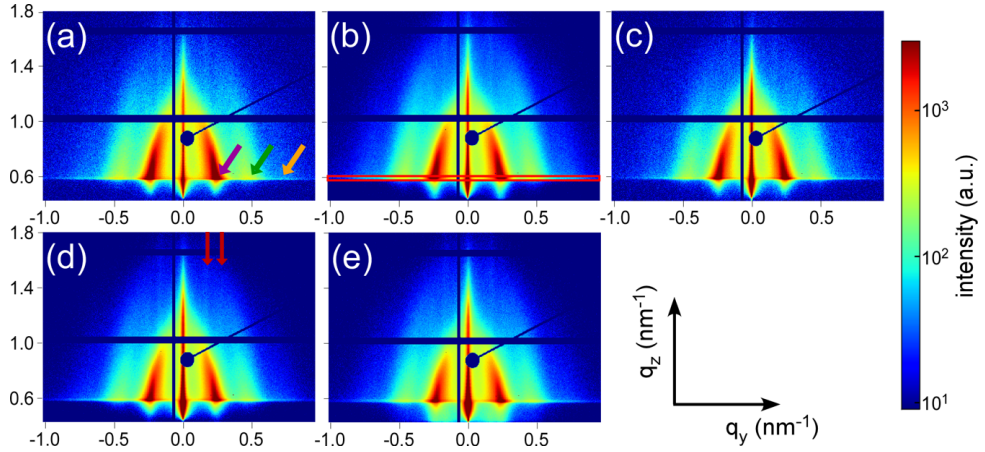

Figure 8.3: 2D GISAXS data of the TiO_2/GeNC films after thermal annealing at 500 °C in air: (a) 0 wt%, (b) 0.5 wt%, (c) 1.0 wt%, (d) 2.5 wt% and (e) 5.0 wt% GeNCs. Colored arrows denote Bragg peaks caused by the highly ordered inner structures: 1st-order (magenta), 2nd-order (green), and 3rd-order (orange). The two red arrows highlight a rod-like Bragg peak and its second-order peak, originating from the surface structures. Reproduced from Ref [219] with permission from JOHN WILEY AND SONS, Copyright 2021.

From the 2D GISAXS data of the TiO_2/GeNC films after thermal annealing in air (Figure 8.3) all samples show a prominent Bragg peak (Figure 8.3a; magenta arrow) in the GISAXS data together with its second-order and weak third-order peaks (Figure 8.3a; green and orange arrows, respectively). The occurrence of higher-order peaks reveals the presence of well-ordered nanostructures within the films. Simultaneously, the observation of a third-order peak, even at higher GeNC contents, suggests that the addition of GeNCs is not accompanied by a loss internal structural order. Moreover, two sharp rod-like Bragg peaks (Figure 8.3d; red arrows) located at $q_y \approx 0.17$ and 0.28 nm^{-1} are observed that originate from the scattering signal of the surface ordered nanostructures [188]. The ratio of the q_y values is 1.65 (close to $\sqrt{3}/1$), which suggests the TiO_2/GeO_x nanoparticles are predominantly hexagonally packed on the film surfaces [188].

To get further insight into the influence of GeNC addition on the internal nanostructure of the presented films, horizontal line cuts of the 2D GISAXS data are made at the Yoneda

peak position of TiO_2/GeO_x (Figure 8.3b; red box). To extract the lateral structure characteristics line cuts are modeled within the framework of the distorted wave Born approximation (DWBA) together with the effective interface approximation (EIA) and the local monodisperse approximation (LMA) [92, 147–149]. Cylinder form factors have been successfully used to model the nanostructures in mesoporous films in the literature [158, 238], and thus are applied in the present data analysis.

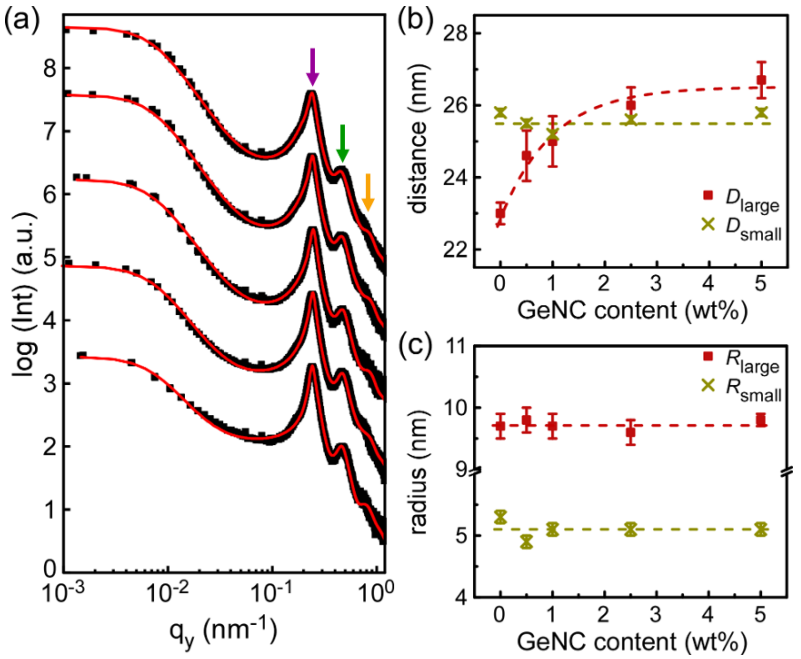

Figure 8.4: (a) Horizontal line cuts of the 2D GISAXS data of the TiO2/GeNC films after thermal annealing at 500 °C in air: 0 wt%, 0.5 wt%, 1.0 wt%, 2.5 wt% and 5.0 wt% GeNCs from bottom to top. Colored arrows highlight peaks arising from the highly ordered inner structures: 1st-order (magenta), 2nd-order (green), and 3rd-order (orange). Extracted characteristic length scales: (b) Center-to-center distances and (c) nanoparticle radii as a function of GeNC content. Olive crosses indicate the small-sized structures, red squares the large-sized structures. The dashed lines are provided as a guide to the eye. Reproduced from Ref [219] with permission from JOHN WILEY AND SONS, Copyright 2021.

The horizontal line cuts and modeling results for the air-annealed films are shown in Figure 8.4a. The strong Bragg peak (magenta arrow) and its two weaker higher-order peaks (green and orange arrows) are evident in all profiles. These features emphasize long-range lateral correlations in the highly-ordered inner nanostructures. Two characteristic center-to-center distances (structure factors) and radii (form factors) are extracted from the GISAXS modeling and plotted as a function of GeNC content in Figure 8.4b and Figure 8.4c. The small-sized structures (i.e., Figure 8.4; olive crosses) exhibit similar

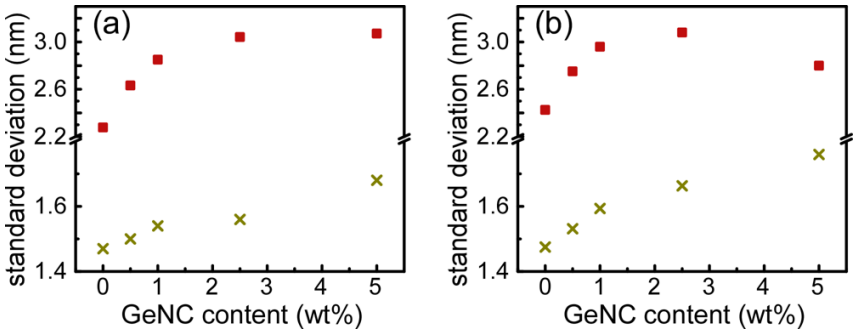

Figure 8.5: Standard deviation of the center-to-center distances for the small-sized structures (olive crosses) and the large-sized structures (red squares) in the case of (a) air-annealed and (b) argon atmosphere-annealed films as a function of GeNC content. Reproduced from Ref [219] with permission from JOHN WILEY AND SONS, Copyright 2021.

nanoparticle radii and center-to-center distances (within error bars) in all films, irrespective of the GeNC content. For example, the pristine mesoporous TiO_2 film has nanoparticle radii and corresponding center-to-center distances of (5.3 ± 0.1) nm and (25.8 ± 0.1) nm, respectively. Compared with the large-sized structures (i.e., Figure 8.4; red squares), the size distribution of the center-to-center distances is narrower for the small-sized structures (Figure 8.5). Thus, the small-sized structures are more ordered compared to their larger counterparts. However, their size distribution broadens with increasing GeNC content as seen in Figure 8.5a (olive crosses). From this, we conclude that, not surprisingly, introducing GeNCs worsens the degree of order. A different tendency is observed for the

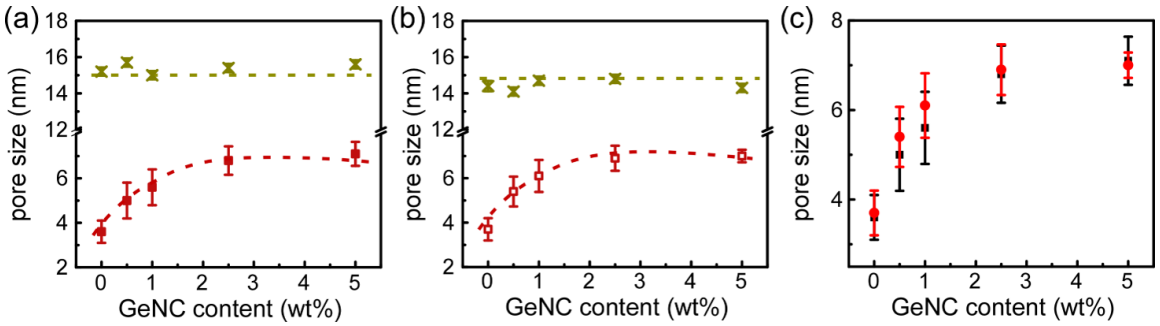

Figure 8.6: Pore sizes for the small-sized structures (olive crosses) and the large-sized structures (red squares) in the case of (a) air-annealed and (b) argon atmosphere-annealed films as a function of GeNC content. (c) A comparison of the pore sizes for the large-sized structures in air-annealed (black squares) and argon atmosphere-annealed (red circles) films. The dashed lines in (a) and (b) are guides to the eyes. Reproduced from Ref [219] with permission from JOHN WILEY AND SONS, Copyright 2021.

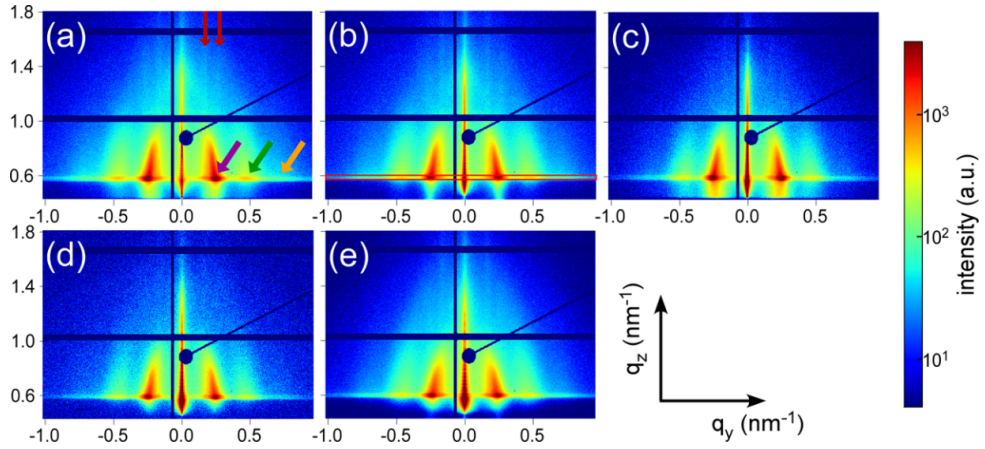

Figure 8.7: 2D GISAXS data of the TiO_2/GeNC films after thermal annealing at 500 °C in argon atmosphere: (a) 0 wt% GeNCs, (b) 0.5 wt% GeNCs, (c) 1.0 wt% GeNCs, (d) 2.5 wt% GeNCs and (e) 5.0 wt% GeNCs. Arrows with different colors indicate the Bragg peaks caused by the highly ordered inner structures: first-order (magenta), second-order (green), and third-order (orange). The red arrows indicate a rod-like Bragg peak and its second-order peak, originating from the film surface. Reproduced from Ref [219] with permission from JOHN WILEY AND SONS, Copyright 2021.

large-sized structures. The corresponding radii (within error bars) again do not change with GeNC addition, but the center-to-center distances (within error bars) increase with increasing GeNC contents. The radii of the large-sized structures for the 0 wt%, 0.5 wt%, 1.0 wt%, 2.5 wt% and 5.0 wt% GeNCs are (9.7 ± 0.2), (9.8 ± 0.2), (9.7 ± 0.2), (9.6 ± 0.2), (9.8 ± 0.1) nm, and the corresponding center-to-center distances are (23 ± 0.3), (24.6 ± 0.7), (25 ± 0.7), (26 ± 0.5), (26.7 ± 0.5) nm. Since the hydrophobic dodecyl chains cause the GeNCs to be preferentially incorporated inside the PS domains of the templating polymer, adding GeNCs expands the PS domains resulting in larger center-to-center distances. We also note a broader size distribution in the center-to-center distances with increasing GeNC contents (Figure 8.5a; red squares). This increase in the interdomain distance and distribution width is similar to the DBC templating of magnetic nanoparticles reported previously [201, 239].

The average pore sizes may be approximated by [110]: Pore size = center-to-center distance – 2 × particle radius. For air-annealed and argon annealed films we find that the pore sizes originating from small-sized structures are independent of GeNC content (Figure 8.6a and Figure 8.6b; olive crosses). In contrast, the average pore sizes of the large-sized structures show a slight dependence on the GeNC content with the largest value reached in the 2.5 wt% GeNCs films (Figure 8.6).

Applying the same analysis to the data of the argon atmosphere-annealed nanocom-

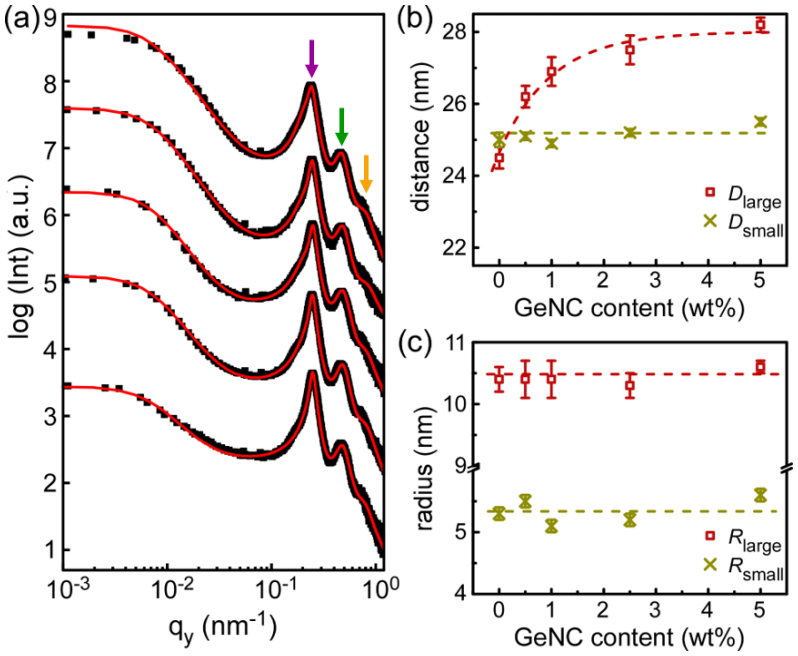

Figure 8.8: Horizontal line cuts of the 2D GISAXS data of the TiO_2/GeNC films after thermal annealing at 500 °C in argon atmosphere: 0 wt% GeNCs, 0.5 wt% GeNCs, 1.0 wt% GeNCs, 2.5 wt% GeNCs and 5.0 wt% GeNCs from bottom to top. Arrows with different colors highlight the peaks caused by the highly ordered inner structures: first-order (magenta), second-order (green), and third-order (orange). Extracted characteristic length scales: (b) Center-to-center distances and (c) nanoparticle radii as a function of GeNC contents. Olive crosses indicate the small-sized structures and red squares indicate the large-sized structures. The dashed lines are a guide to the eye. Reproduced from Ref [219] with permission from JOHN WILEY AND SONS, Copyright 2021.

posite films (Figure 8.7), horizontal line cuts are analyzed (Figure 8.8a) and the corresponding extracted center-to-center distances and radii are determined (Figure 8.8b and Figure 8.8c). In general, the small-sized and large-sized nanostructures show the same general trends as observed for air-annealing. However, when comparing directly, the argon atmosphere-annealed films exhibit larger nanoparticle radii.

To illustrate the influence of GeNC addition on the titania morphology, an illustration of the evolution of the titania-DBC films with incorporated GeNCs is sketched in Figure 8.9. With a so-called good-bad solvent pair, the PS-b-PEO diblock copolymer undergoes a micro-phase separation and self-assembles into spherical micelles [124, 240]. The titania precursor TTIP prefers being coordinated with the PEO domains through hydrogen bonds, while GeNCs favor the PS domains due to the dodecyl surface functionalization (Figure 8.9a). At low concentrations (i.e., $\leq$ 5 wt%), GeNCs are expected to

reside within the PS domains (Figure 8.9b) and cause the PS domains to expand. This expansion results in an increased center-to-center distance. During thermal annealing in air (or argon atmosphere), TiO_2 crystallizes, GeO_x is forming (details are explained below), together with the removal of the organic chains. Due to the applied high-temperature heating, the neighboring nanoparticles fuse into larger ones [241]. The identified size of the GeO_x nanoparticles from high-resolution TEM (HRTEM) of around 10 nm (Figure 8.10), agrees well with the initial GeNC sizes of 7-9 nm [111] and matches well with twice the small-sized radii found in GISAXS (e.g. Figure 8.4c). In addition, it is reasonable to assume that the GeO_x nanoparticles will also fuse to the neighboring TiO_2, and thus develop into larger sizes (more than 10 nm), as referred to the large-sized structures in the GISAXS analysis. Therefore, we observe that the center-to-center distances of the large-sized structures increase, while the majority of the inner morphologies, namely the small-sized structures, remains unchanged due to the absence of GeNC incorporation (Figure 8.9c).

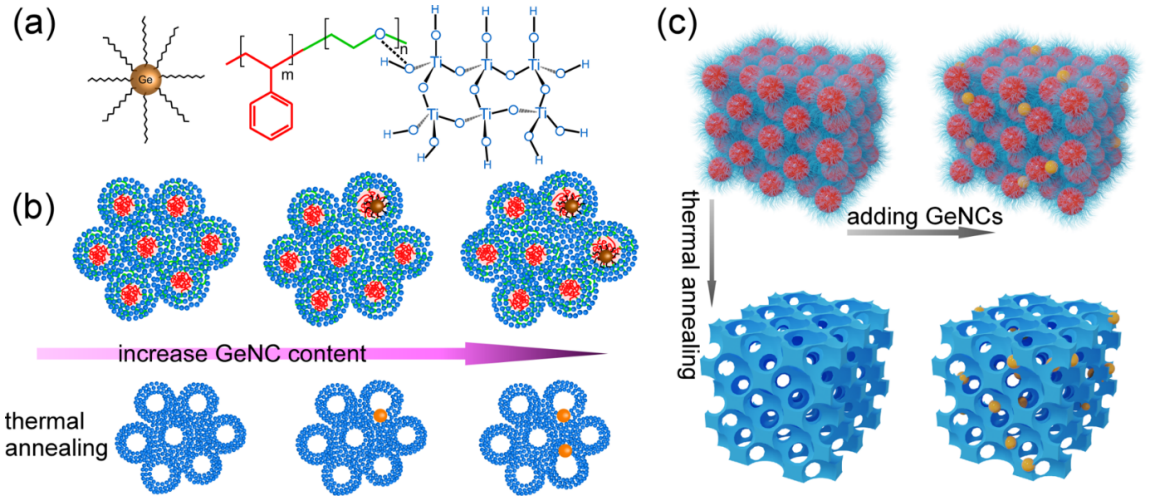

Figure 8.9: Illustrations of (a) dodecyl-capped GeNCs, PS-b-PEO diblock copolymer, titania precursor (blue) and hydrogen bonding interaction between the titania precursor and the PEO block, (b) nanostructure evolution of the TiO_2/PS-b-PEO films with GeNC concentration before and after thermal annealing. (c) A 3D representation of the TiO_2/PS-b-PEO film with and without GeNCs after thermal annealing. In both (b) and (c), hydrolyzed titania nanoparticles are indicated by blue, the PS domains indicated by red, and GeNCs indicated by brown. After thermal annealing, the polymer is removed in (c) and mesoporous crystallized TiO_2 (blue) with or without GeO_x nanoparticles (orange) form. Reproduced from Ref [219] with permission from JOHN WILEY AND SONS, Copyright 2021.

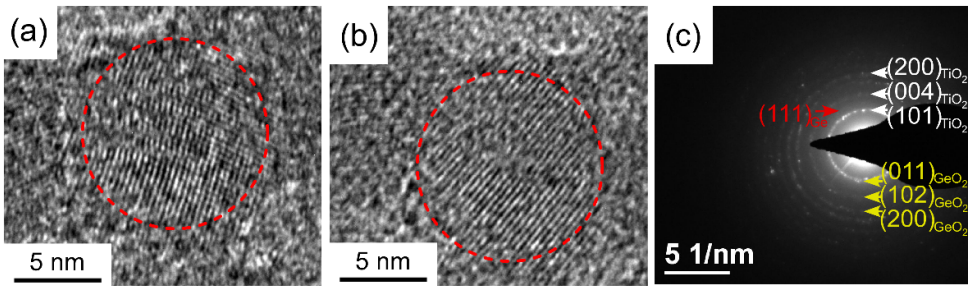

Figure 8.10: (a), (b) Examples of HRTEM images of TiO_2/GeNC film with 5.0 wt% GeNCs after thermal annealing. (c) SAED pattern of the TiO_2/GeNC film with 5.0 wt% GeNCs after thermal annealing in argon atmosphere. Reproduced from Ref [219] with permission from JOHN WILEY AND SONS, Copyright 2021.

8.2 Crystallinity

XRD and TEM are used to identify the crystal phase and crystallinity of the nanocomposite films, since these key parameters play a critical role in the photogenerated charge carrier transport. All diffraction patterns are consistent with the anatase titania phase (PCPDS 21-1272) with its pronounced (101) and (004) diffraction peaks [107] (Figure 8.11a and Figure 8.11b). The crystallite sizes are estimated from the TiO_2 (101) peak via the Scherrer equation, analyzing the XRD line broadening. The crystallite sizes for the 0 wt%, 0.5 wt%, 1.0 wt%, 2.5 wt% and 5.0 wt% GeNCs (annealed in air) almost remain constant within the error bars (7.4 ± 0.3, 7.5 ± 0.3, 7.1 ± 0.3, 7.4 ± 0.3, 7.3 ± 0.3 nm, respectively). A similar tendency is seen in the GISAXS study of the characteristic nanoparticle radii of the air-annealed films. Small differences in the absolute numbers show that not the entire nanoparticles are crystalline. Because of the very low GeNC content, it is difficult to analyze the crystal structure of the GeNCs in the composite films after thermal annealing. Thus, the nanocomposite films with the highest GeNC content (i.e., 5.0 wt%) are further evaluated using TEM. The selected area electron diffraction (SAED) data of the film after annealing in air (Figure 8.12a) presents a series of diffraction rings corresponding to crystallites of the anatase TiO_2 phase and hexagonal GeO_2 (JCPDS 85-0473) [242]. In addition, a diamond cubic Ge phase is detected [243], which is in agreement with the findings from Ge-based thin films prepared via a sol-gel synthesis [244]. From the center to the exterior region, the first three rings of the anatase TiO_2 phase correspond to reflections from the (101), (004) and (200) planes, and the first three rings of the GeO_2 phase correspond to reflections from the (011), (102) and (200) planes [188, 242]. In the case of the Ge phase, only the (111) reflection is observed. The related HRTEM images (Figure 8.12b-d) display well-resolved lattice spacings of 0.351,

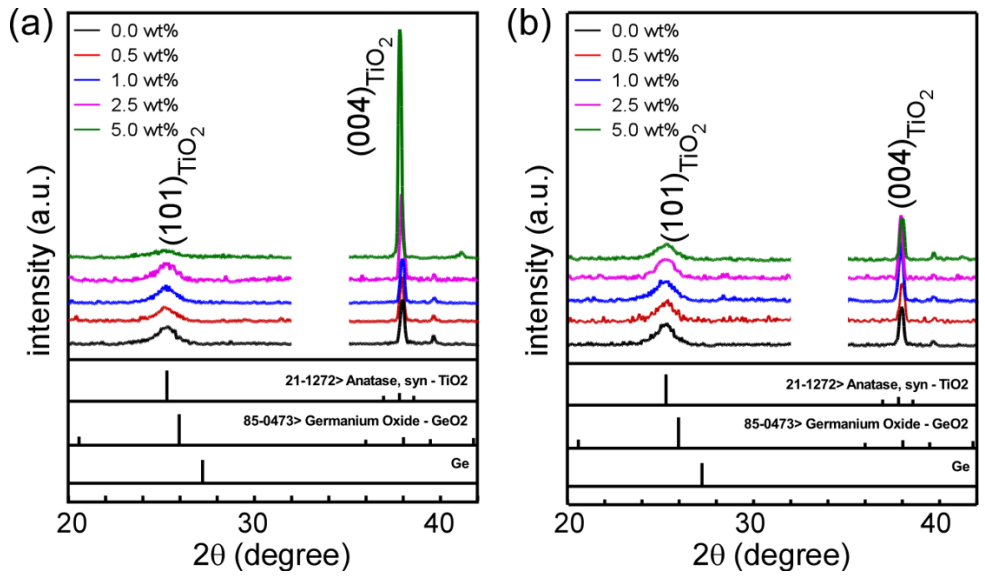

Figure 8.11: XRD patterns of the TiO_2/GeNC films with different GeNC content as indicated after thermal annealing in (a) air and (b) argon atmosphere. The curves are shifted along the y axis for clarity of the presentation and the angular range from 32°to 35°is blocked to avoid the strong Bragg peak of the Si substrate. As a reference, the diffraction peaks from anatase TiO_2, GeO_2 and a diamond cubic Ge phase are indicated at the bottom. Reproduced from Ref [219] with permission from JOHN WILEY AND SONS, Copyright 2021.

0.342, and 0.320 nm, being consistent with the lattice spacing of TiO_2 (101) [188], as well as GeO_2 (011) [242], and Ge (111) planes [243, 244], respectively.

The same results are obtained in the HRTEM images of the argon atmosphere-annealed 5.0 wt% GeNCs film (Figure 8.12e and Figure 8.12f). Evidence for GeO_2 remains, even though its formation is hindered due to the oxygen-poor environment. An explanation for this observation is that the titania precursor and the PEO blocks could deliver oxygen to the system [244]. In addition, one must also consider that the GeNCs themselves could contribute some oxide impurities [111, 243]. The absence of GeO in the TEM measurements for both samples can be explained by the poor crystallinity of GeO [245].

8.3 Chemical composition

To get insight into the elemental composition and speciation of the presented nanocomposite films, we use XPS. This technique is intrinsically surface-sensitive and thus delivers information on the outermost layer of the films (typically < 10 nm below the surface). Figure 8.13a shows the normalized Ge 2p3/2 spectra of the TiO_2/GeNC films after annealing under the indicated conditions. For the TiO_2/GeNC films annealed in air (2.5 and

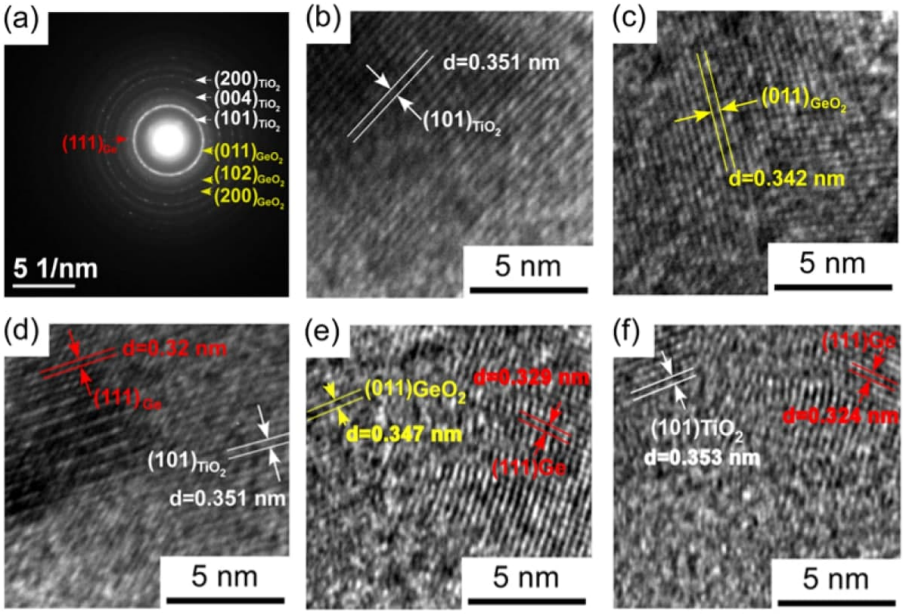

Figure 8.12: (a) SAED pattern and (b-d) HRTEM images of the TiO_2/GeNC film with 5.0 wt% GeNCs after thermal annealing in air, (e) and (f) HRTEM images of a representative TiO_2/GeNC film containing 5.0 wt% GeNCs after thermal annealing in argon atmosphere. Reproduced from Ref [219] with permission from JOHN WILEY AND SONS, Copyright 2021.

5.0 wt% GeNCs), the Ge 2p3/2 core-level emission is shifted to higher binding energies compared to the spectral features of the 5.0 wt% GeNCs films annealed in argon atmosphere. This observation is consistent with more elemental (or incompletely oxidized) Ge being present in the argon atmosphere-annealed films. All XPS spectra are fitted with Gaussian functions after subtraction of a Shirley-type background (Figure 8.13b-d). The spectral component located at a binding energy of ca. 1217.3 eV (green) is associated with elemental Ge, while those at ca. 1218.9 eV (magenta) and ca. 1220.0 eV (red) are attributed to GeO and GeO_2, respectively [246, 247]. Thus, Ge, GeO_2, as well as GeO are present in the nanocomposite films. The presence of GeO can be rationalized by considering that the reversible reaction ($2GeO \longleftrightarrow GeO_2 + Ge$) might happen during thermal annealing at 500 °C [248, 249], in addition to the oxygen deficiency of the argon atmosphere annealing environment. The binding energy positions of individual components are the same in both, the air- and argon atmosphere-annealed films. In the former, the total spectral intensity for the 2.5 wt% GeNCs film is approximately half of that in the 5.0 wt% GeNCs. This intensity ratio is reasonably expected, given the GeNC concentration ratio. Note that the 5.0 wt% GeNCs film annealed in argon atmosphere shows a lower

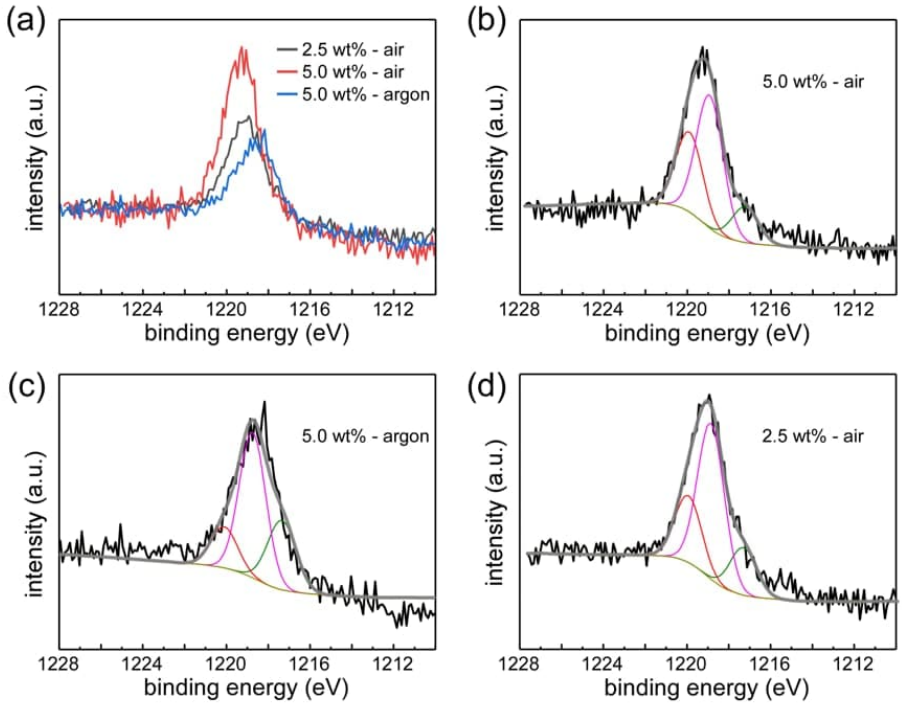

Figure 8.13: Fits of Ge 2p3/2 core-level spectra of the TiO_2/GeNC films after thermal annealing in air: (a) 2.5 wt%, (b) 5.0 wt% GeNCs, and in an argon atmosphere: (c) 5.0 wt% GeNCs. The spectrum is fitted with three Gaussian functions (green, magenta and red) superimposed on a Shirley background (olive). Reproduced from Ref [219] with permission from JOHN WILEY AND SONS, Copyright 2021.

spectra intensity as compared to the air-annealed analogue (Figure 8.13a), which might arise from its unique surface morphology [250], as seen in Figure 8.1j.

8.4 Optical properties

To examine the optical transmittance of the present nanocomposite films in dependence of the GeNC content, the films are deposited on glass substrates. The sharp decrease observed in all transmittance spectra (Figure 8.14) in the 280-350 nm range is related to the optical absorption of the materials. Irrespective of the GeNC content, all air-annealed films exhibit near 100% transparency in the visible spectra region (Figure 8.14a). In contrast, the transmittance of films annealed in an argon atmosphere is reduced, although it remains above 90% in all cases (Figure 8.14b). A reasonable explanation for this lower transmittance is films annealed in argon atmosphere exhibit larger average grain sizes that are known to lead to decreased transmittance [35].

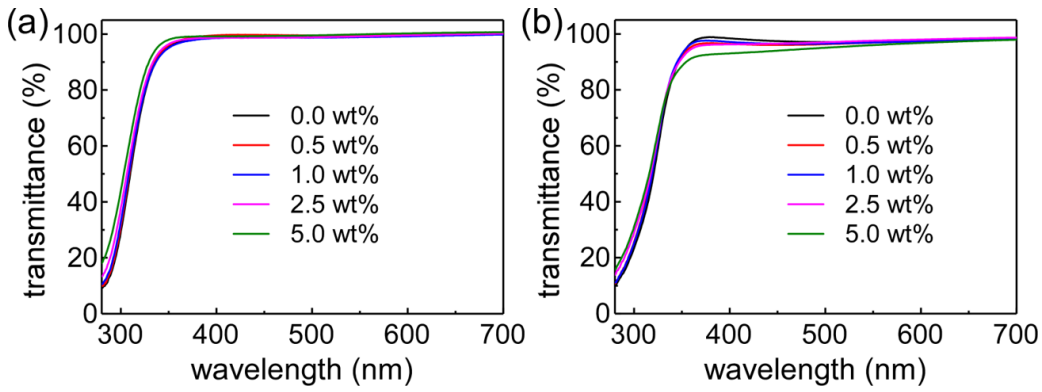

Figure 8.14: Transmittance spectra of the TiO_2/GeNC films containing indicated GeNC contents after thermal annealing in (a) air and (b) argon atmosphere. The glass substrate is used as a reference sample for the transmission measurement. Reproduced from Ref [219] with permission from JOHN WILEY AND SONS, Copyright 2021.

The optical band gap of the synthesized nanocomposite films are estimated using the Tauc equation

$$\alpha h\upsilon = A(h\upsilon - E_g)^n \tag{8.1}$$

in which A is a constant, α is the absorption coefficient of the material, hυ is the photon energy, E_g is the optical band gap and n = 2 for the indirect transition. Figure 8.15 shows the plots of $(\alpha h\upsilon)^{1/2}$ as a function of photon energy for both types of nanocomposite films (air-annealed and argon atmosphere-annealed). The corresponding linear fits (dash

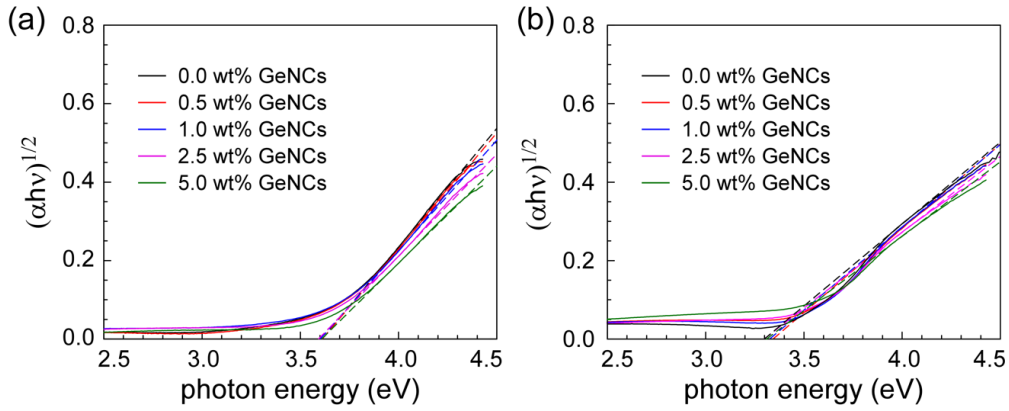

Figure 8.15: Tauc plots of $(\alpha h\upsilon)^{1/2}$ as a function of the photon energy of the TiO_2/GeNC films with different GeNC content as indicated after thermal annealing in (a) air and (b) argon atmosphere. Reproduced from Ref [219] with permission from JOHN WILEY AND SONS, Copyright 2021.

lines) at the adsorption edge give the estimated band gaps for these composite films. Air-annealed and argon atmosphere-annealed films containing GeNCs show a similar band gap as their pristine mesoporous TiO_2, with values agreeing to that reported for mesoporous TiO_2 ($\sim$ 3.4 eV) [37]. Thus, introducing GeNCs in the amount studied here does not significantly impact on the band gap energy. Compared to the air-annealed films ($\sim$ 3.59 eV), however, the argon atmosphere-annealed films display a lower band gap ($\sim$ 3.32 eV). This difference can be explained by the different nanoscale morphology, since with increasing grain sizes the optical band gap shifts to lower energy due to smaller quantum confinement effect [35]. The larger band gap energy estimated for all mesoporous nanostructured films in comparison with the nonporous anatase TiO_2 ($\sim$ 3.2 eV) [36] has been previously reported in other TiO_2 nanomaterials such as nanotube arrays, which might originate from weak quantum confinement effects in TiO_2 nanocrystals with sizes smaller than 10 nm [37].

8.5 Charge carrier dynamics and PSC performance

We further investigate the charge carrier dynamics of the air-annealed films and fabricate perovskite solar cells based on them (Figure 8.16a). The PSC fabrication follows a standard methodology that focuses on realizing identical devices [114], which differ only in the ETL (air-annealed TiO_2-GeNC films). To study charge carrier dynamics in air-annealed nanocomposite films, the perovskite is coated on the ETL of choice. A compacted TiO_2 layer coated on FTO/glass is used as the substrate to maintain the same functional stack as in the PSC device architecture (Figure 8.16d). Compared with the pristine TiO_2 film, marked photoluminescence (PL) quenching is observed in the FTO/compact TiO_2/mesoporous TiO_2-GeNC/perovskite systems (Figure 8.16e), indicating that the electron mobility of the ETLs is enhanced by the introduction of GeNCs. Accordingly, we employ these ETLs in the PSC fabrication. The PSC devices using a pristine TiO_2 anode show the well-known hysteresis behavior in the JV-characteristics (Figure 8.16b), in which the reverse scan shows higher performance than that of the forward scan [251]. In contrast, with the addition of 5.0 wt% GeNCs to the composite film used as the ETL, the hysteresis phenomena are strongly suppressed (Figure 8.16b). Moreover, the addition of GeNCs enhances the J_{sc} (Figure 8.17b), thereby improving the PCE (Figure 8.17a) of the devices. The similar open-circuit voltages (V_{oc}, Figure 8.17c) of the PSCs demonstrate that the energy levels between the ETLs and the perovskite layer remain unchanged [252], because the bandgap of the mesoporous titania films used as the ETLs is not tuned by the GeNCs addition (Figure 8.15). The highest J_{sc} and PCE values are observed in the case of the 2.5 wt% GeNCs films, which might be attributed to the presence of the largest

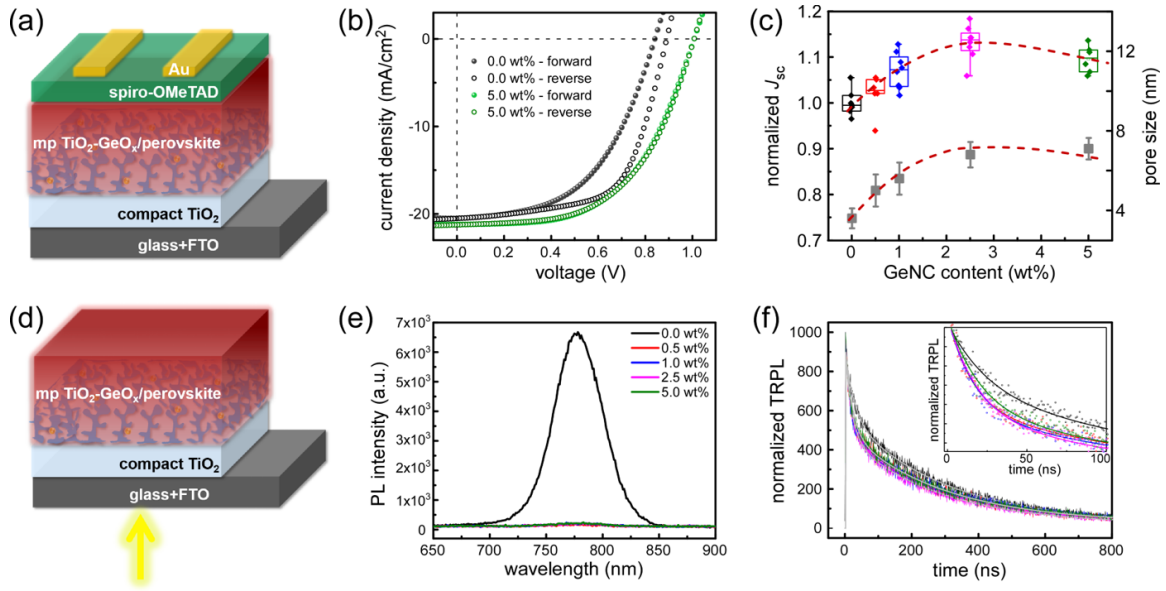

Figure 8.16: Pictorial representation of (a) full PSC device using the investigated ETL layers and (d) respective partial functional stack for steady-state PL and TRPL measurements. (b) Hysteresis behavior in the J-V measurements of PSCs based on the 0.0 wt% (black) and 5.0 wt% GeNCs (green) films. (c) Normalized Jsc values and pore sizes of the large-sized structures (gray squares) as a function of GeNC content. The dashed lines are guides to the eyes. (e) Steady-state PL and (f) TRPL spectra (symbols) with corresponding fits (solid lines) of the TiO_2/GeNC films for different GeNC content after thermal annealing in air. The inset panel in (f) focuses on the spectra within 0-100 ns. Different colors indicate different ETLs: 0.0 wt% GeNCs (black), 0.5 wt% GeNCs (red), 1.0 wt% GeNCs (blue), 2.5 wt% GeNCs (magenta), 5.0 wt% GeNCs (green). Reproduced from Ref [219] with permission from JOHN WILEY AND SONS, Copyright 2021.

pores in these films (as exemplarily highlighted in Figure 8.16c). Larger pores can allow a better infiltration of the perovskite, and a more efficient contact between the mesoporous ETL and perovskite [253]. These improvements can enhance the electron injection from the perovskite into the ETL [253].

To understand the charge carrier separation at the ETL/perovskite interface, we perform time-resolved PL (TRPL) measurements on perovskite deposited on the different ETLs. The TRPL curves are fitted with a two-phase exponential decay function [254], and the corresponding fits are plotted as solid lines in Figure 8.16f. The extracted lifetimes and amplitude fractions are summarized in Figure 8.18. Compared with the pristine film, the charge carrier lifetime is decreased for the composites. Moreover, 1.0 wt% and 2.5 wt% GeNCs samples exhibit clear larger proportions of the fast component, which could indicate a better energy transfer configuration [255]. We deduce that the charge carriers

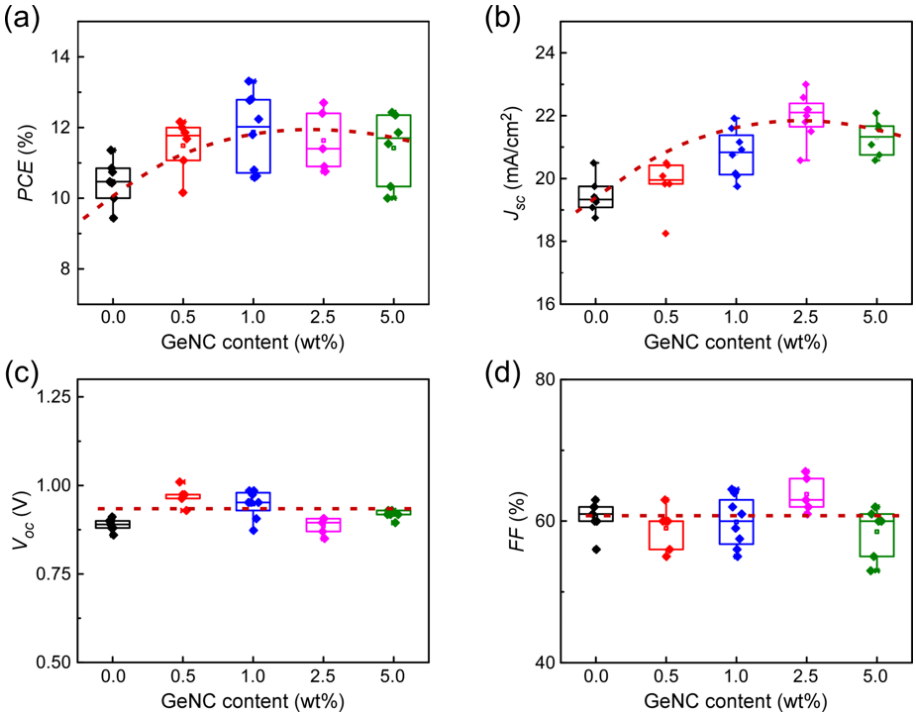

Figure 8.17: Solar cell parameters from the J-V characterization of PSCs based on different mesoporous ETLs: (a) PCE, (b) J_{sc}, (c) V_{oc} and (d) FF. The red dashed lines are guides to the eye. Reproduced from Ref [219] with permission from JOHN WILEY AND SONS, Copyright 2021.

can be efficiently and rapidly separated from the perovskite layer to the ETL due to the GeNC addition [256]. This enhanced charge extraction can be attributed to the intrinsic property of a high electron mobility of the ETLs established by introducing GeNCs. This notably leads to an overall improvement in the photovoltaic performance by increasing the J_{sc} and PCE values. Note also that the shortest average charge carrier lifetime is present in the 2.5 wt% GeNCs sample, which agrees well with the above result of the best performing PSC.

8.6 Summary

In this work, we demonstrate that ordered mesoporous TiO_2 films can be finely tailored through the inclusion of pre-synthesized GeNCs into a diblock-copolymer templating sol-gel synthesis protocol, displaying a successful strategy to obtain efficient photoanodes upon high-temperature annealing. The effect of GeNC addition on the mesoporous TiO_2 film is investigated by means of SEM, GISAXS, TEM, XPS, and UV-Vis spectroscopy. Our measurements reveal that even with GeNC addition, the composite films maintain

Sample	τ_1 (ns)	α_1	τ_2 (ns)	α_2	τ_{av1} (ns)	τ_{av2} (ns)
0.0 wt% GeNCs	25.8 ± 3.9	36%	294.3 ± 3.7	64%	197.6	281.6
0.5 wt% GeNCs	16.0 ± 2.5	44%	280.9 ± 3.8	56%	163.7	269.4
1.0 wt% GeNCs	17.8 ± 2.4	48%	298.9 ± 4.5	52%	164.1	284.3
2.5 wt% GeNCs	19.0 ± 2.3	49%	277.2 ± 3.9	51%	151.4	261.3
5.0 wt% GeNCs	20.8 ± 2.7	46%	289.5 ± 4.3	54%	165.7	273.9

Figure 8.18: Parameters extracted from the fits to the TRPL data of perovskite deposited on the TiO_2/GeNC films with different GeNC contents after thermal annealing in air. Reproduced from Ref [219] with permission from JOHN WILEY AND SONS, Copyright 2021.

ordered mesoporous morphologies, high crystallinity, and good transparency in the visible range. Moreover, the inner morphology consists of small-sized structures, which have similar center-to-center distances and radii irrespective of the GeNC addition. The large-sized structures are also present, which display nearly constant radii and increasing center-to-center distances with the increasing amount of GeNCs. Among the investigated samples, the largest pore sizes are found in the 2.5 wt% GeNCs sample. The air-annealed nanocomposite films are used as ETLs in PSCs. Compared to pristine TiO_2 photoanodes, the GeNC addition enhances the electron transfer, thereby yielding an overall improvement in the J_{sc} and PCE values. Moreover, it strongly suppresses the well-known hysteresis behavior in the PSCs. Best performing devices are observed at 2.5 wt% GeNCs addition.

While the work presented here is far from an optimization of the device parameters, it demonstrates the clear improvements achieved with controllable nanostructures in the ETLs. The simple synthesis protocol makes the composite TiO_2/GeO_x films highly interesting as anode candidates in photovoltaics. Moreover, the method of combining GeNCs with the sol-gel synthesis of mesoporous metal oxide films can be transferred to other metal oxides such as ZnO or SnO_2, thus providing a viable route for fabricating ordered mesoporous nanocomposite films with a variety of materials. The comparison between air and argon annealing paves a way for producing TiO_2/GeO_x nanocomposite semiconductors to meet various needs for applications also beyond PSCs.

9 Conclusion and outlook

In the present thesis, the main focus is on slot-die printed titania films and introducing germanium nanocrystals (GeNCs) into titania films for photovoltaic applications. Within this scope, mesoporous titania films with tailored nanostructures are fabricated via slot-die printing. The crystallization behavior of the model polymer P3HT and the low band gap polymer PffBT4T-2OD induced in printed mesoporous titania films with different pore sizes is discussed as an implication for hybrid solar cells (HSCs). A fundamental insight into the structure evolution of the titania-diblock-copolymer hybrid film is revealed, to understand slot-die printed mesoporous titania films. Finally, titania films are tailored via introducing GeNCs for enhanced electron transfer photoanodes for perovskite solar cells (PSCs).

Using slot-die printing, the titania morphology, including foam-like nanostructures, nanowire aggregates, collapsed vesicles and nanogranules, are achieved via a so-called block-copolymer-assisted sol-gel synthesis. By adjusting the weight fraction of the solvent, catalyst and titania precursor, the ternary morphology phase diagram of the printed titania films is probed after template removal. The foam-like titania nanostructures are investigated in detail as they are of interest for solar cell applications. At a low weight fraction of the titania precursor titanium(IV)isopropoxide (TTIP), foam-like titania films are achieved, which exhibit a high uniformity and possess large pore sizes. Thus, the printing route for structuring foam-like titania nanocomposite films holds high potential for application in solar cell devices.

On the basis of the optimized titania morphology via slot-die printing as mentioned above, a donor polymer is backfilled to form the hybrid active layer. For hybrid solar cells, a high degree of crystallinity of the conjugated polymer and its backbone orientation in face-on direction with respect to the substrate are also significant, in addition to the titania morphology. Therefore, the crystallization behavior of P3HT and PffBT4T-2OD induced in mesoporous titania films via slot-die printing is studied. The correlation between the crystal structure of P3HT and PffBT4T-2OD, and the titania pore size is revealed with a combination of grazing-incidence wide-angle X-ray scattering (GIWAXS) and grazing-incidence small-angle X-ray scattering (GISAXS). Independent of the crystal orientation, a denser stacking of PffBT4T-2OD chains is found for larger pore sizes of the titania

matrix, which is consistent with the results for P3HT-backfilled samples. For an edge-on direction, both PffBT4T-2OD-backfilled and P3HT-backfilled active layers show in general the same trend of increasing crystallite sizes with decreasing titania pore sizes. In contrast and for a face-on direction, the opposite tendency of increasing PffBT4T-2OD crystallite sizes with increasing titania pore sizes is observed. Thus, it is found that a high face-on to edge-on ratio is favored in a titania nano-confinement with larger pores. These findings are of crucial significance for crystalline properties and future efficiency optimization/enhancement in one of the promising material combinations for hybrid photovoltaic applications.

Moreover, self-assembly of slot-die-printed titania/PS-b-PEO micelles into ordered structures is investigated using in situ GISAXS. This synchrotron-based approach provides a vital insight into the structural evolution of titania/PS-b-PEO hybrid films. A well-ordered surface structure is established and remains stable during the entire film formation. In contrast, inside the film, center-to-center distances and radii of the titania/PEO domains decrease rapidly in the initial stage, then decay slowly, and stay constant at the end of the printing process. Thereby a defect-rich mixed FCC and BCC structure establishes in the film bulk, whereas at the film surface an FCC structure is formed. After calcination, the surface and inner morphologies of the obtained nanostructured titania films are compared with the spin-coated analogues. In the printed films, the initially formed nanoscale structure of the hybrid film is preserved, and the resulting mesoporous titania film shows a superior order as compared with the spin-coated thin films. This highly ordered mesoporous titania film prepared via slot-die printing is used in quantum dot-sensitized solar cells (QDSSCs). The working of the exemplary QDSSCs demonstrates that the slot-die printed titania film for large-scale fabrication of solar cells can be promising in the future.

In the last result chapter, ordered mesoporous TiO_2 films can be finely tailored through the inclusion of pre-synthesized GeNCs into a diblock-copolymer templating sol-gel synthesis protocol, displaying a successful strategy to obtain efficient photoanodes upon high-temperature annealing. The effect of GeNC addition on the mesoporous TiO_2 film is investigated by means of SEM, GISAXS, XRD, TEM, XPS, and UV-Vis spectroscopy. These measurements reveal that even with GeNC addition, the composite films maintain ordered mesoporous morphologies, high crystallinity, and good transparency in the visible range. Moreover, the inner morphology consists of small-sized structures, which have similar center-to-center distances and radii irrespective of the GeNC addition. The large-sized structures are also present, which display nearly constant radii and increasing center-to-center distances with the increasing amount of GeNCs. Among the investigated samples, the largest pore sizes are found in the 2.5 wt% GeNC sample. The air-annealed nanocomposite films are used as electron transport layers in PSCs. Compared to pristine

TiO_2 photoanodes, the GeNC addition enhances the electron transfer, thereby yielding an overall improvement in the J_{sc} and PCE values of PSCs. Moreover, it strongly suppresses the well-known hysteresis behavior in the PSCs. Best performing devices are observed at 2.5 wt% GeNC addition.

Based on the present thesis, several recommended projects are put forward for future investigations. Since a successful way of slot-die printing has been established in upscale fabrication of titania photoanodes. The slot-die printing of a low-temperature titania film on the flexible polymer substrate would be an intriguing project, which can make solar cells, i.e. PSCs, possess the similar advantage with polymer semiconducting devices like ease of large-scale production. Also, a new approach that combines GeNCs with sol-gel chemistry can successfully fabricate ordered mesoporous TiO_2/GeO_x films. Simultaneously, the addition of GeNCs has already proven to improve the PSC performance. This simple method of combining GeNCs with the sol-gel synthesis of mesoporous metal oxide films can be transferred to other transparent conducting metal oxides such as ZnO or SnO_2, thus providing a viable route for fabricating ordered mesoporous nanocomposite films with a variety of materials. In the future, the mesoporous titania films obtained in the present thesis can also be used in solid-state dye-sensitized solar cells (ssDSSCs). As an electron transport layer in ssDSSCs, the sol-gel method can produce the nanostrutcured TiO_2 films with a high surface-to-volume ratio, which are beneficial for the dye loading, and thus improving charge carrier generation and device efficiency. Different high-efficiency dye molecules can also be investigated, and will also likely give rise to high ssDSSC performance.

Bibliography

[1] Y. Bai, I. Mora-Sero, F. De Angelis, J. Bisquert, and P. Wang, "Titanium dioxide nanomaterials for photovoltaic applications," *Chemical reviews*, vol. 114, no. 19, pp. 10095–10130, 2014.

[2] R. Zapf-Gottwick, M. Koch, K. Fischer, F. Schwerdt, L. Hamann, M. Kranert, J. H. Werner, *et al.*, "Leaching hazardous substances out of photovoltaic modules," *Int. J. of Advanced Applied Physics Research*, vol. 2, no. 2, pp. 7–14, 2015.

[3] S. R. Gajjela, K. Ananthanarayanan, C. Yap, M. Grätzel, and P. Balaya, "Synthesis of mesoporous titanium dioxide by soft template based approach: characterization and application in dye-sensitized solar cells," *Energy & Environmental Science*, vol. 3, no. 6, pp. 838–845, 2010.

[4] H. Liu, J. Tang, I. J. Kramer, R. Debnath, G. I. Koleilat, X. Wang, A. Fisher, R. Li, L. Brzozowski, L. Levina, *et al.*, "Electron acceptor materials engineering in colloidal quantum dot solar cells," *Advanced Materials*, vol. 23, no. 33, pp. 3832–3837, 2011.

[5] X. Li, M. I. Dar, C. Yi, J. Luo, M. Tschumi, S. M. Zakeeruddin, M. K. Nazeeruddin, H. Han, and M. Grätzel, "Improved performance and stability of perovskite solar cells by crystal crosslinking with alkylphosphonic acid ω-ammonium chlorides," *Nature chemistry*, vol. 7, no. 9, pp. 703–711, 2015.

[6] M. A. Green, E. D. Dunlop, J. Hohl-Ebinger, M. Yoshita, N. Kopidakis, and A. W. Ho-Baillie, "Solar cell efficiency tables (version 55)," *Progress in Photovoltaics: Research and Applications*, vol. 28, no. 1, pp. 3–15, 2020.

[7] Y. Duan, Q. Tang, Z. Chen, B. He, and H. Chen, "Enhanced dye illumination in dye-sensitized solar cells using tio 2/geo 2 photo-anodes," *Journal of Materials Chemistry A*, vol. 2, no. 31, pp. 12459–12465, 2014.

[8] P. Tiwana, P. Docampo, M. B. Johnston, H. J. Snaith, and L. M. Herz, "Electron mobility and injection dynamics in mesoporous zno, sno2, and tio2 films used in dye-sensitized solar cells," *ACS nano*, vol. 5, no. 6, pp. 5158–5166, 2011.

[9] Y. Zhao, C. Li, X. Liu, F. Gu, H. Jiang, W. Shao, L. Zhang, and Y. He, "Synthesis and optical properties of tio2 nanoparticles," *Materials Letters*, vol. 61, no. 1, pp. 79–83, 2007.

[10] M. Gao, L. Zhu, W. L. Ong, J. Wang, and G. W. Ho, "Structural design of tio 2-based photocatalyst for h 2 production and degradation applications," *Catalysis Science & Technology*, vol. 5, no. 10, pp. 4703–4726, 2015.

[11] M. Rawolle, M. A. Ruderer, S. M. Prams, Q. Zhong, D. Magerl, J. Perlich, S. V. Roth, P. Lellig, J. S. Gutmann, and P. Müller-Buschbaum, "Nanostructuring of titania thin films by a combination of microfluidics and block-copolymer-based sol–gel templating," *Small*, vol. 7, no. 7, pp. 884–891, 2011.

[12] Y. Liao, W. Que, Q. Jia, Y. He, J. Zhang, and P. Zhong, "Controllable synthesis of brookite/anatase/rutile tio 2 nanocomposites and single-crystalline rutile nanorods array," *Journal of Materials Chemistry*, vol. 22, no. 16, pp. 7937–7944, 2012.

[13] E. Ortel, A. Fischer, L. Chuenchom, J. Polte, F. Emmerling, B. Smarsly, and R. Kraehnert, "New triblock copolymer templates, peo-pb-peo, for the synthesis of titania films with controlled mesopore size, wall thickness, and bimodal porosity," *Small*, vol. 8, no. 2, pp. 298–309, 2012.

[14] J. Zhang, Y. Deng, D. Gu, S. Wang, L. She, R. Che, Z.-S. Wang, B. Tu, S. Xie, and D. Zhao, "Ligand-assisted assembly approach to synthesize large-pore ordered mesoporous titania with thermally stable and crystalline framework," *Advanced Energy Materials*, vol. 1, no. 2, pp. 241–248, 2011.

[15] C. A. Grimes, "Synthesis and application of highly ordered arrays of tio 2 nanotubes," *Journal of Materials Chemistry*, vol. 17, no. 15, pp. 1451–1457, 2007.

[16] S. Xia, E. Metwalli, M. Opel, P. A. Staniec, E. M. Herzig, and P. Müller-Buschbaum, "Printed thin magnetic films based on diblock copolymer and magnetic nanoparticles," *ACS applied materials & interfaces*, vol. 10, no. 3, pp. 2982–2991, 2018.

[17] W. Ma, G. Yang, K. Jiang, J. H. Carpenter, Y. Wu, X. Meng, T. McAfee, J. Zhao, C. Zhu, C. Wang, *et al.*, "Influence of processing parameters and molecular weight on the morphology and properties of high-performance pffbt4t-2od: Pc71bm organic solar cells," *Advanced Energy Materials*, vol. 5, no. 23, p. 1501400, 2015.

[18] Y. Liu, J. Zhao, Z. Li, C. Mu, W. Ma, H. Hu, K. Jiang, H. Lin, H. Ade, and H. Yan, "Aggregation and morphology control enables multiple cases of high-efficiency polymer solar cells," *Nature communications*, vol. 5, no. 1, pp. 1–8, 2014.

[19] M. Xu, Y. Gao, E. M. Moreno, M. Kunst, M. Muhler, Y. Wang, H. Idriss, and C. Wöll, "Photocatalytic activity of bulk tio 2 anatase and rutile single crystals using infrared absorption spectroscopy," *Physical Review Letters*, vol. 106, no. 13, p. 138302, 2011.

[20] H. Tang, K. Prasad, R. Sanjines, P. Schmid, and F. Levy, "Electrical and optical

properties of tio2 anatase thin films," *Journal of applied physics*, vol. 75, no. 4, pp. 2042–2047, 1994.

[21] U. Bach, D. Lupo, P. Comte, J.-E. Moser, F. Weissörtel, J. Salbeck, H. Spreitzer, and M. Grätzel, "Solid-state dye-sensitized mesoporous tio 2 solar cells with high photon-to-electron conversion efficiencies," *Nature*, vol. 395, no. 6702, pp. 583–585, 1998.

[22] Q. Tay, X. Liu, Y. Tang, Z. Jiang, T. C. Sum, and Z. Chen, "Enhanced photocatalytic hydrogen production with synergistic two-phase anatase/brookite tio2 nanostructures," *The Journal of Physical Chemistry C*, vol. 117, no. 29, pp. 14973–14982, 2013.

[23] A. Di Paola, M. Bellardita, and L. Palmisano, "Brookite, the least known tio2 photocatalyst," *Catalysts*, vol. 3, no. 1, pp. 36–73, 2013.

[24] A. Beltran, L. Gracia, and J. Andres, "Density functional theory study of the brookite surfaces and phase transitions between natural titania polymorphs," *The Journal of Physical Chemistry B*, vol. 110, no. 46, pp. 23417–23423, 2006.

[25] U. Diebold, "The surface science of titanium dioxide," *Surface science reports*, vol. 48, no. 5-8, pp. 53–229, 2003.

[26] L. Kavan, M. Grätzel, S. Gilbert, C. Klemenz, and H. Scheel, "Electrochemical and photoelectrochemical investigation of single-crystal anatase," *Journal of the American Chemical Society*, vol. 118, no. 28, pp. 6716–6723, 1996.

[27] D. Reyes-Coronado, G. Rodríguez-Gattorno, M. Espinosa-Pesqueira, C. Cab, R. d. De Coss, and G. Oskam, "Phase-pure tio2 nanoparticles: anatase, brookite and rutile," *Nanotechnology*, vol. 19, no. 14, p. 145605, 2008.

[28] D. T. Cromer and K. Herrington, "The structures of anatase and rutile," *Journal of the American Chemical Society*, vol. 77, no. 18, pp. 4708–4709, 1955.

[29] W. Baur, "Atomabstände und bindungswinkel im brookit, tio2," *Acta Crystallographica*, vol. 14, no. 3, pp. 214–216, 1961.

[30] S.-D. Mo and W. Ching, "Electronic and optical properties of three phases of titanium dioxide: Rutile, anatase, and brookite," *Physical review B*, vol. 51, no. 19, p. 13023, 1995.

[31] D. O. Scanlon, C. W. Dunnill, J. Buckeridge, S. A. Shevlin, A. J. Logsdail, S. M. Woodley, C. R. A. Catlow, M. J. Powell, R. G. Palgrave, I. P. Parkin, *et al.*, "Band alignment of rutile and anatase tio 2," *Nature materials*, vol. 12, no. 9, pp. 798–801, 2013.

[32] G. Moretti, "Auger parameter and wagner plot in the characterization of chemical states by x-ray photoelectron spectroscopy: a review," *Journal of electron spectroscopy and related phenomena*, vol. 95, no. 2-3, pp. 95–144, 1998.

[33] L. Ding, S. Yang, Z. Liang, X. Qian, X. Chen, H. Cui, and J. Tian, "Tio2 nanobelts with anatase/rutile heterophase junctions for highly efficient photocatalytic overall water splitting," *Journal of colloid and interface science*, vol. 567, pp. 181–189, 2020.

[34] N. H. Hong, "Introduction to nanomaterials: basic properties, synthesis, and characterization," in *Nano-Sized Multifunctional Materials*, pp. 1–19, Elsevier, 2019.

[35] C. Ramana, R. Smith, and O. Hussain, "Grain size effects on the optical characteristics of pulsed-laser deposited vanadium oxide thin films," *Physica status solidi (a)*, vol. 199, no. 1, pp. R4–R6, 2003.

[36] R. Asahi, Y. Taga, W. Mannstadt, and A. J. Freeman, "Electronic and optical properties of anatase tio 2," *Physical Review B*, vol. 61, no. 11, p. 7459, 2000.

[37] H. Uchida, M. N. Patel, R. A. May, G. Gupta, K. J. Stevenson, and K. P. Johnston, "Highly-ordered mesoporous titania thin films prepared via surfactant assembly on conductive indium–tin-oxide/glass substrate and its optical properties," *Thin Solid Films*, vol. 518, no. 12, pp. 3169–3176, 2010.

[38] I. Gur, N. A. Fromer, M. L. Geier, and A. P. Alivisatos, "Air-stable all-inorganic nanocrystal solar cells processed from solution," *Science*, vol. 310, no. 5747, pp. 462–465, 2005.

[39] P. J. Flory, "Thermodynamics of high polymer solutions," *The Journal of chemical physics*, vol. 10, no. 1, pp. 51–61, 1942.

[40] M. L. Huggins, "Thermodynamic properties of solutions of long-chain compounds," *Annals of the New York Academy of Sciences*, vol. 43, no. 1, pp. 1–32, 1942.

[41] Y.-C. Tseng and S. B. Darling, "Block copolymer nanostructures for technology," *Polymers*, vol. 2, no. 4, pp. 470–489, 2010.

[42] F. S. Bates and G. H. Fredrickson, "Block copolymer thermodynamics: theory and experiment," *Annual review of physical chemistry*, vol. 41, no. 1, pp. 525–557, 1990.

[43] M. W. Matsen and F. S. Bates, "Unifying weak-and strong-segregation block copolymer theories," *Macromolecules*, vol. 29, no. 4, pp. 1091–1098, 1996.

[44] L. Zhang, K. Yu, and A. Eisenberg, "Ion-induced morphological changes in "crew-cut" aggregates of amphiphilic block copolymers," *Science*, vol. 272, no. 5269, pp. 1777–1779, 1996.

[45] Y. Yu and A. Eisenberg, "Control of morphology through polymer- solvent interactions in crew-cut aggregates of amphiphilic block copolymers," *Journal of the American Chemical Society*, vol. 119, no. 35, pp. 8383–8384, 1997.

[46] H. Shen, L. Zhang, and A. Eisenberg, "Multiple ph-induced morphological changes in aggregates of polystyrene-block-poly (4-vinylpyridine) in dmf/h2o mixtures," *Journal of the American Chemical Society*, vol. 121, no. 12, pp. 2728–2740, 1999.

[47] Y. Mai and A. Eisenberg, "Self-assembly of block copolymers," *Chemical Society Reviews*, vol. 41, no. 18, pp. 5969–5985, 2012.

[48] H. Shen and A. Eisenberg, "Morphological phase diagram for a ternary system of block copolymer ps310-b-paa52/dioxane/h2o," *The Journal of Physical Chemistry B*, vol. 103, no. 44, pp. 9473–9487, 1999.

[49] L. Zhang and A. Eisenberg, "Formation of crew-cut aggregates of various morphologies from amphiphilic block copolymers in solution," *Polymers for Advanced Technologies*, vol. 9, no. 10-11, pp. 677–699, 1998.

[50] S. Reghunath, D. Pinheiro, and S. D. KR, "A review of hierarchical nanostructures of tio2: Advances and applications," *Applied Surface Science Advances*, vol. 3, p. 100063, 2021.

[51] C. Natarajan and G. Nogami, "Cathodic electrodeposition of nanocrystalline titanium dioxide thin films," *Journal of the Electrochemical Society*, vol. 143, no. 5, p. 1547, 1996.

[52] M. C. Orilall and U. Wiesner, "Block copolymer based composition and morphology control in nanostructured hybrid materials for energy conversion and storage: solar cells, batteries, and fuel cells," *Chemical Society Reviews*, vol. 40, no. 2, pp. 520–535, 2011.

[53] P. Lim Soo and A. Eisenberg, "Preparation of block copolymer vesicles in solution," *Journal of Polymer Science Part B: Polymer Physics*, vol. 42, no. 6, pp. 923–938, 2004.

[54] C.-C. Wang and J. Y. Ying, "Sol- gel synthesis and hydrothermal processing of anatase and rutile titania nanocrystals," *Chemistry of materials*, vol. 11, no. 11, pp. 3113–3120, 1999.

[55] L. Zhang, H. Shen, and A. Eisenberg, "Phase separation behavior and crew-cut micelle formation of polystyrene-b-poly (acrylic acid) copolymers in solutions," *Macromolecules*, vol. 30, no. 4, pp. 1001–1011, 1997.

[56] X. Liao, L. Zhang, L. Chen, X. Hu, Q. Ai, W. Ma, and Y. Chen, "Room temperature processed polymers for high-efficient polymer solar cells with power conversion efficiency over 9%," *Nano Energy*, vol. 37, pp. 32–39, 2017.

[57] Y.-J. Cheng and J. S. Gutmann, "Morphology phase diagram of ultrathin anatase tio2 films templated by a single ps-b-peo block copolymer," *Journal of the American Chemical Society*, vol. 128, no. 14, pp. 4658–4674, 2006.

[58] G. A. McConnell, A. P. Gast, J. S. Huang, and S. D. Smith, "Disorder-order transitions in soft sphere polymer micelles," *Physical review letters*, vol. 71, no. 13, p. 2102, 1993.

[59] C. J. Brinker, Y. Lu, A. Sellinger, and H. Fan, "Evaporation-induced self-assembly: nanostructures made easy," *Advanced materials*, vol. 11, no. 7, pp. 579–585, 1999.

[60] M. Rawolle, E. V. Braden, M. A. Niedermeier, D. Magerl, K. Sarkar, T. Fröschl, N. Hüsing, J. Perlich, and P. Müller-Buschbaum, "Low-temperature route to crystalline titania network structures in thin films," *ChemPhysChem*, vol. 13, no. 9, pp. 2412–2417, 2012.

[61] L. Song, A. Abdelsamie, C. J. Schaffer, V. Körstgens, W. Wang, T. Wang, E. D. Indari, T. Fröschl, N. Hüsing, T. Haeberle, *et al.*, "A low temperature route toward hierarchically structured titania films for thin hybrid solar cells," *Advanced Functional Materials*, vol. 26, no. 39, pp. 7084–7093, 2016.

[62] W. Wang, T. Widmann, L. Song, T. Fröschl, N. Hüsing, G. Mo, Z. Wu, P. Zhang, S. V. Roth, H. Fan, *et al.*, "Aging of low-temperature derived highly flexible nanostructured tio 2/p3ht hybrid films during bending," *Journal of Materials Chemistry A*, vol. 7, no. 17, pp. 10805–10814, 2019.

[63] Z. Zhang, M. Liao, H. Lou, Y. Hu, X. Sun, and H. Peng, "Conjugated polymers for flexible energy harvesting and storage," *Advanced Materials*, vol. 30, no. 13, p. 1704261, 2018.

[64] L. Schmidt-Mende and J. Weickert, *Organic and hybrid solar cells: an introduction*. Walter de Gruyter GmbH & Co KG, 2016.

[65] W. J. Beenken, "Excitons in conjugated polymers: Do we need a paradigma change?," *physica status solidi (a)*, vol. 206, no. 12, pp. 2750–2756, 2009.

[66] T. Förster, "Zwischenmolekulare energiewanderung und fluoreszenz," *Annalen der physik*, vol. 437, no. 1-2, pp. 55–75, 1948.

[67] Y. Tamai, H. Ohkita, H. Benten, and S. Ito, "Exciton diffusion in conjugated polymers: from fundamental understanding to improvement in photovoltaic conversion efficiency," *The journal of physical chemistry letters*, vol. 6, no. 17, pp. 3417–3428, 2015.

[68] B. R. Saunders and M. L. Turner, "Nanoparticle–polymer photovoltaic cells," *Advances in colloid and interface science*, vol. 138, no. 1, pp. 1–23, 2008.

[69] N. Kopidakis, N. Neale, K. Zhu, J. Van De Lagemaat, and A. Frank, "Spatial location of transport-limiting traps in ti o 2 nanoparticle films in dye-sensitized solar cells," *Applied Physics Letters*, vol. 87, no. 20, p. 202106, 2005.

[70] D. R. Baker and P. V. Kamat, "Photosensitization of tio2 nanostructures with cds quantum dots: particulate versus tubular support architectures," *Advanced Functional Materials*, vol. 19, no. 5, pp. 805–811, 2009.

[71] P. K. Santra and P. V. Kamat, "Mn-doped quantum dot sensitized solar cells: a strategy to boost efficiency over 5%," *Journal of the American Chemical Society*, vol. 134, no. 5, pp. 2508–2511, 2012.

[72] C. Yuan, L. Li, J. Huang, Z. Ning, L. Sun, and H. Ågren, "Improving the photocurrent in quantum-dot-sensitized solar cells by employing alloy pbxcd1- xs quantum dots as photosensitizers," *Nanomaterials*, vol. 6, no. 6, p. 97, 2016.

[73] L. M. Peter, K. U. Wijayantha, D. J. Riley, and J. P. Waggett, "Band-edge tuning in self-assembled layers of bi2s3 nanoparticles used to photosensitize nanocrystalline tio2," *The Journal of Physical Chemistry B*, vol. 107, no. 33, pp. 8378–8381, 2003.

[74] A. Zaban, O. Mićić, B. Gregg, and A. Nozik, "Photosensitization of nanoporous tio2 electrodes with inp quantum dots," *Langmuir*, vol. 14, no. 12, pp. 3153–3156, 1998.

[75] S. Rühle, M. Shalom, and A. Zaban, "Quantum-dot-sensitized solar cells," *ChemPhysChem*, vol. 11, no. 11, pp. 2290–2304, 2010.

[76] J.-Y. Jeng, Y.-F. Chiang, M.-H. Lee, S.-R. Peng, T.-F. Guo, P. Chen, and T.-C. Wen, "Ch3nh3pbi3 perovskite/fullerene planar-heterojunction hybrid solar cells," *Advanced Materials*, vol. 25, no. 27, pp. 3727–3732, 2013.

[77] S. Sun, T. Salim, N. Mathews, M. Duchamp, C. Boothroyd, G. Xing, T. C. Sum, and Y. M. Lam, "The origin of high efficiency in low-temperature solution-processable bilayer organometal halide hybrid solar cells," *Energy & Environmental Science*, vol. 7, no. 1, pp. 399–407, 2014.

[78] J. M. Ball, M. M. Lee, A. Hey, and H. J. Snaith, "Low-temperature processed meso-superstructured to thin-film perovskite solar cells," *Energy & Environmental Science*, vol. 6, no. 6, pp. 1739–1743, 2013.

[79] I. Hussain, H. P. Tran, J. Jaksik, J. Moore, N. Islam, and M. J. Uddin, "Functional materials, device architecture, and flexibility of perovskite solar cell," *Emergent Materials*, vol. 1, no. 3, pp. 133–154, 2018.

[80] S. N. Habisreutinger, T. Leijtens, G. E. Eperon, S. D. Stranks, R. J. Nicholas, and H. J. Snaith, "Enhanced hole extraction in perovskite solar cells through carbon

nanotubes," *The journal of physical chemistry letters*, vol. 5, no. 23, pp. 4207–4212, 2014.

[81] W.-J. Yin, T. Shi, and Y. Yan, "Unusual defect physics in ch3nh3pbi3 perovskite solar cell absorber," *Applied Physics Letters*, vol. 104, no. 6, p. 063903, 2014.

[82] G.-J. A. Wetzelaer, M. Scheepers, A. M. Sempere, C. Momblona, J. Ávila, and H. J. Bolink, "Trap-assisted non-radiative recombination in organic–inorganic perovskite solar cells," *Advanced Materials*, vol. 27, no. 11, pp. 1837–1841, 2015.

[83] L. M. Herz, "Charge-carrier dynamics in organic-inorganic metal halide perovskites," *Annual review of physical chemistry*, vol. 67, pp. 65–89, 2016.

[84] T. Leijtens, G. E. Eperon, A. J. Barker, G. Grancini, W. Zhang, J. M. Ball, A. R. S. Kandada, H. J. Snaith, and A. Petrozza, "Carrier trapping and recombination: the role of defect physics in enhancing the open circuit voltage of metal halide perovskite solar cells," *Energy & Environmental Science*, vol. 9, no. 11, pp. 3472–3481, 2016.

[85] S. van Reenen, M. Kemerink, and H. J. Snaith, "Modeling anomalous hysteresis in perovskite solar cells," *The journal of physical chemistry letters*, vol. 6, no. 19, pp. 3808–3814, 2015.

[86] K. Miyano, M. Yanagida, N. Tripathi, and Y. Shirai, "Hysteresis, stability, and ion migration in lead halide perovskite photovoltaics," *The journal of physical chemistry letters*, vol. 7, no. 12, pp. 2240–2245, 2016.

[87] H. Röhm, T. Leonhard, A. D. Schulz, S. Wagner, M. J. Hoffmann, and A. Colsmann, "Ferroelectric properties of perovskite thin films and their implications for solar energy conversion," *Advanced Materials*, vol. 31, no. 26, p. 1806661, 2019.

[88] M. Tolan and M. Tolan, *X-ray scattering from soft-matter thin films: materials science and basic research*, vol. 148. Springer, 1999.

[89] J. Als-Nielsen and D. McMorrow, *Elements of modern X-ray physics*. John Wiley & Sons, 2011.

[90] P. Müller-Buschbaum, "Gisaxs and gisans as metrology technique for understanding the 3d morphology of block copolymer thin films," *European Polymer Journal*, vol. 81, pp. 470–493, 2016.

[91] A. Stokes and A. Wilson, "A method of calculating the integral breadths of debye-scherrer lines," in *Mathematical Proceedings of the Cambridge Philosophical Society*, vol. 38, pp. 313–322, Cambridge University Press, 1942.

[92] R. Lazzari, "Isgisaxs: a program for grazing-incidence small-angle x-ray scattering analysis of supported islands," *Journal of Applied Crystallography*, vol. 35, no. 4, pp. 406–421, 2002.

[93] H. Masunaga, H. Ogawa, T. Takano, S. Sasaki, S. Goto, T. Tanaka, T. Seike, S. Takahashi, K. Takeshita, N. Nariyama, *et al.*, "Multipurpose soft-material saxs/waxs/gisaxs beamline at spring-8," *Polymer journal*, vol. 43, no. 5, pp. 471–477, 2011.

[94] G. Santoro and S. Yu, "Grazing incidence small angle x-ray scattering as a tool for in-situ time-resolved studies," *X-ray Scattering*, pp. 29–59, 2017.

[95] P. Müller-Buschbaum, "Grazing incidence small-angle x-ray scattering: an advanced scattering technique for the investigation of nanostructured polymer films," *Analytical and bioanalytical chemistry*, vol. 376, no. 1, pp. 3–10, 2003.

[96] Y. Yoneda, "Anomalous surface reflection of x rays," *Physical review*, vol. 131, no. 5, p. 2010, 1963.

[97] M. Rawolle, K. Sarkar, M. A. Niedermeier, M. Schindler, P. Lellig, J. S. Gutmann, J.-F. Moulin, M. Haese-Seiller, A. S. Wochnik, C. Scheu, *et al.*, "Infiltration of polymer hole-conductor into mesoporous titania structures for solid-state dye-sensitized solar cells," *ACS applied materials & interfaces*, vol. 5, no. 3, pp. 719–729, 2013.

[98] P. Müller-Buschbaum, "The active layer morphology of organic solar cells probed with grazing incidence scattering techniques," *Advanced materials*, vol. 26, no. 46, pp. 7692–7709, 2014.

[99] Z. Jiang, "Gixsgui: a matlab toolbox for grazing-incidence x-ray scattering data visualization and reduction, and indexing of buried three-dimensional periodic nanostructured films," *Journal of Applied Crystallography*, vol. 48, no. 3, pp. 917–926, 2015.

[100] J. L. Baker, L. H. Jimison, S. Mannsfeld, S. Volkman, S. Yin, V. Subramanian, A. Salleo, A. P. Alivisatos, and M. F. Toney, "Quantification of thin film crystallographic orientation using x-ray diffraction with an area detector," *Langmuir*, vol. 26, no. 11, pp. 9146–9151, 2010.

[101] P. S. Kumar, K. G. Pavithra, and M. Naushad, "Characterization techniques for nanomaterials," in *Nanomaterials for solar cell applications*, pp. 97–124, Elsevier, 2019.

[102] A. Buffet, A. Rothkirch, R. Döhrmann, V. Körstgens, M. M. Abul Kashem, J. Perlich, G. Herzog, M. Schwartzkopf, R. Gehrke, P. Müller-Buschbaum, *et al.*, "P03, the microfocus and nanofocus x-ray scattering (minaxs) beamline of the petra iii storage ring: the microfocus endstation," *Journal of synchrotron radiation*, vol. 19, no. 4, pp. 647–653, 2012.

[103] G. Benecke, W. Wagermaier, C. Li, M. Schwartzkopf, G. Flucke, R. Hoerth, I. Zizak, M. Burghammer, E. Metwalli, P. Müller-Buschbaum, *et al.*, "A customizable soft-

ware for fast reduction and analysis of large x-ray scattering data sets: applications of the new dpdak package to small-angle x-ray scattering and grazing-incidence small-angle x-ray scattering," *Journal of applied crystallography*, vol. 47, no. 5, pp. 1797–1803, 2014.

[104] J. Schlipf, *The Morphology of Hybrid Perovskite Thin Films for Photovoltaic Application*. PhD thesis, Technische Universität München, 2018.

[105] J. R. Lakowicz, *Principles of fluorescence spectroscopy*. Springer science & business media, 2013.

[106] M. Murali, A. D. Rao, S. Yadav, and P. C. Ramamurthy, "Narrow band gap conjugated polymer for improving the photovoltaic performance of p3ht: Pcbm ternary blend bulk heterojunction solar cells," *Polymer Chemistry*, vol. 6, no. 6, pp. 962–972, 2015.

[107] L. Song, W. Wang, V. Körstgens, D. M. González, Y. Yao, N. K. Minar, J. M. Feckl, K. Peters, T. Bein, D. Fattakhova-Rohlfing, *et al.*, "Spray deposition of titania films with incorporated crystalline nanoparticles for all-solid-state dye-sensitized solar cells using p3ht," *Advanced Functional Materials*, vol. 26, no. 10, pp. 1498–1506, 2016.

[108] H. Cha, S. Wheeler, S. Holliday, S. D. Dimitrov, A. Wadsworth, H. H. Lee, D. Baran, I. McCulloch, and J. R. Durrant, "Influence of blend morphology and energetics on charge separation and recombination dynamics in organic solar cells incorporating a nonfullerene acceptor," *Advanced Functional Materials*, vol. 28, no. 3, p. 1704389, 2018.

[109] Z. Li, K. Jiang, G. Yang, J. Y. L. Lai, T. Ma, J. Zhao, W. Ma, and H. Yan, "Donor polymer design enables efficient non-fullerene organic solar cells," *Nature communications*, vol. 7, no. 1, pp. 1–9, 2016.

[110] N. Li, L. Song, L. Bießmann, S. Xia, W. Ohm, C. J. Brett, E. Hadjixenophontos, G. Schmitz, S. V. Roth, and P. Müller-Buschbaum, "Morphology phase diagram of slot-die printed tio2 films based on sol–gel synthesis," *Advanced Materials Interfaces*, vol. 6, no. 12, p. 1900558, 2019.

[111] M. Javadi, V. K. Michaelis, and J. G. Veinot, "Thermally induced evolution of "ge (oh) 2": Controlling the formation of oxide-embedded ge nanocrystals," *The Journal of Physical Chemistry C*, vol. 122, no. 30, pp. 17518–17525, 2018.

[112] F. C. Krebs, "Fabrication and processing of polymer solar cells: A review of printing and coating techniques," *Solar energy materials and solar cells*, vol. 93, no. 4, pp. 394–412, 2009.

[113] D. W. Schubert and T. Dunkel, "Spin coating from a molecular point of view: its concentration regimes, influence of molar mass and distribution," *Materials Research Innovations*, vol. 7, no. 5, pp. 314–321, 2003.

[114] L. K. Reb, M. Böhmer, B. Predeschly, S. Grott, C. L. Weindl, G. I. Ivandekic, R. Guo, C. Dreißigacker, R. Gernhäuser, A. Meyer, *et al.*, "Perovskite and organic solar cells on a rocket flight," *Joule*, vol. 4, no. 9, pp. 1880–1892, 2020.

[115] Y. Zhang, Y. Kan, K. Gao, M. Gu, Y. Shi, X. Zhang, Y. Xue, X. Zhang, Z. Liu, Y. Zhang, *et al.*, "Hybrid quantum dot/organic heterojunction: A route to improve open-circuit voltage in pbs colloidal quantum dot solar cells," *ACS Energy Letters*, vol. 5, no. 7, pp. 2335–2342, 2020.

[116] S. Haque, M. J. Mendes, O. Sanchez-Sobrado, H. Águas, E. Fortunato, and R. Martins, "Photonic-structured tio2 for high-efficiency, flexible and stable perovskite solar cells," *Nano Energy*, vol. 59, pp. 91–101, 2019.

[117] M. Andersson, L. Österlund, S. Ljungstroem, and A. Palmqvist, "Preparation of nanosize anatase and rutile tio2 by hydrothermal treatment of microemulsions and their activity for photocatalytic wet oxidation of phenol," *The Journal of Physical Chemistry B*, vol. 106, no. 41, pp. 10674–10679, 2002.

[118] J. Zheng, L. Liu, G. Ji, Q. Yang, L. Zheng, and J. Zhang, "Hydrogenated anatase tio2 as lithium-ion battery anode: size–reactivity correlation," *ACS applied materials & interfaces*, vol. 8, no. 31, pp. 20074–20081, 2016.

[119] X. Lu, G. Wang, T. Zhai, M. Yu, J. Gan, Y. Tong, and Y. Li, "Hydrogenated tio2 nanotube arrays for supercapacitors," *Nano letters*, vol. 12, no. 3, pp. 1690–1696, 2012.

[120] A. M. Díez-Pascual and A. L. Díez-Vicente, "Nano-tio2 reinforced peek/pei blends as biomaterials for load-bearing implant applications," *ACS applied materials & interfaces*, vol. 7, no. 9, pp. 5561–5573, 2015.

[121] O. Carp, C. L. Huisman, and A. Reller, "Photoinduced reactivity of titanium dioxide," *Progress in solid state chemistry*, vol. 32, no. 1-2, pp. 33–177, 2004.

[122] N. Hohn, S. J. Schlosser, L. Bießmann, S. Grott, S. Xia, K. Wang, M. Schwartzkopf, S. V. Roth, and P. Müller-Buschbaum, "Readily available titania nanostructuring routines based on mobility and polarity controlled phase separation of an amphiphilic diblock copolymer," *Nanoscale*, vol. 10, no. 11, pp. 5325–5334, 2018.

[123] K. Kardarian, D. Nunes, P. M. Sberna, A. Ginsburg, D. A. Keller, J. V. Pinto, J. Deuermeier, A. Y. Anderson, A. Zaban, R. Martins, *et al.*, "Effect of mg doping on cu2o thin films and their behavior on the tio2/cu2o heterojunction solar cells," *Solar Energy Materials and Solar Cells*, vol. 147, pp. 27–36, 2016.

[124] L. Song, W. Wang, V. Körstgens, D. M. González, F. C. Löhrer, C. J. Schaffer, J. Schlipf, K. Peters, T. Bein, D. Fattakhova-Rohlfing, *et al.*, "In situ study of spray deposited titania photoanodes for scalable fabrication of solid-state dye-sensitized solar cells," *Nano Energy*, vol. 40, pp. 317–326, 2017.

[125] M. A. Niedermeier, I. Groß, and P. Müller-Buschbaum, "Structuring of titania thin films on different length scales via combining block copolymer assisted sol–gel templating with wet-imprinting," *Journal of Materials Chemistry A*, vol. 1, no. 43, pp. 13399–13403, 2013.

[126] A. I. Kontos, A. G. Kontos, D. S. Tsoukleris, M.-C. Bernard, N. Spyrellis, and P. Falaras, "Nanostructured tio2 films for dsscs prepared by combining doctor-blade and sol–gel techniques," *Journal of materials processing technology*, vol. 196, no. 1-3, pp. 243–248, 2008.

[127] B. Su, H. A. Caller-Guzman, V. Körstgens, Y. Rui, Y. Yao, N. Saxena, G. Santoro, S. V. Roth, and P. Müller-Buschbaum, "Macroscale and nanoscale morphology evolution during in situ spray coating of titania films for perovskite solar cells," *ACS applied materials & interfaces*, vol. 9, no. 50, pp. 43724–43732, 2017.

[128] R. Cherrington, D. J. Hughes, S. Senthilarasu, and V. Goodship, "Inkjet-printed tio2 nanoparticles from aqueous solutions for dye-sensitized solar cells (dsscs)," *Energy Technology*, vol. 3, no. 8, pp. 866–870, 2015.

[129] I. Bernacka-Wojcik, P. Wojcik, H. Aguas, E. Fortunato, and R. Martins, "Inkjet printed highly porous tio2 films for improved electrical properties of photoanode," *Journal of colloid and interface science*, vol. 465, pp. 208–214, 2016.

[130] S. Ito, P. Chen, P. Comte, M. K. Nazeeruddin, P. Liska, P. Péchy, and M. Grätzel, "Fabrication of screen-printing pastes from tio2 powders for dye-sensitised solar cells," *Progress in photovoltaics: research and applications*, vol. 15, no. 7, pp. 603–612, 2007.

[131] K. Fan, M. Liu, T. Peng, L. Ma, and K. Dai, "Effects of paste components on the properties of screen-printed porous tio2 film for dye-sensitized solar cells," *Renewable Energy*, vol. 35, no. 2, pp. 555–561, 2010.

[132] M. Chason, P. W. Brazis, J. Zhang, K. Kalyanasundaram, and D. R. Gamota, "Printed organic semiconducting devices," *Proceedings of the IEEE*, vol. 93, no. 7, pp. 1348–1356, 2005.

[133] H. Yan, Z. Chen, Y. Zheng, C. Newman, J. R. Quinn, F. Dötz, M. Kastler, and A. Facchetti, "A high-mobility electron-transporting polymer for printed transistors," *Nature*, vol. 457, no. 7230, pp. 679–686, 2009.

[134] F. Garnier, R. Hajlaoui, A. Yassar, and P. Srivastava, "All-polymer field-effect transistor realized by printing techniques," *Science*, vol. 265, no. 5179, pp. 1684–1686, 1994.

[135] C. M. Palumbiny, F. Liu, T. P. Russell, A. Hexemer, C. Wang, and P. Müller-Buschbaum, "The crystallization of pedot: Pss polymeric electrodes probed in situ during printing," *Advanced materials*, vol. 27, no. 22, pp. 3391–3397, 2015.

[136] F. Liu, S. Ferdous, E. Schaible, A. Hexemer, M. Church, X. Ding, C. Wang, and T. P. Russell, "Fast printing and in situ morphology observation of organic photovoltaics using slot-die coating," *Advanced materials*, vol. 27, no. 5, pp. 886–891, 2015.

[137] S. Pröller, D. Moseguí González, C. Zhu, E. Schaible, C. Wang, P. Müller-Buschbaum, A. Hexemer, and E. M. Herzig, "Note: Setup for chemical atmospheric control during in situ grazing incidence x-ray scattering of printed thin films," *Review of Scientific Instruments*, vol. 88, no. 6, p. 066101, 2017.

[138] K. Chen, Q. Fu, S. Ye, and J. Ge, "Multicolor printing using electric-field-responsive and photocurable photonic crystals," *Advanced Functional Materials*, vol. 27, no. 43, p. 1702825, 2017.

[139] Z. Yang, Y. Shi, and B. Wang, "Photocatalytic activity of magnetically anatase tio2 with high crystallinity and stability for dyes degradation: Insights into the dual roles of sio2 interlayer between tio2 and cofe2o4," *Applied Surface Science*, vol. 399, pp. 192–199, 2017.

[140] K. Wang, V. Körstgens, D. Yang, N. Hohn, S. V. Roth, and P. Müller-Buschbaum, "Morphology control of low temperature fabricated zno nanostructures for transparent active layers in all solid-state dye-sensitized solar cells," *Journal of Materials Chemistry A*, vol. 6, no. 10, pp. 4405–4415, 2018.

[141] D. T. Toolan, N. Pullan, M. J. Harvey, P. D. Topham, and J. R. Howse, "In situ studies of phase separation and crystallization directed by marangoni instabilities during spin-coating," *Advanced Materials*, vol. 25, no. 48, pp. 7033–7037, 2013.

[142] K. Sarkar, M. Rawolle, E. M. Herzig, W. Wang, A. Buffet, S. V. Roth, and P. Müller-Buschbaum, "Custom-made morphologies of zno nanostructured films templated by a poly (styrene-block-ethylene oxide) diblock copolymer obtained by a sol–gel technique," *ChemSusChem*, vol. 6, no. 8, pp. 1414–1424, 2013.

[143] K. Yu and A. Eisenberg, "Bilayer morphologies of self-assembled crew-cut aggregates of amphiphilic ps-b-peo diblock copolymers in solution," *Macromolecules*, vol. 31, no. 11, pp. 3509–3518, 1998.

[144] P. E. Shaw, A. Ruseckas, and I. D. Samuel, "Exciton diffusion measurements in poly (3-hexylthiophene)," *Advanced Materials*, vol. 20, no. 18, pp. 3516–3520, 2008.

[145] A. Hexemer and P. Müller-Buschbaum, "Advanced grazing-incidence techniques for modern soft-matter materials analysis," *IUCrJ*, vol. 2, no. 1, pp. 106–125, 2015.

[146] K. Sarkar, C. J. Schaffer, D. M. González, A. Naumann, J. Perlich, and P. Müller-Buschbaum, "Tuning the pore size of zno nano-grids via time-dependent solvent annealing," *Journal of Materials Chemistry A*, vol. 2, no. 19, pp. 6945–6951, 2014.

[147] G. H. Vineyard, "Grazing-incidence diffraction and the distorted-wave approximation for the study of surfaces," *Physical Review B*, vol. 26, no. 8, p. 4146, 1982.

[148] S. Sinha, E. Sirota, Garoff, S, and H. Stanley, "X-ray and neutron scattering from rough surfaces," *Physical Review B*, vol. 38, no. 4, p. 2297, 1988.

[149] M. Rauscher, T. Salditt, and H. Spohn, "Small-angle x-ray scattering under grazing incidence: The cross section in the distorted-wave born approximation," *Physical review B*, vol. 52, no. 23, p. 16855, 1995.

[150] G. Kaune, M. Memesa, R. Meier, M. A. Ruderer, A. Diethert, S. V. Roth, M. D'Acunzi, J. S. Gutmann, and P. Muller-Buschbaum, "Hierarchically structured titania films prepared by polymer/colloidal templating," *ACS applied materials & interfaces*, vol. 1, no. 12, pp. 2862–2869, 2009.

[151] T. J. Savenije, J. M. Warman, and A. Goossens, "Visible light sensitisation of titanium dioxide using a phenylene vinylene polymer," *Chemical physics letters*, vol. 287, no. 1-2, pp. 148–153, 1998.

[152] B. Su, V. Körstgens, Y. Yao, D. Magerl, L. Song, E. Metwalli, S. Bernstorff, and P. Müller-Buschbaum, "Pore size control of block copolymer-templated sol–gel-synthesized titania films deposited via spray coating," *Journal of Sol-Gel Science and Technology*, vol. 81, no. 2, pp. 346–354, 2017.

[153] A. O. T. Patrocinio, J. Schneider, M. França, L. M. Santos, B. Caixeta, A. E. H. Machado, and D. W. Bahnemann, "Charge carrier dynamics and photocatalytic behavior of tio 2 nanopowders submitted to hydrothermal or conventional heat treatment," *RSC advances*, vol. 5, no. 86, pp. 70536–70545, 2015.

[154] Z. Li, Z. Ren, Y. Qu, S. Du, J. Wu, L. Kong, G. Tian, W. Zhou, and H. Fu, "Hierarchical n-doped tio2 microspheres with exposed (001) facets for enhanced visible light catalysis," *European Journal of Inorganic Chemistry*, vol. 2014, no. 12, pp. 2146–2152, 2014.

[155] D. Dambournet, I. Belharouak, and K. Amine, "Tailored preparation methods of tio2 anatase, rutile, brookite: mechanism of formation and electrochemical properties," *Chemistry of materials*, vol. 22, no. 3, pp. 1173–1179, 2010.

[156] D. A. Hanaor and C. C. Sorrell, "Review of the anatase to rutile phase transformation," *Journal of Materials science*, vol. 46, no. 4, pp. 855–874, 2011.

[157] G. Grancini, C. Roldán-Carmona, I. Zimmermann, E. Mosconi, X. Lee, D. Martineau, S. Narbey, F. Oswald, F. De Angelis, M. Graetzel, *et al.*, "One-year stable perovskite solar cells by 2d/3d interface engineering," *Nature communications*, vol. 8, no. 1, pp. 1–8, 2017.

[158] N. Li, L. Song, N. Hohn, N. Saxena, W. Cao, X. Jiang, and P. Müller-Buschbaum, "Nanoscale crystallization of a low band gap polymer in printed titania mesopores," *Nanoscale*, vol. 12, no. 6, pp. 4085–4093, 2020.

[159] B. O'regan and M. Grätzel, "A low-cost, high-efficiency solar cell based on dye-sensitized colloidal tio 2 films," *nature*, vol. 353, no. 6346, pp. 737–740, 1991.

[160] S. Pröller, F. Liu, C. Zhu, C. Wang, T. P. Russell, A. Hexemer, P. Müller-Buschbaum, and E. M. Herzig, "Following the morphology formation in situ in printed active layers for organic solar cells," *Advanced Energy Materials*, vol. 6, no. 1, p. 1501580, 2016.

[161] S. Guldin, S. Huttner, M. Kolle, M. E. Welland, P. Muller-Buschbaum, R. H. Friend, U. Steiner, and N. Tétreault, "Dye-sensitized solar cell based on a three-dimensional photonic crystal," *Nano letters*, vol. 10, no. 7, pp. 2303–2309, 2010.

[162] B. E. Hardin, H. J. Snaith, and M. D. McGehee, "The renaissance of dye-sensitized solar cells," *Nature photonics*, vol. 6, no. 3, pp. 162–169, 2012.

[163] B. Lee, J. He, R. P. Chang, and M. G. Kanatzidis, "All-solid-state dye-sensitized solar cells with high efficiency," *Nature*, vol. 485, no. 7399, pp. 486–489, 2012.

[164] A. Yella, H.-W. Lee, H. N. Tsao, C. Yi, A. K. Chandiran, M. K. Nazeeruddin, E. W.-G. Diau, C.-Y. Yeh, S. M. Zakeeruddin, and M. Grätzel, "Porphyrin-sensitized solar cells with cobalt (ii/iii)–based redox electrolyte exceed 12 percent efficiency," *science*, vol. 334, no. 6056, pp. 629–634, 2011.

[165] E. Lancelle-Beltran, P. Prené, C. Boscher, P. Belleville, P. Buvat, and C. Sanchez, "All-solid-state dye-sensitized nanoporous tio2 hybrid solar cells with high energy-conversion efficiency," *Advanced Materials*, vol. 18, no. 19, pp. 2579–2582, 2006.

[166] Y. Cao, Y. Saygili, A. Ummadisingu, J. Teuscher, J. Luo, N. Pellet, F. Giordano, S. M. Zakeeruddin, J.-E. Moser, M. Freitag, *et al.*, "11% efficiency solid-state dye-sensitized solar cells with copper (ii/i) hole transport materials," *Nature communications*, vol. 8, no. 1, pp. 1–8, 2017.

[167] V. Skrypnychuk, N. Boulanger, V. Yu, M. Hilke, S. C. Mannsfeld, M. F. Toney, and D. R. Barbero, "Enhanced vertical charge transport in a semiconducting p3ht thin film on single layer graphene," *Advanced Functional Materials*, vol. 25, no. 5, pp. 664–670, 2015.

[168] M. Aryal, K. Trivedi, and W. Hu, "Nano-confinement induced chain alignment in ordered p3ht nanostructures defined by nanoimprint lithography," *ACS nano*, vol. 3, no. 10, pp. 3085–3090, 2009.

[169] J. Martín, M. Campoy-Quiles, A. Nogales, M. Garriga, M. I. Alonso, A. R. Goñi, and M. Martín-González, "Poly (3-hexylthiophene) nanowires in porous alumina: internal structure under confinement," *Soft matter*, vol. 10, no. 18, pp. 3335–3346, 2014.

[170] Z.-Q. Li, Y. Ding, L.-E. Mo, L.-H. Hu, J.-H. Wu, and S.-Y. Dai, "Fine tuning of nanocrystal and pore sizes of tio2 submicrospheres toward high performance dye-sensitized solar cells," *ACS applied materials & interfaces*, vol. 7, no. 40, pp. 22277–22283, 2015.

[171] T. K. Yun, S. S. Park, D. Kim, Y.-K. Hwang, S. Huh, J. Y. Bae, and Y. S. Won, "Pore-size effect on photovoltaic performance of dye-sensitized solar cells composed of mesoporous anatase-titania," *Journal of Power Sources*, vol. 196, no. 7, pp. 3678–3682, 2011.

[172] J. Schlipf, P. Docampo, C. J. Schaffer, V. Körstgens, L. Bießmann, F. Hanusch, N. Giesbrecht, S. Bernstorff, T. Bein, and P. Müller-Buschbaum, "A closer look into two-step perovskite conversion with x-ray scattering," *The journal of physical chemistry letters*, vol. 6, no. 7, pp. 1265–1269, 2015.

[173] A. Ashokan, T. Wang, M. K. Ravva, and J.-L. Brédas, "Impact of solution temperature-dependent aggregation on the solid-state packing and electronic properties of polymers for organic photovoltaics," *Journal of Materials Chemistry C*, vol. 6, no. 48, pp. 13162–13170, 2018.

[174] C. R. McNeill, "Morphology of all-polymer solar cells," *Energy & Environmental Science*, vol. 5, no. 2, pp. 5653–5667, 2012.

[175] C. Scharsich, R. H. Lohwasser, M. Sommer, U. Asawapirom, U. Scherf, M. Thelakkat, D. Neher, and A. Köhler, "Control of aggregate formation in poly (3-hexylthiophene) by solvent, molecular weight, and synthetic method," *Journal of Polymer Science Part B: Polymer Physics*, vol. 50, no. 6, pp. 442–453, 2012.

[176] H. Hu, P. C. Chow, G. Zhang, T. Ma, J. Liu, G. Yang, and H. Yan, "Design of donor polymers with strong temperature-dependent aggregation property for efficient organic photovoltaics," *Accounts of chemical research*, vol. 50, no. 10, pp. 2519–2528, 2017.

[177] K. Thamaphat, P. Limsuwan, and B. Ngotawornchai, "Phase characterization of tio2 powder by xrd and tem," *Agriculture and Natural Resources*, vol. 42, no. 5, pp. 357–361, 2008.

[178] M. A. Ruderer, S. Guo, R. Meier, H.-Y. Chiang, V. Körstgens, J. Wiedersich, J. Perlich, S. V. Roth, and P. Müller-Buschbaum, "Solvent-induced morphology in polymer-based systems for organic photovoltaics," *Advanced Functional Materials*, vol. 21, no. 17, pp. 3382–3391, 2011.

[179] N. D. Treat, M. A. Brady, G. Smith, M. F. Toney, E. J. Kramer, C. J. Hawker, and M. L. Chabinyc, "Interdiffusion of pcbm and p3ht reveals miscibility in a photovoltaically active blend," *Advanced Energy Materials*, vol. 1, no. 1, pp. 82–89, 2011.

[180] E. Verploegen, C. E. Miller, K. Schmidt, Z. Bao, and M. F. Toney, "Manipulating the morphology of p3ht–pcbm bulk heterojunction blends with solvent vapor annealing," *Chemistry of Materials*, vol. 24, no. 20, pp. 3923–3931, 2012.

[181] W. Wang, L. Song, D. Magerl, D. Moseguí González, V. Körstgens, M. Philipp, J.-F. Moulin, and P. Müller-Buschbaum, "Influence of solvent additive 1, 8-octanedithiol on p3ht: Pcbm solar cells," *Advanced functional materials*, vol. 28, no. 20, p. 1800209, 2018.

[182] Y. Guan, G. Liu, P. Gao, L. Li, G. Ding, and D. Wang, "Manipulating crystal orientation of poly (ethylene oxide) by nanopores," *ACS Macro Letters*, vol. 2, no. 3, pp. 181–184, 2013.

[183] W. Hu and D. Frenkel, "Polymer crystallization driven by anisotropic interactions," *Interphases and Mesophases in Polymer Crystallization III*, pp. 1–35, 2005.

[184] A. Nogales, G. R. Mitchell, and A. S. Vaughan, "Anisotropic crystallization in polypropylene induced by deformation of a nucleating agent network," *Macromolecules*, vol. 36, no. 13, pp. 4898–4906, 2003.

[185] H. Wu, W. Wang, Y. Huang, and Z. Su, "Orientation of syndiotactic polystyrene crystallized in cylindrical nanopores," *Macromolecular rapid communications*, vol. 30, no. 3, pp. 194–198, 2009.

[186] H. Wu, W. Wang, H. Yang, and Z. Su, "Crystallization and orientation of syndiotactic polystyrene in nanorods," *Macromolecules*, vol. 40, no. 12, pp. 4244–4249, 2007.

[187] R. M. Michell, I. Blaszczyk-Lezak, C. Mijangos, and A. J. Müller, "Confinement effects on polymer crystallization: From droplets to alumina nanopores," *Polymer*, vol. 54, no. 16, pp. 4059–4077, 2013.

[188] N. Li, W. Chen, L. Song, R. Guo, M. A. Scheel, D. Yang, V. Körstgens, M. Schwartzkopf, S. V. Roth, and P. Müller-Buschbaum, "In situ study of order formation in mesoporous titania thin films templated by a diblock copolymer during slot-die printing," *ACS Applied Materials & Interfaces*, 2020.

[189] X. Feng, J. Zhai, and L. Jiang, "The fabrication and switchable superhydrophobicity of tio2 nanorod films," *Angewandte Chemie*, vol. 117, no. 32, pp. 5245–5248, 2005.

[190] Y. Xu, T. F. Tay, L. Cui, J. Fan, C. Niu, D. Chen, Z. X. Guo, C. Sun, X. L. Zhang, and R. A. Caruso, "Trace-level fluorination of mesoporous tio2 improves photocatalytic and pb (ii) adsorbent performances," *Inorganic Chemistry*, vol. 59, no. 23, pp. 17631–17637, 2020.

[191] B. Qiu, M. Xing, and J. Zhang, "Mesoporous tio2 nanocrystals grown in situ on graphene aerogels for high photocatalysis and lithium-ion batteries," *Journal of the American Chemical Society*, vol. 136, no. 16, pp. 5852–5855, 2014.

[192] N.-G. Park, "Research direction toward scalable, stable, and high efficiency perovskite solar cells," *Advanced Energy Materials*, vol. 10, no. 13, p. 1903106, 2020.

[193] M. Gnanaseelan, U. Kalita, A. Janke, J. Pionteck, B. Voit, and N. K. Singha, "All methacrylate block copolymer/tio2 nanocomposite via atrp and in-situ sol-gel process," *Materials Today Communications*, vol. 22, p. 100728, 2020.

[194] M. Hu, L. Zhang, S. She, J. Wu, X. Zhou, X. Li, D. Wang, J. Miao, G. Mi, H. Chen, *et al.*, "Electron transporting bilayer of sno2 and tio2 nanocolloid enables highly efficient planar perovskite solar cells," *Solar RRL*, vol. 4, no. 1, p. 1900331, 2020.

[195] A. G. Tomulescu, V. Stancu, C. Beşleagă, M. Enculescu, G. A. Nemneş, M. Florea, V. Dumitru, L. Pintilie, I. Pintilie, and L. Leonat, "Reticulated mesoporous tio2 scaffold, fabricated by spray coating, for large-area perovskite solar cells," *Energy Technology*, vol. 8, no. 1, p. 1900922, 2020.

[196] G. Ruani, C. Ancora, F. Corticelli, C. Dionigi, and C. Rossi, "Single-step preparation of inverse opal titania films by the doctor blade technique," *Solar energy materials and solar cells*, vol. 92, no. 5, pp. 537–542, 2008.

[197] S. V. Roth, "A deep look into the spray coating process in real-time—the crucial role of x-rays," *Journal of Physics: Condensed Matter*, vol. 28, no. 40, p. 403003, 2016.

[198] W. Chen, H. Tang, N. Li, M. A. Scheel, Y. Xie, D. Li, V. Körstgens, M. Schwartzkopf, S. V. Roth, K. Wang, *et al.*, "Colloidal pbs quantum dot stacking kinetics during deposition via printing," *Nanoscale horizons*, vol. 5, no. 5, pp. 880–885, 2020.

[199] Y.-J. Cheng, P. Müller-Buschbaum, and J. S. Gutmann, "Ultrathin anatase tio2 films with stable vesicle morphology templated by pmma-b-peo," *Small*, vol. 3, no. 8, pp. 1379–1382, 2007.

[200] P. Müller-Buschbaum and M. Stamm, "Correlated roughness, long-range correlations, and dewetting of thin polymer films," *Macromolecules*, vol. 31, no. 11, pp. 3686–3692, 1998.

[201] S. Xia, L. Song, W. Chen, V. Körstgens, M. Opel, M. Schwartzkopf, S. V. Roth, and P. Müller-Buschbaum, "Printed thin diblock copolymer films with dense magnetic nanostructure," *ACS applied materials & interfaces*, vol. 11, no. 24, pp. 21935–21945, 2019.

[202] N. Olichwer, A. Meyer, M. Yesilmen, and T. Vossmeyer, "Gold nanoparticle superlattices: correlating chemiresistive responses with analyte sorption and swelling," *Journal of Materials Chemistry C*, vol. 4, no. 35, pp. 8214–8225, 2016.

[203] X. Huang, J. Zhu, B. Ge, K. Deng, X. Wu, T. Xiao, T. Jiang, Z. Quan, Y. C. Cao, and Z. Wang, "Understanding fe3o4 nanocube assembly with reconstruction of a consistent superlattice phase diagram," *Journal of the American Chemical Society*, vol. 141, no. 7, pp. 3198–3206, 2019.

[204] H.-S. Jang, T.-H. Kim, C. Do, M.-J. Lee, and S.-M. Choi, "Single-walled carbon nanotube induced re-entrant hexagonal phases in a pluronic block copolymer system," *Soft Matter*, vol. 9, no. 11, pp. 3050–3056, 2013.

[205] K. Bian, J. J. Choi, A. Kaushik, P. Clancy, D.-M. Smilgies, and T. Hanrath, "Shape-anisotropy driven symmetry transformations in nanocrystal superlattice polymorphs," *ACS nano*, vol. 5, no. 4, pp. 2815–2823, 2011.

[206] J. J. Choi, K. Bian, W. J. Baumgardner, D.-M. Smilgies, and T. Hanrath, "Interface-induced nucleation, orientational alignment and symmetry transformations in nanocube superlattices," *Nano letters*, vol. 12, no. 9, pp. 4791–4798, 2012.

[207] W. Cao, S. Xia, M. Appold, N. Saxena, L. Bießmann, S. Grott, N. Li, M. Gallei, S. Bernstorff, and P. Müller-Buschbaum, "Self-assembly in ultrahigh molecular weight sphere-forming diblock copolymer thin films under strong confinement," *Scientific reports*, vol. 9, no. 1, pp. 1–9, 2019.

[208] D. Cheneler and J. Bowen, "Degradation of polymer films," *Soft Matter*, vol. 9, no. 2, pp. 344–358, 2013.

[209] K. Bian, Z. Wang, and T. Hanrath, "Comparing the structural stability of pbs nanocrystals assembled in fcc and bcc superlattice allotropes," *Journal of the American Chemical Society*, vol. 134, no. 26, pp. 10787–10790, 2012.

[210] M. C. Weidman, D.-M. Smilgies, and W. A. Tisdale, "Kinetics of the self-assembly of nanocrystal superlattices measured by real-time in situ x-ray scattering," *Nature materials*, vol. 15, no. 7, pp. 775–781, 2016.

[211] J. Perlich, J. Rubeck, S. Botta, R. Gehrke, S. Roth, M. Ruderer, S. Prams, M. Rawolle, Q. Zhong, V. Körstgens, *et al.*, "Grazing incidence wide angle x-ray scattering at the wiggler beamline bw4 of hasylab," *Review of Scientific Instruments*, vol. 81, no. 10, p. 105105, 2010.

[212] P. W. Majewski and K. G. Yager, "Reordering transitions during annealing of block copolymer cylinder phases," *Soft Matter*, vol. 12, no. 1, pp. 281–294, 2016.

[213] J. Zhang, D. Posselt, D.-M. Smilgies, J. Perlich, K. Kyriakos, S. Jaksch, and C. M. Papadakis, "Lamellar diblock copolymer thin films during solvent vapor annealing studied by gisaxs: different behavior of parallel and perpendicular lamellae," *Macromolecules*, vol. 47, no. 16, pp. 5711–5718, 2014.

[214] P. Ziherl and R. D. Kamien, "Maximizing entropy by minimizing area: Towards a new principle of self-organization," 2001.

[215] N. Goubet, J. Richardi, P.-A. Albouy, and M.-P. Pileni, "Which forces control supracrystal nucleation in organic media?," *Advanced Functional Materials*, vol. 21, no. 14, pp. 2693–2704, 2011.

[216] B. A. Korgel and D. Fitzmaurice, "Small-angle x-ray-scattering study of silver-nanocrystal disorder-order phase transitions," *Physical Review B*, vol. 59, no. 22, p. 14191, 1999.

[217] G. Renaud, R. Lazzari, and F. Leroy, "Probing surface and interface morphology with grazing incidence small angle x-ray scattering," *Surface Science Reports*, vol. 64, no. 8, pp. 255–380, 2009.

[218] S. Guldin, "Tunable mesoporous bragg reflectors based on block copolymer self-assembly," in *Inorganic Nanoarchitectures by Organic Self-Assembly*, pp. 117–127, Springer, 2013.

[219] N. Li, R. Guo, W. Chen, V. Körstgens, J. E. Heger, S. Liang, C. J. Brett, M. A. Hossain, J. Zheng, P. S. Deimel, *et al.*, "Tailoring ordered mesoporous titania films via introducing germanium nanocrystals for enhanced electron transfer photoanodes for photovoltaic applications," *Advanced Functional Materials*, p. 2102105, 2021.

[220] K. Lan, R. Wang, Q. Wei, Y. Wang, A. Hong, P. Feng, and D. Zhao, "Stable ti3+ defects in oriented mesoporous titania frameworks for efficient photocatalysis," *Angewandte Chemie*, vol. 132, no. 40, pp. 17829–17836, 2020.

[221] H. Liu, W. Li, D. Shen, D. Zhao, and G. Wang, "Graphitic carbon conformal coating of mesoporous tio2 hollow spheres for high-performance lithium ion battery anodes," *Journal of the American Chemical Society*, vol. 137, no. 40, pp. 13161–13166, 2015.

[222] C. Yi, X. Li, J. Luo, S. M. Zakeeruddin, and M. Grätzel, "Perovskite photovoltaics with outstanding performance produced by chemical conversion of bi-

layer mesostructured lead halide/tio2 films," *Advanced Materials*, vol. 28, no. 15, pp. 2964–2970, 2016.

[223] W. S. Yang, J. H. Noh, N. J. Jeon, Y. C. Kim, S. Ryu, J. Seo, and S. I. Seok, "High-performance photovoltaic perovskite layers fabricated through intramolecular exchange," *Science*, vol. 348, no. 6240, pp. 1234–1237, 2015.

[224] H. Nagaoka, F. Ma, D. W. Dequilettes, S. M. Vorpahl, M. S. Glaz, A. E. Colbert, M. E. Ziffer, and D. S. Ginger, "Zr incorporation into tio2 electrodes reduces hysteresis and improves performance in hybrid perovskite solar cells while increasing carrier lifetimes," *The journal of physical chemistry letters*, vol. 6, no. 4, pp. 669–675, 2015.

[225] H. Zhou, Q. Chen, G. Li, S. Luo, T.-b. Song, H.-S. Duan, Z. Hong, J. You, Y. Liu, and Y. Yang, "Interface engineering of highly efficient perovskite solar cells," *Science*, vol. 345, no. 6196, pp. 542–546, 2014.

[226] D. Wang, Y.-L. Chang, Q. Wang, J. Cao, D. B. Farmer, R. G. Gordon, and H. Dai, "Surface chemistry and electrical properties of germanium nanowires," *Journal of the American Chemical Society*, vol. 126, no. 37, pp. 11602–11611, 2004.

[227] K. A. Mengle, S. Chae, and E. Kioupakis, "Quasiparticle band structure and optical properties of rutile geo2, an ultra-wide-band-gap semiconductor," *Journal of Applied Physics*, vol. 126, no. 8, p. 085703, 2019.

[228] H. Wu, J. Liu, M. Ge, L. Niu, Y. Zeng, Y. Wang, G. Lv, L. Wang, G. Zhang, and J. Jiang, "Preparation of monodisperse geo2 nanocubes in a reverse micelle system," *Chemistry of Materials*, vol. 18, no. 7, pp. 1817–1820, 2006.

[229] M. M. Bentlohner, M. Waibel, P. Zeller, K. Sarkar, P. Müller-Buschbaum, D. Fattakhova-Rohlfing, and T. F. Fässler, "Zintl clusters as wet-chemical precursors for germanium nanomorphologies with tunable composition," *Angewandte Chemie International Edition*, vol. 55, no. 7, pp. 2441–2445, 2016.

[230] A. Kitiyanan, T. Kato, Y. Suzuki, and S. Yoshikawa, "The use of binary tio2–geo2 oxide electrodes to enhanced efficiency of dye-sensitized solar cells," *Journal of Photochemistry and Photobiology A: Chemistry*, vol. 179, no. 1-2, pp. 130–134, 2006.

[231] S. Chatterjee, "The optoelectronic properties of titania–germanium nanocomposites," *Journal of Physics D: Applied Physics*, vol. 41, no. 5, p. 055301, 2008.

[232] M. Ahmad, A. Pandey, and N. Rahim, "Effect of germanium on the tio2 photoanode for dye sensitized solar cell applications. a potential sintering aid," in *IOP Conference Series: Materials Science and Engineering*, vol. 358, p. 012015, IOP Publishing, 2018.

[233] A. F. Khan, M. Mehmood, T. Ali, and H. Fayaz, "Structural and optical studies of nanostructured tio2–ge multi-layer thin films," *Thin Solid Films*, vol. 536, pp. 220–228, 2013.

[234] J. Gutierrez, A. Tercjak, and I. Mondragon, "Conductive behavior of high tio2 nanoparticle content of inorganic/organic nanostructured composites," *Journal of the American Chemical Society*, vol. 132, no. 2, pp. 873–878, 2010.

[235] J. N. Albert and T. H. Epps III, "Self-assembly of block copolymer thin films," *Materials Today*, vol. 13, no. 6, pp. 24–33, 2010.

[236] S. Xia, L. Song, N. Hohn, K. Wang, S. Grott, M. Opel, M. Schwartzkopf, S. V. Roth, and P. Müller-Buschbaum, "Spray-coating magnetic thin hybrid films of ps-b-pnipam and magnetite nanoparticles," *Advanced Functional Materials*, vol. 29, no. 15, p. 1808427, 2019.

[237] Q. Ma, T. P. Qin, S. J. Liu, L. Q. Weng, and W. Y. Dong, "Morphology and photocatalysis of mesoporous titania thin films annealed in different atmosphere for degradation of methyl orange," *Applied Physics A*, vol. 104, no. 1, pp. 365–373, 2011.

[238] L. Song, M. Rawolle, N. Hohn, J. S. Gutmann, H. Frielinghaus, and P. Müller-Buschbaum, "Deformation of mesoporous titania nanostructures in contact with d2o vapor," *Small*, vol. 14, no. 30, p. 1801461, 2018.

[239] S. Xia, L. Song, V. Körstgens, M. Opel, M. Schwartzkopf, S. V. Roth, and P. Müller-Buschbaum, "Magnetic nanoparticle-containing soft–hard diblock copolymer films with high order," *Nanoscale*, vol. 10, no. 25, pp. 11930–11941, 2018.

[240] N. M. Al-Hada, E. B. Saion, A. H. Shaari, M. A. Kamarudin, M. H. Flaifel, S. H. Ahmad, and S. A. Gene, "A facile thermal-treatment route to synthesize zno nanosheets and effect of calcination temperature," *PloS one*, vol. 9, no. 8, p. e103134, 2014.

[241] X. Wang, Z. Xue, and J. Li, "Investigation of the reactivity and grain size of lime calcined at extra-high temperatures by flash heating," *Journal of the Southern African Institute of Mining and Metallurgy*, vol. 116, no. 12, pp. 1159–1164, 2016.

[242] Y. Son, M. Park, Y. Son, J.-S. Lee, J.-H. Jang, Y. Kim, and J. Cho, "Quantum confinement and its related effects on the critical size of geo2 nanoparticles anodes for lithium batteries," *Nano letters*, vol. 14, no. 2, pp. 1005–1010, 2014.

[243] M. Javadi, D. Picard, R. Sinelnikov, M. A. Narreto, F. A. Hegmann, and J. G. Veinot, "Synthesis and surface functionalization of hydride-terminated ge nanocrystals obtained from the thermal treatment of ge (oh) 2," *Langmuir*, vol. 33, no. 35, pp. 8757–8765, 2017.

[244] N. Hohn, A. E. Hetzenecker, M. A. Giebel, S. Geier, L. Bießmann, V. Körstgens, N. Saxena, J. Schlipf, W. Ohm, P. S. Deimel, *et al.*, "Amphiphilic diblock copolymer-mediated structure control in nanoporous germanium-based thin films," *Nanoscale*, vol. 11, no. 4, pp. 2048–2055, 2019.

[245] J. Zhao, L. Yang, J. A. McLeod, and L. Liu, "Reduced geo 2 nanoparticles: Electronic structure of a nominal geo x complex and its stability under h 2 annealing," *Scientific reports*, vol. 5, no. 1, pp. 1–10, 2015.

[246] K. Prajwal, A. C. M. Esther, and A. Dey, "Rf transparent vanadium oxide based single and bi-layer thin films as passive thermal control element for satellite antenna application," *Ceramics International*, vol. 44, no. 13, pp. 16088–16091, 2018.

[247] K. Prabhakaran and T. Ogino, "Oxidation of ge (100) and ge (111) surfaces: an ups and xps study," *Surface Science*, vol. 325, no. 3, pp. 263–271, 1995.

[248] K. Prabhakaran, F. Maeda, Y. Watanabe, and T. Ogino, "Thermal decomposition pathway of ge and si oxides: observation of a distinct difference," *Thin Solid Films*, vol. 369, no. 1-2, pp. 289–292, 2000.

[249] W. L. Jolly and W. M. Latimer, "The equilibrium ge (s)+ geo2 (s)= 2geo (g). the heat of formation of germanic oxide," *Journal of the American Chemical Society*, vol. 74, no. 22, pp. 5757–5758, 1952.

[250] S. Golczak, A. Kanciurzewska, M. Fahlman, K. Langer, and J. J. Langer, "Comparative xps surface study of polyaniline thin films," *Solid State Ionics*, vol. 179, no. 39, pp. 2234–2239, 2008.

[251] Q. Jiang, Z. Chu, P. Wang, X. Yang, H. Liu, Y. Wang, Z. Yin, J. Wu, X. Zhang, and J. You, "Planar-structure perovskite solar cells with efficiency beyond 21%," *Advanced materials*, vol. 29, no. 46, p. 1703852, 2017.

[252] D. Yang, R. Yang, K. Wang, C. Wu, X. Zhu, J. Feng, X. Ren, G. Fang, S. Priya, and S. F. Liu, "High efficiency planar-type perovskite solar cells with negligible hysteresis using edta-complexed sno 2," *Nature communications*, vol. 9, no. 1, pp. 1–11, 2018.

[253] X. Sun, J. Xu, L. Xiao, J. Chen, B. Zhang, J. Yao, and S. Dai, "Influence of the porosity of the tio2 film on the performance of the perovskite solar cell," *International Journal of Photoenergy*, vol. 2017, 2017.

[254] N. Kholmicheva, P. Moroz, H. Eckard, G. Jensen, and M. Zamkov, "Energy transfer in quantum dot solids," *ACS Energy Letters*, vol. 2, no. 1, pp. 154–160, 2017.

[255] Y. Li, L. Meng, Y. M. Yang, G. Xu, Z. Hong, Q. Chen, J. You, G. Li, Y. Yang, and Y. Li, "High-efficiency robust perovskite solar cells on ultrathin flexible substrates," *Nature communications*, vol. 7, no. 1, pp. 1–10, 2016.

[256] P.-W. Liang, C.-Y. Liao, C.-C. Chueh, F. Zuo, S. T. Williams, X.-K. Xin, J. Lin, and A. K.-Y. Jen, "Additive enhanced crystallization of solution-processed perovskite for highly efficient planar-heterojunction solar cells," *Advanced materials*, vol. 26, no. 22, pp. 3748–3754, 2014.

List of publications

Publications related to the dissertation

- N. Li, L. Song, L. Bießmann, S. Xia, W. Ohm, C. J. Brett, E. Hadjixenophontos, G. Schmitz, S. V Roth and P. Müller-buschbaum, "Morphology phase diagram of slot-die printed TiO_2 films based on sol–gel synthesis", *Adv. Mater. interface*, 1900558, 1–9, 2019.
- N. Li, L. Song, N. Hohn, N. Saxena, W. Cao, X. Jiang, P. Müller-Buschbaum, "Nanoscale crystallization of a low band gap polymer in printed titania mesopores", *Nanoscale*, 12, 4085–4093, 2020.
- N. Li, W. Chen, L. Song, R. Guo, M. A. Scheel, D. Yang, V. Körstgens, M. Schwartzkopf, S. V. Roth, P. Müller-Buschbaum, "In situ study of order formation in mesoporous titania thin films templated by a diblock copolymer during slot-die printing", *ACS Appl. Mater. Interfaces*, 12, 57627–57637, 2020.
- N. Li, R. Guo, W. Chen, V. Körstgens, J. E. Heger, S. Liang, C. J. Brett, M. A. Hossain, J. Zheng, P. S. Deimel, A. Buyruk, F. Allegretti, M. Schwartzkopf, J. G. C. Veinot, G. Schmitz, J. V. Barth, T. Ameri, S. V. Roth, P. Müller-Buschbaum, "Tailoring ordered mesoporous titania films via introducing germanium nanocrystals for enhanced electron transfer photoanodes for photovoltaic applications", *Adv. Funct. Mater.*, 2102105, 2021.

Further publications

- W. Cao, S. Xia, M. Appold, N. Saxena, L. Bießmann, S. Grott, N. Li, M. Gallei, S. Bernstorff, P. Müller-Buschbaum, "Self-assembly in ultrahigh molecular weight sphere-forming diblock copolymer thin films under strong confinement", *Sci. Rep.*, 9, 1–9, 2019.

- N. Saxena, B. Pretzl, X. Lamprecht, L. Bießmann, D. Yang, N. Li, C. Bilko, S. Bernstorff, P. Müller-Buschbaum, "Ionic liquids as post-treatment agents for simultaneous improvement of seebeck coefficient and electrical conductivity in PEDOT:PSS films", *ACS Appl. Mater. Interfaces*, 11, 8060–8071, 2019.
- W. Chen, H. Tang, N. Li, M. A. Scheel, Y. Xie, D. Li, V. Körstgens, M. Schwartzkopf, S. V. Roth, K. Wang, et al., "Colloidal PbS quantum dot stacking kinetics during deposition via printing", *Nanoscale Horizons*, 5, 880–885, 2020.
- D. Yang, B. Cao, V. Körstgens, N. Saxena, N. Li, C. Bilko, S. Grott, W. Chen, X. Jiang, J. E. Heger, et al., "Tailoring morphology compatibility and device stability by adding PBDTTPD-COOH as third component to fullerene-based polymer solar cells", *ACS Appl. Energy Mater.*, 3, 2604–2613, 2020.
- W. Chen, S. Liang, F. Löhrer, S. J. Schaper, N. Li, W. Cao, L. P. Kreuzer, H. Liu, H. Tang, V. Körstgens, et al., "In situ grazing-incidence small-angle x-ray scattering observation of gold sputter deposition on a PbS quantum dot solid", *ACS Appl. Mater. Interfaces*, 12, 46942–46952, 2020.
- W. Chen, H. Tang, Y. Chen, J. E. Heger, N. Li, L. Kreuzer, L. P. Kreuzer, Y. Xie, D. Li, C. Anthony, Z. Pikramenou, et al., "Spray-deposited PbS colloidal quantum dot solid for near-infrared photodetectors", *Nano Energy*, 78, 105254, 2020.
- M. Gensch, M. Schwartzkopf, C. J. Brett, S. J. Schaper, L. P. Kreuzer, N. Li, W. Chen, S. Liang, J. Drewes, O. Polonskyi, T. Strunskus, F. Faupel, P. Müller-Buschbaum, and S. V. Roth, "Selective Silver Nanocluster Metallization on Conjugated Diblock Copolymer Templates for Sensing and Photovoltaic Applications", *ACS Appl. Nano Mater.*, 4, 4245–4255, 2021.
- S. Yin, W. Cao, Q. Ji, Y. Cheng, L. Song, N. Li, C. L. Weindl, M. Schwartzkopf, S. V. Roth, and P. Müller-Buschbaum, "Multidimensional morphology control for PS-b-P4VP templated mesoporous iron (III) oxide thin films", *Adv. Mater. Interfaces*, 2100141, 2021.
- W. Chen, R. Guo, H. Tang, K. S. Wienhold, N. Li, Z. Jiang, J. Tang, X. Jiang, L. P. Kreuzer, H. Liu, M. Schwartzkopf, X. W. Sun, S. V. Roth, K. Wang, B. Xu, and P. Müller-Buschbaum, "Operando structure degradation study of PbS quantum dot solar cells", *Energy Environ. Sci.*, 14, 3420–3429, 2021.

Scientific reports

- N. Li, L. Song, L. Bießmann, P. Muller-Buschbaum, "Morphology phase diagram of printed titania films derived from block copolymer assisted sol-gel templating", *Lehrstuhl für Funktionelle Materialien, Annual Report*, 2017.
- N. Li, L. Song, N. Saxena, W. Cao, X. Jiang, P. Muller-Buschbaum, "Nano-scale crystallization of poly(3-hexylthiophene) in printed titania pores", *Lehrstuhl für Funktionelle Materialien, Annual Report*, 2018.
- N. Li, J. E. Heger, R. Schaffrinna, P. Muller-Buschbaum, "Highly ordered titania films with incorporated germanium nanocrystals used as photoanodes", *Lehrstuhl für Funktionelle Materialien, Annual Report*, 2019.
- N. Li, R. Guo, S. Bernstorff, P. Muller-Buschbaum, "In operando GISAXS study of degradation in titania-based solid-state dyesensitized solar cells", *Lehrstuhl für Funktionelle Materialien, Annual Report*, 2020.

Conference talks

- N. Li, X. Jiang, R. Schaffrinna, "UV-VIS spectroscopy", *E13 Polymer Physics Summer School*, Obertauern, Austria, June 2018.
- N. Li, "Nanoscale crystallization of a low band gap polymer in printed titania pores", *4th internal biennial science meeting of the MLZ*, Grainau, Germany. June 2019.
- N. Li, R. Guo, W. Chen, V. Körstgens, J. E. Heger, S. Liang, C. J. Brett, M. A. Hossain, J. Zheng, P. S. Deimel, A. Buyruk, F. Allegretti, M. Schwartzkopf, J. G. C. Veinot, G. Schmitz, J. V. Barth, T. Ameri, S. V. Roth, P. Müller-Buschbaum, "Tailoring ordered mesoporous titania films via introducing germanium nanocrystals for enhanced electron transfer photoanodes", *ACS Spring 2021*, online, April 2021.

Conference poster presentations

- N. Li, B. Su, S. Xia, P. Müller-Buschbaum, "Morphology phase diagram of printed titania films derived from block copolymer assisted sol-gel templating", *DPG-Frühjahrstagung*, Berlin (Germany), March 2018.
- N. Li, L. Song, L. Bießmann, S. Xia, W. Ohm, C. Brett, S, V. Roth, P. Müller-Buschbaum, "Morphology phase diagram of printed titania films assisted a sol-gel technique", *8th Colloquium of the Munich School of Engineering*, Garching (Germany), July 2018.

- N. Li, L. Song, L. Bießmann, W. Ohm, C. Brett, S, V. Roth, S. Xia, P. Müller-Buschbaum, "Morphology phase diagram of printed titania films derived from block copolymer template assisted a sol-gel technique", *4th German SNI Conference*, Garching (Germany), September 2018.
- N. Li, L. Song, L. Bießmann, S. Xia, W. Ohm, C. Brett, S, V. Roth, P. Müller-Buschbaum, "Morphology phase diagram of printed titania films derived from block copolymer template assisted sol-gel synthesis", *7th SolTech Conference: Solar Technologies go Hybrid*, Würzburg (Germany), October 2018.
- N. Li, L. Song, N. Hohn, N. Saxena, W. Cao, X. Jiang, P. Müller-buschbaum, "Nanoconfinement on chain alighment and crystallization of conjugated polymers P3HT and PffBT4T-2OD by printed mesoporous TiO_2 photoanodes", *9th Colloquium of the Munich School of Engineering*, Garching (Germany), August 2019.
- N. Li, S. Yin, J. E. Heger1, R. Schaffrinna1, C. J. Brett2, M. A. Hossain, J. Zheng, P. S. Deime, F. Allegretti, M. Schwartzkopf, G. Schmitz, J. V. Barth, J. G. C. Veinot, S. V. Roth, P. Müller-Buschbaum,"Highly ordered titania films with incorporated germanium nanoparticles calcined under different atmospheres", *MLZ User Meeting 2019*, Munich (Germany), December 2019.
- N. Li, L. Song, N. Hohn, N. Saxena, W. Cao, X. Jiang, P. Müller-buschbaum, "Nanoconfinement on chain alighment and crystallization of conjugated polymers P3HT and PffBT4T-2OD by printed mesoporous TiO_2 photoanodes", *10th Colloquium of the Munich School of Engineering*, online, July 2020.
- N. Li, R. Guo, W. Chen, V. Körstgens, J. E. Heger, S. Liang, C. J. Brett, M. A. Hossain, J. Zheng, P. S. Deimel, A. Buyruk, F. Allegretti, M. Schwartzkopf, J. G. C. Veinot, G. Schmitz, J. V. Barth, T. Ameri, S. V. Roth, P. Müller-Buschbaum, "Highly ordered titania films with incorporated germanium nanoparticles for photoanodes", *MLZ User Meeting 2020*, online, December 2020.
- N. Li, R. Guo, W. Chen, V. Körstgens, J. E. Heger, S. Liang, C. J. Brett, M. A. Hossain, J. Zheng, P. S. Deimel, A. Buyruk, F. Allegretti, M. Schwartzkopf, J. G. C. Veinot, G. Schmitz, J. V. Barth, T. Ameri, S. V. Roth, P. Müller-Buschbaum, "Tuning ordered mesoporous titania films via introducing germanium nanocrystals for high-efficient photoanodes", *DPG-Frühjahrstagung*, online, March 2021.

Acknowledgments

First, I would like to thank Prof. Dr. Peter Müller-Buschbaum for offering the opportunity to work in E13 group of Physics Department in Technical University of Munich, and for providing the access to the field of titania-based solar cells. Via this nice topic, I learnt a lot of basic principles and had deep understanding on semiconducting materials and photovoltaics. Also, many thanks for him to provide me the rare chances to work with the advanced synchrotron radiation based scattering techniques. During my PhD study, he was highly supportive and always gave me key suggestions in my research work. Even though he was very busy, he was always quite patient to discuss with me about the data analysis, and to answer the questions which confused me. Moreover, he highly encouraged me to attend conferences ranging from the international conference like ACS, to some important workshops like MSE. In addition, he also kindly reminded me some points which I need to improve, including talking and discussing more with my colleagues about the professional skills, reinforcing basic theoretical aspects and being more positive to express myself. With these precious feedback and suggestions, I also made some progresses on my shortage, which was invaluable for the success of my study, and would also be useful for my job in the future.

I am very grateful that the China Scholarship Council (CSC) provided me the funding to support my living costs in Germany and allowed me to focus on my PhD study.

I would like to thank the beamline scientists at both DESY (Hamburg, Germany) and Elettra (Trieste, Italy). They provided me the access to learning and operating the synchrotron based large facility. I would like to thank Prof. Dr. Stephan V. Roth, Dr. Matthias Schwartzkopf and Dr. Wiebke Ohm at DESY and Dr. Sigrid Bernstorff at Elettra. Without their great contributions and high supporting, the successful data cannot be obtained, which is an important and highlighted part in the present thesis. In addition, many thanks for Calvin J. Brett for his help on the ”in situ spray” beamtime topic. I am very glad to work with him.

I am thankful to the help from Dr. Lin Song and Dr. Bo Su at the beginning of my PhD study. Especially for Dr. Lin Song, he taught me many professional knowledge, did extensive data discussion with me, and gave me a quantity of useful suggestions. Without his help, I cannot move so fast in my projects. Also, thanks for the exchanged master

student, Magdalini Spyranti. The working time with her ($\sim$ 1 year) enriched my PhD study and hope she will have a wonderful future.

I enjoyed the working with my colleagues who highly supported me at the beamline. Here, I want to thank Dr. Volker Körstgens, Dr. Lorenz Bießmann, Dr. Nitin Saxena, Dr. Dan Yang, Julian E. Heger, Anna-lena Oechsle, Shanshan Yin, Roy Schaffrinna, Dr. Wei Chen, Renjun Guo and Manuel A. Scheel (no specific order) for their kind help, extreme patience and nice discussion. I am very happy to have and work with these team members, with whom I spent wonderful and unforgettable time. Especially thank Dr. Lorenz Bießmann and Dr. Dan Yang to work with me, and show me how to measure GISAXS/GIWAXS at DESY and Elettra, respectively.

Simultaneously, I really appreciate the help and contributions from the internal group members. First, I would like to thank Prof. Dr. Christine Papadakis to be my mentor. At the last and key moment, she very nicely provided me the chance for finishing my teaching points. She was so nice and patient to me and gave me a lot of encouragements for the exercise lecture. Second, I want to thank Dr. Florian Jung and Dr. Wei Chen for explaining the theoretical knowledge about X-ray scattering. Via the discussion with them, I had better understanding on GISAXS, and also deep insights into it. Third, I sincerely appreciate that Renjun Guo supported me for my soar cell fabrication and Simon Jakob Schaper showed me how to measure the SAXS/GISAXS with the in-house Genesha SAXSLAB instrument. Also, thank them for nice discussion about my PhD work.

I am really grateful that Dr. Volker Körstgens, Lennart Reb, Julian E. Heger, Christian L. Weindl, Manuel A. Scheel, Christina Geiger, Julija Reitenbach, Christopher R. Everett, Anna Lena Oechsle, Ting Tian, Dominik Schwaiger, Renjun Guo and Suzhe Liang for the thesis revision. Especially thank Lennart Reb to translate my abstract from English to German.

Beside, there are many other kind colleagues during my PhD study who I do not mention yet, but also want to thank in no specific order: Dr. Senlin Xia, Dr. Kun Wang, Wei Cao, Xinyu Jiang, Tianxiao, Xiao, Chia-Hsin Ko, Jia-Jhen Kang, Sebastian Grott, Franziska Löhrer, Shambhavi Pratap, Lucas P. Kreuzer, Marc Gensch, Tobias Widmann, Yuqin Zou, Suo Tu, Yanan Li, Peixi Wang, Tianfu Guan and so on. I really enjoyed the wonderful time with them, and the nice and friendly atmosphere in our group.

I really enjoyed the collaboration with the several groups as follow. First, I would like to thank Prof. Dr. Jonathan G. C. Veinot and Dr. Md Asjad Hossain for providing me the germanium nanocrystals. I am grateful for Prof. Dr. Jonathan G. C. Veinot for his corrections and suggestions in my manuscript and for Dr. Md Asjad Hossain for the discussion about the germanium nanocrystals. Second, I want to thank Dr. Peter S. Deimel, Dr. Ali Buyruk and Prof. Johannes V. Barth for providing me the access to XPS

measurements. In addition, I want to thank Jianshu Zheng, Dr. Efi Hadjixenophontos and Prof. Guido Schmitz for the TEM measurements, and Ali Buyruk and Prof. Tayebeh Ameri for the PL/TRPL measurements. Finally, I am highly appreciated that Prof. Alexander Holleitner and Peter Weiser provided me the chance for operating the SEM device. Especially for Peter Weiser, he helped me to solve some difficult problems and trusted me a lot during the long operation time ($\sim$ 3 year).

I am sincerely grateful that our secretaries Marion Waletzki and Carola Kappauf gave me so many helps during my PhD period, including dealing with the visa extension, contract, reimbursements, and organizing many activities such as summer school, hiking and so on.

Last but not least, I would like to thank my parents and my sister. They highly support me to pursue my dream, and watch me to move forward step by step. Their love and encouragements drive me to become better myself in both work and daily life. Simultaneously, I would like to thank my friends who have accompanied me for many years. After walking for a long journey, they are still there, and never far away from me.